Effects of Martensite Tempering on HAZ-Softening and Tensile Properties of Resistance Spot Welded Dual-Phase Steels

by

Victor Hugo Baltazar Hernandez

A thesis
presented to the University of Waterloo
in fulfilment of the
thesis requirement for the degree of
Doctor of Philosophy
in
Mechanical Engineering

Waterloo, Ontario, Canada, 2010

I hereby declare that I am the sole author of this thesis. This is a true copy of the thesis, including any required final revisions, as accepted by my examiners.

I understand that my thesis may be made electronically available to the public.

Abstract

The main purpose of this thesis is to improve the fundamental knowledge of non-isothermal tempering of martensite phase and its effects on the reduction in hardness (softening) with respect the base metal occurring at the heat affected zone (HAZ) of resistance spot welded dual-phase (DP) steels. This thesis also aims at understanding the influence of HAZ-softening on the joint performance of various DP steel grades.

The tempering of martensite occurring at the sub-critical HAZ (SC-HAZ) of resistance spot welded DP600, DP780 and DP980 steels has been systematically evaluated by microhardness testing through Vickers indentation and the degree of tempering has been correlated to the HAZ-softening. From the joint performance analysis of similar and dissimilar steel grade combinations assessed through standardized testing methods, three important issues have been targeted: a) the joint strength (maximum load to failure), b) the location of failure (failure mode), and c) the physical characteristic of the weld that determines certain type of failure (weld nugget size). In addition, a partial tensile test has been conducted in order to evaluate the initiation of failure in dissimilar steel grade combinations. It has been shown that HAZ-softening lowered the weld size at which transition from interfacial to pullout failure mode takes place along with increased load-bearing capacity and higher energy absorption. Thus, it is concluded from mechanical testing that HAZ-softening benefits the lap-shear tensile joint performance of resistance spot welded DP steels by facilitating pullout failures through failure initiation at the SC-HAZ (tempered region).

Instrumented nanoindentation testing was employed to further investigate HAZ-softening along the SC-HAZ by evaluating individual phases of ferrite matrix and tempered martensite islands. Although the ferrite matrix presented a slight reduction in hardness at nanoscale, higher reduction in hardness (softening) resulted for tempered martensite; thus confirming that tempered martensite is the major contributor to softening at micro-scale. A comparison between nanohardness and microhardness testing made at different distances from the line of lower critical temperature of transformation (Ac_1) allowed revealing the actual extension of the SC-HAZ. In this regard, good correlation was obtained between nanohardness results along the SC-HAZ and the microstructural changes analyzed by electron microscopy (*i.e.*, the tempering of martensite occurring at various distances far from Ac_1 was correlated to

low temperature tempering of dual phase steels).

An in-depth analysis of the tempering of martensite phase at high temperature in DP steel subjected non-isothermal conditions *i.e.*, rapid heating, extremely short time at peak temperature and rapid cooling (resistance spot welding), has been carried out mainly through analytical transmission electron microscopy (TEM). In addition, an isothermal tempering condition (*i.e.*, slow heating and long time at peak temperature) in DP steel has been evaluated for complementing the analysis. Both non-isothermal and isothermal conditions have been correlated to the softening behaviour. TEM analysis of the base metal in the DP steel indicated that the morphology of the martensite phase is dependent on its carbon content, and its tempering characteristics are similar to that of equal carbon containing martensitic steel. The isothermally tempered structure is characterized by coarsening and spheroidization of cementite (θ) and complete recovery of the martensite laths; whereas precipitation of fine quasi-spherical intralath θ-carbides, coarser plate-like interlath θ-carbides, decomposition of retained austenite into elongated θ-carbides, and partial recovery of the lath structure were observed after non-isothermal tempering of DP steel. This difference in tempering behaviour is attributed to synergistic effect of delay in cementite precipitation due to higher heating rate, and insufficient time for diffusion of carbon that delays the third stage of tempering process (cementite coarsening and recrystalization) during non-isothermal. The finer size and the plate-like morphology of the precipitated carbides along with the partial recovery of the lath structure observed after non-isothermal tempering strongly influenced the softening behaviour of DP steel. The chemical analysis of θ-carbides through extraction replicas for three different DP steels revealed that the chemistry of the carbides is inherited from the parent DP steel during non-isothermal tempering at high temperature confirming that non-isothermal tempering DP steel is predominantly controlled by carbon diffusion.

Acknowledgements

This research project would not have been possible without the advising of my supervisor Dr. Norman Y. Zhou, I sincerely appreciate his unconditional support and guidance.

I would like to acknowledge Dr. Scott Lawson for his ever punctual feedback and wise comments. I would like to express my sincere appreciation to the committee members, Dr. Kaan Inal, Dr. Scott Walbridge, and Dr. Stephen Liu for their valuable comments and suggestions.

I would like to acknowledge the encouragement and assistance of Dr. Sushanta K. Panda. I also would like to thank Dr. Michael Kuntz and Dr. Ibraheem Khan for their support and friendship.

I would like to recognize the invaluable lab work and contribution done to this reasearch by Mr. Yasuaki Okita from JFE Steel Corp. I want to thank the comments from Elliot Biro from Arcelor Mittal Dofasco, and the discussions with Dr. Sashank Nayak from CAMJ.

I want to express my appreciation to Jorge Cruz and his family. I want to thank Juan Ulloa for his help in the machine shop. I want to thank John Boldt, Martha Morales and Jose Imbert-Boyd for their help and friendship. I am very thankful to all fellows in CAMJ for their friendship and all friends at University of Waterloo. I would also like to thank Julia and Edgar an all my friends at McMaster University in Hamilton.

I want to recognize the help and friendship of Family Ricardez Carbajal and Family Santillan Perez and all my Mexican Friends in the University of Waterloo. I want to express my gratitude to Fam. Mastrapa, and all my Cuban and Guatemalan friends in Waterloo.

I am indebted to my sisters Elena and Lupita for their love and unconditional support. Thanks to my brothers Juan and Armando. I am thankful to my brothers-in-law for their moral support. I want to thank all my family in Mexico, especially to those who where always in touch during this journey.

I would like to acknowledge the Mexican National Council for Science and Technology (CONACYT), for providing the financial support to this thesis. This research was made also possible by the support of the Autonomous University of Zacatecas (UAZ). I would like to thank all fellows in the MPyM and EPMM especially to those who kept in contact during all these years.

Last but not the least, I would like to express my gratitude and love to my wife Seyla Karina for her patience and everlasting support. I would also like to acknowledge and recognize the yielded time of my daughters Geraldine Alejandra and Fernanda Paola; I love you so much.

In memory of my father

Juan Baltazar Robles

To my lovely family

Seyla Karina

Geraldine Alejandra

Fernanda Paola

To my mother with love

Amalia

Table of Contents

List of figures

List of Tables

1. Introduction

1.1. Dual-phase Steel

Advanced high strength steels (AHSS) are engineering materials that combine higher strength (performance), good ductility (formability) and excellent energy absorption (crashworthiness). Amongst all AHSS *viz.* transformation-induced plasticity (TRIP), complex phase (CP), martensitic steel (MS), ferritic-bainitic (FB), twinning-induced plasticity (TWIP), dual-phase (DP) steel has met ample range of applications in the automobile industry [1].

DP steel is composed of a ferritic matrix with varied volume fractions of martensite phase (i.e. 15~50 %) and, in some cases, small additions of retained austenite, bainite and/or pearlite [1]. The amount of martensite phase is an essential factor governing the mechanical properties of dual-phase steel; for example, DP steel has a number of particular properties like: continuous yielding behaviour (no yield point), low yield strength (i.e. 0.2 percent offset), high tensile strength (up to 1000 MPa), high work-hardening rate, and usually high uniform and total elongation [2].

In-service benefits like weight reduction (gas consumption) are realized when using DP steel, and because of the inherent mechanical properties; DP steel has become an attractive material for applications in the autobody construction. An increased number of automotive parts such as rails, bumpers, pillars, panels, etc. made with traditional high strength low alloy steel (HSLA), are being gradually replaced with DP steel [3].

The introduction of DP steel in auto-body constructions makes resistance spot welding the favoured process for joining this steel. Resistance spot welding (RSW) is a joining method that consists of pressing two or more overlapped metals together while a current is passed through a localized contact area in order to heat the metal to adequate temperature and form the weld nugget [4]. The resistance spot weldability [5,6] of DP steel is however narrower when compared to typical HSLA steel because of the multiphase structure characteristic and the relatively higher alloying level in the former. For instance, it is well established that the tensile

performance of spot weldments is highly dependent on the geometric characteristics (size) of the weld nugget [7,8]; however, phase transformations occurring at the fusion zone (FZ) and/or heat affected zone (HAZ) have strong influence on the tensile properties of resistance spot welded dual-phase (RSW-DP) steel [9].

1.2. HAZ-Softening

One interesting issue is the reduction in hardness with respect to base metal (softening) occurring in the HAZ of welded DP steels. For example, softening has been observed upon different welding processes such as gas metal arc welding [10], laser welding [11], flash welding [12], and resistance spot welding [13]. Moreover, HAZ-softening has been reported to be responsible for diminished mechanical properties of welded DP steel; for instance, it has been found that HAZ-softening affects the uniaxial tensile properties of laser butt welded DP steel by strain localization and earlier fractures [14]. Recent reports have shown that formability of welded DP steel is significantly reduced due to formation of soft zones in the outer HAZ [15]. Numerical simulations and experimental results have confirmed that a local decrease in strength in the softened HAZ is responsible in the overall strength and ductility of the tested specimens [16]. In laser welding of various DP steels; both martensite content and heat input have been found to strongly influence the HAZ-softening behaviour; in this regard, it has been observed that softening is proportional to martensite content and the heat input controls the completion of softening [11].

On the other hand, HAZ-softening in resistance spot welding of DP steel (RSW-DP) has been reported several times in literature [13-19]. It has been observed that softening modifies the lap-shear tensile properties and the failure mode of RSW-DP steel [19,20]. Moreover, it is believed that softening region is weaker in comparison to that of the base material and hence is more susceptible to failure initiation [13]. Interestingly, HAZ-softening in RSW-DP steel has been essentially attributed to the tempering of martensite phase but no details have been provided about this metallurgical issue [9,19]. It is noteworthy to mention that there is a lack of information in the literature regarding to the tempering of martensite subjected to rapid thermal cycles of heating and cooling and with extremely short times at peak temperature (non-isothermal) such as those developed by welding processes, particularly, in the HAZ.

1.3. Tempering of Martensite

Existent literature regarding to the tempering of iron-martensite has been mostly addressed to fully martensitic steels upon isothermal heat treatments [21- 31]. Basically, the tempering of martensite occurs at temperatures below the lower critical (Ac_1) [24] and during isothermal heat treatments is highly dependent on the maximum peak temperature, the time at peak temperature, the prior microstructure and the alloying level [26]. The process of tempering is developed in series of overlapped stages which can be outlined as: (a) the precipitation and coarsening of carbides, (b) the decomposition of retained austenite, and (c) the recovery or recrystallization of the martensitic sub-structure [21].

Furthermore, there exists little research regarding to tempering of martensite phase in dual-phase steels [32- 38]. Most of these studies have related conventional isothermal tempering heat treatment at various peak temperatures to mechanical behaviour. For instance, it has been found that the tensile strength decreases when increasing the tempering temperature. Moreover, a more complex phenomena occurs with the yield strength as it first increases with temperature but decreases as tempering temperature increases, this was attributed to a number of factors such as carbon segregation, transition from continuous to discontinuous yielding behaviour, and the relief of residual stresses [32].

On the other hand, few details have been provided regarding the microstructural characteristics and the kinetics of tempering of martensite phase in DP steel. In this regard; it has been observed that the carbon content within the martensite structure plays an important role on the tempering mechanism. For example, high-carbon martensites are more susceptible to form low-temperature carbides (i.e. ε-carbide) [37,35], whereas rod plate-shape cementite was certainly promoted on low-carbon martensites [36]. It is not clear, however the influence of the martensitic sub-structure on the formation of carbides. Interestingly, the tempering of martensite in dual-phase steel when subjected to non-isothermal transformations upon fast heating and fast cooling conditions lacks of serious attention, to date; this subject has not been studied.

1.4. Problem

There is an increased demand for extending the number of applications of DP steel in automobile constructions. There are, however, several practical issues along with a lack of fundamental knowledge that limit their applicability; the analysis and study of such practical and fundamental issues will enable more efficient utilization of this steel. The following paragraphs comprise the main problems that are found in resistance spot welding of dual-phase steel.

a) There is a lack of systematic studies in the literature regarding to the softening phenomena occurring in the sub-critical HAZ of RSW-DP steel. First, it is not well understood if HAZ-softening impairs the mechanical performance of DP steels and to what degree. Second, it is not clear about the severity or degree of softening for the different grades of DP steel. Third, softening has been associated to the tempering of martensite; however there are no reports characterizing the tempered structure while connecting with the degree or severity of softening.

b) The degree of non-isothermal tempering of martensite islands should be measured with higher resolution techniques in order to avoid the contribution of other phases to hardness. Typically, tempering has been linked to softening by employing microhardness indentation techniques; however, in the case of dual-phase steel, the size of microhardness indentation is larger that the individual constituents and the contribution of individual phases to softening is not clear. Therefore, accurate measurements are required to assess the severity of martensite tempering (i.e. non-isothermal) in DP and obtain mechanical properties at micro and nano-scale.

c) Even though there is extensive literature regarding to the fundamentals of the tempering of iron-martensite in fully martensitic steels under isothermal conditions; there exist gaps in the literature with regards to fundamental understanding of the tempering of martensite in dual-phase steels. More importantly, there are no related studies about the kinetics of tempering of martensite phase upon non-isothermal conditions such as those developed in resistance spot welding. Particularly, there is a lack of knowledge on the structural characteristics of the non-isothermally tempered martensite. Efforts must be addressed to the following critical areas: effects of the rapid thermal cycle, effects of prior microstructure, and effects of chemistry.

1.5. Objectives

The aim of this research is to conduct experimental and theoretical studies on resistance spot welded dual phase steels (process), analyze the metallurgical transformations at sub-critical temperatures (structure), and its effects on the hardness characteristic and mechanical performance (property). Therefore, the objectives of this thesis are as follows:

1. To analyze the influence of HAZ-softening and the effects of martensite tempering on the tensile performance of resistance spot welded dual-phase steel in similar and dissimilar steel grade combinations.
2. To evaluate the tempering of martensite in dual phase steel through instrumented nano-indentation testing (nanohardness) measurements on a range of sub-critical heat affected zone microstructures (tempered region).
3. To study the fundamental mechanism and characteristics of martensite tempering at high temperature occurring in the heat affected zone of resistance spot welded dual-phase steel by considering the influence of thermal cycle (isothermal and non-isothermal), prior martensite structure, and chemical composition.

1.6. Justification, Criteria and Constraints

Improving the knowledge regarding to the microstructural characteristics in the heat affected zone, is a priority for the successful implementation of DP steel in automotive applications. The current understanding of the process-structure-property relationships is limited and the control of the microstructual gradients through the welding process would permit the avoidance of undesirable failures. The knowledge in this thesis work can be extended to similar welding and manufacturing processes, i.e. laser welding, arc welding, induction heating, etc., where non-isothermal conditions along with rapid heating and fast cooling applied to dual-phase steels are primary features.

The assessment of the spot weld behaviour in this research is based upon recommended practices according to American Welding Society (AWS) standards. Instrumented indentation testing (nanoindentation) has been carried out according to International Organization for Standarization (ISO). Other mechanical testing methods used in this research are detailed in the

following chapters.

This research work is part of a larger project carried out in the Centre for Advanced Materials Joining at the University of Waterloo involving HSLA, TRIP, MS, FB steels, etc. aiming to investigate process-structure-property relationships (see “Publications” in this thesis). However this thesis work is limited to investigate different grades of DP steel. Attention has been addressed towards DP600, DP780 and DP980, since: a) there exists little microstructural information about welded DP steels; and b) there exist a potential application of DPs in auto-body constructions. This limitation is also based on material availability and is required to limit the thesis scope.

1.7. Thesis outline

This thesis report has been organized in seven chapters as follows: Chapter 1 is an introduction to; background, problem, objectives, justification and constraints of this research. Chapter 2 introduces the literature review covering the characteristics of resistance spot welding process, the fundamentals of martensite phase, dual-phase steels, tempering of martensite, and the advantages and basics of instrumented indentation testing for assessing mechanical properties (hardness) at the nano-level. Chapter 3 provides details of the materials, the instrumentation methods, and the experimental procedures utilized in this research. Chapter 4 covers the influence of HAZ-softening on the tensile performance of RSW dual-phase steel. Chapter 5 focuses on the evaluation of tempered martensite at the sub-critical heat affected zone of dual phase steel by means of instrumented indentation testing (nanoindentation) and electron microscopy. Chapter 6 presents an in-depth study through transmission electron microscopy of the tempering of martensite in dual-phase steel under non-isothermal (RSW) and isothermal conditions. Chapter 7 summarizes the main findings, the knowledge and contributions attained to this research work. In addition, a proposed future work is described.

2. Literature Review

2.1. Resistance Spot Welding

Resistance spot welding (RSW) is a joining method carried out by pressing two or more overlapped metals together by means of a pair of electrodes through which current is passed thus heating the localized contact area and creating localized melting to form the weld nugget [4]. RSW is one of the oldest processes and the predominant method for joining steel sheets in automotive manufacturing and is the preferred welding process for auto-body construction because it is fast, easily automated, economical, clean and no additional material is required [39]. Amongst the automotive welding processes, RSW is characterized by providing rapid thermal cycles; for instance, very fast heating (i.e. well above 2000 °C/s), extremely short holding times (i.e. few milliseconds) at peak temperature, followed by very rapid cooling rates [40]. The rapid thermal cycle in RSW is accomplished by quick generation of heat at the sheet/sheet interface owing to the high resistance to the welding current flow, which in fact results in formation of molten material first at that interface. Furthermore, once the current flow has been cut off, the electrodes remain in contact with the sheet surface (holding time) for a controlled period of time. During the holding time, the molten material solidifies and the water-cooled electrodes assist in heat removal from the weld zone. Thus, the thermal cycle (RSW) is completed in few seconds and is characterized as providing clearly non-equilibrium conditions within the material. Even though time-temperature-transformation (TTT) and continuous cooling transformation (CCT) diagrams are available for making interpretation of the dynamic nature and kinetics of phase transformations, they are basically material chemistry dependent. Since most AHSS involve relatively novel and proprietary compositions for which CCT data are not available, there is a serious lack of information regarding the metallurgical transformations occurring during the rapid thermal cycles in RSW [41].

2.1.1. Fundamentals

The heat necessary to create fusion in RSW is generated by applying an electric current through the stack-up of sheets between the electrodes as shown schematically in Figure 2.1. The general expression of the heat generated in an electric circuit is:

$$Q = I^2 Rt \qquad \textbf{Equation 2-1}$$

where Q is the heat, I is current, R is electrical resistance of the circuit, and t is time the current is allowed to flow in the circuit [41]. It is evident from Equation 2-1 that the magnitude of the heat energy generated can be varied by changing the value of any of the three factors of the equation; however, a small modification of I results in a significant change in heat input. The current and time can be readily varied by adjustment of the welding parameters. There are two types of electrical resistance present in the secondary circuit: the bulk resistance of the material(s) and the interfacial resistance of the contact surfaces [4]. The bulk resistance is a function of the material composition and it varies with temperature, the actual resistance is termed effective resistance and is directly proportional to the conductor length and nearly inversely proportional to the sectional area. On the other hand, the contact resistance is related to the bulk material electrical resistivity and mechanical properties, to the detail of the surface topography (i.e. surface roughness and flatness), and to the properties of any coatings and contaminants that may be present on the surfaces, as well as the contact pressure [42].

2.1.2. Welding Parameters

Current

The weld current is the electrical current in the welding circuit during the making of a weld. From Equation 2-1, it is shown that the heat generated is proportional to the square of the current. Therefore, neglecting losses, doubling the current will quadruple the heat developed over any period of time. The spot welding process has been primarily developed using line-frequency AC current as its electrical power source. DC power has been limited to more specialized applications. In the recent years, the technology of the new DC spot welding power supply, known as the mid-frequency DC (MFDC) inverter, has become more popular due to increased energy savings [43].

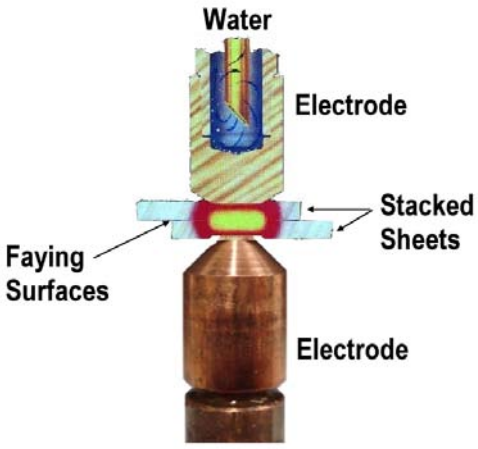

Figure 2.1 Generation of heat in RSW.

Time

To a certain extent, time and current may be complementary; that is, a desired change of heat may be secured either by a change of current or by a change of time. The time cannot be shortened too much regardless of the increase of current. The effect of a very short time, high current welding procedure is generation of heat too rapidly at interfaces resulting in pitting and surface flashing [4]. The typical time range (commonly measured by cycles) lies between 10 to 25 cycles for the case of RSW of steel.

Force

In RSW the applied force is directly related to the contact resistance. For a given electrode geometry and work surface condition, the contact resistance is approximately inversely proportional to the electrode force. At a given ambient temperature, for a given set of material properties and surface topography, the electrical resistance across the contact interface between two solids decreases as any applied load increases [42].

2.1.3. Electrodes

Resistance welding electrodes perform three important functions: they conduct the welding current to the work; they transmit the proper electrode pressure or force to the work in order to produce a satisfactory weld; and they help dissipate heat from the welded zone. In the third function, the electrodes, which are normally hollow and internally cooled by flowing water, must possess higher thermal conductivity because they conduct the heat away from the

exterior surfaces of the material being welded. This last function sometimes assumes considerable importance when dissimilar metal are to be welded, and it becomes necessary or desirable to obtain a thermal balance. In such cases one electrode with a lower thermal conductivity may be chosen to prevent too rapid heat dissipation from one part of the dissimilar combination [4].

2.1.4. Hold Time

Hold time in resistance spot welding is that time, after termination of the current in which the part is held under force of the electrodes in the welding machine to allow the weld to solidify. Hold time is a very important parameter and is related to the cooling-time. Therefore, the final hardness in the welded metal is strongly dependent on this parameter. Reducing the hold time tends to reduce the cooling rate and soften the material. Hold time sensitivity, as defined in many automotive specifications, is related to variations in fracture characteristics as a function of cooling rate. The occurrence of hold time sensitivity indicates that bond line-fracture of welds can occur under some RSW conditions [44,45].

2.1.5. Weld Thermal Cycle

During welding, the weld thermal cycle is produced by the heat source and is composed by the heating cycle, the time held at peak temperature (dwell time) and the cooling cycle. In resistance spot welding; a non-isothermal condition is accomplished by the material because of the extremely short dwell time at peak temperature. The thermal cycle in resistance spot welding can be very rapid throughout the weld, though it can decrease with increasing the distance from the faying surface. It is difficult however to measure experimentally the thermal cycle in RSW because of the strong magnetic fields developed during the current flow. Thermal models have been used to semi-quantitatively estimate the thermal cycles in RSW. For instance, the heating rates are estimated to be as large as 3000°C/s depending on specific location within the weld [46,47]. On the other hand, cooling rates in RSW have been estimated by a range of modeling techniques such as closed-form and numerical. These approaches have shown that RSW can achieve cooling rates on the order of 10^5 °C/s [40]. Figure 2.2 shows typical weld thermal cycles in RSW generated at the center of the weld nugget (fusion zone), at the heat affected zone (coarse grain region) and, at the intercritical HAZ [48]. It might be noted from Figure 2.2 that

the shape of the thermal cycle might be comparatively different for the various weld zones as the distance from the weld nugget towards the base metal increases, *i.e.*, lower heating rate is shown for the intercritical heat affected zone.

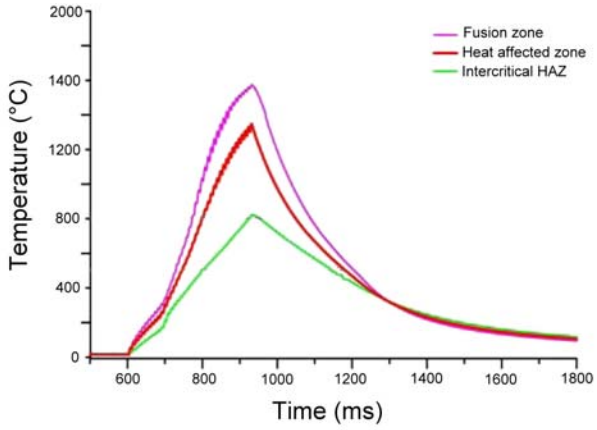

Figure 2.2 Temperature-time profile for various weld zones [48].

In addition, the cooling rate is closely related to the hold time in RSW as discussed in previous section. The hardness achieved in resistance spot welds is directly associated with the cooling rate (hold time). Figure 2.3 illustrates the effect of hold time on the shape of the thermal cycle curve obtained from the weld nugget [49].

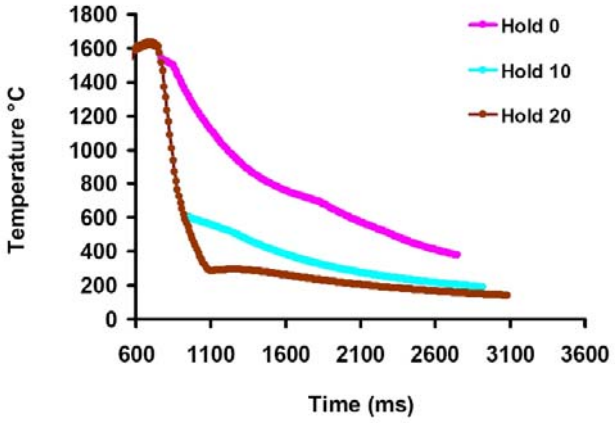

Figure 2.3 Fusion zone temperature profiles during cooling as calculated using SORPAS^{TM} RSW simulation software [49].

According to Figure 2.3; variations in hold time *i.e.*, 0 cycles (hold 0) or 20 cycles (hold 20) leads to significant differences in cooling rates in the RSW specimen [49]. The above mentioned observations can be extended for the thermal analysis at the subcritical HAZ in which variations in hold time might affect the dwell time at peak temperature, and hence the degree of

tempering.

2.1.6. Weld Zones

When structural members are joined by fusion welding the material of the components to be joined has to be heated to its melting point and then cooled again rapidly under conditions of restraint imposed by the geometry of the joint. As a result of this very severe thermal cycle, the original microstructure and properties of the weld metal are changed. The fusion zone (FZ) and the heat affected zone (HAZ) are to be identified as shown in Figure 2.4. Moreover, the HAZ can be conveniently divided in a number of sub-zones and this is illustrated for the case of transformable steel [50].

Fusion Zone

The composition of weld metal and the circumstances under which it freezes have a strong influence on the ability of the weld metal to form a sound, serviceable joint. The features of fusion welding which have to be taken into consideration are: impurities in the weld pool, dilution, turbulence (therefore good mixing), the relative volume of the molten metal with respect to the base metal, the composition of the molten metal and the temperature gradient, among others [51]. During welding, solidification of a liquid is similar to that in a metal casting. It consists of two steps: nucleation of a solid phase and subsequent crystal growth. The crystallization process is controlled by the heat dissipation. The direction and rate of cooling, in addition to the alloy's composition, decisively affect the type, size, and orientation of the crystals formed.

Initial solidification of a weld is by epitaxial growth from the grains of the base metal. Hence, the initial crystal size of the weld metal is inherited directly from the grain growth zone of the base metal (fusion line). Each grain forms initially as a continuation of one of the grains that lie along that part of the fusion boundary where the weld width is greatest. As the fusion boundary moves forwards, grain continue to grow in a columnar fashion. Competition between grains results in some change in relative size, but in general the primary grain size of the weld metal is determined by the grain size of the solid metal at the fusion boundary [52].

During solidification a change in composition occurs in the crystals being precipitated compared to that of the bulk material. The type of substructure that appears in weld metal

depends on the form of the solidification front. This in turn is influenced by the solute content of the liquid weld metal and by a solidification parameter equal to the temperature gradient *G* in the direction of solidification divided by the rate of advance *R* of the solidification front. The various solidification modes will undergo planar → cellular → cellular dendritic → columnar dendritic as the ration G/R decreases (*i.e.*, the microstructure tends to become more dendritic).

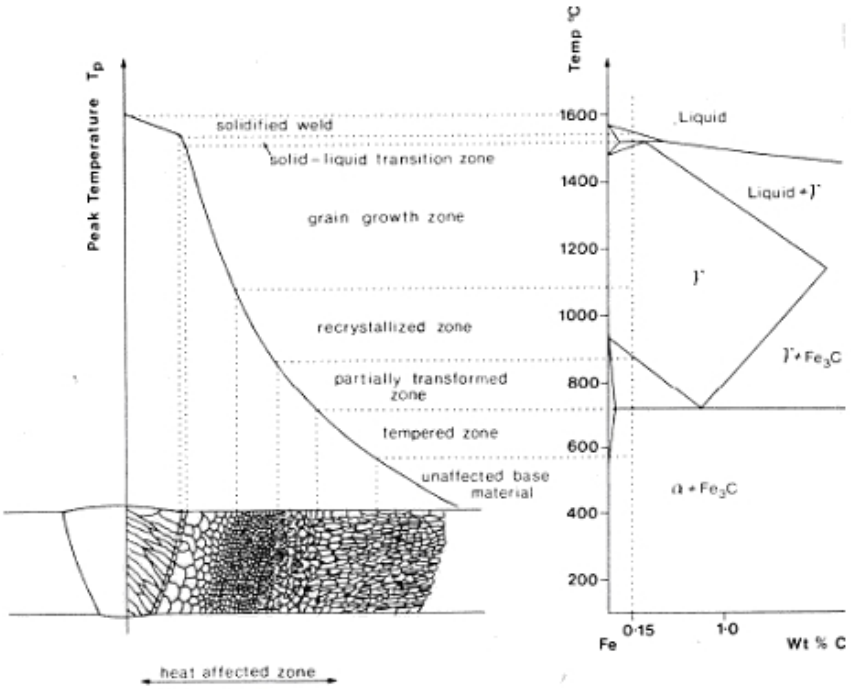

Figure 2.4 A schematic diagram of the various zones of the weld region corresponding to the alloy C_o (0.15 wt % C) indicated on the Fe – Fe_3C equilibrium diagram [50].

Heat Affected Zone

Microstructural transformations in the HAZ are governed by the local thermal cycle, thus resulting in a heterogeneous region [53]. Regions farther away from the nugget (where the melting temperature or higher is reached) will experience a lower peak temperature, so that various zones of the HAZ may be defined. The different zones of the HAZ shown in Figure 2.4 refer to regions of different microstructure and, perhaps more important different mechanical properties. The structure type and its sub-zone width are partially determined by the thermal cycle. The region adjacent to the fusion line (i.e. supercritical region) in transformable steels may be divided in two parts: the grain growth and recrystallized (grain-refined) regions. Above the grain-coarsening temperature the thermal cycle during welding promotes grain growth, and below it the thermal cycle refines the grain structure. The intercritical (IC) region experiences

partial phase transformation. The peak temperature is lower than those in the supercritical region. New phases that do not exist in the original base metal may form in this region, and such transformation depends on the duration that the metal is exposed to the peak temperature and the cooling rate. The sub-critical or tempered region does not normally show any major observable microstructural changes as the temperature range is below those that would cause phase transformations. It is difficult to distinguish this region from the base metal. In some cases very fine precipitates may appear in this region. However, the changes in the HAZ are also dependent upon the prior thermal and mechanical history of the material. For example, the recrystalization behaviour during the heating cycle is affected by whether the original material was in cold rolled or annealed condition prior to welding. The onset and extent of the grain growth zone is influenced by the presence of precipitates and their solubility at high temperatures. Thus in order to understand the HAZ it is necessary to consider how the microstructure of the base metal reacts to the complete thermal cycle and its effect on phase transformations and precipitate reactions [50].

2.1.7. Mechanical Performance of Spot Welds

Shear and Cross Tension Test

In strength or weldability tests on spot welded joints, lap shear samples or cross tension samples are often used. The tests using lap-shear geometry provide the “shear strength” (Figure 2.5a), and the tests using cross tension samples give the “tensile strength” of the joint normal to the sheet surface (Figure 2.6a) [54].

Observation during tensile testing of lap-shear samples reveals the failure process as schematically demonstrated in Figure 2.5. During the lap-shear test as the sample is pulled initially, the weld nugget experiences a rotation (Figure 2.5b), which essentially aligns the nugget with the loading line. In stage (c) the material surrounding the nugget is subjected to a predominantly tensile load and the deformation near the nugget is similar to a rigid button embedded in a ductile sheet. As the load increases, localized necking of the sheet metal occurs at the two places, i.e. θ=0 and 180 deg at the locations near the juncture of the nugget and the base metal. If assuming pullout failure mode, fracture then initiates at one of these two points (d). Optical micrographs have demonstrated that the failure mechanism of lap-shear sample at the material level is *tensile*, even though the global loading mode to the test sample is *shear*.

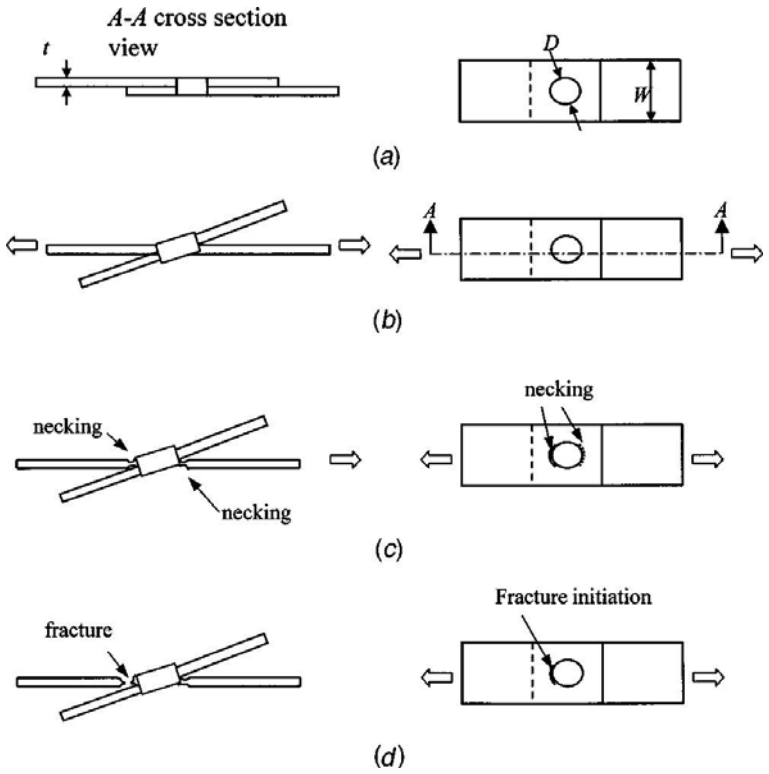

Figure 2.5 Failure process of a lap-shear spot-weld sample: (a) initial configuration, (b) nugget rotation, (c) stretching, thinning, and necking, and (d) tensile fracture due to localized necking [55].

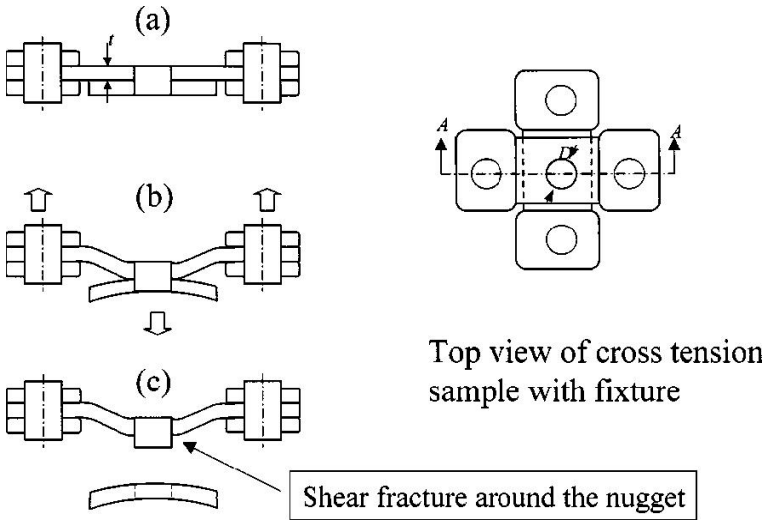

Figure 2.6 Deformation pattern and weld nugget pullout failure of a cross tension sample [55]

The deformation pattern and failure process of a cross tension sample is demonstrated in Figure 2.6. As the sample is loaded, large bending deformation of the sheet occurs initially (b).

Eventually the weld nugget is pulled out from one coupon and stays with the other coupon (c). Besides the initial global bending of the sheet, the failure can be well characterized as through thickness shear around the weld nugget. The fracture mechanism at the material level is ductile and *shear*, despite the fact that the global loading mode to the sample is *tensile* [55].

Failure Mode & Weld Size

The AWS standards have defined eight combinations of failure modes for spot welds which include: button pull, partial thickness fracture with button pull, partial thickness fracture, interfacial fracture with button pull and partial thickness fracture, interfacial fracture with button pull, interfacial fracture with partial thickness fracture, interfacial fracture, and no fusion [56]. A schematic representation of three main failure modes (*i.e.*, interfacial, partial interfacial and pullout) are depicted in Figure 2.7. However, for theoretical analysis and for practical reasons sometimes just two failure modes for spot welds are considered: nugget pullout and interfacial. In a large weld, nugget pullout failure may occur, in which the weld nugget is completely pulled out from one of the metal sheets, leaving a circular hole in the sheet. Interfacial fracture propagates through the weld nugget and often occurs in a small weld. Interfacial failure, which is associated with lower load carrying capacity and considerably less energy absorption capability, is considered unsatisfactory and industry standards are often designed to avoid this occurrence [54].

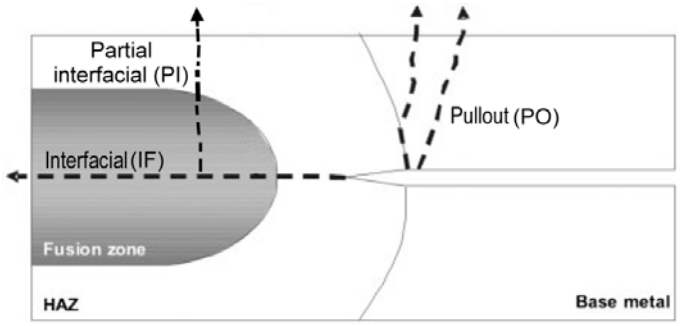

Figure 2.7 Schematic representation of interfacial and pullout failure modes [9].

Weld diameter has been shown to be the primary factor influencing the type of weld fracture mode [73]. Various industry standards recommend the optimum or minimum size of the spot weld for a given sheet metal thickness. For example, the American Welding Society, the Society of Automotive Engineering (SAE), and the American National Standards Institute

(ANSI) [57], together recommend a weld nugget diameter given by:

$$d = 4\sqrt{t} \qquad \textbf{Equation 2-2}$$

where d and t are the weld nugget diameter and thickness respectively. This recommended formula, however, is empirical in nature and is derived from extensive experimental testing.

Critical Nugget Size & Failure Mode Prediction

Investigations regarding the prediction of failure mode have been based on empirical or theoretical formulations or a combination of both [58]. Such models have been related to weld diameter as primary factor and have been validated from experimental data. For instance, for the lap-shear geometry, Equation 2-3 describes a three-dimensional surface that separates conditions for interfacial fracture from those for button-pullout fracture. Any spot weld that has a diameter smaller than d_c is likely to fail via interfacial fracture. Thus, d_c is typically called critical nugget size. Conversely, any weld that has a larger diameter is expected to fail via button-pullout fracture. As implied by Equation 2-3, prevention of interfacial fracture in thicker coupons requires welds with larger diameters. Also, large H_{max}/H_{min} (H_{max} = maximum hardness (FZ), H_{min} minimum hardness, *i.e.,* BM) will allow a reduction in weld diameters for prevention of interfacial fracture [20].

$$d_c = 0.53t^{3.22} + 8.48\left(\frac{H_{max}}{H_{min}}\right)^{-1.24} \qquad \textbf{Equation 2-3}$$

Failure is a competitive process i.e. spot weld failure occurs in a mode which needs less force. Therefore, to construct a model for predicting failure mode, first is necessary to obtain mathematical equations expressing failure load for both interfacial and pullout modes.

Considering a nugget as a cylinder with diameter d and height $2t$, failure load at the interfacial failure mode P_{IF} could be expressed as Equation 2-4 assuming uniform distribution of shear stress on the weld interface.

$$P_{IF} = \left(\frac{\pi d^2}{4}\right)\tau_{WN} \qquad \textbf{Equation 2-4}$$

where τ_{WN} is the weld nugget shear strength and d is the weld nugget diameter.

As it was mentioned before, pullout failure mode occurs under a tensile mechanism. It is assumed that failure occurs when the maximum radial stress at the circumference of one half of the cylindrical nugget reaches the ultimate strength of the failure location. Therefore, Equation 2-5 is suggested for pullout failure of a spot weld in a shear tensile test:

$$P_{PF} = \pi dt\left(\sigma_{UTS}\right)_{FL} \qquad \textbf{Equation 2-5}$$

where $(\sigma_{UTS})_{FL}$ is the ultimate tensile strength of the failure location. In Equation 2-5 thickness reduction owing to indentation is neglected.

Figure 2.8 illustrates failure load versus nugget diameter for both interfacial (broken line) and pullout (solid line) failure modes according to Equation 2-4 and Equation 2-5. Below the critical nugget diameter, interfacial failure is dominant, while for nugget diameters larger than the critical size, pullout failure is the dominant failure mode. To obtain the critical nugget diameter d_{cr}, Equation 2-4 and Equation 2-5 are intersected resulting in Equation 2-6:

$$d_{cr} = 4t\frac{\left(\sigma_{UTS}\right)_{FL}}{\tau_{WN}} \qquad \textbf{Equation 2-6}$$

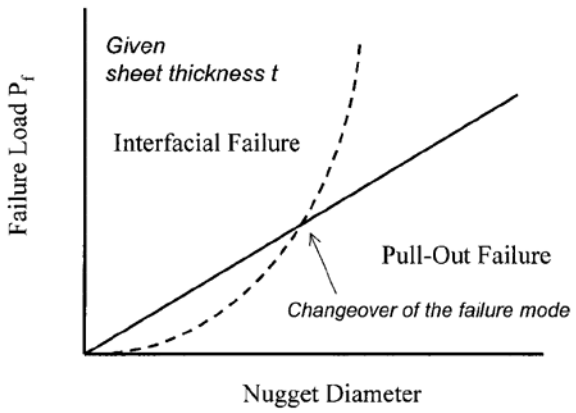

Figure 2.8 Schematic diagram showing competition between interfacial failure (broken line) and nugget pullout failure (solid line) [54].

It is found that d_{cr} depends on the weld nugget strength and strength of the failure location. Since determination of mechanical properties of various regions of a spot weld is

difficult, owing to the small scale, a hardness profile can be used for estimating ultimate strength. It is well known that the ultimate strength of metal is proportional to its hardness. On the other hand, according to the Tresca criterion, shear ultimate strength is half of the tensile ultimate strength. Therefore equation Equation 2-6 can be rewritten as:

$$d_{cr} = 4t\frac{(\sigma_{UTS})_{FL}}{(0.5\sigma_{UTS})_{WN}} = 8t\frac{(H)_{FL}}{(H)_{WN}} \qquad \textbf{Equation 2-7}$$

Equation 2-7 attributes critical weld nugget diameter to failure location/weld nugget hardness ratio, in addition to the sheet thickness. For constant thickness; decreasing $\frac{(H)_{WN}}{(H)_{FL}}$ increases the tendency to interfacial failure mode tendency [59].

2.2. Ferrous Martensite

2.2.1. Introduction

The name *martensite* is after the German scientist Martens. It was used originally to describe the hard micro-constituent found in quenched steels. Solid-state phase transformation of martensite occurs in many other materials than steel and is frequently called *martensitic transformation*, *shear* or *displacive transformation*.

Martensitic transformations are of diffusionless character. The evidence for this statement is that martensite can form at very low temperatures, where diffusion, even of interstitial atoms, is not conceivable over the time period of experiment. Moreover, martensite plates can growth at speeds which approach that of sound in the metal. In steel this can be as high as 1100 m/s, such large speeds are inconsistent with diffusion during transformation. Finally, the chemical composition of martensite can be measured and shown to be identical to that of the parent austenite. The totalities of these observations demonstrate convincingly that martensitic transformations are of diffusionless character [60].

2.2.2. Morphology & structure

There are two general morphologies of ferrous martensites, *viz.* dislocated laths and twinned plates. The carbon ranges of formation and M_s of the two morphologies are illustrated

in Figure 2.9. The dislocated laths are composed of elongated bundles of slightly misoriented subgrains, within which, the dislocation density may vary with the composition and cooling rate and is associated with the $\{111\}_\gamma$ habit. In low carbon steels adjacent laths appear to adopt different variants of the Kurdjumov-Sachs (K-S) relation [61].

K-S orientation relationship $\{111\}_\gamma \parallel \{110\}_{\alpha'}$, $\langle 1\bar{1}0\rangle \parallel \langle 1\bar{1}1\rangle$

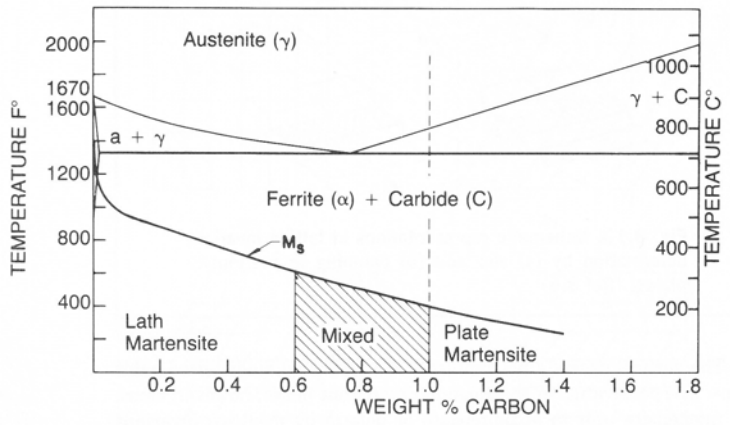

Figure 2.9 Ranges of lath and plate martensite formation in iron-carbon alloys [24].

Lath martensite is found in plain carbon and low alloy martensites with carbon contents up to about 0.4% to 0.5% [22,23]. In low-alloy steel the morphology of martensite is lath- or plate-like where the laths are very long and about 0.5 μm wide. The laths are grouped into blocks. For example, a block consists of a group of laths with the same variant (i.e. K-S variant), namely the same orientation and the identical habit plane, and is separated by one another by high angle boundaries [62]. The block is contained within a larger arrangement of packets; such packets are made up of parallel blocks separated by high-angle boundaries, the laths within the packets have the same habit plane i.e. $\{111\}_\gamma$. The schematic of the sub-structure of lath martensite is illustrated in Figure 2.10.

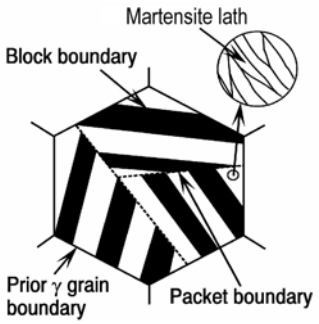

Figure 2.10 Schematic illustration showing the morphological characteristics of lath martensite sub-structure [62]

On the other hand, plate martensites contain fine transformation twins. Those within which the twin density varies and in which the twins do not extend completely across the plates are associated with $\{225\}_\gamma$, $\{259\}_\gamma$ habits, whereas fully twinned plates correspond to the $\{3, 10, 15\}_\gamma$ habit. An example of twin structure is shown in Figure 2.11. In many fully martensitic steels, the microstructures are often complex mixtures of dislocated and twinned martensites so that microstructural analyses are very difficult to carry out [61].

There are several factors that thought to be important in the control of the martensitic substructure [61]:

1 *Composition:* increasing the total solute content tends to change the morphology from dislocated laths to twinned plate martensite. From this, carbon appears to have the strongest effect in promoting twinning.

2 *M_s temperature: concurrently with composition there is usually a decrease in M_s temperature with increasing solute content. In a given alloy series the M_s can be kept constant and then the composition determines whether laths or plates forms.*

3 *The strength of the martensite: since the lattice invariant shear involves plastic deformation, the sub-structure must depend on the yield strength of martensite. This property also depends on composition and temperature.*

4 *Austenite stacking fault energy*: there is no simple relationship. High stacking fault energy (SFE) is supposed to promote laths if M_s is relatively high, but if M_s is relatively low, twinned plates are formed. However, increasing the concentration of all solutes seems to promote twinning, e.g. manganese and nickel, yet manganese lowers SFE and nickel raises SFE of austenite.

5 *Cooling rate*: cooling rate affects M_s and in many martensites the dislocation density varies, in alloy steels precipitation on slow cooling raises M_s so that the martensite is diluted and hence is lath type. Fast cooling retains solutes in solution and twinned plate results.

6 *Thermal-mechanical:* plastic deformation can cause precipitation in austenite (austforming), so that transformation to lath martensite occurs. Likewise prior austaging can affect the subsequent martensitic structure.

7 *Pressure*: twinned plates can be produced at 40 kbar (kb) whereas at atmospheric pressure, the martensite is lath type.

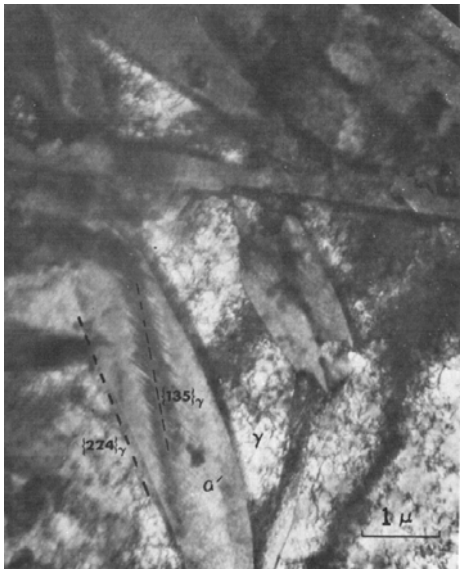

Figure 2.11 Fe-25Ni-0.3V-0.3C bulk-transformed in liquid nitrogen. The lens-shaped plate with $\langle 112 \rangle_\alpha$ twinned midrib coexist with dislocated γ and untransformed γ. Notice the dense dislocation tangles, *i.e.*, work-hardened appearance in the austenite [61].

2.2.3. Effects of carbon

Carbon (and nitrogen) seems to be the most potent of the alloying elements in promoting twinning. Thus the stronger the steel, the more difficult it is for slip to occur and then twinning is preferred [61]. The effect of carbon on both M_s and M_f is shown in Figure 2.12, from which it can be seen that 1 wt% of carbon lowers the M_f by over 300°C. Note that above 0.7 wt% the M_f temperature is below room temperature and consequently higher carbon steels quenched into water will normally contain substantial amounts of retained austenite. The relative effect of other alloying elements is indicated in the following empirical relationship [63].

$$M_s(°C) = 539 - 423(\%C) - 30.4(\%Mn) - 17.7(\%Ni) - 12.1(\%Cr) - 7.5(\%Mo) \quad \textbf{equation 2-8}$$

2.2.4. The strength of martensite

The high hardness and brittleness of rapidly quenched steels is the result of the formation of martensite, yet many shear transformations in non-ferrous alloys systems do not produce this dramatic hardening. Indeed, if carbon is eliminated from the steel the resulting hardness is very much lower. The origin of the high strength of martensite is a difficult issue, compounded by the complexity of the structure, a tetragonal lattice with interstitial carbon in solid solution, formed by shear which leads to high densities of dislocations and fine twins [63].

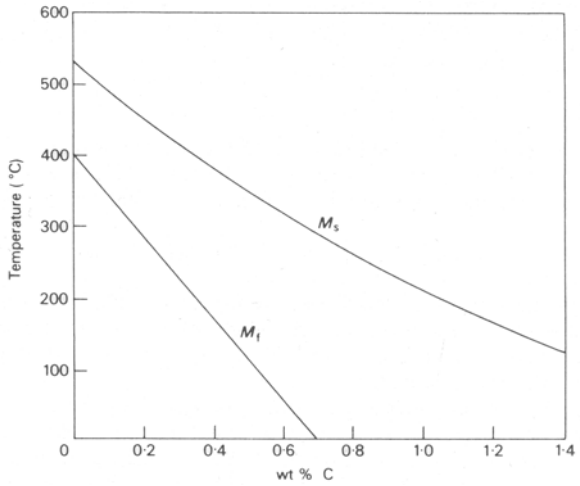

Figure 2.12 The effect of carbon on M_s and M_f (Petty, E. R. (ed.), *Martensite: Fundamentals and Technology*, Longmans, 1970) [63].

There are several possible strengthening mechanisms [63]:

1. Substitutional and interstitial solid solution.
2. Dislocation strengthening, i.e. work hardening.
3. Fine twins.
4. Grain size.
5. Segregation of carbon atoms.
6. Precipitation of iron carbides.

The proposal that the fine twins characteristic of higher carbon martensites make a major contribution to strength has not received wide acceptance. Certainly, a large increase in strength is not found when the transition from dislocated martensite to twinned martensite takes place. However, the high dislocation densities of twin-free martensite must make some contribution to strength, estimated not to be not greater than 300 MN/m^2, and there is reason to believe that the fine twinning makes a similar, but not additive, contribution [63].

2.3. Dual-Phase Steel

2.3.1. Introduction

Automotive steels are classified in three different ways considering: the metallurgical designation, the strength, and various mechanical properties or forming parameters.

The metallurgical designation includes: the low-strength steels, i.e. interstitial-free and

mild steels; conventional high strength steels (HSS), i.e. carbon-manganese, bake hardenable, high-strength interstitial-free; and high-strength low-alloy steels (HSLA); and the relatively newer types of AHSS, i.e. dual-phase, transformation-induced plasticity, complex phase, and martensitic steels. Additional higher strength steels for the automotive market include ferritic-bainitic, twinning-induced plasticity, nano, hot-formed, and post-forming heat treated steels.

The second classification related to the strength defines High-Strength Steels (HSS) as tensile strengths from 210–550 MPa, while Ultra-High-Strength Steels (UHSS) steels have tensile strengths greater than 550 MPa.

Various mechanical properties or forming parameters of different steels, such as total elongation, work hardening exponent *n*, or hole expansion ratio define the third classification. For example, the "banana" curve from Figure 2.13 compares total elongations – a steel property related to formability – for the different metallurgical types of steel [1].

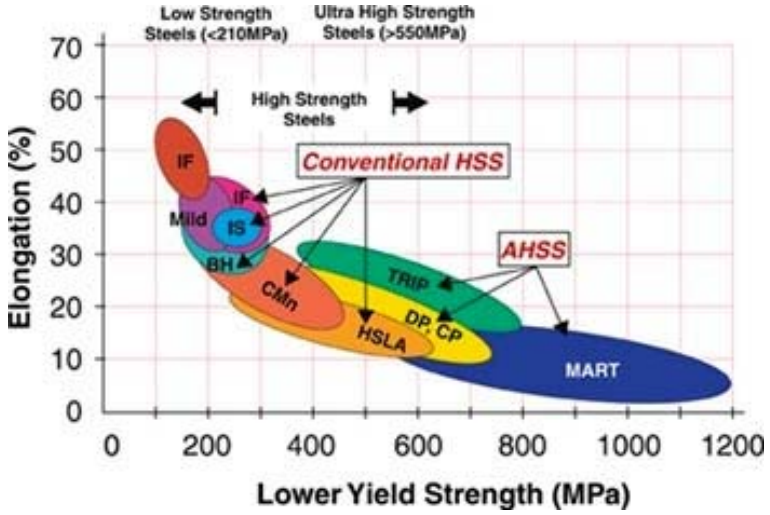

Figure 2.13 Schematic of automotive steels [1].

2.3.2. Dual-Phase Microstructure

The term "dual-phase" refers to the predominance of two phases that consist of a soft, ductile, polygonal ferrite matrix with hard martensite islands (Figure 2.14), and in some cases a small amount of retained austenite, bainite and/or pearlite [64]. Dual-phase (DP) steel is produced either by controlling the transformation of austenite after hot rolling or by inter-critical annealing after cold rolling [65].

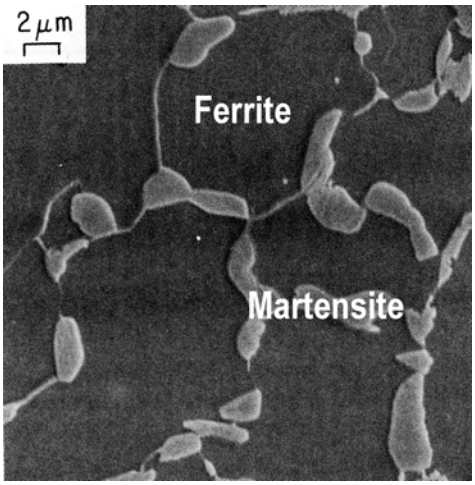

Figure 2.14 Ferrite-martensite microstructure of dual-phase steel [2].

DP steel typically exhibits a low yield point and a high strain-hardening coefficient. The strength-ductility balance is controlled first by the volume fraction of martensite (typically in a range between 7-50%) and secondly on the dispersion of this hard phase.

The physical metallurgy of DP steel is complex, mainly due to presence of carbon and additions of manganese. Essentially, carbon enables the formation of martensite at practical cooling rates due to carbon segregation into austenite during the inter-critical annealing treatment. The addition of Mn further promotes the formation of austenite during inter-critical processing. Increasing the Mn content increases the tensile strength and the fracture elongation due to the finer dispersion of the hard martensite phase [66]. Other alloying elements like chromium, molybdenum, vanadium and nickel can also be present within the steel. As a matter of fact, the inter-critical annealing treatment, the cooling rates and the material chemistry determine in high degree the final microstructure of the DP steel.

2.3.3. Inter-critical Annealing

The dual-phase microstructure is produced by inter-critical annealing (generally in a continuous annealing line) followed by a critical cooling rate (usually within the range of 15 ~ 50 °C/s) which promotes the required amount of fine well dispersed martensite necessary to obtain the desired dual-phase mechanical properties [67].

The aim of the inter-critical annealing is to form austenite/ferrite mixture by reheating the material up to the inter-critical region. The formation of austenite is basically carried out by the nucleation and growth from ferrite-cementite aggregates. For instance, the formation of

austenite is explained by separating the process into various steps [68]. Nucleation of austenite at the ferrite-pearlite interface and further rapid growth of austenite into pearlite. The higher the temperature the faster the completion of dissolution of pearlite: after dissolution of pearlite, further growth of austenite into ferrite occurs. The growth of austenite is controlled by carbon diffusion at high temperatures and shorter times, however if lower temperatures are used, then longer times are required and the growth is controlled by Mn diffusion into ferrite. Final equilibration of Mn content of the austenite and ferrite phases is controlled by Mn diffusion in the austenite which is much slower process than Mn diffusion in ferrite. The times for completion of this process are extraordinarily long.

The carbon content of the austenite is governed by the inter-critical temperature. Basically, the hardenability of the austenite phase varies with the inter-critical temperature, for instance, at low temperatures the carbon content of the austenite is high and the hardenability is high. Similarly, at high temperatures the carbon content of the austenite is low, hence the hardenability is low [2].

The carbon content in the inherited martensite of dual-phase steel depends mainly on the intercritical annealing temperature or alternatively on the volume fraction of martensite. The amount of carbon in martensite can be estimated from a mass balance equation in the form [69]:

$$|\%C|_a \ \rho_a = |\%C|_m \ \nu_m \rho_m + |\%C|_f \ (1-\nu_m)\rho_f \qquad \textbf{equation 2-9}$$

where ν_m=volume fraction of martensite. $|\%C|_m$, $|\%C|_f$, $|\%C|_a$=carbon contents in martensite, ferrite and in the alloy, respectively, and ρ_m, ρ_f, ρ_a=densities of martensite, ferrite and alloy respectively. With a reasonable assumption that the density of ferrite equals that of martensite and that the carbon in ferrite is negligible, then [69]:

$$|\%C|_m = |\%C|_a \ / \nu_m \qquad \textbf{equation 2-10}$$

Furthermore, at higher inter-critical temperatures, the fraction of austenite that transforms into non-martensitic products is very large, whereas at lower inter-critical temperature this fraction is small. The higher hardenability of the austenite phase at lower inter-critical temperatures is in part, simply as a result of its higher carbon content [2].

The martensite formation substructure in dual-phase steel can vary from the lath martensite typical of low carbon martensites, to internally twinned substructures typical of high carbon martensites. These changes in morphology reflect the effect of inter-critical annealing

temperature on the carbon content of the austenite phase and in turn its effect on the M_s temperature. Presumably autotempering of these martensites could also occur at slower cooling rates [2].

On the other hand, there are marked effects of cold rolling and heating rates on the austenite formation in the inter-critical temperature range as depicted by the schematic in Figure 2.15. Upon slow heating (1 °C/s) to intercritical temperature, the distribution of islands of austenite follows the prior distribution of pearlite in the as hot-rolled material, and a substantial amount of ferrite boundaries will be free of austenite.

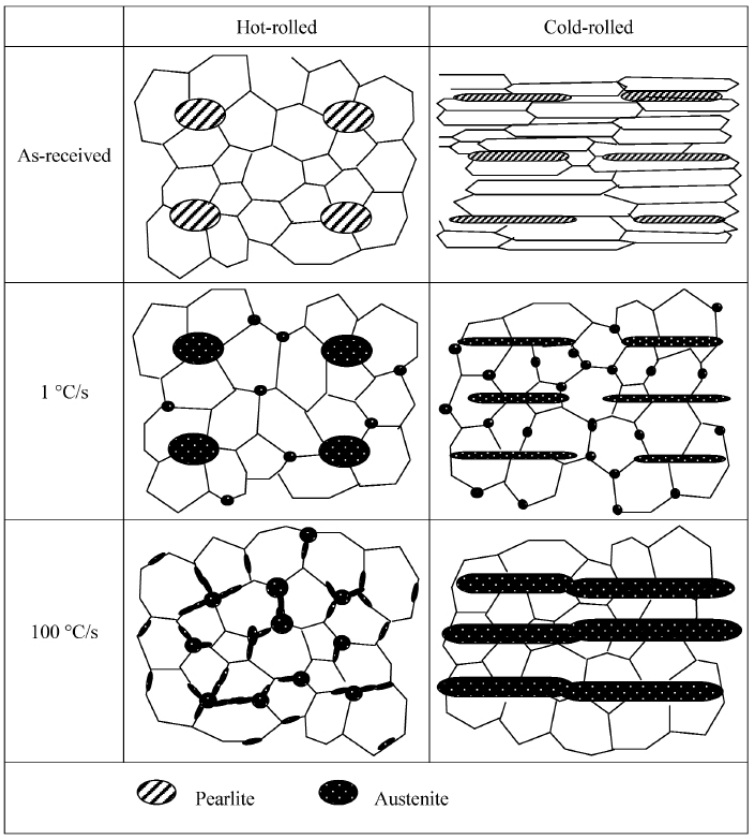

Figure 2.15 Schematic illustration for the microstructure evolution of cold-rolled Fe-C-Mn-Mo steel annealed with different heating rates to holding temperatures [70].

For increased heating rate (i.e. 100 °C/s) in the hot-rolled material, a complete network of austenite along the ferrite boundaries connecting to the pearlite nucleated austenite emerges, thus there is no competition of growth between pearlite sites and ferrite boundaries. On the other hand, the distribution and shape of the pearlite colonies are geometrically modified by cold rolling. Recrystallization of ferrite is completed before austenite nucleation occurs upon slow heating but austenite is elongated because the initial pearlite colonies have been modified by the

cold rolling process. In the case of fast heating cold rolled material, much larger elongated austenite islands are observed. The shape and geometric arrangement of these islands corresponds to the as rolled pearlite distribution [70].

Changes in the ferrite phase also occur during intercritical annealing. Recrystallization of ferrite occurs rapidly and is generally completed before the steel reaches the inter-critical annealing temperature, even during the rapid heating encountered on most continuous-annealing lines. Grain growth of ferrite is restricted because of the pinning action of the second-phase austenite particles [2].

2.3.4. Weldability

The weldability [51] of DP steel is a fundamental issue due to the relatively high content of alloying elements and the rapid cooling rates associated with RSW. DP steels differ from HSS in chemical composition and thermal processing, resulting in a different microstructure. DP steel is designed with a richer chemistry to have higher strength at equivalent thickness compared to HSS. As a result, the sensitivity to heat input is greater and DP has a narrower process window in which acceptable welds can be achieved. Optimization of the welding process, through the understanding of the influence of the weld process parameters, has allowed the weld window to be enlarged to encompass DPs [71].

The resistance spot weldability of DP steel is related to the welding parameters [6]. The most influencing welding parameters in RSW are displayed in a “weld lobe”. An example of weldability lobe for DP600 is depicted in Figure 2.16.

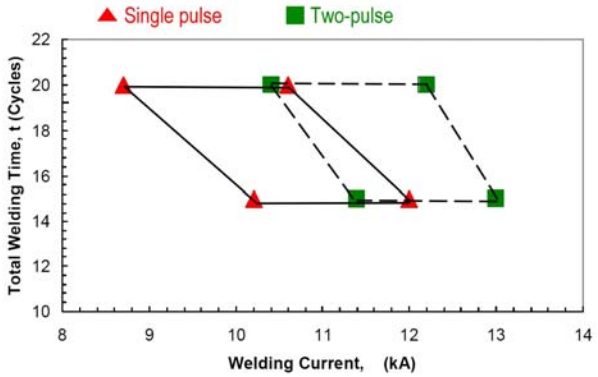

Figure 2.16 Weldability lobe for DP600 steel [6].

The effects of resistance spot welding parameters (weldability) on the weld performance

has been extensively investigated for the lower grades of dual-phase steel, *i.e.* DP600, DP780, [9,18, 48,72- 78]. Iinterfacial failure (IF) mode propagates along the centerline of the weld nugget, resulting in sudden low-ductility failure. Because of its low ductility, IF is generally considered a non desirable failure mode in spot welds, hence, IF is detrimental to weldability. The occurrence of interfacial fractures in DP600 contrast with the traditional automotive steel, where weld fracture is known to occur consistently in the fusion zone periphery, promoting the so-called “weld button” or pullout button. It is considered that for spot welds to be reliable during a vehicle lifetime including proper performance during a crash, they are required to generate button failure during production quality control testing [73]. The susceptibility of interfacial failures in DP600 steel has been attributed to weld defects (*i.e.* shrinkage voids, inclusions, segregation), expulsion at higher current, short holding times, large faying surface gaps, variations in fusion zone hardness, etc [73,75]. However, the primary factor for interfacial fractures has been attributed to the weld button diameter as a function of current, weld time, force, and sheet thickness [74].

2.3.5. Heat Affected Zone Softening

Reduction in hardness with respect to the base metal (softening) has been measured at the heat affected zone of welded dual-phase steels. As a matter of fact, softening phenomena in welded DP steel has been several times reported in literature [9-13,79-80].

Extensive softening has been measured in the outer heat affected zone of resistance spot welded DP steel where the developed peak temperatures were believed to be around 600~700 °C [17]. It has been stated that this region is weaker in comparison to the base material and hence is more susceptible to failure initiation [13], in fact, localized necking has been observed at the HAZ-BM boundary [9]. Thus, softening phenomena have been reported as a potential factor to promote full pullout failure mode in spot welds [9,20]. Softening in the heat affected zones facilitates the development of local plastic strains in the HAZ instead of the harder weld nugget region, a condition that clearly correlated with more frequent button-pullout fractures [20].

Softening has been measured in various grades of DP steels; and it seems to be greatest at the higher grades of DP steel such as DP980, barely detectable at the intermediate grades (DP780) and apparently non existent in the lower grades (DP600) when applying conventional microhardness testing [20]. Interestingly, HAZ-softening in RSW-DP steel has been essentially

attributed to the tempering of martensite phase but no major details have been provided so far [9,19]. The tempering of martensite may have improved the overall ductility of the weld, but its promotion of early local necking under tensile loading possibly impairs the strength of the weldment. Tempering of martensite at the outer HAZ may create a susceptible zone of rupture [13]. For example, it has been reported that the mechanical properties (especially the formability of flash butt welded dual phase steel) shall be governed by the plastic flow characteristics of the various regions of the HAZ [12].

Softening phenomena have been measured in the heat affected zone of dual-phase steel when welded using various other welding processes such as: arc welding, laser welding and flash welding [10-12]. It has been observed that the extent and degree of softening increases when increasing the welding heat input applied to the steel and that the material chemistry can modify the softening behaviour [10]. Furthermore, it has been claimed that the martensite content in dual-phase steel strongly influences on the degree of softening in the outer heat affected zone. For instance, by increasing the martensite volume fraction the amount of softening is proportionally decreased; thus, being an important role in determining the maximum amount of softening [11]. On the other hand, studies have demonstrated that softening behaviour can be modified if variations or manipulation of the weld thermal cycle are carried out. For example, samples have been rapidly cooled down from peak to room temperature by employing water spray, chilled water, or compressed air; the increase in cooling rate was found to reduce the softening of HAZ and this has been attributed to reduction of the tempering of martensite (possibly to the degree of tempering) [12,80].

2.4. Tempering

2.4.1. Introduction

Mechanical properties of martensitic steel can be modified when heating the steel within the temperature range of 150-700 °C. This process is called *tempering* and is one of the oldest heat treatments applied to steels. Essentially, martensite is a highly supersaturated solid solution of carbon in iron in which during tempering, rejects carbon in the form of finely divided carbide phases. The end result of tempering is a fine dispersion of carbides in a α-iron matrix which often bears little structural similarity to the original as-quenched martensite [23].

During isothermal heat treatments; the tempering of martensite is highly dependent on: the maximum (peak) temperature, the time at peak temperature, the prior microstructure and the alloying level [26]. The tempering of iron-martensite occurs at temperatures below the lower critical of transformation (Ac_1) [24], and is developed in series of overlapped stages which are classified as follows [21, 22]:

Preliminary stage: segregation to lattice defects and/or clustering of carbon.

First stage (T1): formation of low temperature carbides (*i.e.*, epsilon carbide).

Second stage (T2): decomposition of retained austenite.

Third stage (T3): formation and growth of cementite, and the recovery and/or recrystallization of martensite.

2.4.2. Segregation of carbon to lattice defects and clustering

Changes occurring during aging or tempering of martensite are largely related to the movement of carbon atoms from their as-quenched sites to lower energy locations. The movement of carbon can occur during quenching (autotempering) on high M_s steels [81], during aging at room temperature, or in some cases at sub-ambient temperatures, and at low temperature during heating to tempering or aging (~ 70°C) [22]. There are two types of carbon redistribution during low-temperature tempering, which possibly compete with each other namely: carbon trapping to lattice defects and carbon-cluster formation [27].

Carbon segregation to dislocations and to sub-boundary sites occurs in low-carbon and low-alloyed steel after quenching; thus, the dislocation sites become saturated above 0.2% of carbon. The octahedral interstitial sites (OIS) near a dislocation are energetically favoured over other OIS because of the expansion of the size by the strain field of the dislocation. In addition, because of the high rate of interstitial carbon diffusion, there is sufficient time for segregation of carbon to dislocations to occur [22].

Even though no actual carbide precipitation was observed; it has been postulated that carbon atoms segregate to dislocations and to sub-boundaries in very rapidly quenched thin samples in low-carbon high M_s martensites. The OIS near a dislocation are energetically favoured over other OIS because of the expansion in the size of the OIS by the strain field of the dislocation. In the case of lath martensite with an estimated dislocation density of 10^{12} to 10^{13} /cm^2, it is not surprising that a large fraction of the carbon in low-carbon martensites might be

segregated to dislocations sites or lath boundaries. Also because the distance between lath boundaries is only about 0.25 μm and because the high rate of interstitial carbon diffusion. There have been calculations of the amount of carbon that would be bound to dislocations, it has been observed that this binding energy is greater than that in low-temperature carbides (epsilon carbide). The binding energy to a dislocation is greatest near the core and decreases rapidly with increasing distance from the core [22].

On the other hand, clustering (grouping) or spinodal decomposition (fine dispersion) of carbon might be a competitive process with carbon segregation to dislocations. Aging above -40°C to about 70°C is accompanied by the diffusion-controlled clustering of carbon atoms. This regime, in fact, is followed above 100°C by the precipitation of ε-carbide (*i.e.*, the conventional third stage of tempering). At still higher temperatures, cementite forms separately (*i.e.,* the conventional third stage of tempering) in competition with ε-carbide [27].

Electrical resistivity measurements have been adopted in order to determine the overall aging and tempering kinetics of Fe-Ni-C martensites. From resistivity measurements, electron microscopy and X-ray diffraction experiments, it has been revealed that there are not significant differences in aging behaviour among the different morphologies of martensite (*i.e.,* lath and or twin martensite), instead, all of the carbon-containing martensites exhibit the same kinds of aging regimes, and both of the magnitudes and kinetics of such changes depend explicit on the carbon content rather than on the morphology [27].

At sub-ambient temperatures, the first changes are martensite-related and diffusion-controlled. Aging from subzero to about 70°C is accompanied by the formation of carbon-rich clusters which, at first, have only a few carbon atoms per cluster. These clusters coarsen to become larger domains (probably Fe_4C), and deplete the martensite lattice of carbon with the attendant emergence of low-tetragonal martensite. At higher temperatures this also results in the formation of ε-carbide and eventually cementite. There is some reason to believe that ε-carbide forms directly from the carbon clusters. The two carbide precipitations, corresponding to the usual first and third stages of tempering, overlap and their kinetics appear to be controlled by iron and substitutional atom diffusion along dislocations paths. Figure 2.17 summarizes the time and temperature regimes in which the above mentioned changes occur. Martensite morphology is found to have no measurable effect on the aging and tempering behaviour [27].

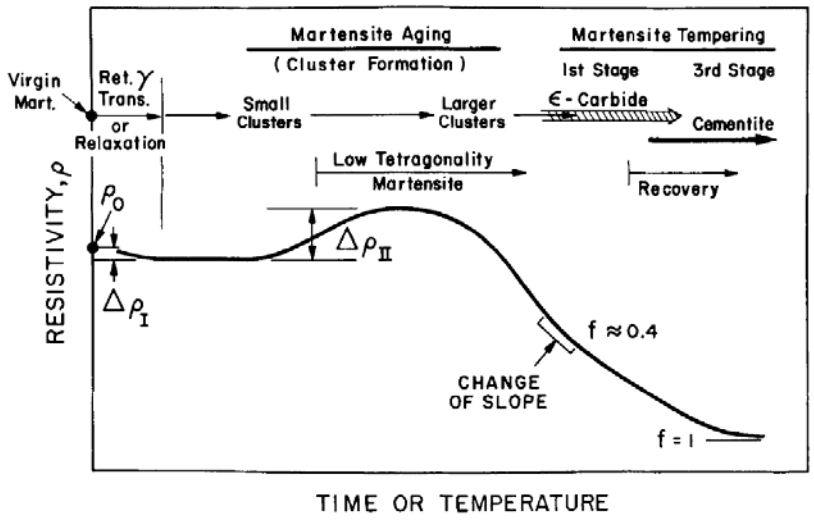

Figure 2.17 Schematic summary of structural changes during the aging and tempering of virgin martensites correlated with accompanying resistivity changes [27].

2.4.3. Formation of low temperature carbides

The first stage of tempering (T1) is associated with the appearance of transition carbide, which precipitates uniformly through the martensite phase. The precipitation of the transition carbide proceeds in a few minutes in the temperature range of 100°C to 450°C. In fact, this precipitation has been reported to adopt a variety of transition carbides at low temperature, *i.e.*, η-, ε-, χ- carbide. The formation of these carbides is accompanied by a particular crystal structure, habit plane, and orientation relationship, as listed in Table 2-1 [82].

It has been established that the first low-temperature carbide to precipitate upon tempering above 100°C in the first stage of tempering is the η-carbide [83- 87]. It has been found that the precipitation of η-carbide occurs in both morphologies, *viz.* plate-like and lath martensites (the precipitated carbide is η-Fe_2C). In general the precipitation occurs along dislocations, but it has been found that grain boundary precipitation also takes place in the non-parallel lath region and that in fine grains in this region the precipitation does not occur [84]. The shape of carbide is a very fine disk or ribbon whose largest area plane is parallel to the $\{100\}_M$ or $\{011\}_M$ plane, and the carbides parallel to the $\{100\}_M$ and $\{011\}_M$ planes are arranged along the $\langle 100\rangle_M$ and $[001]_M$ directions, respectively, forming an apparent rod or plate shape [87].

Table 2-1 Crystal structure, habit plane and orientation relationship for the η, ε, χ, and θ-iron carbides [82].

Iron carbide	Crystal structure	Habit plane	Orientation relationship
ε	Hexagonal	$\{100\}_\alpha$	$(0001)_\varepsilon // (011)_\alpha$ $(10\bar{1}1)_\varepsilon // (101)_\alpha$ $[11\bar{2}0]_\varepsilon \wedge [100]_\alpha = 5°$
η	Orthorhombic	$\{100\}_\alpha$	$(010)_\eta // (011)_\alpha$ $[001]_\eta // [100]_\alpha$ $[100]_\eta // [0\bar{1}1]_\alpha$
χ	Monoclinic	$\{112\}_\alpha$	$(100)_\chi // (\bar{1}\bar{2}1)_\alpha$ $(010)_\chi // (101)_\alpha$ $[001]_\chi \wedge [\bar{1}11]_\alpha = 7.74°$
θ	Orthorhombic	$\{110\}_\alpha$ $\{112\}_\alpha$	$(001)_\theta // (211)_\alpha$ $[100]_\theta // [0\bar{1}1]_\alpha$ $[010]_\theta // [\bar{1}11]_\alpha$

The precipitation of η-carbide does not deny the presence of ε-carbide, both are different carbides and the latter has been synthesized by several authors. If fact, the complexity of the change in specific heat below 200°C seems to suggest the possibility of transition from η-carbide to ε-carbide.

ε-carbide which is considered non-stoichiometric precipitates in the first stage of tempering and exists in tempered martensite up to 300°C with a fine and uniform distribution [88-91]. The nucleation of epsilon carbide is heterogeneous, at least in martensites that undergo spinodal decomposition [92] prior to T1 carbide precipitation. The apparent selection of only a limited number of possible orientation variants is explained in terms of the symmetry of the parent martensitic phase [22,91]. The martensitic substructure is not found to exert any significant influence on its overall precipitation behaviour.

A variety of morphologies have been reported for the ε-carbide: platelike with a $\{100\}_\alpha$ habit plane, rodlike along $\langle 100\rangle_\alpha$, and rodlike with the long axis nearly parallel to $\langle 211\rangle_\alpha$, the disparity among the above observations suggests that the alloy composition might exert an important influence on the actual carbide morphology. For instance, Figure 2.18 indicates that the ε-carbides are either rod- or platelike particles; either morphology can give rise to linear features under suitable imaging conditions.

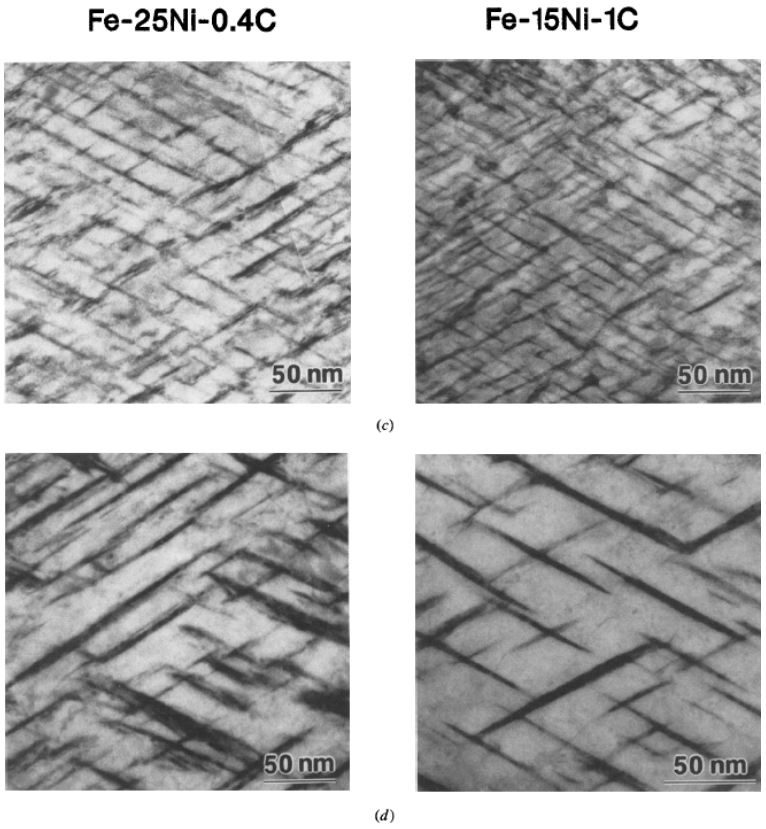

Figure 2.18 Electron micrographs from Fe-25Ni-0.4C and Fe-15Ni-1C aging/tempered martensites. (c) 100°C/1 h, bright field, B=100; and (d) 150°C/1 h bright field, B=711 [91].

It is clear that certain elements, notably silicon, can stabilize the ε-iron carbide to such an extent that it is still present in the microstructure after tempering at 400 °C in steels with 1-2% wt Si and at even higher temperatures if the silicon is further increased. While the tetragonality of martensite disappears by 300 °C in plain carbon steels, in steels containing some alloying elements, e.g. Cr, Mo, W, V, Ti, Si, the tetragonal lattice is still observed after tempering at 450 °C and even as high as 500 °C. It is clear that these alloying elements increase the stability of the supersaturated iron-carbide solid solution. In contrast manganese and nickel decrease the stability [63].

Over about 250°C ε-carbide becomes unstable and gradually fades away or transforms into χ- or θ-carbide [82,93]. The crystal structure of the χ-carbide is monoclinic structure of Fe_5C_2 type and has been observed at temperatures up to 400°C. The habit plane of χ-carbide, being $\{112\}_\alpha$ suggests preferential precipitation of this carbide on twin-matrix interfaces. Since its morphology and habit are quite different from those of ε-carbide, the transition, $\varepsilon \rightarrow \chi$, may be through a separate nucleation [82]. The transition of the twin nucleated χ-carbide to cementite

occurs in the temperature range between 350°C to 500°C [93]. As an example, the ranges of precipitation in accordance with electron microscopic observations are illustrated in Figure 2.19 for the precipitations of η-, ε-, χ-, carbides of 1.34% steel [82].

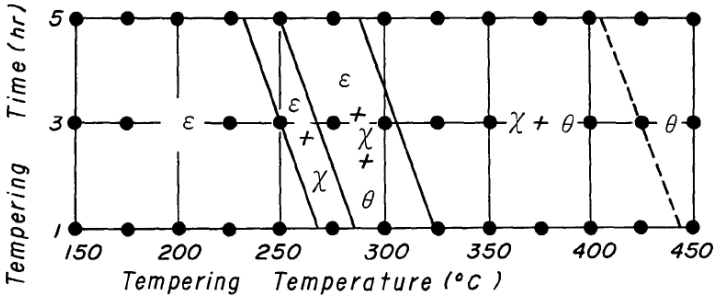

Figure 2.19 Temperature-time diagram showing the precipitation range of η-, ε-, χ- *and* θ-carbide in the tempering process of 1.34% steel. Observation points are indicated by solid circles. The dotted line shows ambiguous boundary of the precipitation range [82].

It is worth indicating that the precipitation of the above mentioned carbides, *i.e.*, η-, ε-, χ-, has been observed for steels with carbon contents above 0.45 pct. and up to 1.25%. Although ε-carbide is thought to form as the transition carbide during the first stage of tempering, it has never been positively identified in low carbon martensites, but its presence has been inferred from habit plane relationships. According to X-ray data, steels containing less than 0.25% carbon should not form ε-carbide [94].

2.4.4. Decomposition of retained austenite

Small amounts of retained austenite (RA) have been measured by Mössbauer Spectroscopy contained in medium- and some low- carbon hardened steels within the lath sub-structure of martensite. The interlath retained austenite films are quite thin and are revealed by careful selected area of diffraction and dark-field imaging in the transmission electron microscope [95]. Figure 2.20 shows an example of a RA analysis in which a $(200)_\gamma$ dark field image clearly reveals the interlath austenite films which are more or less continuous throughout the packet [96].

The austenite is considered to be beneficial to the toughness of high strength medium carbon steels, but it is also associated with tempered martensite embrittlement as a result of its decomposition to cementite during tempering [95]. Temper martensite embrittlement occurs when retained austenite decomposes at the lath boundaries to form M_3C. Alloying elements which disfavour M_3C precipitation and its growth appear to postpone the onset of the

embrittlement to a higher tempering temperature. Thus, Mn, Cr promote its decomposition at a lower temperature while Si, Al and Ni postpone it to a higher temperature [96].

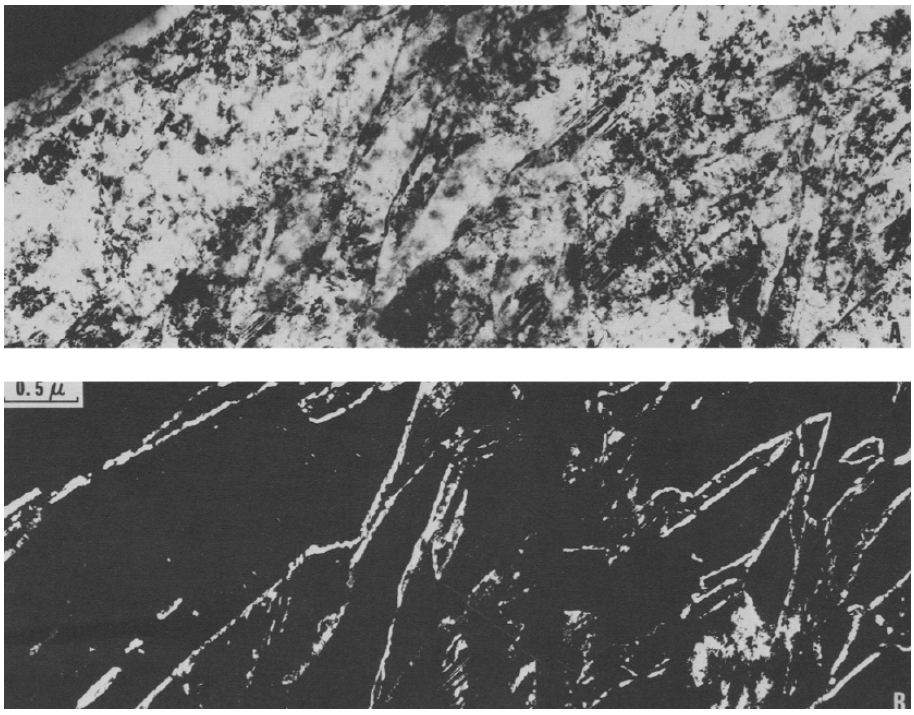

Figure 2.20 Bright field image (a) and dark field image (b) of an Fe-1Cr-1Mo-0.3C steel quenched from 870°C into ice water. Note that the interlath retained austenite films do not show good contrast in the bright field image, but are very clear in the $(200)_\gamma$ dark-field image [96].

The decomposition of RA has been associated to the second stage of tempering (T2). Inter-lath films of RA were observed to decompose into a mixture of ferrite and cementite (an orthorhombic M_3C carbide) [22]. The decomposition of retained austenite into M_3C carbide occurs upon tempering in the range of 250°C to 400°C. Moreover, intralath Widmastätten (morphology) Fe_3C forms from epsilon carbide.

Localized RA regions which contain relatively high concentrations of C are nucleation sites for eventual formation of carbides [97]. It is well known that increasing the carbon content of steels above 0.5 percent increases the volume fraction of retained austenite. The presence of relatively high amounts of Mn also contributes to carbon diffusivity and promotes rapid nucleation and growth of cementite [96]. After tempering one hour, at 300°C the retained austenite no longer exist in the two percent Mn alloys because it decomposes intro stringers of interlath carbides [97].

2.4.5. Precipitation, structure and growth of cementite

The third stage of tempering (T3) is associated with precipitation in the martensite of Fe_3C or cementite (θ carbide), the most stable of the various carbides. A number of thermally activated processes such as spheroidization of cementite, recovery, recrystallization, and grain growth occur at higher temperatures in the T3 regime. Precipitation of cementite generally begins in the temperature range of 200 to 300 °C. It is common for considerable overlap to exist between T2 and T3; both stages feature the same reaction product, *i.e.*, a mixture of ferrite and cementite [22]. In terms of structure, the lattice symmetry of cementite is orthorhombic (Table 2-1); the lattice constants for Fe_3C are a=0.5090nm, b=0.6744nm, c=0.4525nm. The structure of cementite can be described as layers of trigonal prisms stacked upon each other. The basic "building block" of this structure, a carbon coordinated by six iron atoms which together form a trigonal prism, is illustrated in Figure 2.21 (a). The manner in which the edges and corners of the prism are connected to form a layer, and how such layers are stacked in an A B A B A B… sequence, are shown in Figure 2.21(b) and (c), respectively.

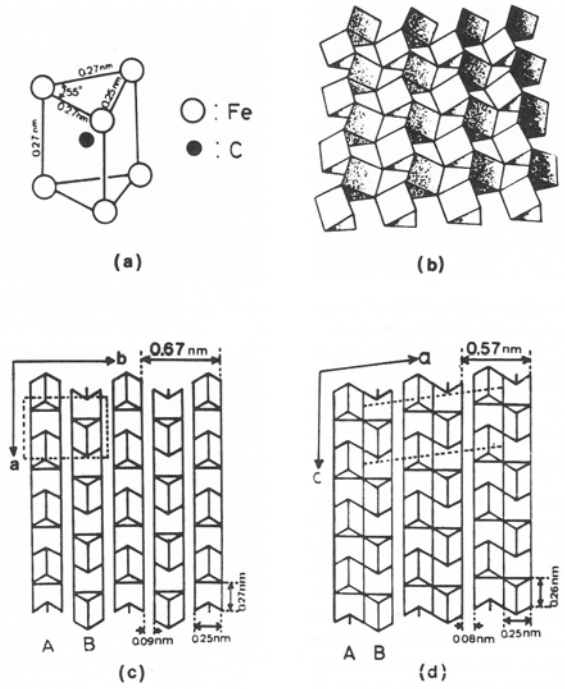

Figure 2.21 Schematic representation of cementite (θ-carbide). (a) The basic building block: a trigonal prism of iron atoms with a carbon atom at the center. (b) A single layer of trigonal prisms sharing edges and corners. (c) The stacking sequences of the layers for the cementite structure, projected along $[001]_\theta$. (d) The stacking sequence of the layers for the χ-carbide structure, projected along $[010]_\chi$ [22].

Two simple ways of distorting the octahedron of metal atoms in ferrite to give a trigonal

prism of the type found in cementite are illustrated in Figure 2.22. One distortion, involving displacements primarily along a cube edge, apparently does not occur, based on known orientation relationships. The other, involving smaller displacements primarily along a close-packet direction, leads to the Bagaryatskii orientation relationship often observed for cementite in ferrite and martensite [22]:

$$(010)_\theta \,||\, (11\bar{2})_\alpha$$

$$(100)_\theta \,||\, [111]_\alpha$$

and

$$[001]_\theta \,||\, [1\bar{1}0]_\alpha$$

It is well known that the addition of certain substitutional elements modifies the tempering characteristics of martensite. Additions of Mn, Si or Cr to advanced high strength steels have attracted more attention because of their recyclability and low material cost. The growth of θ is known to occur concurrently with the gradual redistribution of alloying elements during tempering of martensite, then, there exists remarkably retardation in the growth of cementite by the addition of alloying elements. This alloying effect has been considered to occur due to partitioning of these substitutional elements between the ferrite matrix and θ [30].

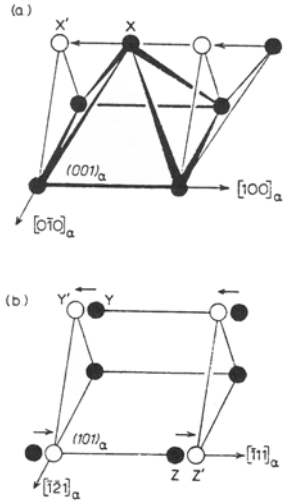

Figure 2.22 Possible atomic rearrangements to form a trigonal prism from a bcc lattice. The distortion in (a) does not lead to a known orientation relationship, whereas, (b) is equivalent to the Bagaryatskii orientation of Fe_3C in ferrite [22].

The kinetics theories of diffusional phase transformations in alloys containing both substitutional and interstitial elements are well developed. An important characteristic of the various kinetics models is that these assume equilibrium at the interface. Depending on the

interface velocity during transformation, the kinetics models are classified in three distinct modes: partitioning local equilibrium (PLE) or orthoequilibrium (OM), non-partitioning local equilibrium (NPLE) and paraequilibrium (PE) [98,99]. The expected concentration-depth profiles for cementite growth from martensite for all three transformation modes are schematically illustrated in Figure 2.23.

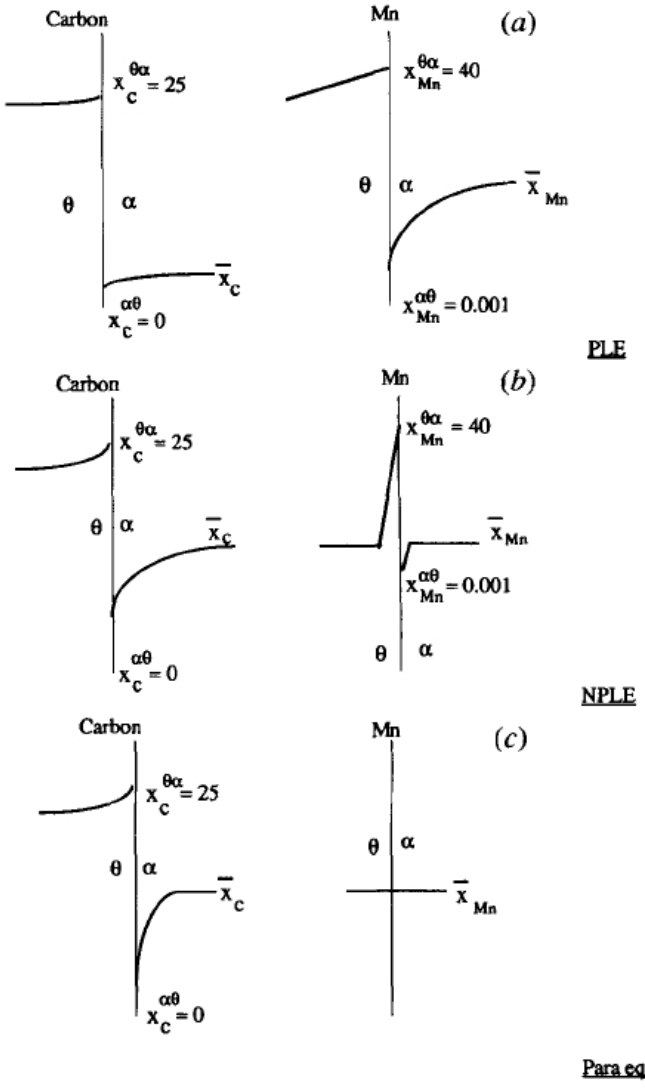

Figure 2.23 Schematic illustration of the concentration-depth profiles for the diffusional growth of cementite from martensite while tempering. The horizontal axis corresponds to distance and the vertical axis to concentration. The concentrations given in this figure are equilibrium concentrations (note that these concentrations are not calculated interface concentrations; nevertheless, the interface concentrations should be close to these values) calculated by the MTDATA program for Fe-1.84C-3.84Si-2.95Mn (at. pct.) steel tempered at 350°C [99].

In PLE; there exist low supersaturation and low interface velocity, the transformation is controlled by the slow diffuser (substitutional elements). In NPLE; there exist high

supersaturation and high interface velocity, and the transformation is controlled by the fast diffuser (interstitial atoms). PE is a kinetically constrained equilibrium when diffusivity of the Substitutional species is negligible compared to that of interstitial species. The kinetics of PE is governed by the fastest diffusing specie (*i.e.*,C or N) in steel. If carbon diffuses appreciably faster than the substitutional alloying elements, then the growing phase inherits the substitutional alloy contents [98]. If local equilibrium fails due to high undercooling, then the diffusion-spike width reduces to the order of the atomic spacing and then PE condition is achieved, in PE condition, there is no redistribution of substitutional elements between the precipitated phase and the matrix [99].

Mn actually retards cementite coarsening because it gradually enriches the cementite carbide during tempering, [31]. It has been seen that at a temperature of 400°C, the retardation of cementite growth by Mn addition is observed only after tempering for 1.2 ks. Cementite without partitioning of Mn is initially formed, and then gradually enriches cementite during tempering [100]. Quantification of the substitutional elements in cementite confirms its paraequilibrium state with ferrite at the very early stage of tempering (*i.e.,* at low temperatures) [98]. By tempering the sample for an extended period of time or at higher temperatures, a clear indication of partitioning of Mn in the cementite is observed. This suggests that the growth mode changes as follows: PE → local equilibrium [99].

In contrast, Si tends to partition in ferrite so that tempering resistance was attributed to the stabilization of ε-carbide by Si enrichment in ferrite. Thermodynamic calculations have suggested that under equilibrium conditions Si will partition into ferrite from cementite and an opposite effect for Mn [101]. In fact, the Si-added alloys exhibit large resistance to softening at all the tempering temperatures, whereas softening retardation by Mn addition is small at low tempering temperatures and increases with temperature. In tempering at 450°C and 650°C, Si is rejected from cementite at an early stage of precipitation. [100].

Reports on the partitioning behavior of Cr during tempering have pointed out that Cr does not redistribute in the early stage of tempering and the concentration of this element in cementite gradually increases during tempering. Cr partitioning has been observed to occur at higher rates with elevated temperatures close to Ac_1, in fact, Cr was observed to segregate preferentially to cementite at temperatures in the range 450°C to 730°C [102]. Atom probe field ion microscopy studies have demonstrated that there is no partitioning of Cr between cementite

and martensite after tempering at 350°C for times up to 40h. The enrichment behaviour and interface concentration of Cr in the cementite was found after prolonged aging at 450°C for 187h, thus switching from PE nature to that of equilibrium (orthoequilibrium). These results demonstrated that cementite, in Cr containing alloys, precipitates from supersaturated ferrite via a paraequilibrium transformation mechanism [103].

If strong carbide-formers (*i.e., Cr, Mo, V, W, etc.*) are present in considerable amounts, a fourth stage of tempering (T4) may occur. In this stage the cementite particles dissolve and are replaced by more stable alloy carbides. The formation of these carbides is controlled by the diffusion of substitutional elements; hence the alloyed carbides are formed in the 500°C to 700°C temperature range and in a much finer dispersion than the cementite dispersion which they replace. As a result, hardness may increase during tempering at these higher temperatures, resulting in "secondary hardening" [22].

2.4.6. Recovery and/or recrystallization of martensite

The tempering of martensite has been evaluated primarily in terms of carbide precipitation reactions that develop on heating quenched medium and high carbon steels [104]. As part of the third stage of tempering, the dislocation substructure in martensite is annealed-out, resulting in the dislocation-free ferrite grain structure [22].

Recovery includes all annealing phenomena which occur before the appearance of recrystallized grains, whether these are detected by conventional or electron microscopy. Following the generally accepted concept, recrystallized grains are taken as those virtually strain-free grains which grow in the deformed matrix by the movement of large-angle grain boundaries [105].

The recovery and recrystallization of isothermally tempered low-carbon lath martensite is an important feature at high temperatures (i.e. 600 °C to 700 °C) because the grain boundaries and the random dislocations are reduced and a new ferrite structure with carbides distributed throughout is developed [21].

During the tempering process of as-quenched martensite; the low angle lath boundaries change to sub-grains rapidly by recovery, thus the block regions turn into ferrite grains containing sub-grains. By sub-grain growth or coalescence, the density of sub-grains is decreased and finally block regions which consist of parallel laths with the same orientation,

turn into ferrite grains because the block boundary is essentially a high angle boundary. The high angle boundary component of total grain boundary area per unit volume drops only gradually with time, the initial decreases becoming more pronounced at higher tempering temperatures. Then the fine lath structure coarsens but retains the elongated packet-lath morphology until very late stages of tempering when an equiaxed structure gradually develops [104].

The stages of the recovery process can be summarized as follows: a) an initial stage dominated by recovery that significantly lowers the low boundary content of as-quenched martensite, b) an intermediate stage where recrystallization is suppressed because of the pinning of grain boundaries by carbide particles and recovery proceeds by polygonization or low angle boundary formation, c) a final stage where grain growth converts the aligned coarsened lath morphology that persist through earlier stages to an equiaxed ferritic grain structure [104].

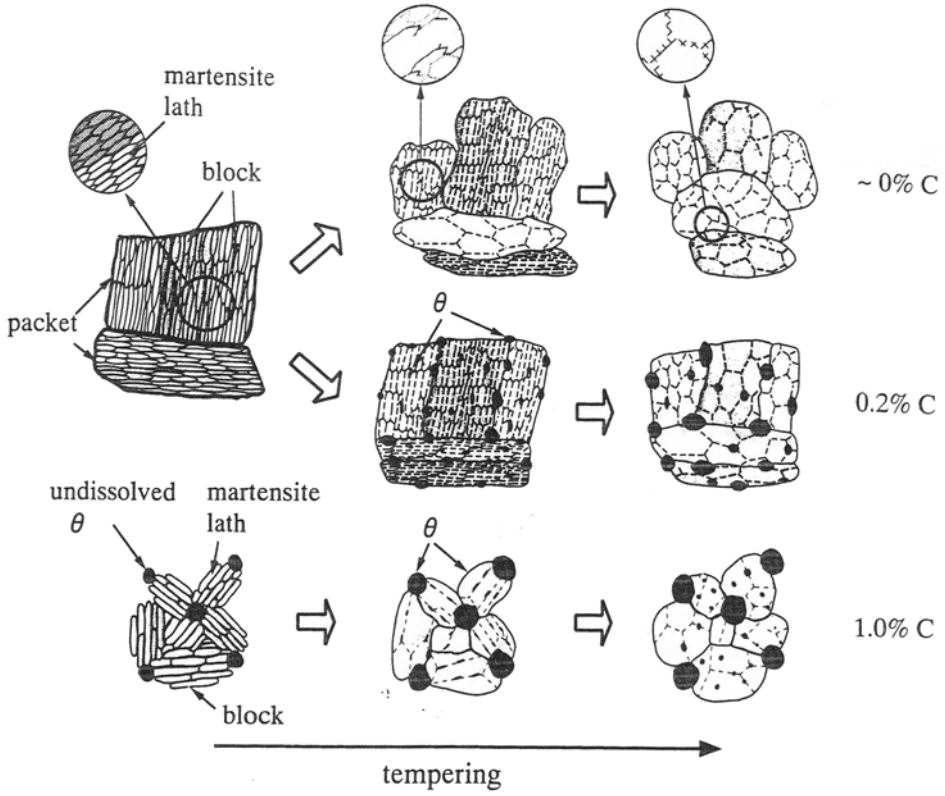

Figure 2.24 Schematic of the change in tempered matrix with carbon [107].

Considering the role of the carbides on the recovery process, lath boundary carbides can play an important role through the recovery process, while block boundary carbides contribute

to the suppression of the recrystallization through the sub-grain boundary pinning only in the latter annealing stage. For the reason of retarded recrystallization in low carbon martensitic steels, it is believed that carbides obstruct the movement of dislocations [106].

The grain growth of ferrite is inhibited due to a pinning effect by the precipitated carbides, this in turn is strongly dependent on the C content and the alloying level of the steel as depicted by the schematic in Figure 2.24 [107].

The recovery of the lath substructure develops gradually with time, however, no certain evidence of the nucleation of equiaxed strain free grain, *i.e.* classical recrystallization, is observed during tempering [104]. The recrystallization of lath martensite is not observed in as-quenched martensite on tempering even at high temperatures such as just below Ac_1; however, deformed lath martensite easily recrystallized on subsequent tempering [108].

2.4.7. Fast heating rate tempering

Few attempts have been made to investigate the tempering of low and medium carbon low alloyed martensitic steels subjected to rapid heating rates under isothermal conditions [109-112]. In such literature, experimental induction heating (IH) was used in order to perform rapid heating rates i.e. up to 1000 °C/s. It has been found that cementite is refined by increasing the heating rate and this refining was attributed to a higher nucleation rate. The time-temperature-precipitation (TTP) diagram in Figure 2.25 schematically describes the effect of heating rate on the temperature at which cementite nucleation occurs [109].

During precipitation, cementite is distributed mainly at the lath boundaries upon slow heating, but uniform distribution within the laths and lath boundaries was found at rapid heating rates, cementite is then refined. Moreover, the toughness is improved owing to refined cementite [110]. It has also been observed that upon rapid heating, spheroidization of cementite starts at higher temperature (i.e. 600 °C) in contrast to low heating rates in which sphere shaped cementite was observed at lower temperature (500 °C). Insufficient tempering time for the matrix softening including dislocation annihilation and recovery resulted in the retardation of the softening even at high temperatures [111]. It has been analyzed that the magnetic field in IH does not affect the nucleation sites or the total amount of cementite, but IH has strong effect on the directional growth of cementite and delays the process of recovery for the ferrite matrix. Obvious retardation of recovery and recrystallization and enhancement of ⟨001⟩ texture

component along the direction of magnetic field appeared in most of the materials investigated during magnetic field annealing [112].

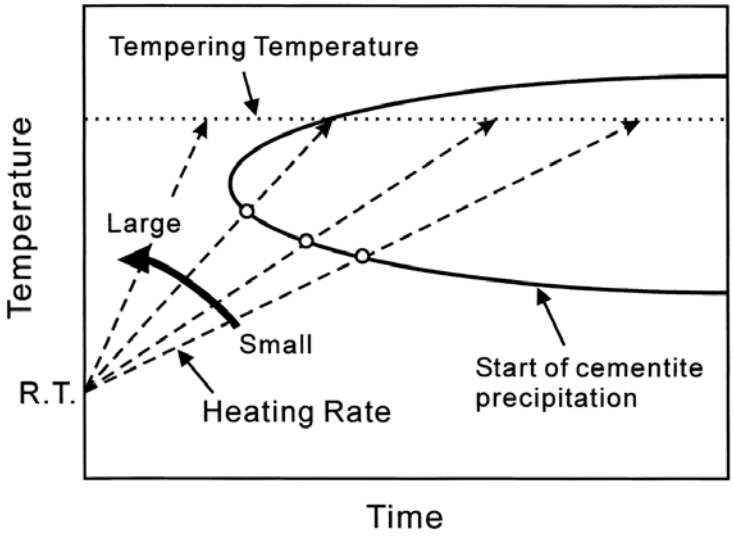

Figure 2.25 Schematic PPT diagram describing the effect of heating rate on cementite precipitation [109].

2.4.8. Tempering of DP steel

The tempering of martensite in dual-phase steel is a very limited subject in open literature, and most research in this field has been addressed towards the changes in the yield behaviour, the strength and the ductility of DP steel when isothermally heat treated. In such reports, DP steel has been mostly isothermally tempered for 3600 seconds within the range of temperatures between 200~600 °C [32,33,35,37].

The structural characteristics of the isothermally tempered of martensite in dual-phase steel has been hardly reported in literature [33,36,37]. There have been observed significant structural changes of the tempered martensite matrix upon high temperature tempering (i.e. 600 °C), for example, spheroidized cementite particles were observed at the matrix and all retained austenite was fully decomposed [33]. In a Mn-Si-V dual-phase steel the decrease in tensile ductility has been attributed to the decomposition of retained austenite to bainite which eliminates its contribution to tensile strength [32]. It has also been claimed that recovery of the lath substructure occurs when tempering is performed for extended time [36]. Spheroidization and recovery have been observed irrespective the carbon content of the parent martensite [37].

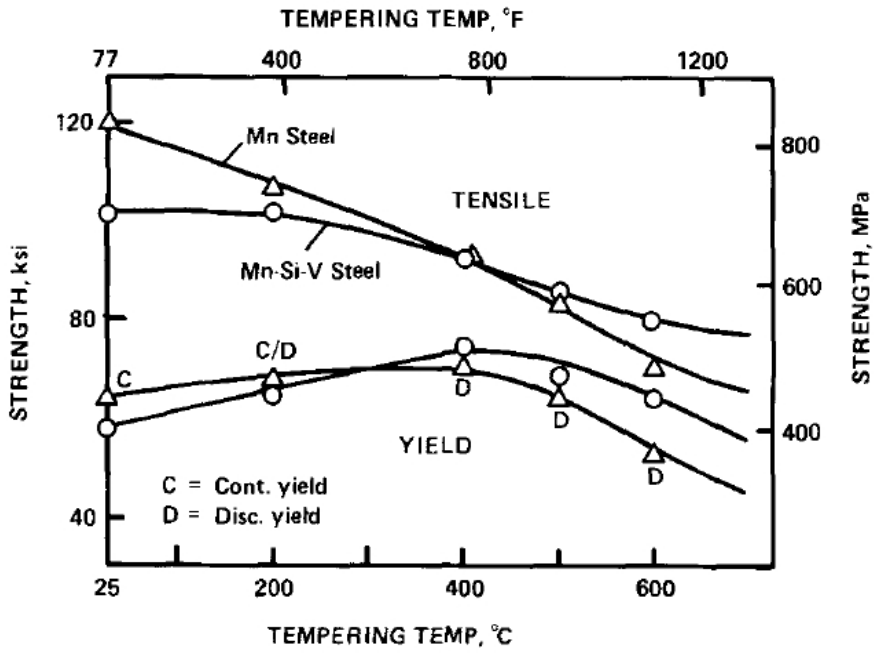

Figure 2.26 Effect of tempering on yield and tensile strength of DP steels [32].

Figure 2.26 summarizes the effects of tempering upon the yield and tensile strength of dual-phase steel.

The yield strength increases upon tempering up to 400°C, and then decreases. Discontinuous yielding did not completely return until the steels had been tempered at 400°C or higher. In contrast, the tensile strength decreased continuously upon tempering, although the tensile strength (and yield strength above 400°C) of Mn steels decreased more rapidly than that of the Mn-Si-V steel. On the other hand, the uniform elongation of Mn-DP steel decreased slightly upon tempering up to 400 °C, and then increased upon tempering at higher temperatures as shown by Figure 2.27a. Moreover, the total elongation of the Mn steel increased continuously upon tempering, consistent with the decrease in strength. In contrast, the total elongation of the Mn-Si-V steel first decreased upon tempering up to 400°C, and then increased upon tempering at higher temperatures, and then both steels had similar total elongations at temperatures above 500°C as depicted in Figure 2.27b [32].

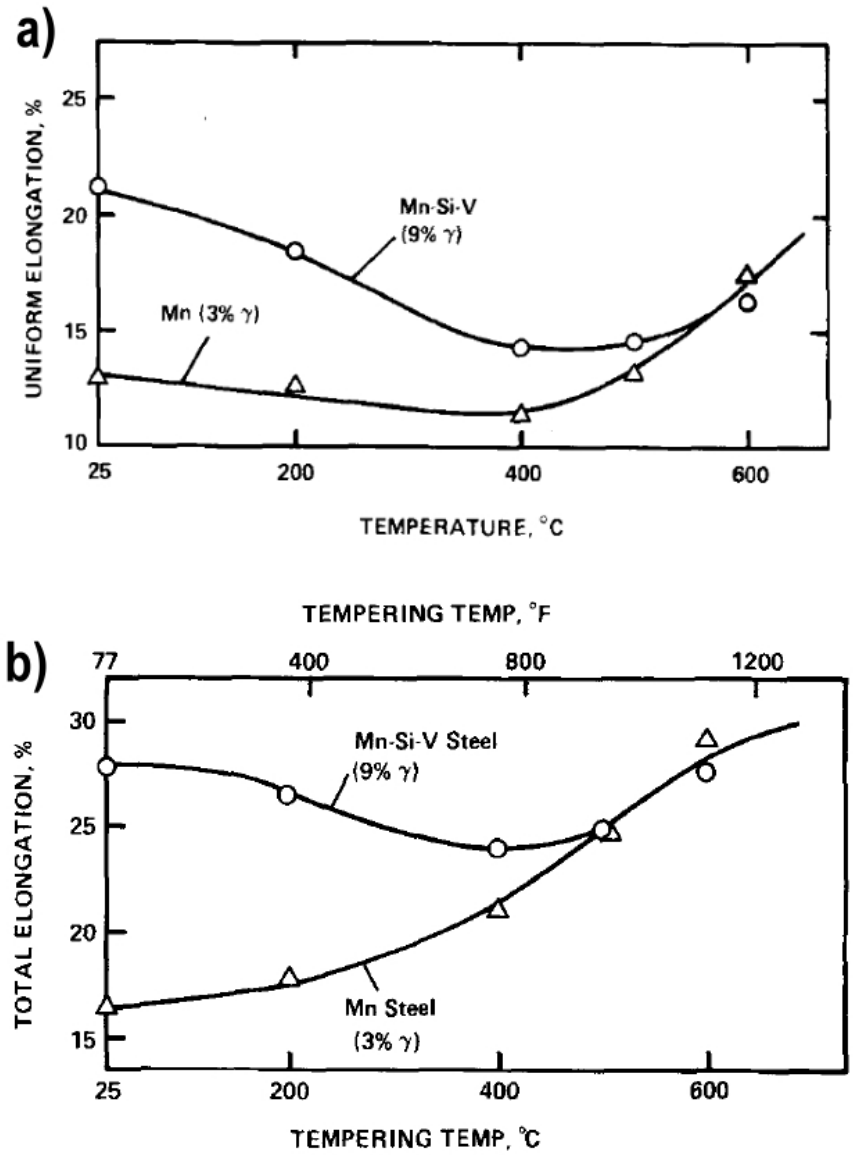

Figure 2.27 Effect of tempering on (a) uniform elongation and (b) total elongation of DP steels [32]

Microhardness has been reported for a range of isothermal tempering temperatures of dual-phase steel. Figure 2.28 shows microhardness results for two different DP steels after tempering for one hour. At 200°C an explicit hardening of martensite occurs, the magnitude of this hardening is related to the martensite carbon content. Moreover, tempering at 400°C and above, leads to a continuous softening in all martensites regardless of the carbon content, however, their softening rate is significantly lower than those of the corresponding Fe-C martensites [35].

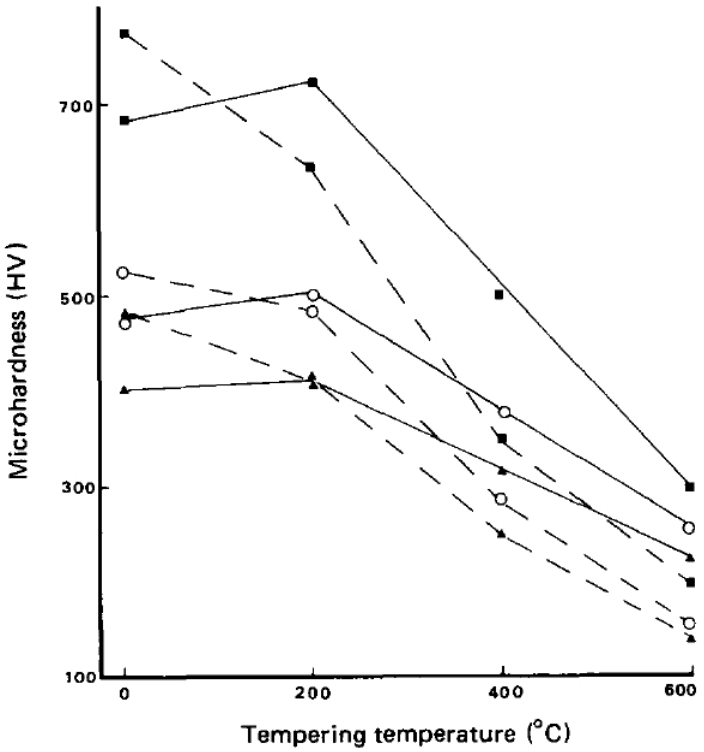

Figure 2.28 Variation in the martensite microhardness as a function of tempering temperature: ▲, Q Steel; ○, SQ steel, ■, IA steel; - - -, data of Grange *et. al.* [35]

2.5. Nanoindentation

2.5.1. Introduction

Instrumented indentation testing (IIT) is a relatively new method introduced in 1992 for measuring hardness and elastic modulus and is used in the characterization of mechanical behaviour of materials at small scale. Its attractiveness stems largely from the fact that mechanical properties can be determined directly from indentation load and displacement measurements without imaging the hardness impression [113]. Actually, the readings in IIT give an indirect measure of the area of contact at full load, from which the mean contact pressure, and thus the hardness, may be estimated. The test procedures for different indenters, usually involves an elastic-plastic loading sequence followed by unloading. The forces involved are usually in the millinewton (10^{-3}) range and are measured with a resolution of a few nanonewtons (10^{-9}). The depths of penetration are on the order of nanometres with a resolution of less than a nanometre [114].

Nanoindentation finds wide applications, the test results provide information on: the

elastic modulus, hardness, strain-hardening, cracking, phase transformations, creep, fracture toughness, and energy absorption of the assessed material [114].

2.5.2. Fundamentals

Conventional indentation hardness testing involves the measurement of the size of a residual plastic impression in the specimen as a function of the indenter load. This procedure provides a measure of the area of contact for a given indenter load. In a nanoindentation test, the size of the residual impression is often less than a micron or few microns and this makes it very difficult to obtain a direct measure using optical techniques. In nanoindentation testing, the depth of penetration beneath the specimen surface is measured as the load is applied to the indenter. The known geometry of the indenter then allows the size of the area of contact to be determined [114].

Berkovich indenter

Nanoindentation hardness test are generally made with either spherical or pyramidal indenters. One of the most utilized; the Berkovich indenter (Figure 2.29) is generally used in small-scale indentation studies and has the advantage that the edges of the pyramid are more easily constructed to meet at a single point. The face angle of the Berkovich indenter normally used for nanoindentation testing is 65.27°, which gives the same actual surface area to depth ratio as the Vickers indenter.

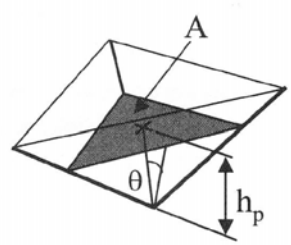

Figure 2.29 Indentation parameters for Berkovich indenter: A → projected area of contact, θ → angle of opposite faces, h_p → penetration depth [114].

Load-displacement (P-h) curves

A schematic representation of a typical data set obtained with a Berkovich indenter is presented in Figure 2.30 where the parameter *P* designates the load and *h* the displacement relative to the initial un-deformed surface. There are important quantities that must be measured

from the *P-h* curves: the *maximum load*, P_{max}, the *maximum displacement*, h_{max}, and the elastic unloading *stiffness*, $S=dP/dh$, defined as the slope of the upper portion of the unloading curve during initial stages of unloading (also called *contact stiffness*). Another important parameter is the *final depth*, h_f, the permanent depth of penetration after the indenter is fully unloaded [113].

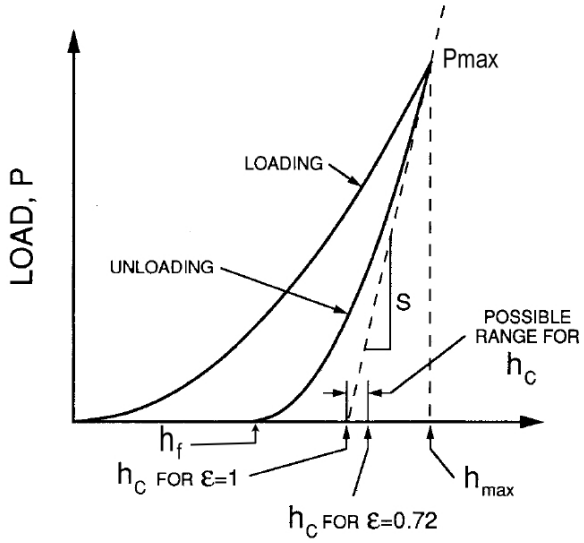

Figure 2.30 Schematic illustration of indentation load-displacement data showing important measured parameters [113].

Experiments have shown that unloading curves are distinctly curved and usually well approximated by the power law relation:

$$P = \alpha(h - h_f)^m \qquad \textbf{equation 2-11}$$

where α and *m* are the power law fitting constants. The variation of the power law exponents in the range $1.2 \leq m \leq 1.6$ demonstrates not only that the flat punch approximation is inadequate (m = 1 for the flat punch), but also that the indenter appears to behave more like a paraboloid of revolution for which m = 1.5. This result was somewhat surprising because the axisymmetric equivalent of the Berkovich indenter is a cone, for which m = 2. This discrepancy is explained by the concept of an *effective shape indenter* [113].

The exact procedure used to measure hardness (H) and elastic modulus (E) is based on the unloading processes shown schematically in Figure 2.31; illustrating a cross section of an indentation and identifies the parameters used in the analysis. At any time during loading, the total displacement h (max) is written as [115]:

$$h = h_c + h_s \qquad \textbf{equation 2-12}$$

where h_c is the vertical distance along which contact is made (hereafter called contact depth) and h_s is the displacement of the surface at the perimeter of the contact, and the radius of the contact circle is a.

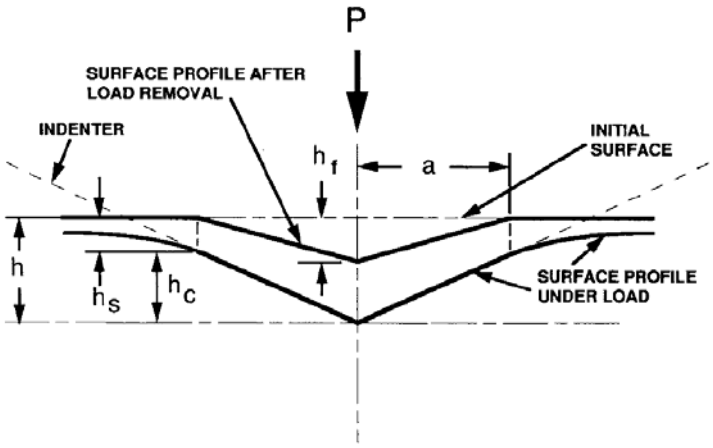

Figure 2.31 A schematic representation of a section through an indentation showing various parameters used in the analysis [115].

Upon unloading, the elastic displacements are recovered, and when the indenter is fully withdrawn, the final depth of the residual hardness impression is h_f.

Assuming that pile-up (tendency to form a crater in the periphery of the indentation) is negligible, the elastic models show that the amount of sink-in, h_s, is given by:

$$h_s = \varepsilon \frac{P_{\max}}{S} \qquad \textbf{equation 2-13}$$

where ε is a constant that depends on the geometry of the indenter. Important values are: ε = 0.75 for a paraboloid of revolution (which approximates to a sphere at small depths), and ε = 1.00 for a flat punch.

Using equation 2-13 to approximate the vertical displacement of the contact periphery, it follows from the geometry of Figure 2.31 that the depth along which contact is made between the indenter and the specimen, $h_c = h_{max} - h_s$, is:

$$h_c = h_{\max} - \varepsilon \frac{P_{\max}}{S} \qquad \textbf{equation 2-14}$$

letting *F(d)* be an "area function" that describes the projected (or cross sectional) area of the indenter at distance *d* back from its tip, the contact area is then:

$$A = F(h_c) \qquad \textbf{equation 2-15}$$

Once the contact area is determined, the hardness is estimated from:

$$H = \frac{P_{\max}}{A}$$ **equation 2-16**

Note that because this definition of hardness is based on the contact area under load, it may deviate from the traditional hardness measured from the area of the residual hardness impression if there is significant elastic recovery during unloading.

Pop-in behaviour

In some metals, the initial indentation behaviour is completely elastic, with fully reversible loading. At some point, as the load increases, the material undergoes irreversible plastic deformation that, in load-controlled-instrumented indentation, manifest as a "pop-in" or excursion in depth. An example of pop-in behaviour or excursion in an annealed Ni sample obtained using a spherical indenter is provided in Figure 2.32 [116]. With increasing development of load and depth sensing technology, it is possible to clearly identify the onset of plasticity during indentation by analyzing the load-displacement curve. Many experiments have observed that the excursions or the discontinuity in the load-depth curves corresponds to the transition between elastic and plastic behaviour of the material [117]. These observations were thus related to dislocation motion in general and in particular to dislocation nucleation [117], or the onset of dislocation plasticity [116].

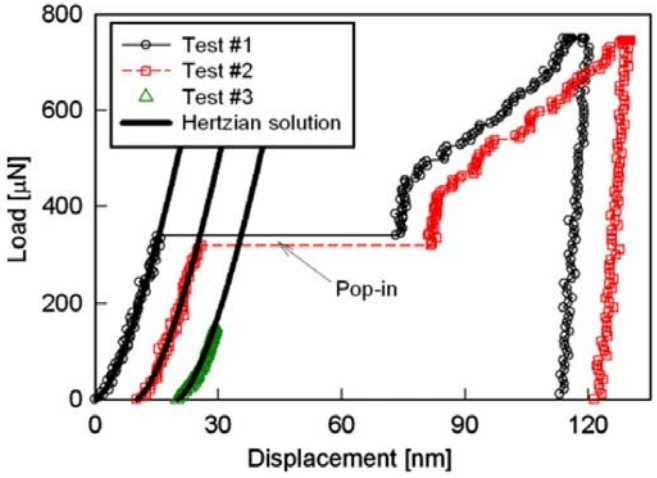

Figure 2.32 Typical nanoindentation load-displacement data for annealed (100) Ni obtained using a 0.58 μm radius spherical indenter. Elastic contact (Hertzian) solutions are shown for the data below the pop-in loads [116].

Pile-up

According to the discussion of equation 2-13, one significant problem with the method is that it does not account for pile-up of material around the contact impression, as it is observed in many elastic-plastic materials. When pile-up occurs, the contact area is greater than that predicted by the method, and the hardness is overestimated, sometimes by as much as 50 pct. This inability to deal with pile-up is a direct consequence of using an elastic contact analysis to determine contact depth.

The fundamental materials properties affecting pile-up are the ratio of the effective modulus to the yield stress, E_{eff}/σ_y, and the work-hardening behaviour. In general, pile-up is greatest in materials with large E_{eff}/σ_y and little or no capacity for work hardening (*i.e.*, "soft" metals that have been cold worked prior to indentation).

2.5.3. Nanoindentation of martensitic steel

Tempering of martensite has been documented as the main cause of softening in fully martensitic steels, and the degree of tempering has been extensively studied through traditional micro-hardness testing. Few studies of tempering have so far been attempted using instrumented nanoindentation techniques.

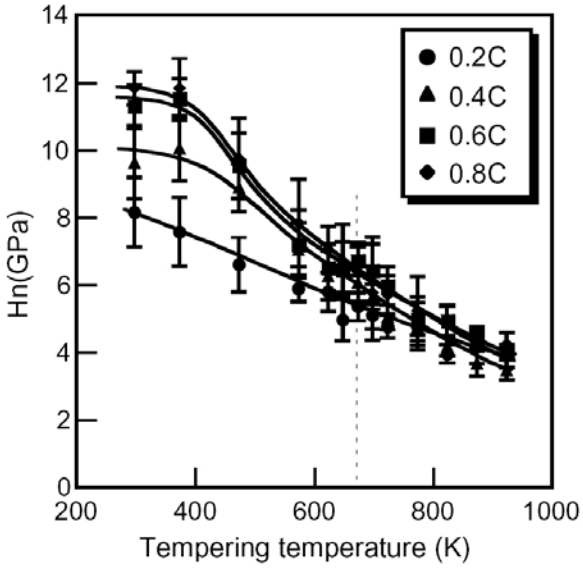

Figure 2.33 Tempering temperature dependence of the nanohardness H_n for the Fe-C martensite [118].

For example, martensitic steels were held at tempering temperature for extended periods

of time of up to 5400 seconds; nanoindentations were made on tempered martensite and the effect of grain boundaries on the nanohardness was discussed [118]. The nanohardness H_n for various Fe-C steels are plotted as a function of tempering temperature in Figure 2.33. The nanohardness obviously decreases with increasing tempering temperature, indicating that the temper softening occurs in the martensitic matrix. The plot also shows the carbon content dependence, *i.e.*, larger hardness in high carbon content steel [118].

Additionally, the difference in nanohardness with changing carbon content is gradually decreased with increased tempering temperature [118]. The basic indentation-induced deformation behaviour should be observed on load-depth curves obtained by nanoindentation test. Typical load-depth curves for the Fe-0.6C binary steel at various temperatures are represented in Figure 2.34 [140]. The contact depths increase with increasing tempering temperature at the same peak load, indicating significant temper softening. The loading curves showed continuous deformation for the 473 K tempered specimen while the specimens tempered at higher temperatures at 773 K and 923 K represent obvious pop-in behaviour at the initial stage of the loading curves as indicated by an arrow [140].

2.5.4. Nanoindentation of dual-phase steel

Very little efforts have been made to assess properties of individual phases in dual-phase steel by IIT [119]. *Delincé et.al.*, nanoindented ferrite and martensite in DP steels with different grain sizes (0.7 to 4μm) and separated the various contributors to strengthening (size effect, grain size, natural hardening of ferrite and reinforcement by the martensite) by changing the indentation depth with respect to size of the microstructure.

The variation of hardness as a function of the indentation depth is presented in Figure 2.35 for ferrite and martensite [119]. Martensite hardness decreased continuously by increasing indentation depth as classically observed for the indentation size effect. At lower forces, for which the interactions between the phases are minimised, the hardness of martensite is about 2-3 times larger that that of ferrite. The hardness of the ferrite decreases with increasing indentation depth up to 100 nm. The hardness then significantly increases. From the above results, it can be summarized that the hardness reaches a minimum and then increases when the plastic zone starts interacting with grain boundaries and second phases up to a maximum. The maximum corresponds to the full interaction regime where the indentation zone encompasses a

representative volume element of the microstructure [119].

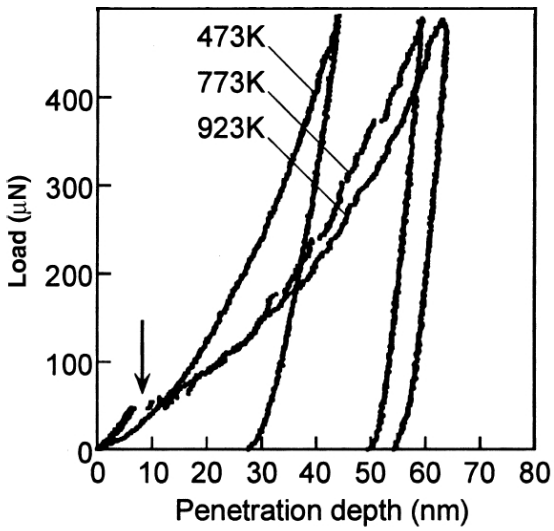

Figure 2.34 Typical load-depth curves obtained by nanoindentation test for Fe-0.6C binary steel. The tempering temperatures are indicated in the figure [140].

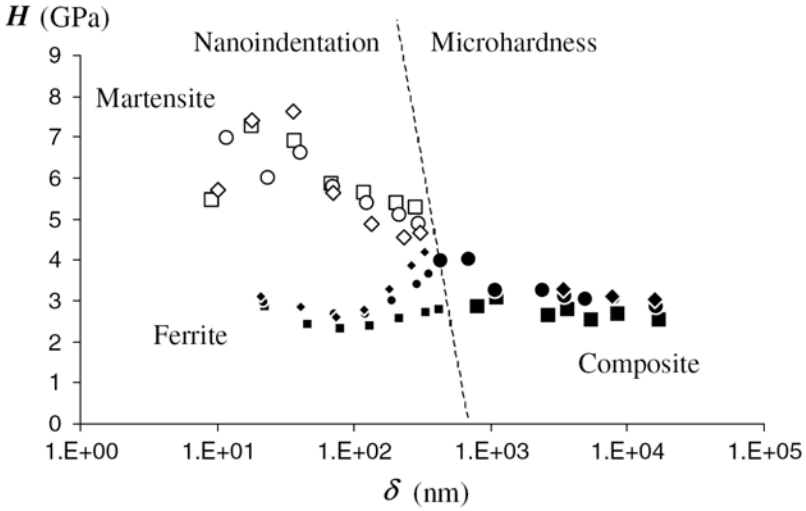

Figure 2.35 Variation of the hardness as a function of the indentation depth in the CG (■,□), FG (●,○), and VFG (♦,◊) steels. Open symbols are used for the martensite while black symbols refer either ferrite at small depths (small symbols) or to the composite response at large depths (large symbols) [119].

3. Experimental Methods

3.1. Materials

Dual-phase (DP) steels with different chemical compositions and distinct mechanical properties were used in this study with the purpose of examining a variety of DP steel grades potentially applicable to auto-body construction [3]. The DP steels used in this work were supplied from several sources (*i.e.,* steelmakers). Details about their manufacturing processing are not disclosed here; however, it can be mentioned that all steels were primarily cold rolled, followed by an inter-critical annealing heat treatment.

3.1.1. Chemical Composition

The batch of DPs studied in this research includes: two lower grades of DP steel, *i.e.*, DP600, three medium grades, *i.e.*, DP780 and DP800 and two higher grades, *i.e.*, DP980. The bulk chemical compositions of the various DP steels used in this work are listed in Table 3-1. In order to summarize the bulk chemistry of the materials and make further comparison; the carbon equivalent (*CE*) has been calculated using Yurioka's formula [120] and is additionally provided in Table 3-1.

3.1.2. Base Metal Properties

The volume fraction of martensite (f_m) indicated in Table 3-2 was obtained by standard metallographic analysis. By assuming that the DP microstructure is a mixture of two phases *i.e.*, ferrite and martensite of equal density, calculation of the carbon content within the martensite was done by employing [121]:

$$|\%C|_m = \frac{|\%C|_a - |\%C|_f\ (1 - f_m)}{f_m} \qquad \textbf{equation 3-1}$$

where $|\%C|_m$, $|\%C|_f$ and $|\%C|_a$ are carbon contents of martensite, ferrite and bulk alloy, respectively, and f_m is the volume fraction of martensite. By assuming a carbon content of

0.005% in ferrite at room temperature [122], by using the f_m from Table 3-2 and the bulk carbon content from Table 3-1; the martensite carbon content was estimated for all DP steels using equation 3-1. It is noteworthy to point out that the carbon content within martensite increases while decreasing the volume fraction of martensite (Table 3-2). For instance, this indicates that higher strength steel (i.e., DP980) is characterized by containing low carbon martensite islands.

Table 3-1 Base Metal Chemical Composition

	Steel						
Element	***DP600$_A$***	***DP600$_B$***	***DP780$_A$***	***DP780$_B$***	***DP800***	***DP980$_A$***	***DP980$_B$***
C	0.106	0.099	0.149	0.113	0.147	0.132	0.150
Mn	1.530	1.523	0.880	2.082	1.719	1.907	1.500
P	0.011	0.009	0.020	0.016	0.013	0.014	0.010
S	0.002	0.007	0.001	0.004	0.002	0.006	0.006
Si	0.183	0.157	0.230	0.036	0.294	0.030	0.313
Cu	0.041	0.044	0.058	0.031	0.039	0.036	0.021
Ni	0.020	0.015	0.017	0.013	0.040	0.019	0.010
Cr	0.193	0.197	0.325	0.239	0.612	0.161	0.021
Sn	0.007	0.001	0.004	0.002	0.002	0.007	0.009
Mo	0.205	0.196	0.108	0.181	0.018	0.036	0.006
Al	0.040	0.039	0.034	0.053	0.036	0.058	0.047
Nb	0.003	0.001	0.003	0.003	0.004	0.003	0.002
Ti	0.021	0.019	0.022	0.001	0.007	0.002	0.002
V	0.005	0.005	0.006	0.004	0.008	0.005	0.003
N	0.005	0.004	0.005	0.007	0.006	0.009	0.009
CE	***0.342***	***0.326***	***0.368***	***0.427***	***0.525***	***0.475***	***0.391***

The nominal steel sheet thickness and the zinc coating (type and the average weight from the top side of the hot-dipped galvanized coil) are provided in Table 3-2. As can be noted, the nominal thickness of the steels was kept consistently to 1.2 mm.

Table 3-2 Base Metal Properties & Steel Sheet Characteristics

Steel	f_m	*Calculated Carbon content in martensite (wt. pct.)*	*Sheet Thickness (mm)*	*Sheet Zinc Coating*	
				*Type**	*Average Weight g/m^2***
$DP600_A$	15	0.678	1.2	GA	46.4
$DP600_B$	14	0.676	1.2	GI	55.1
$DP780_A$	21	0.690	1.2	GI	71.8
$DP780_B$	26	0.420	1.2	GA	58.8
DP800	40	0.360	1.25	GI	55.9
$DP980_A$	48	0.269	1.2	GA	56.3
$DP980_B$	54	0.273	1.2	GI	59.6

*GI – Galvanized, GA – Galvannealed, ** Data from top side (one side)

3.1.3. Tensile Properties

The experimentally determined uniaxial tensile properties 0.2% yield strength (YS), ultimate tensile strength (UTS), % elongation for longitudinal samples for the base metals of all DP steels are listed in Table 3-3. The mechanical properties listed in Table 3-3 correlate well to the volume fraction of martensite; for example, DP steel with higher f_m value corresponded to higher UTS and lower elongation.

Table 3-3 Tensile Properties of the DP steels

Steel	*YS (MPa)*	*UTS (MPa)*	*Total Elongation (%)*
$DP600_A$	369	631	25
$DP600_B$	380	612	28
$DP780_A$	496	827	18
$DP780_B$	480	834	18
DP800	524	820	18
$DP980_A$	534	979	15
$DP980_B$	674	1061	12

3.2. Resistance Spot Welding

3.2.1. Equipment

Welding Machine

Welds were conducted using a pedestal-type, pneumatically controlled, 250 kVA single phase AC resistance spot welding machine with constant current control operating at 60 Hz. A Robotrom^{TM} Series 400 system controller was attached to a Centerline Ltd AC resistance spot welding machine. The AC machine setup used in this work is shown in Figure 3.1.

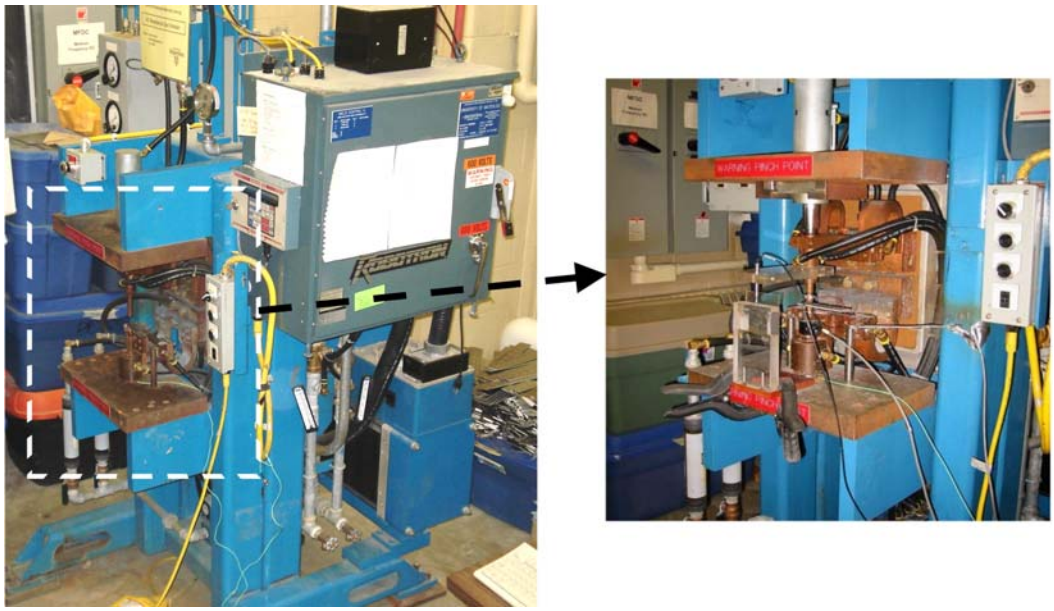

Figure 3.1 Single phase AC RSW machine.

Two type of electrodes were used according to the Resistance Welding Manufacturing Alliance [4] (RWMA): one type of electrode for welding was female, 40-degree truncated, class-2 type-E with a 6 mm face diameter, the second type of electrode was dome radius, class-20, with 6 mm nominal face diameter and 40 mm tip radius. Electrodes were cooled following AWS standards [57] with a water flow rate of 4 l/min and temperature of 20°C. New electrodes were applied for each combination and a stabilization procedure suggested by the AWS was employed to break-in the contact tips.

DAQ System

A data acquisition system (DAQ) system was attached to the RSW machine (Figure 3.1)

in order to monitor load, displacement, current and voltage simultaneously as a function of time. The load cell was positioned under the bottom electrode holder in order to measure the force applied by the pneumatic cylinder. A linear transducer was mounted to the top electrode holder to measure the displacement. A calibrated coil collected the dI/dt; it was adapted to attain current as a function of time. A couple of conductors were installed on both top and bottom electrodes in order to capture the corresponding voltage signal. The data acquisition rate was 25000 points per second. An example of collected data from the DAQ device is provided in Figure 3.2.

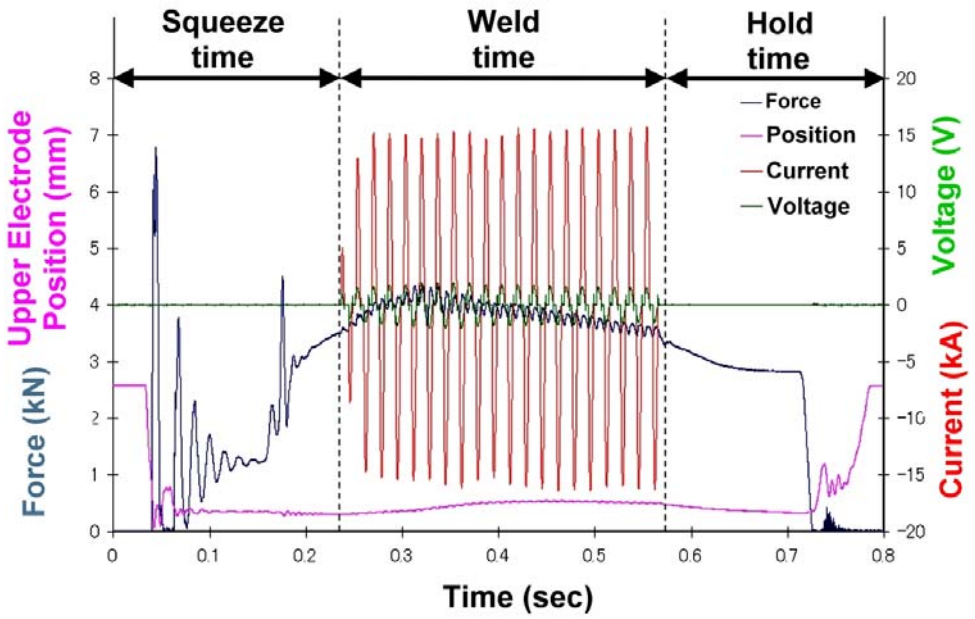

Figure 3.2 Experimental DAQ output.

3.2.2. Welding Procedure

A representative resistance spot welding cycle utilized in this study can be visualized by the experimental DAQ graph illustrated in Figure 3.2. Three continuous steps for completion of single spot weld indicated in the upper portion of the graph (Figure 3.2) consist in: a) squeeze time; the electrode makes contact with the steel sheet developing some instability in the force curve *(i.e.*, at around 0.05 seconds) owing to initial contact/impact between electrode-sheet surface (Figure 3.2), b) weld time; after force has been stabilized, a current density is delivered to the stacked sheets, thus developing heat input and melting at the faying surfaces, and c) hold time (Figure 3.2). After the current has been cut off, the electrodes remain pressing the stacked

sheets with two purposes: first, perform further cooling to specimens (solidification process), and second, minimize expulsion of melted material from the faying surfaces. The above described cycle represents a single pulse welding schedule in resistance spot welding. The single pulse welding schedules were used with the starting parameters shown in Table 3-4. Some selected welding schedules were developed in previous work [123] and designed to produce a target weld size in excess of 5.0 mm, or $5\sqrt{t}$, where *t* is the sheet thickness (1.2 mm), which is commonly used as a minimum setup weld size. The electrodes were released from the work 5 cycles after the termination of weld current, this being a recognized standard feature of RSW procedures for sheet steel welding. The purpose of electrode release is to reduce the post-weld cooling rate.

Table 3-4 Welding Schedule Setup

Steel Weld Combination	*Force (kN)*	*Current (kA)*	*Time (cycles)*	*Hold Time (cycles)*	*Squeeze Time (cycles)*	*Electrode Type*
$DP600_A$ – $DP600_A$	4.5	7 – 9	20	5	25	Dome
$DP780_A$ – $DP780_A$	4.5	7 – 9	20	5	25	Dome
$DP980_A$ – $DP980_A$	4.5	7 – 9	20	5	25	Dome
$DP600_B$ – $DP600_B$	3.5	8 – 11	20	5	25	Truncated
$DP780_B$ – $DP780_B$	3.5	7 – 9	20	5	25	Truncated
$DP600_B$ – $DP780_B$	3.5	7 – 9.5	20	5	25	Truncated
DP800 – DP800	4	8	20	5	25	Dome
$DP980_B$ – $DP980_B$	3.5 – 4	8	20	5	25	Truncated

3.2.3. Weld Size Measurements

Two methods were used to measure the weld size as per AWS specifications [56]: peel test and metallographic inspection of the fused area. Steel sheets in the similar and dissimilar material combination were peeled back in separate tests in order to have consistent measurements. Upon peel testing, the weld button size was measured as an average of the minimum (d) and maximum (D) button dimensions, as depicted in Figure 3.3. In the case of dissimilar combinations, both steel sheets were alternatively peeled back.

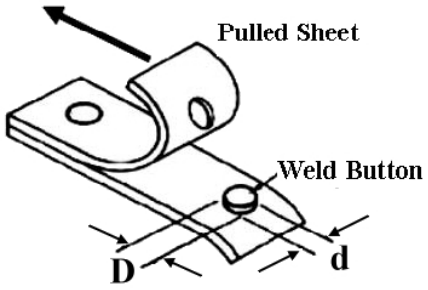

Figure 3.3 Peel test setup. The black arrow indicates the direction of the peeled sheet. Coupon dimension in mm was 120x40.

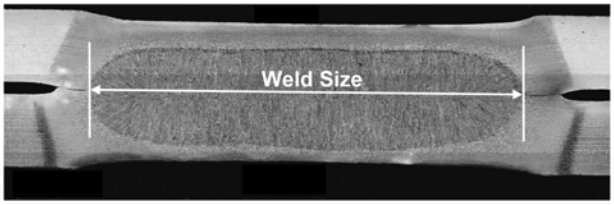

Figure 3.4 Weld size by destructive inspection of the nugget width in metallographic inspection.

Weld size measurements were also performed from metallographic cross-sections of the fused area by using image analysis. An example of a weld size measurement made on the cross-section fusion zone of resistance spot welded steel is illustrated in Figure 3.4. The apparent fracture area as an indication of weld size of some lap-shear interfacial failure welds was measured for completing the analysis. A stereo microscope Olympus™ attached with a Futaba Pulscale SA 105A™ measurement device with resolution of 0.05 mm was used for all measurements.

3.2.4. Tensile Testing

Lap-Shear Tensile and Cross Tension Testing

The lap-shear tension test and the cross-tension test were used to characterize the mechanical properties of the welds; a schematic representation is depicted in Figure 3.5a and Figure 3.6a, respectively. The tensile tests were conducted by employing an Instron™ 4206 universal testing machine. Samples were prepared following AWS standards [57]; so accordingly, coupon dimensions for lap-shear and cross tension were 105x45 mm and 150x50 mm, respectively. The cross-head velocity was maintained at a constant rate of 10 mm/min and all tests were performed at room temperature. Shims of same thickness bulk material were used for all lap-shear specimens in order to maintain alignment in shear tensile testing (Figure 3.5b).

The typical load-displacement curves for lap-shear tensile testing and cross tension are shown in Figure 3.5c and Figure 3.6b, respectively.

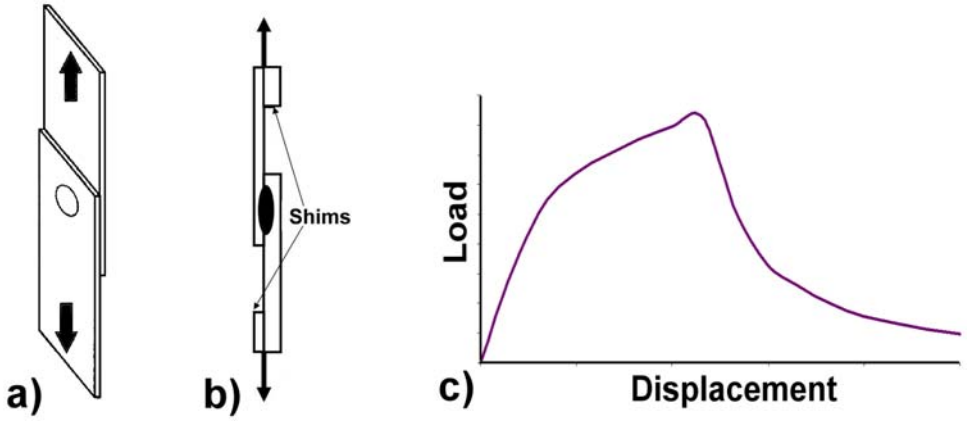

Figure 3.5 Mechanical testing of lap-shear tensile: a) schematic, b) side view showing the positioning of shims c) typical load-displacement curve. Black arrows indicate the loading direction.

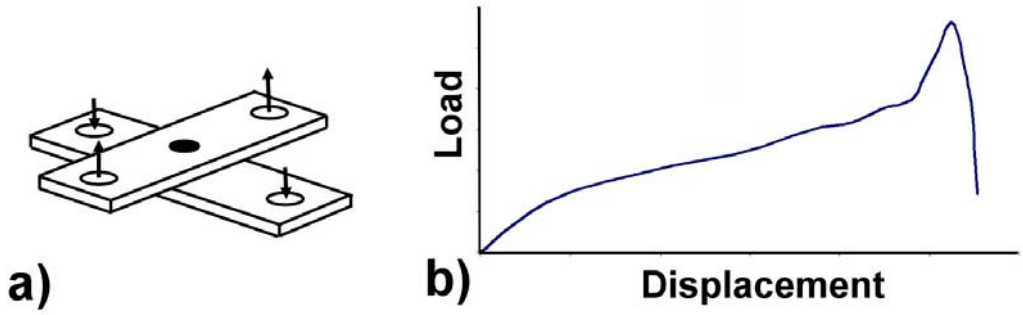

Figure 3.6 Mechanical testing of cross tension: a) schematic, b) typical load-displacement curve. Black arrows indicate the loading direction.

Larger displacements are expected under cross tension configuration (Figure 3.6c) before necking and failure in comparison to lap-shear configuration. Larger displacement is owing to extended bending developed under cross tension specimens at the onset of the pulling process. The area under the curve (if no sliding occurs) represents the energy absorption of the tested sample during the tensile test.

Partial Tensile Testing

Partial lap-shear tensile tests were conducted by stopping the cross-head before the maximum or peak load at 1.0 mm, just after the peak load at a displacement of 2.0 mm, after the final fracture in both sheets at 2.4 mm of displacement, and just before final steel sheet separate

apart at 3.8 mm of displacement. $DP600_B$ paired to $DP780_B$ specimens were used in this particular trial. Details about the stop positions for the partial lap-shear test are indicated by dotted lines in the lap-shear load-displacement curve of the dissimilar $DP600_B$-$DP780_B$ (Figure 3.7).

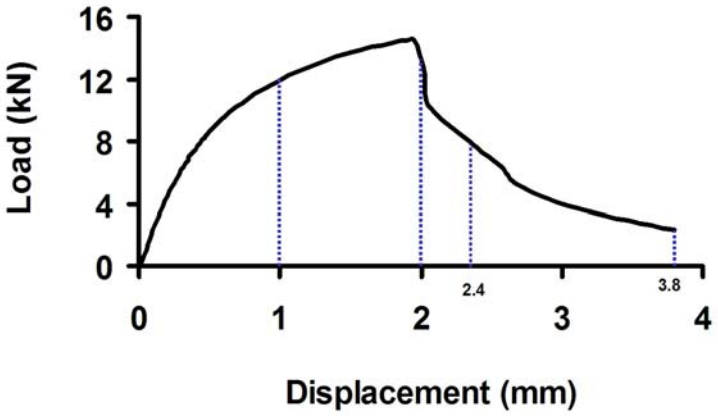

Figure 3.7 Lap-shear tensile test load-displacement curve indicating the stop of the cross-head at various displacements.

3.3. Isothermal Heat Treatments

In addition to the resistance spot welding trials on DP steel; isothermal heat treatments were performed upon varied time-temperature cycles by using conventional muffle furnace. Figure 3.8 depicts a schematic comparing a resistance spot welding cycle (non-isothermal) and an isothermal heat treatment case carried at peak temperatures of about 650 °C. Figure 3.8 indicates that under non-isothermal condition; the material easily achieves heating rates above 2000 °C/s, the sharp edge at the top of the curve indicates holding times of few milliseconds (i.e. log scale in the time axis), followed by short cooling time from peak to room temperature (i.e. approximately 10s).

The heating rates for the isothermal case were lower *i.e.*, 0.5 °C/s, followed by various holding times (t) and cooling in air atmosphere from peak to room temperature in around 10 s. The maximum (peak) temperatures in the range between 200-700 °C were employed for periods of time of 300s and 5400s. DP was isothermally tempered upon various conditions of time and temperature by utilizing a box muffle furnace Lindberg /blue M^{TM}.

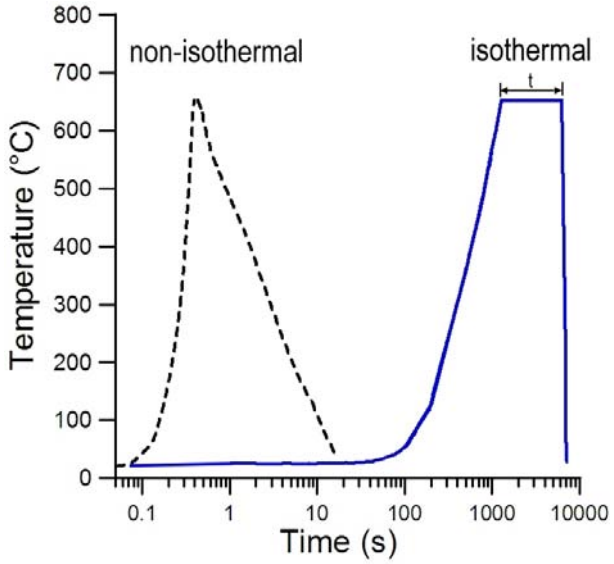

Figure 3.8 Thermal cycles for non-isothermal *vs.* isothermal tempering. Dotted line indicates the simulated thermal cycle for RSW.

3.4. Materials Characterization

Metallographic cross-section samples were prepared and weld microstructure was examined by optical microscopy, scanning electron microscopy (SEM) and X-ray diffraction (XRD) characterization techniques.

The specimens for optical microscopy were cross-sectioned along and parallel to the rolling direction of the steel sheet. After the cutting process; the specimens were cold mounted in epoxy resin, mechanically ground, and polished with diamond particles of 0.25 μm in size. After mechanical polishing, specimens were etched by immersion (for 5-10 seconds) in either of the following solutions: Nital etching; a solution of 1 pct. HNO_3 and 99 pct. Ethanol, LePera's etching: 1 g $Na_2S_2O_5$ + 100 ml distilled water and 4 g $C_2H_3N_3O_7$ + 100 ml ethanol. Optical microscopy was conducted on an optical microscope Olympus™ BX51M coupled with image analysis software QCapture Pro Ver. 5.1.

Specimens for SEM observations were ground and polished through the above mentioned metallographic sample preparation techniques. However, electropolishing was also utilized in various specimens. Electropolishing procedures consisted of immersing the specimen in a solution of 90 percent of CH_3COOH and 10 percent of $HClO_4$ by employing a voltage of 25 V for periods of 15 to 30 seconds. SEM observations were performed in a microscope JEOL7000F® attached with field emission filament. XRD specimens were prepared by

following the above mentioned metallographic procedures. Particularly, the sub-critical HAZ of DP steel and the isothermally heat treated specimens were analyzed in a Rigakku® micro-XRD diffractometer equipped with Cu radiation. The XRD analysis at the SC-HAZ was conducted on cross-sectioned specimens and on electropolished prepared samples.

Specimens for microhardness testing were prepared utilizing conventional metallographic techniques. Hardness indentations were performed in a Shimadzu^{TM} HMV-2000 apparatus. Cross-weld hardness profiles were obtained at room temperature using a Vickers micro-hardness tester according to AWS standards [57]. An applied load of 200 g and a dwell time of 15 s were used. The indentations were spaced 200 μm apart. The microhardness traverses were done on a diagonal covering base metal, heat-affected zones and fusion zones of both steels.

3.5. Instrumented Nano-indentation Technique

3.5.1. Apparatus

The IIT tests were performed in a Hysitron triboindenter TI-900 equipped with a scanning probe microscope (SPM) for imaging. A Berkovich indenter attached to the apparatus was utilized for all nanoindentaion trials in this study. The nanoindenter setup is illustrated in Figure 3.9.

Figure 3.9 Nanoindentation apparatus setup.

3.5.2. Sample Preparation

The base metal specimens were cross sectioned along the rolling direction, mechanically ground, and polished by conventional metallographic techniques. Three different surface conditions were investigated and samples were prepared according to the following procedures: 1) *mechanically fine polished*, consisted of polishing down to 0.25 μm followed by fine polishing with 0.05 μm colloidal silica; 2) *chemically etched*, consist of mechanically fine polishing followed by etching with 2% nital solution for a period of 8 to 10 seconds in order to further remove possible hardened layers; 3) *electropolished*, after grinding and polishing, specimens were immersed in a solution of 90% of acetic acid and 10% of $HClO_4$, a voltage of 25 V was applied for a period of sixty seconds. It was assumed that the electropolishing procedure fully removed any hardened layer on the surface.

Roughness parameters were calculated from the topographic profiles obtained under scanning probe microscopy (SPM). Roughness was measured in selected areas of 100 μm^2 per surface condition. Roughness was also obtained for individual phases in the case of the chemically etched and the electropolished specimens. The average of the absolute value (R_a) along with the maximum height of the profile (R_t) were estimated.

3.5.3. Nanoindentation Procedure

The attached Berkovich indenter was calibrated using a standard fused silica specimen following standard procedures ISO 14577. A range of indentation loads between 750 μN and 6000 μN was utilized in order to obtain varied displacements for the indenter by penetrating individual phases in the dual-phase steel. The range of loads was limited to the maximum indentation size that permits covering of the selected phases, *i.e.*, ferrite matrix and martensite islands and in order to avoid contribution of other regions to nanohardness, a schematic of indentation on individual phases is depicted in Figure 3.10. Accordingly, after performing several trials at different load conditions, a constant load of 3000 μN was established for the remainder of the tests. Nanoindentation trials were conducted by applying a minimum of 10 indentations per assessed phase (i.e. martensite, ferrite, etc.). A loading-unloading cycle of 20 seconds was programmed.

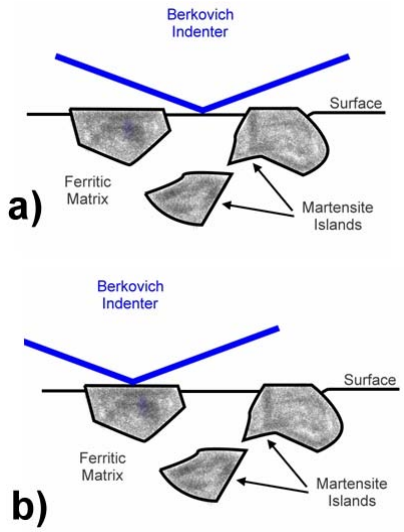

Figure 3.10 Example of nanoindentation on individual phases, *i.e.*,a) ferrite and b) martensite.

Two regions, namely base metal and sub-critical HAZ, were systematically evaluated by nanoindentation testing. The schematic cross-section of resistance spot welded DP steel in Figure 3.11 shows the distribution of different regions that form after welding. The fusion zone (FZ) is displayed at the far left side and the unaffected base metal (BM) at the right. The heat affected zone (HAZ) has been conveniently sub-divided at the location of Ac_1 as: upper-critical HAZ and sub-critical HAZ. Nanoindentation trials were performed at the location schematically indicated by the subscripts a, b c d e f, and g, specifically at 100 μm, 200 μm, 400 μm, 600 μm, 800 μm, 1000 μm, and BM, respectively.

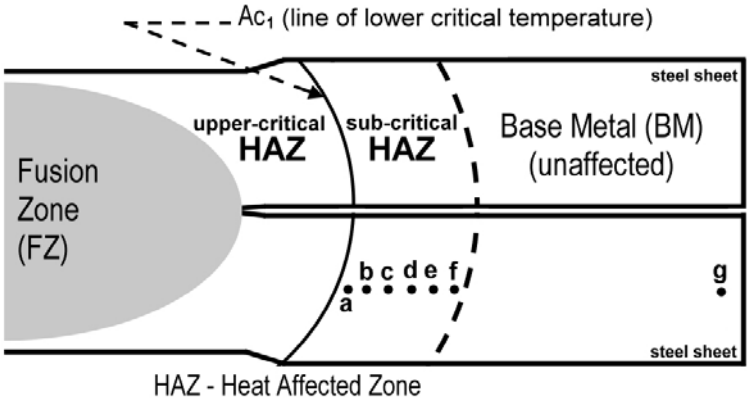

Figure 3.11 Schematic cross-section of a resistance spot weld showing the different regions formed during welding, for instance: fusion zone (FZ), heat affected zone (HAZ) and base metal (BM).

3.5.4. Numerical Simulations Along the SC-HAZ

Numerical simulations were conducted in order to obtain an estimate of the peak temperature profile along the sub-critical HAZ. Simulations were carried out using commercial finite element software: Quick Spot (by Research Center of Computational Mechanics, Inc., Japan) with coupled electrical-thermal-mechanical analysis [124]. A two-dimensional axisymmetric elastic-plastic model with a total number of 1442 nodes was introduced as depicted by Figure 3.12. Mesh density in the heat affected zone was of 53 elements per mm^2 where nodes were separated from each other by 0.125 mm in "x" direction and 0.15 mm in "y" direction.

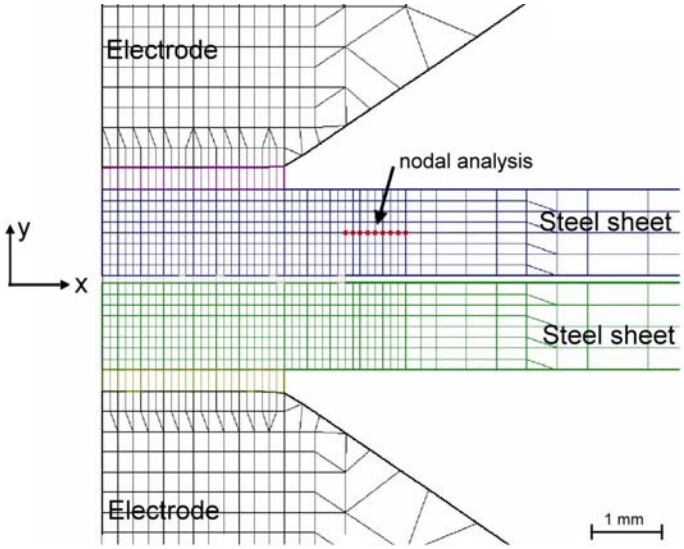

Figure 3.12 Two dimensional axisymmetric model showing the details of meshing for the stacked $DP980_A$ steel sheets.

Material properties (i.e. thermal conductivity, specific heat, thermal expansion coefficient, density, electrical conductivity, Young's modulus and yield strength) for $DP980_A$ steel were considered to be temperature dependent. Example of properties at room temperature has been listed in Table 3-5 [125,126]. Welding parameters used in these calculations were similar to those established experimentally (*i.e.*, 8 kA, 3.5kN during 20 cycles). The peak temperature at the sub-critical HAZ was obtained through nodal analysis as detailed by the highlighted points in Figure 3.12.

Table 3-5 Material properties of $DP980_A$ at room temperature

Thermal Conductivity (W/m/K)	*Specific Heat (J/(kg ・K))*	*Thermal Expansion Coefficient (1/K)*	*Density (kg/mm^3)*	*Electrical Conductivity (1/(Ω ・mm))*	*Young Modulus (GPa)*	*Yield Strength (MPa)*
55	458	11.8E-06	7.85E-06	2410	218	600

3.6. Transmission Electron Microscopy Procedures

3.6.1. Sample preparation

TEM samples were prepared by employing focused ion beam (FIB), carbon extraction replicas and standard twin-jet electropolishing techniques. Lift-out FIB technique for extracting TEM samples was utilized for both base metal (BM) and non-isothermally tempered specimens. TEM-FIB sample was obtained from a location 100 μm far from Ac_1 line at the sub-critical HAZ as marked by "**a**" in Figure 3.11. Calculations in previous report [145] have shown that RSW-DP steel achieves temperatures slightly above 650 °C at 100 μm from Ac_1 (i.e. location **a** in Figure 3.11).

Focused Ion Beam

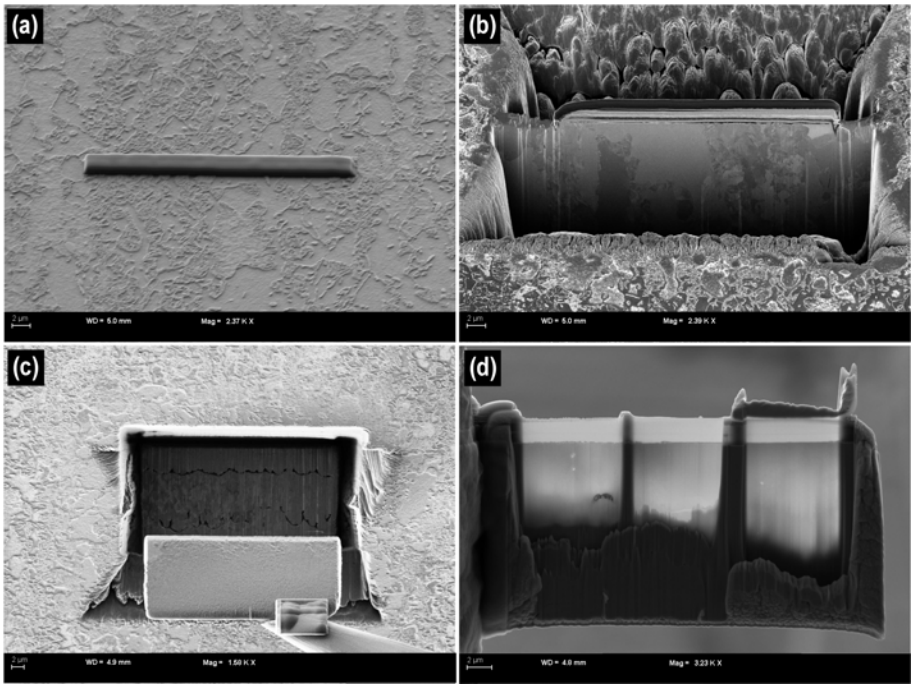

Figure 3.13 Focused ion beam sampling: (a) target location and carbon film deposit, (b) cutting and initial shaping of lamella, (c) use of manipulator for extracting lamella from the bulk metal, (d) TEM specimen after fine milling.

FIB sampling was developed in a series of steps as depicted in Figure 3.13. At the early stages of FIB sampling, a carbon film is deposited on the sub-critical HAZ surface (100 μm far from Ac_1) as shown in Figure 3.13a. The milling process starts by shaping a thin lamella (future specimen) within the bulk metal (Figure 3.13b). After, the specimen is fully shaped and cut, a micro-manipulator then is employed in order to lift out the specimen Figure 3.13c. In a later stage, the specimen is attached to a Cu grid holder. Further milling procedure of thinning is performed just before finalizing the FIB process (Figure 3.13d)

Twinned Jet-Electropolishing

Discs of 3.0 mm of diameter were punched from isothermally heat treated and mechanically grinded DP steel sheets. Thin-foil specimens for TEM observation were prepared by twin-jet electropolishing technique by employing a Struers TenuPol-5® equipment with an electrolytic solution of 10 percent $HClO_4$ and 90 percent of ethanol at -45 °C and constant voltage of 15 V.

Carbon Extraction Replicas

After masking off non-desirable regions from the spot welded DP specimen, carbon extraction replica was employed at the sub-critical HAZ in order to extract the precipitated carbides from the bulk specimen. A thin carbon film was deposited over the pre-etched surface with Nital solution. The carbon film was then floated off in a solution of 4 pct Nitric acid in ethanol and collected in a Cu grid. A representative number of precipitated carbides trapped on the carbon film were further analyzed by electron diffraction, electron energy loss spectrometry (EELS) and energy dispersive X-ray (EDX) techniques.

3.6.2. Equipment

Microstructural observations and electron diffraction analysis were carried in a conventional microscope TEM Phillips CM12® (120 keV) coupled with a Gatan EDX detector ®. EELS analysis was conducted in TITAN II 800-300® (300 keV) cryo-In-Situ TEM-microscope operated at 300 keV and equipped with an image filtering and analytical polepiece.

4. Influence of HAZ-Softening on the Joint Performance of RSW-DP Steel

In this chapter, the joint performance of resistance spot welded dual-phase (DP) steel is investigated and correlated to the reduction in hardness (softening) with respect the base metal occurring in the heat affected zone (HAZ). DP600, DP780 and DP980 steels have been utilized as starting materials and have been resistance spot welded in similar and dissimilar steel grade combinations. DP steels with different chemical compositions have been incorporated for completing the analysis.

The microstructural gradient along the weldment has been characterized by optical and electron microscopy, whereas more attention has been paid to the changes in microstructure occurring at the sub-critical HAZ (SC-HAZ) *i.e.*, tempering of martensite. Hardness through Vickers indentations has been systematically evaluated and correlated to the degree of tempering of the different DP steel grades.

The joint performance of resistance spot welded dual-phase steel is assessed by employing standardized tensile testing methods *viz.* lap-shear tensile and cross tension; from which three important issues are analyzed: a) the joint strength (maximum load to failure), b) the location of failure (failure mode), and c) the physical characteristic of the weld that determines the failure (weld nugget size). In addition, a partial tensile test has been conducted in order to evaluate the initiation of failure in a dissimilar steel combination, *i.e.*, DP600 paired to DP780.

Discussion in this chapter focuses on the effects of softening (tempering) on the mechanical behaviour of the RSW of DP steel weldments and, accordingly, to whether or not softening is detrimental to RSW weldments of DP steel when subjected to shear and/or tensile loading.

4.1. Weldment Microstructure

Representative weld cross-section macrostructure along with the microstructure details of different regions for three different grades of DP steel *viz.* $DP600_A$, $DP780_A$ and $DP980_B$ are illustrated in Figure 4.1, Figure 4.2 and Figure 4.3 respectively. The various regions of the weld cross-section on each sample were identified as follows: base metal (BM), heat affected zone (HAZ) and fusion zone (FZ) as indicated in the macrostructures. The HAZ was observed under the optical microscope to be conveniently sub-divided at the line of critical temperature Ac_1 as: sub-critical (SC) and upper-critical (UC). Moreover, the upper-critical HAZ can be further subdivided as: inter-critical (IC), fine-grained (FG), and coarse-grained (CG) as indicated by the lettering “c”, “e” and “d” in Figure 4.1a, Figure 4.2a and Figure 4.3a.

The base metal microstructure of $DP600_A$, $DP780_A$ and $DP980_B$ steels is comprised of ferrite matrix (white area) and dispersed islands of martensite (tan coloured) as observed in Figure 4.1a, Figure 4.2a and Figure 4.3a, respectively. As expected, ferrite fraction in BM was observed to decrease (white area), or in other words martensite fraction increases (tan coloured), with increasing grade of steels *viz.* DP600, DP780, DP980. Moreover, a banded structure of martensite islands is observed in the base metal of $DP780_A$ and $DP980_B$; such banded morphology appeared aligned parallel to the rolling direction of the steel sheet. On the other hand, $DP600_A$ showed a more dispersed islands of martensite phase.

The fraction of white region (ferrite matrix) appeared on increasing whereas the tan coloured area seemed less bright at the SC-HAZ of all three DP steels (Figure 4.1b, Figure 4.2b and Figure 4.3b). It is expected that tempering occurs in this region as the developed temperatures are below the lower critical temperature of transformation Ac_1 (Figure 2.4). Owing to important microstructural transformations occurring at the SC-HAZ; this particular region of the HAZ is subjected of further analysis in this thesis work.

Figure 4.1c, Figure 4.2c and Figure 4.3c illustrates the IC-HAZ of DP600, DP780 and DP980 steels, respectively. The ferrite area decreased and changed gradually to martensite structure consistently in all three DP steels. This region results of partial transformation of the prior base metal structure (mainly carbides in pearlitic and/or bainitic regions or martensite) into austenite during the thermal cycle; such partial austenitization is further transformed to martensite upon cooling. By moving away from BM, the peak temperature increased, increasing the fraction of constituents that were dissolved into austenite.

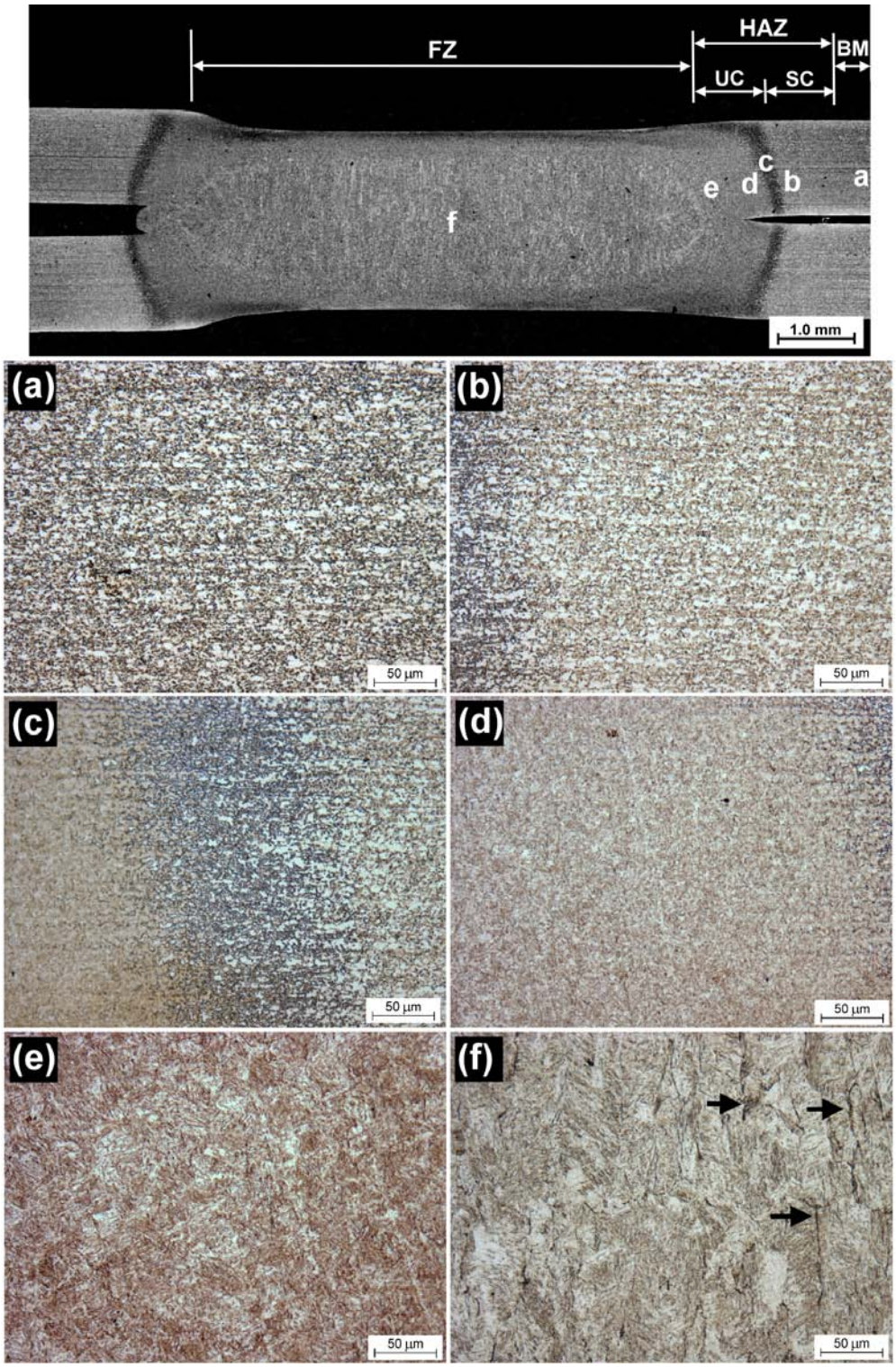

Figure 4.1 Weld cross-section macrostructure and detailed microstructure of different regions in RSW-DP600$_A$ steel: a) Base metal (BM), and heat affected zone (HAZ); b) coarse grain region (CG), c) fine grain region (FG), d) intercritical region (IC), e) sub-critical region (SC), and f) fusion zone (FZ).

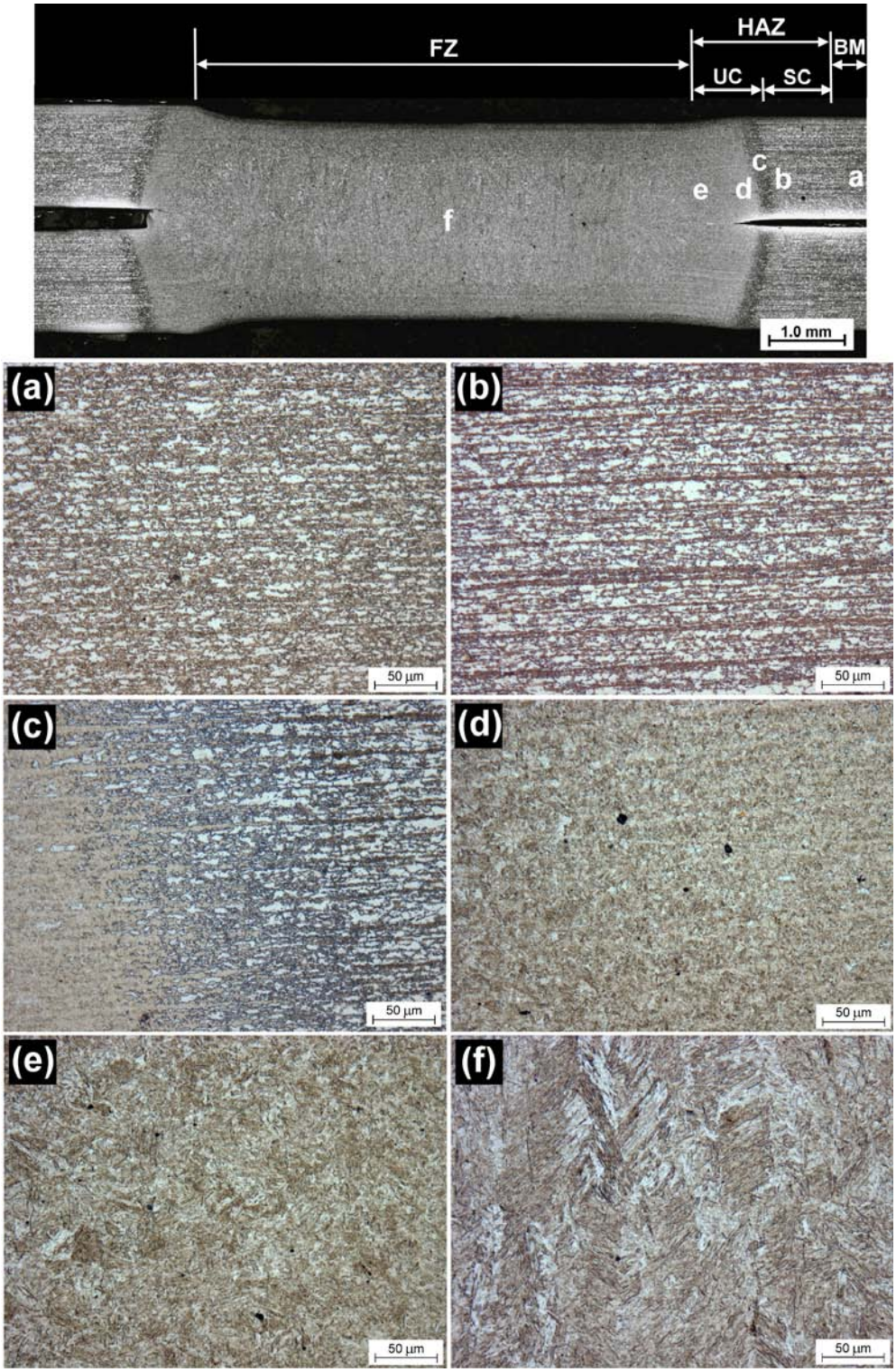

Figure 4.2 Weld cross-section macrostructure and detailed microstructure of different regions in RSW-DP780$_A$ steel: a) Base metal (BM), and heat affected zone (HAZ); b) coarse grain region (CG), c) fine grain region (FG), d) intercritical region (IC), e) sub-critical region (SC), and f) fusion zone (FZ).

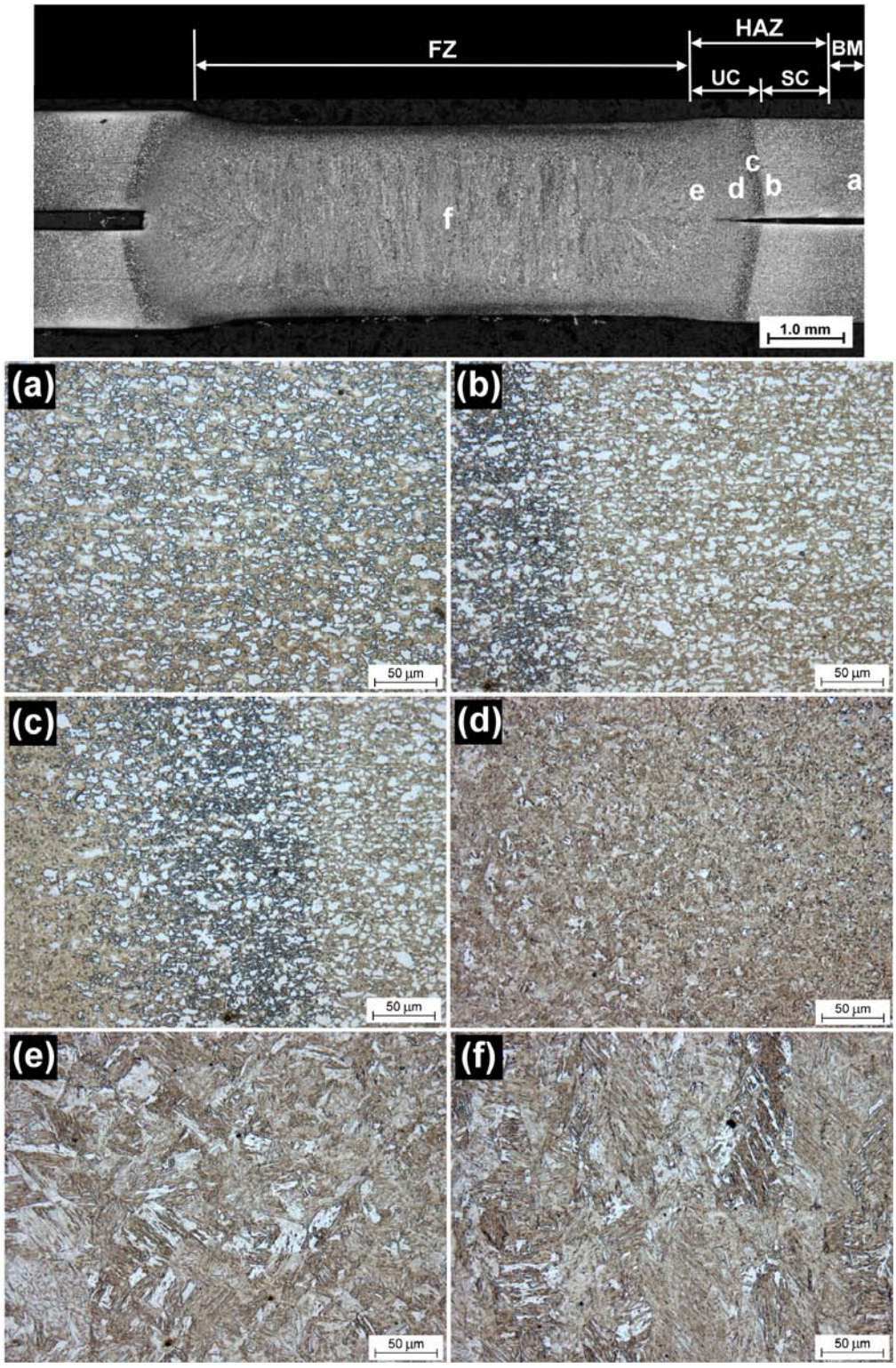

Figure 4.3 Weld cross-section macrostructure and detailed microstructure of different regions in RSW-DP980$_B$ steel: a) Base metal (BM), and heat affected zone (HAZ); b) coarse grain region (CG), c) fine grain region (FG), d) intercritical region (IC), e) sub-critical region (SC), and f) fusion zone (FZ).

Micrographs from the FG-HAZ and CG-HAZ delineated fully martensite structure

(Figure 4.1d-e, Figure 4.2d-e and Figure 4.3d-e) irrespective of the grade of DP steel. Martensite in FG-HAZ and CG-HAZ resulted from decomposition austenite upon cooling. Austenitization in this region occurs during the weld thermal cycle in which temperatures well above Ac_3 are developed. However, grain growth is developed with further increasing of the austenitization temperature, thus resulting in coarsening of the inherited phase (*i.e.*, martensite) upon cooling.

Furthermore, the FZ microstructures shown in Figure 4.1f, Figure 4.2f and Figure 4.3f, were characterized by columnar morphology as a result of solidification. Such columnar morphology is composed predominantly of needle-like martensite. On the other hand, $DP600_A$ steel resulted in low fraction of side-plate morphology of ferrite along the columnar grain boundaries as indicated by the arrows in Figure 4.1f. The formation of side-plates of ferrite is attributed to the leaner bulk chemistry of $DP600_A$ steel compared to other grades. Hence, it is clear that the resultant FZ microstructure is strongly dependent on the bulk chemistry of the particular DP steel for a given welding schedule.

4.2. Sub-critical HAZ Microstructure

Microstructure characterization by SEM of welds was addressed to the BM and SC-HAZ of the various DP steels in this section in order to benchmark and analyze the extent/degree of microstructural transformations occurring at the SC-HAZ. Figure 4.4a through Figure 4.4c show the representative SEM images of BM. Figure 4.4d, Figure 4.4e and Figure 4.4f illustrate microstructure of respective SC-HAZ of $DP600_A$, $DP780_A$ and $DP980_B$ resistance spot welds obtained at an approximate distance of 100 μm from Ac_1 towards the BM.

It is seen that irrespective of the grade of DP steel, BM showed dual-phase structure containing ferrite (α) matrix and martensite (α') phase. According to Figure 4.4a-c, it is to be confirmed that the martensite volume fraction was seen to be increased (Table 3-2) with increasing the grade of DP steel; moreover, a similar trend is also observed in the tensile strength of the DPs (Table 3-3) *i.e.*, higher strength steels containing larger fraction of α'-phase. Along with α-matrix and α'-phase, occasional presence of chunky retained austenite (RA) was also observed as the second phase particularly in the lower steel grades *i.e.*, $DP600_A$ and $DP780_A$ (Figure 4.4a-b).

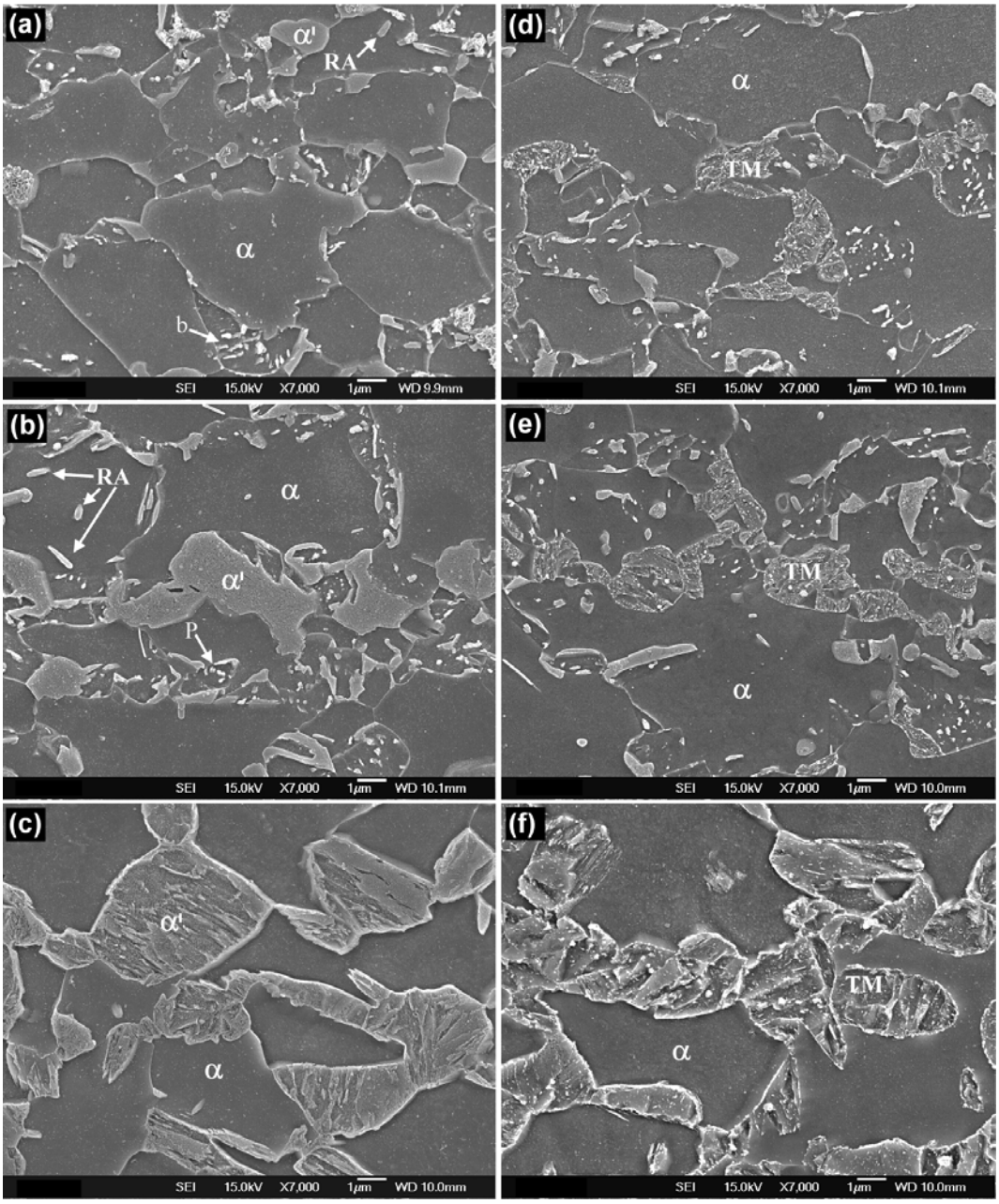

Figure 4.4 Representative SEM micrographs illustrating: a-c) BM microstructure, and d-e) the SC-HAZ microstructures of $DP600_A$, $DP780_A$ and $DP980_B$, respective.

Moreover, $DP600_A$ and $DP780_A$ seemed to be comprised of additional aggregates like pearlite (P) as indicated in Figure 4.4b. Presence of pearlite and in some cases bainite aggregates in the DP steel is attributable to partial austenitization of prior cold rolled microstructure during inter-critical annealing treatment and further decomposition. Thus, it might be expected that the formed austenite would decompose by growth of ferrite inward from the ferrite/austenite boundary followed by decomposition of remaining austenite into pearlite; in fact, it appears that

the core transforms into pearlite at high temperature followed by transformation of the rim into martensite at lower temperature [68].

SEM micrographs shown in Figure 4.4d-f were obtained from the SC-HAZ regions (Figure 4.1e, Figure 4.2e, and Figure 4.3e) of the different DP steels. Figure 4.4d represent the SC-HAZ of $DP600_A$ steel from which clear decomposition of the prior α'-phase is observed. The morphology of the prior α'-phase appears broken with presence of sub-micron particles which contrasts well to the smooth featureless morphology of α'-phase in BM (Figure 4.4a). This change in morphology of the α'-phase is attributed to the tempering of martensite (TM); hence, the sub-micron particles corresponded to precipitation of carbides. Evidently, extended fraction of tempered martensite is observed at the SC-HAZ while increasing the steel grade from $DP780_A$ to $DP980_B$ steel (Figure 4.4e and Figure 4.4f). Owing to larger TM grain size in $DP980_B$ steel; detailed features of the substructure of the tempered martensite are revealed in the SC-HAZ (Figure 4.4f); for instance, the precipitated carbides are larger in size and these are dispersed thoroughly, moreover, these carbides were seen aligned along the substructure of TM (Figure 4.4f).

The possible pearlite regions observed in the BM; seemed little affected by the thermal cycles developed at the SC-HAZ as per its original morphology is still observed. Furthermore, the chunky retained austenite (RA) seen in the BM microstructure are still intact as the temperature encountered in the SC-HAZ was below Ac_1 temperature which does not allow transformation to occur in retained austenite which was stabilized by the alloying elements, like Mn and Cr, in the DP steels studied.

4.3. Hardness Measurements

Hardness profiles across the weldment of $DP600_A$, $DP780_A$ and $DP980_B$ steels studied in this work are shown in Figure 4.5. The hardness profiles of the various regions clearly indicate that high hardness was accomplished at the FZ, CG and FG regions of all three DP steels due to formation of martensite as depicted in Figure 4.1 to Figure 4.3. Significant reduction in hardness (softening) with respect to that of the BM hardness (right of the plot) is measured at the SC-HAZ of $DP980_B$ steel. This measurable softening revealed in SC-HAZ of $DP980_B$ was larger just beside Ac_1. Hence, it is confirmed that the measurable softening in $DP980_B$ is associated with tempering of martensite at SC-HAZ as illustrated in Figure 4.4f.

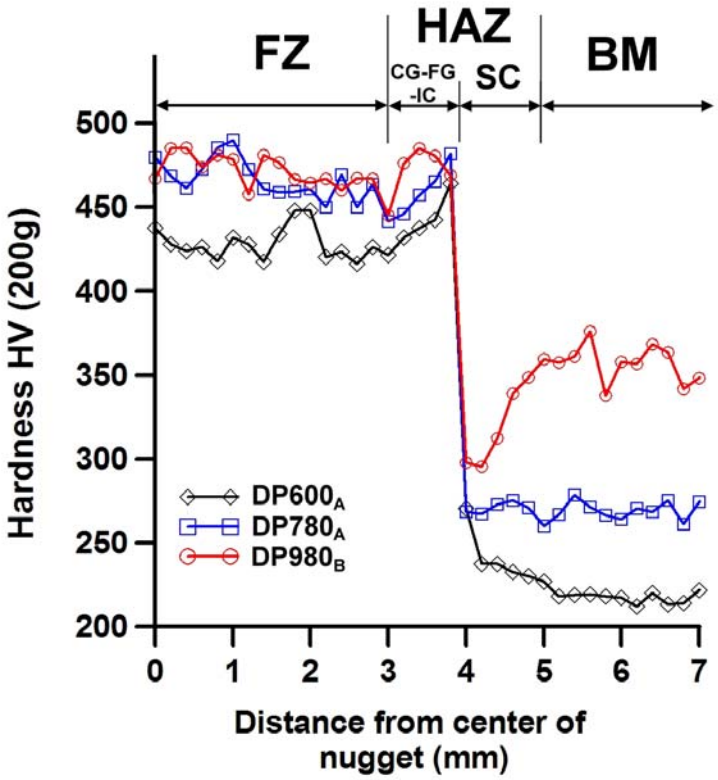

Figure 4.5 Hardness (HV) profiles across the weldment of three RSW-DP steels

On the other hand, softening was not measured in $DP600_A$ steel, and it was barely observable in the hardness profile of $DP780_A$ steel (Figure 4.5).

In order to improve the reliability of hardness measurements obtained from specific regions; series of hardness indentations were performed at center of the FZ, at the SC-HAZ (just beside Ac_1), and at the BM as depicted by the schematic in Figure 4.6a. The resultant hardness of the above mentioned regions was averaged and plotted in Figure 4.6b. Figure 4.6b confirms higher BM hardness with increasing the volume fraction of martensite phase in the DP steels (Figure 4.4). On the other hand, the slightly lower FZ hardness in $DP600_A$ is attributed to the leaner bulk chemistry (CE) among the DP steels and hence to the formation side-plate structures of ferrite during welding (Figure 4.1f).

By comparing the results in Figure 4.6b; softening was found to be high for $DP980_B$ steel with an averaged reduction in hardness of 75 HV. Softening was barely observed in $DP780_A$ steel; however, small reduction in hardness was measured in this steel, for instance, the averaged BM hardness was measured to be 260±8 HV which contrasted the hardness at the SC-HAZ of 256±4 HV (Figure 4.6b). In spite of the decomposed appearance of the martensite phase in

$DP600_A$ steel (Figure 4.4d); softening was not obtained on this ordinary lower grade, in fact, a slight increase in hardness resulted in the SC-HAZ of $DP600_A$.

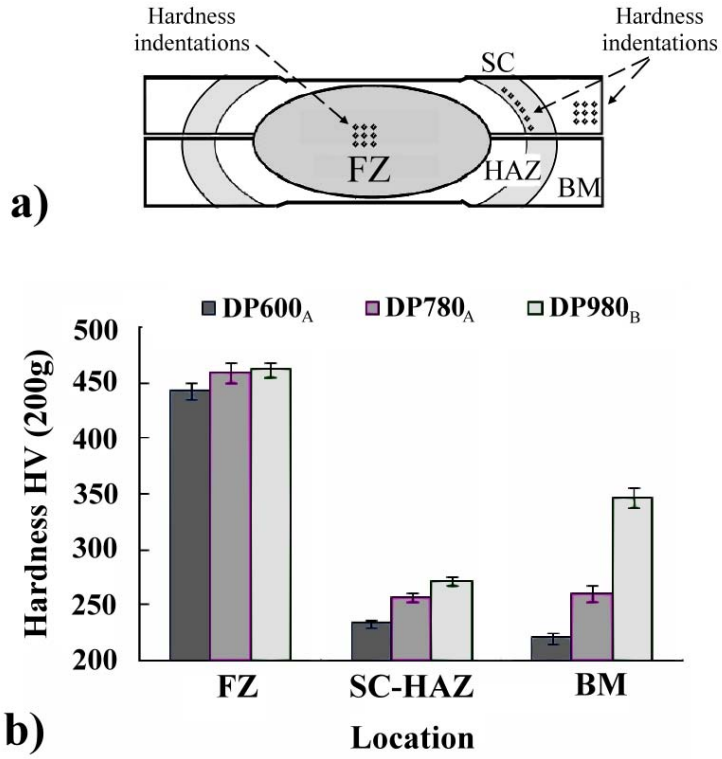

Figure 4.6 Averaged hardness of three DP steels in three regions: FZ, SC-HAZ and BM.

The volume fraction of martensite phase in the BM prior to tempering has an important effect on softening. For example, high volume fraction of BM martensite resulted in higher fraction of tempered martensite at the SC-HAZ; hence, measurable softening is attained (Figure 4.6). On the other hand, it might be noted that coarser carbides and severely decomposed substructure in $DP980_B$ steel (Figure 4.4f) are observed when compared to other steel grades ($DP780_A$ and $DP600_A$); so this being another important factor that influenced on the reduction in hardness.

From the above mentioned hardness results it is concluded that both volume fraction and the degree of decomposition of the martensite substructure (tempering) are responsible for measurable softening in the dual-phase steels.

$DP600_B$ and $DP780_B$ steels (it might be noted that these steels correspond to different chemistry as listed in Table 3-1) were paired in dissimilar and similar combinations (*i.e.,*

dissimilar $DP600_B$-$DP780_B$ and similar $DP600_B$-$DP600_B$ or $DP780_B$-$DP780_B$) in this study. The hardness profile across the weldment for the dissimilar pair $DP600_B$-$DP780_B$ steels are shown in Figure 4.7a. In addition, partial hardness profiles *i.e.*, from FZ to BM, for $DP600_B$ and $DP780_B$ steels paired to themselves have been plotted in Figure 4.7a. The weld cross-section and the fusion zone microstructure the dissimilar $DP600_B$-$DP780_B$ steel combination are shown in Figure 4.7b and Figure 4.7c, respectively.

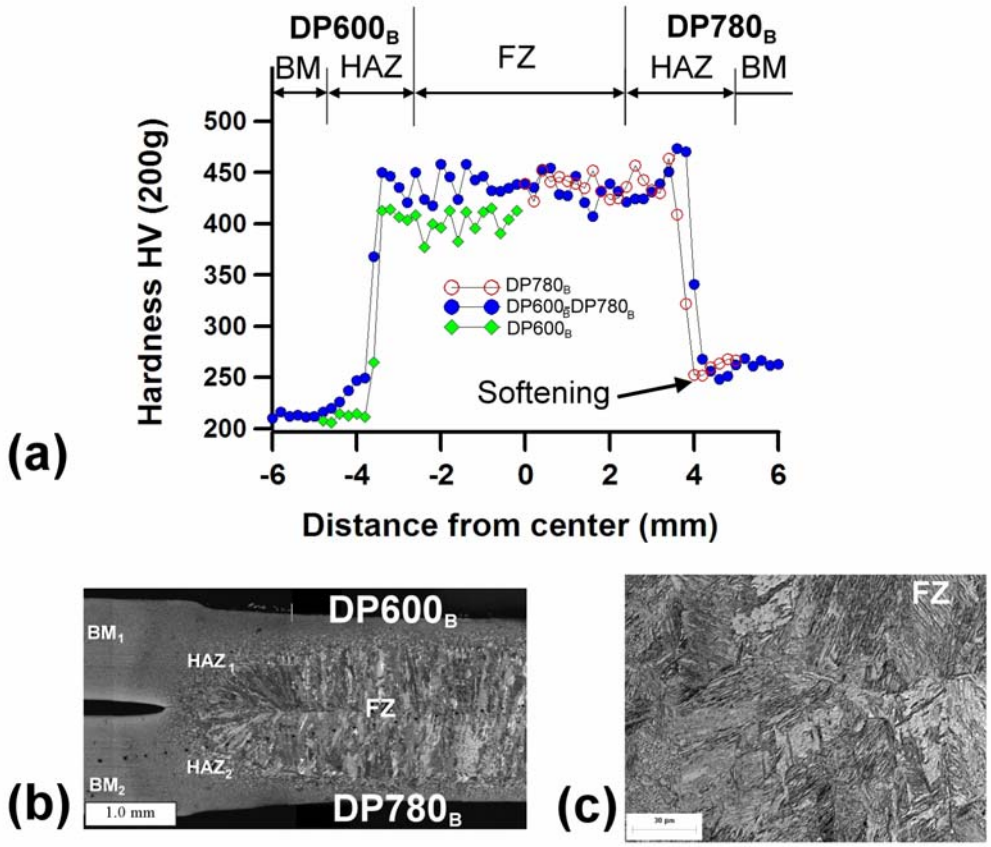

Figure 4.7 Dissimilar RSW $DP600_B$-$DP780_B$ steel combination: a) cross-weld hardness profile, b) cross-section macrostructure, c) FZ microstructure. Partial hardness profiles (from center of FZ towards BM) for $DP600_B$ and $DP780_B$ paired to themselves have been additionally plotted in a).

The three distinct regions, including base metal ($BM_{1,2}$), heat-affected-zone ($HAZ_{1,2}$), and fusion zone (FZ) are labelled with the subscripts 1 and 2 referring to the $DP600_B$ and the pairing $DP780_B$ steel, respectively (Figure 4.7b). The presence of welding defects was not observed in the FZ of the dissimilar $DP600_B$-$DP780_B$ (Figure 4.7b).

The $DP600_B$ steel was plotted to the left of the diagram for consistency (Figure 4.7a). The fusion zone hardness increased when $DP600_B$ was paired with increasingly highly alloyed

steel such as $DP780_B$, *i.e.*, dissimilar combination, as shown in Figure 4.7a. For instance, FZ hardness for $DP600_B$ itself paired averaged 403 HV, FZ for DP780 averaged 438 HV, whereas the dissimilar pair of these steels averaged 435 HV. The above results indicate that the welding process was able to thoroughly mix the liquid metals originating from the respective steels during melting; thus resulting in FZ hardness values in between the FZ hardness of the similar pair combinations. The fusion zone microstructure for the dissimilar combination depicted in Figure 4.7b indicates predominantly martensitic microstructure showing directional, columnar solidification from the fusion boundary towards the center. Figure 4.7c shows a nearly fully martensitic fusion zone microstructure for the DP600 paired to the DP780. Overall, the observed fusion zone microstructures correlated well with the fusion zone hardness trends.

Furthermore, the peak HAZ hardness values were similar to those observed in RSW of the steels to themselves. Evidently, measurable softening was found in the outer, SC-HAZ of the $DP780_B$, where the local hardness of 248 Hv was lower than the base metal hardness as a result of martensite tempering. It is noteworthy to mention that the measurable softening was higher in $DP780_B$ (Figure 4.7) in comparison to that of $DP780_A$ (Figure 4.5) owing to larger fraction of tempered martensite (Table 3-2). Measurable softening was not observed in the HAZ of $DP600_B$ steel.

From the microhardness results and the microstructure observations analyzed; it can be summarize that softening is clearly measured in DP980 steel, barely obtained in DP780 steels and non-measurable in DP600 steels, in spite of the tempering of martensite observed in all three DP steels. It can be inferred that the higher degree/extent of measurable HAZ-softening in DP980 welds amongst all the studied DP steels is attributed to: a) larger volume fraction of α'-phase, and b) differences in the tempered martensite substructure and differences in carbide precipitation (Figure 4.4). Additionally, it is not clear whether tempered martensite is the solely responsible or if ferrite matrix also contributes to SC-HAZ softening, this issue is subjected of further analysis in the next chapter of this thesis work.

4.4. Joint Strength and Failure Mode

Lap-shear tensile testing was mainly employed for assessing the weld performance of the different DP steels upon similar and dissimilar steel grade weld combinations. Basically, three issues were targeted in the analysis of the tensile behavior of resistance spot welded dual-phase

steel: a) joint strength (maximum load to failure), b) the location of failure (failure mode), and c) the physical characteristic of the weld that determines certain type of failure (weld nugget size).

4.4.1. Similar DP Steel Weld Combination

By examining the weld cross-section macrostructures of the different DPs (Figure 4.1, Figure 4.2 and Figure 4.3); it may be noted that no defects such voids and/or solidification cracks were observed in all the three RSW-DP macrostructures that might deteriorate the mechanical performance of the weldment.

Amongst the typical failure modes in lap-shear tensile testing of spot welds *viz.* interfacial failure (IF), partial interfacial failure (PI) and button pullout failure (PO); the most desired failure is PO due to its plastic behaviour. A schematic representation of all the three failure modes has been illustrated in Figure 2.7. The weld nugget size at which the transition between If or PI to PO occurs, is commonly denominated *critical diameter* (d_c) [54].

Representative fractured surfaces of lap-shear tensile specimens of DP steel showing: IF, PI and PO are shown in Figure 4.8a, Figure 4.8b and Figure 4.8c, respectively. It might be noted that expulsion of melted metal on the IF failed specimens was not observed (Figure 4.8a); thus meaning that IF failed specimens were not influenced by this type of weld defect. It is also noteworthy to mention that PO failure is basically associated to the failure occurring along the periphery of the outer HAZ (SC-HAZ) as depicted by Figure 4.8c.

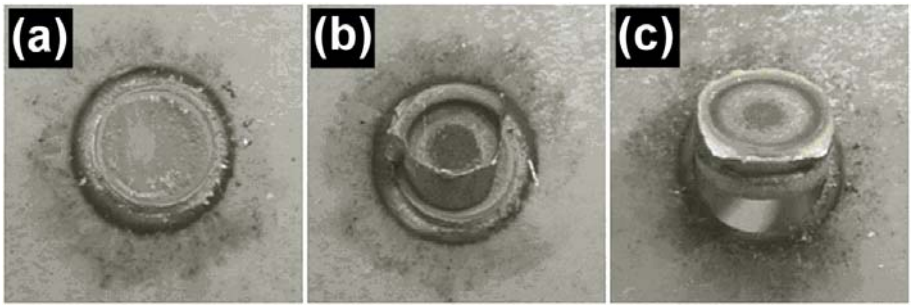

Figure 4.8 Representative fractured surfaces of lap-shear tensile tested DP steel showing: a) interfacial failure (IF), b) partial interfacial failure (PI) and c) button pullout failure (PO).

The failure path for the PO failed specimens in lap-shear testing of all three DP steels was additionally investigated. Figure 4.9a, Figure 4.9b, and Figure 4.9c shows the cross-sections of the PO failed specimens for $DP600_A$, $DP780_A$ and $DP980_B$, respectively. The failure was

observed at the SC-HAZ extended through sheet thickness. As can be seen in Figure 4.9 the failure path is seen at the region in which tempering of martensite islands occurs, *i.e.*, just beside Ac_1 line of critical temperature (Figure 4.1, Figure 4.2, and Figure 4.3). It may be mentioned that, the failure was consistent at the same location for all DP steels (Figure 4.9).

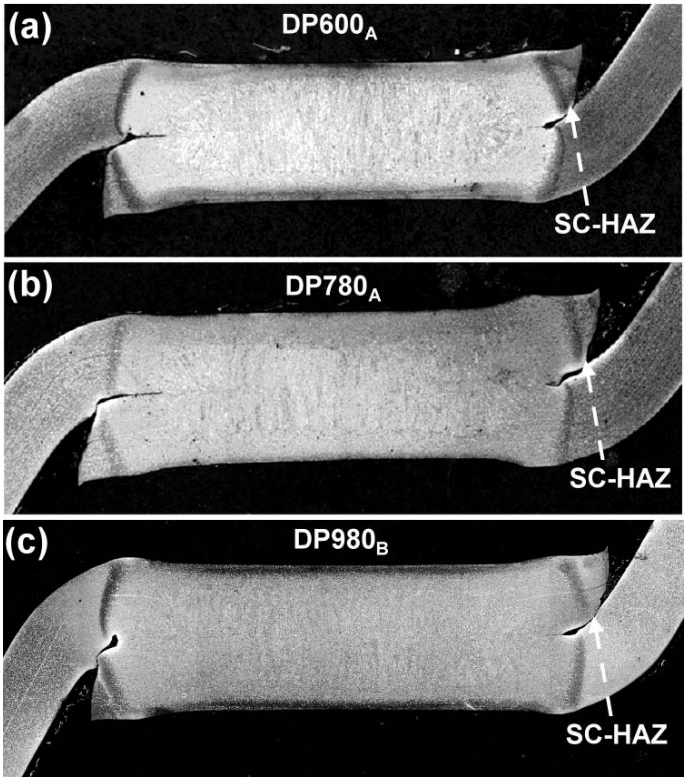

Figure 4.9 Representative cross-sections of pullout failed specimens showing the failure path along the SC-HAZ for: a) $DP600_A$, b) $DP780_A$ and c) $DP980_B$.

Figure 4.10a, Figure 4.10b and Figure 4.10c show the maximum lap-shear tensile load plotted against the weld nugget size for: a) $DP600_A$, b) $DP780_A$, and c) $DP980_B$ steels, respectively. The weld nugget size was measured from cross-section metallographic measurements and it was obtained within the range of 5.1 mm to 6.4 mm for all steels. It can be noted from Figure 4.10a ($DP600_A$); that for smaller weld nugget size (*i.e.*, approximately 5.1 mm) expectedly IF failure occurred with corresponding lower maximum load (*i.e.*, approximately 13 kN). While increasing the weld size the maximum load became higher and the failure mode changed to a mixture of IF and PI. By further increasing the weld size, the transition to pullout was achieved with higher values of maximum load *i.e.*, above 14.7 kN.

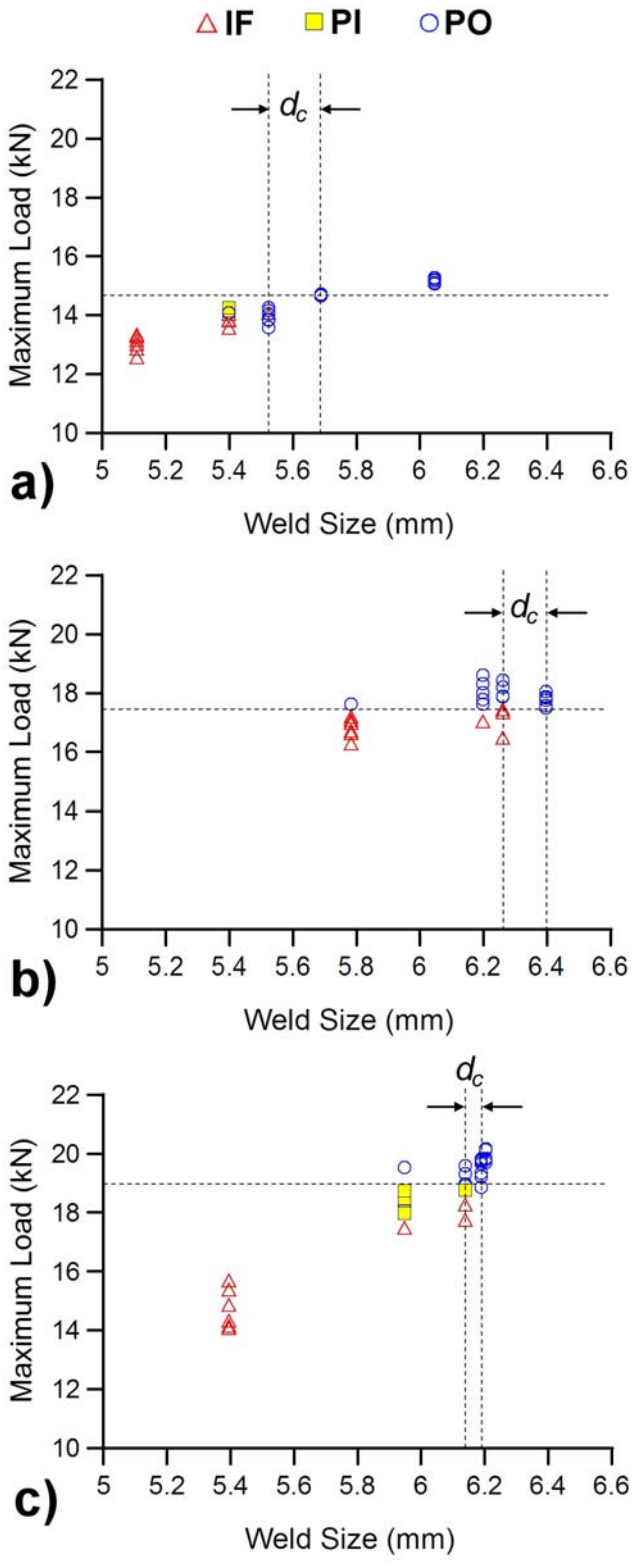

Figure 4.10 Maximum lap-shear tensile peak loads *vs*. weld nugget size for: a) $DP600_A$, b) $DP780_A$, and c) $DP980_B$.

Even though full PO failure was observed upon a weld size of 5.7 mm for $DP600_A$ steel, exact value of d_c which denotes the transition region from IF or PI to PO failure mode is contained within the range depicted by the dashed lines in the graph (5.53 mm ~ 5.68 mm).

The above mentioned transitioning mechanism of failure modes is also observed in the case of higher grades of steels *viz.* $DP780_A$ and $DP980_B$. However, d_c for $DP780_A$ was in the range 6.27 mm ~ 6.39 mm whereas that for $DP980_B$ was in the range of 6.14 mm ~ 6.18 mm. So d_c increased in order of $DP600_A \rightarrow DP980_B \rightarrow DP780_A$ as listed in Table 4-1. It is also worth to observe in Figure 4.10 that the maximum lap-shear tensile load for full PO failure mode increased in order of $DP600_A \rightarrow DP780_A \rightarrow DP980_B$ with a value of 14.7 kN → 17.5 kN → 19.2 kN, respectively.

Table 4-1 Critical weld nugget size for the different RSW-DP steels

Steel	***Observed Mixed Failures Weld Size (mm)***	***Observed PO failure Weld Size (mm)***	***Critical Diameter d_c (mm)***
$DP600_A$	$5.52 \geq$	≤ 5.68	5.53 – 5.68
$DP780_A$	$6.26 \geq$	≤ 6.39	6.27 – 6.39
$DP980_B$	$6.13 \geq$	≤ 6.18	6.14 – 6.18

It can be inferred that the demanded weld size to get the PO failure mode becomes larger for higher steel grades *i.e.,* from $DP600_A$ to $DP780_A$ due to softening was not measured or was barely observed in $DP780_A$. However, $DP980_B$ steel achieves higher maximum load with appropriate PO failure mode upon smaller nugget size in comparison to that of $DP780_A$ steel. This means that $DP980_B$ resulted in improved lap-shear tensile performance than $DP780_A$ attributed to the greatest measurable softening at sub-critical HAZ and hence to larger fraction of tempered martensite.

Figure 4.11 shows the lap-shear tensile load-displacement curves for $DP600_A$, $DP780_A$ and $DP980_B$. The curves represent the points at which PO is first observed for each of the tested DP steels (Figure 4.10). Accordingly, the energy absorption which calculated by integrating the area under the load-displacement curve up to the maximum load; indicate that higher energy absorption was accomplished in $DP980_B$ steel (Figure 4.11), *i.e.*, 38 J, followed by DP780 (36 J) and DP600 (25 J). Interestingly, by comparing $DP780_A$ to $DP980_B$ steel; it is seen that higher energy absorption is accomplished by $DP980_B$ steel in spite of its lower nugget size.

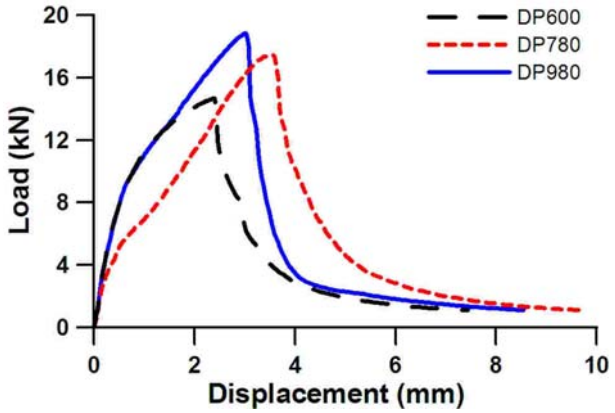

Figure 4.11 Load-displacement curves for $DP600_A$, $DP780_A$ and $DP980_B$ steels.

Evidently the tensile properties *viz.* PO failure mode along with higher load to failure and energy absorption in $DP980_B$; are strongly influenced by softening occurring at the SC-HAZ due to tempering of martensite islands. It might be inferred that HAZ-softening benefits the mechanical behavior of DP steels by facilitating PO failure. Thus, plastic collapse mode (PO) instead of the sudden brittle fracture of the undesirable interfacial failures is accomplished in DP steels having extended HAZ-softening. However, the tempering kinetics of the martensite islands in dual-phase steels is not well understood; hence, the tempering characteristics of martensite islands in the DP steel is further analyzed in the following chapters of this thesis work.

4.4.2. Dissimilar DP Steel Grade Combination

The mechanical performance of RSW of dissimilar grades of DP steel was assessed by employing both: lap-shear tensile and cross tension test. $DP600_B$ and $DP780_B$ were paired in similar and dissimilar steel combinations. Figure 4.12a and Figure 4.12b show representative fracture surfaces for the cross-tension and lap-shear tensile tests, respectively.

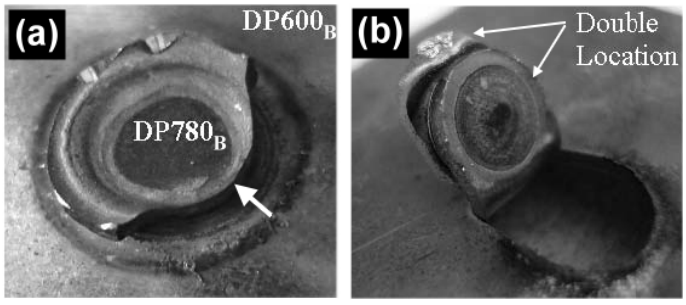

Figure 4.12 RSW weld failures in dissimilar pair $DP600_B$-$DP780_B$: a) cross-tension, b) lap-shear tensile

Under cross tension loading, the failure was consistently located in the higher grade steel of the combination, *i.e.*, $DP780_B$ as shown in Figure 4.12a. The fracture path was nucleated at the harder HAZ (*i.e.*, fusion line) as indicated by the arrow in Figure 4.12a; however, with further increase in displacement of the crosshead, the failure was redirected and extended through the SC-HAZ. Again, it might be inferred that the measurable softening in $DP780_B$ influenced on the failure mode upon cross-tension loading test by redirecting and extending the failure to towards SC-HAZ.

On the other hand, final fracture in lap-shear tensile test results of the $DP600_B$-$DP780_B$ weld combination seemed to occur in the $DP780_B$ HAZ softened zone (SC-HAZ); however, a double-thickness failure was observed in this steel pair as depicted in Figure 4.12b.

Representative load-displacement curves for lap-shear tensile and cross-tension loading of the dissimilar $DP600_B$-$DP780_B$ combination are shown in Figure 4.13. The average peak loads to failure and the displacement to peak load for both lap-shear and cross tension testing with the dissimilar $DP600_B$-$DP780_B$ steel combination resulted in 16.4±0.16 kN with 2.6±0.2 mm, and 8.5±0.26 kN with 25±0.2 mm, respectively. As can be seen, the peak load in cross tension was two times lower than that upon the lap-shear tensile loading.

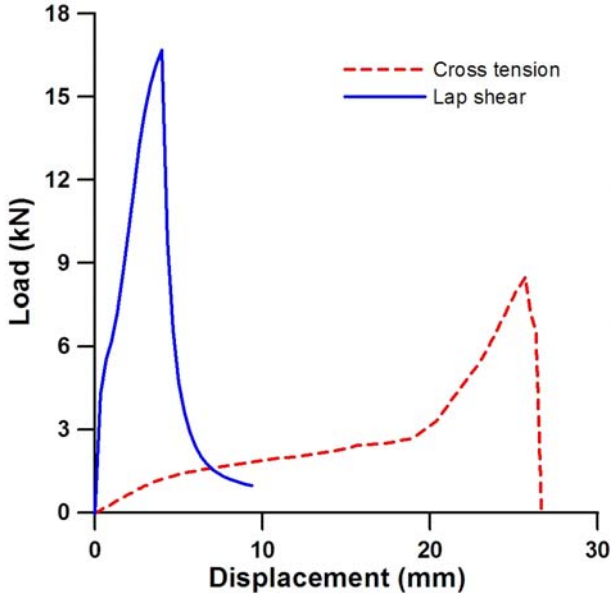

Figure 4.13 Load-displacement curves for lap-shear and cross-tension loading conditions in dissimilar steel grade combination $DP600_B$-$DP780_B$.

$DP600_B$-$DP780_B$ combination showed interesting features unique to this combination because it produced a double-thickness failure in the lap-shear tensile loading condition (Figure

4.12b). Thus, the $DP600_B$-$DP780_B$ combination served as a basis for further comparison of the effects of welding conditions and weld size on failure characteristics in similar vs. dissimilar stack-ups upon lap-shear tensile loading, which is detailed in the remainder of this chapter.

It is well known that the strength and failure characteristics of spot welds are functions of the nugget size, sheet thickness, and weld/HAZ hardness [20,59]. From a basic stress analysis, it can be shown that the transition from interfacial failure to pull-out failure occurs when the weld size exceeds a critical value [55]. Some materials, DP600 in particular, have shown interfacial failure at weld sizes that are above the recommended minimum [9]. However, observations in related work on RSW of dissimilar AHSS have shown that the interfacial failure mode for a DP600 steel changes to a pullout failure mode when welded in combination with dissimilar steels such as transformation induced plasticity steel (TRIP) or high strength low alloy steel (HSLA), given the same weld size [20].

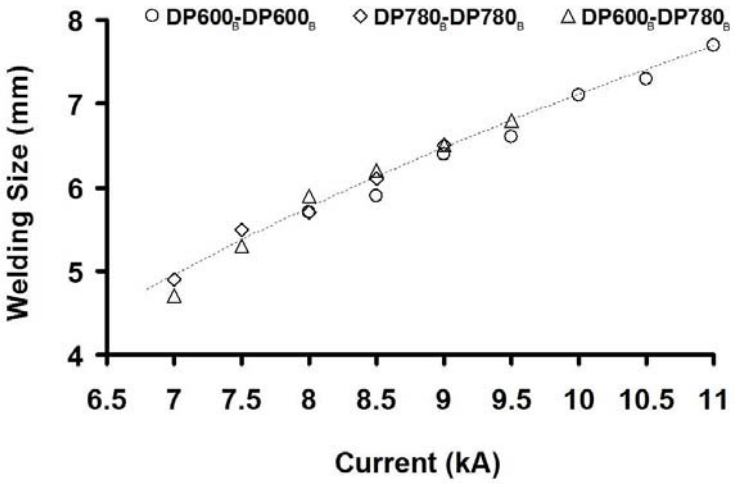

Figure 4.14 Weld growth curve for similar ($DP600_B$, $DP780_B$) and dissimilar ($DP600_B$-$DP780_B$) weld stack-ups.

A RSW growth curve, shown in Figure 4.14, shows the effect of increasing current on weld size, as measured using the peel test, for similar ($DP600_B$ and $DP780_B$) and dissimilar ($DP600_B$-$DP780_B$) welds, with constant weld time and force of 20 cycles and 3.5 kN, respectively. There was little effect of material combination on the relationship between weld size and current; however, the results were subject to some inaccuracy due to the effects of HAZ material present around the button periphery, which was not consistent for each combination. Regardless, the relationship between weld size and current is clearly established in Figure 4.14.

In Figure 4.15, the tensile strength versus weld current is given upon a force of 3.5 kN

and 20 cycles for weld time. Additionally, information regarding the failure mode *i.e.*, IF or PO has been also provided, for instance, PO failures were identified by the solid graph symbols whereas the open symbols indicate IF failure. Figure 4.15a shows the dissimilar $DP600_B$-$DP780_B$ combination; from this results, it is apparent that the transition from an IF to a PO failure mode occurs between 7.5 kA and 8 kA (Figure 4.15a). The transition to PO failure occurred at a peak load of 15.7 kN and from reference to Figure 4.14, it can be said that the transition weld size is between 5.3~5.8 mm. This was confirmed by visual inspection of the interfacial failure fracture surface diameters at the transition point, which averaged 5.3 mm.

Figure 4.15b and Figure 4.15c show results for the similar material welds in $DP600_B$ and $DP780_B$, respectively. In $DP600_B$ welds, the transition from interfacial failure to pullout failure occurred over a range of 8.5 to 10 kA. The transition was marked by a failure load of 15.6 kN. Correlation with Figure 4.14 shows that the transition weld size is around 5.9~7.1 mm in $DP600_B$ welds, visual inspection of the interfacial fracture surfaces at the transition point gave an average weld size of 6.1 mm. On the other hand, for the $DP780_B$ welds, the transition occurred from 7.5 to 8.5 kA, corresponding to a weld size of approximately 5.5~6.1 mm and a peak load of 17.3 kN. From the interfacial fracture surfaces, the transition diameter was greater than the average of 5.7 mm. The scatter in the results in Figure 4.15a to Figure 4.15c is most likely due to random variation in weld size for welds produced at constant settings, which is common in RSW. The notable feature on these charts was that the transition peak load was clearly demarcated in the results and was apparently related to a constant transition weld size.

The $DP600_B$-$DP600_B$ welds showed the highest transition weld size at 6.1 mm, which is well above the $5\sqrt{t}$ setup weld size of 5.5 mm, and significantly more than the $4\sqrt{t}$ minimum weld size of 4.5 mm that is commonly specified in the AWS standards. These results are consistent with what has been observed in previous work which has claimed that interfacial failures were common in DP600 even when the weld size exceeded commonly used standards. In the $DP780_B$-$DP780_B$ welds, the transition weld size was found to be around 5.7 mm, which still exceeds the specifications, but is significantly lower than the $DP600_B$. For the dissimilar DP600-DP780 combination, the transition size was found to be 5.3 mm, which was lower than both the DP600 and DP780 cases. Also worth noting is that at the transition point, the speak loads of the $DP600_B$-$DP600_B$ and $DP600_B$-$DP780_B$ welds were the same at around 15.6-15.7 kN, while the peak loads of the DP780-DP780 welds was higher at 17.3 kN.

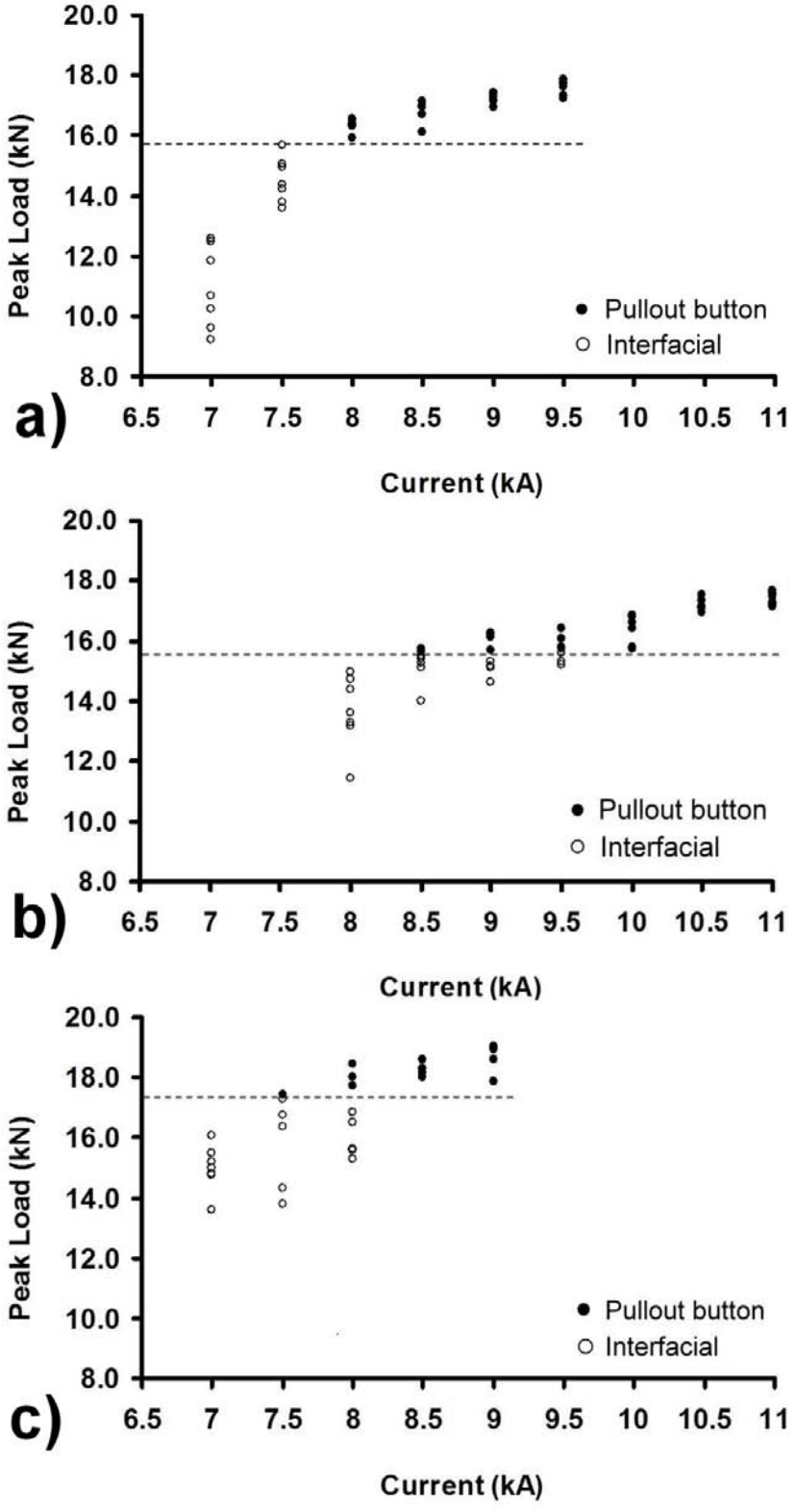

Figure 4.15 Peak load versus current at 3.5 kN electrode force and 20 cycle weld time: a) $DP600_B$-$DP780_B$, b) $DP600_B$-$DP600_B$ and c) $DP780_B$-$DP780_B$.

Despite softening in the HAZ of the $DP780_B$, the transition peak failure loads of the $DP780_B$-$DP780_B$ welds were higher than the $DP600_B$-$DP780_B$ combination, which was function of larger weld size, higher fusion zone strength and higher base-metal/HAZ strength.

4.5. Failure analysis

As previously explained, the transition from interfacial to pullout failure modes generally occurs when the stress in the HAZ exceeds the local yield strength. Increasing the weld size or fusion zone strength or the HAZ properties, promotes this transition. In the cases above, the weld microstructure was predominately martensitic; however, bainite and tempered martensite were also thought to be present in some fraction.

As shown in Figure 4.7 the average fusion zone hardness of the $DP600_B$-$DP780_B$ weld was somewhere between the peak hardness in the $DP780_B$ HAZ, which was higher, and the peak hardness in the DP600 HAZ_B, which was lower. The final microstructure, hardness, and ultimately, strength of the fusion zone was a function of the alloying level (CE), which is an indication of hardenability, and the C content, which is the primary factor in the hardness of martensite. The $DP600_B$ had a lower CE (0.326) with a lower C content (0.099 pct.) than the $DP780_B$ (CE = 0.427, and C = 0.113), and thus had a lower hardness. Due to mixing and dilution, the hardness of the $DP600_B$-$DP780_B$ fusion zone was between the two. Thus, it is reasonable to say that the fusion zone strength of the welds increased in the order of $DP600_B$-$DP600_B$, $DP600_B$-$DP780_B$, and $DP780_B$-$DP780_B$. This might explain in terms of FZ properties why the transition weld size for the DP600 was higher.

It has been mentioned that the HAZ hardness is another factor in the transition weld size. The characteristic mechanism of the button pullout failure mode in lap shear testing include: rotation of the weld nugget, and stretching, thinning, and necking in the HAZ [58,127]. In fact, even though the loading condition is nominally shear; the failure mode is predominantly tensile through rotation and preferential necking in the ductile region of the HAZ [55]. In the $DP600_B$-$DP780_B$ combination, partial tensile tests were completed to facilitate observation of failure initiation. Partial lap-shear tensile was performed by stopping the displacement of the crosshead at different positions, for example at 1.0 mm, 2.0 mm, 2.4 mm and 3.8 mm. A schematic of the load displacement curve for lap-shear tensile testing showing the position at which the cross-head was stopped has been provided in Figure 3.7.

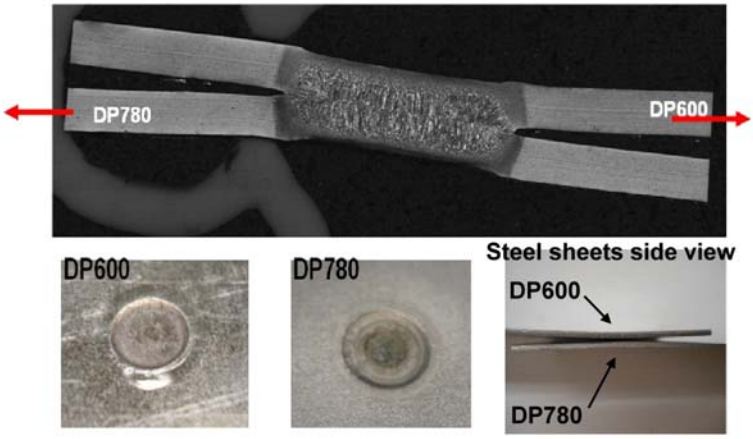

Figure 4.16 Cross-section of $DP600_B$-$DP780_B$ partial lap-shear tensile test at 1.0 mm displacement of the crosshead showing rotation of the weld nugget.

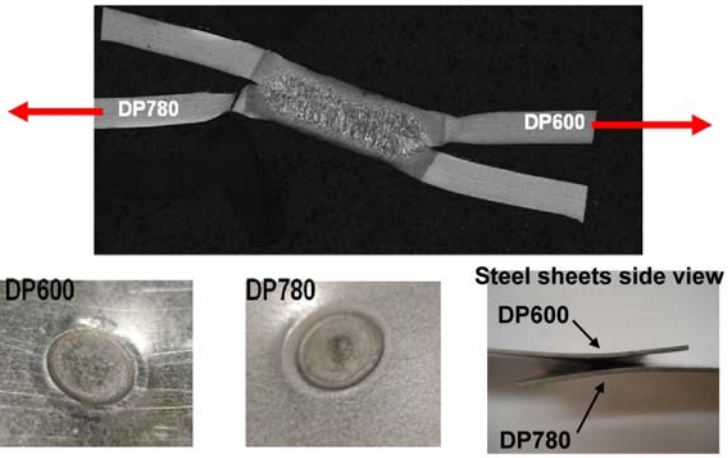

Figure 4.17 Cross-section of $DP600_B$-$DP780_B$ partial lap-shear tensile test at 2.0 mm displacement of the crosshead just after peak load.

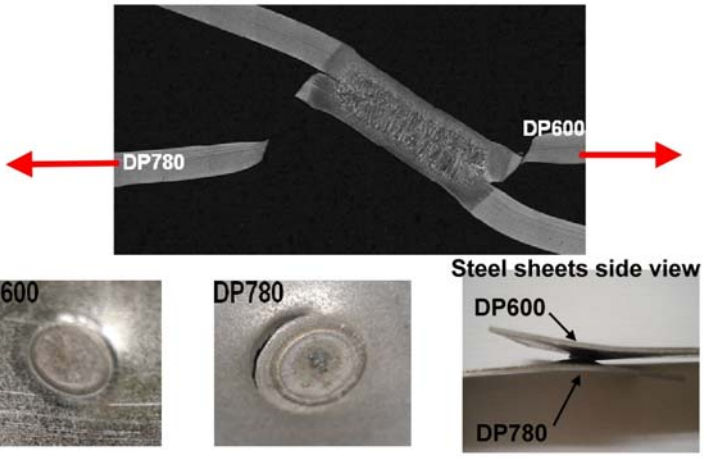

Figure 4.18 Cross-section of $DP600_B$-$DP780_B$ partial lap-shear tensile test at 2.4 mm displacement of the crosshead just after final fracture.

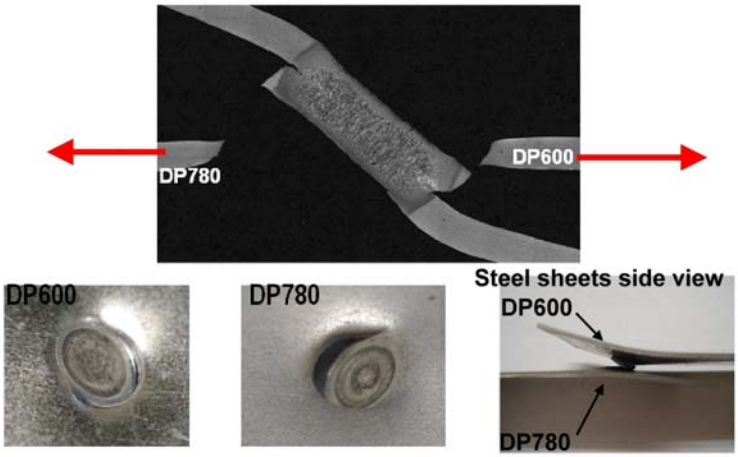

Figure 4.19 Cross-section of $DP600_B$-$DP780_B$ partial lap-shear tensile test at 3.8 mm displacement of the crosshead just after final separation of the steel sheets.

Figure 4.16, Figure 4.17, Figure 4.18 and Figure 4.19 show the cross-section of the lap-shear partial tensile specimens stopped at 1.0 mm, 2.0 mm, 2.4 mm and 3.8 mm, respectively. The loading direction in the tensile test is indicated by the arrows. Cross-sections of the partial tensile tests show details of fracture initiation and propagation. In addition, the surface appearance (at the location of RSW electrode indentation of both steels, *i.e.*, $DP600_B$ and $DP780_B$) and the side view of the paired steel sheets have been included.

At 1.0 mm of the cross-head displacement and before the steel has reached the peak load (Figure 3.7); rotation of the weld nugget along with slight necking at the SC-HAZ of $DP780_B$ steel is observed (Figure 4.16). The surface appearance of both steel sheets seemed unaffected; however rotation of lap-shear sample is confirmed by the steel sheets side view. Figure 4.17 showed that necking was localized in the HAZs of both the $DP600_B$ and $DP780_B$ sheet, and that fracture occurred first in the $DP780_B$. Necking (localized) and fracture are clearly observed in the $DP780_B$ steel sheet surface which contrasts the apparently undamaged surface at $DP600_B$ side. Upon continued displacement of the cross-head (2.4 mm), fracture also occurred just outside of the $DP600_B$, as shown in Figure 4.18. The steel sheet surface clearly appears fractured in the $DP780_B$ steel side, whereas visible necking is apparently observed in the $DP600_B$ side. Larger rotation of the specimen is revealed in the steel sheets side view.

Finally, at the last recorded displacement of the cross-head (3.8 mm); complete separation of the steel sheets is observed in Figure 4.19. Large plastic deformation and fracture

is depicted in both steel sheet surfaces, while close to total separation of the paired sheets as illustrated by the side view in the inset image.

From Figure 4.7, the cross-weld hardness profiles in the outer, SC-HAZ of the $DP780_B$ exhibited softening as a result of martensite tempering. Softening served to locally lower the yield strength in the $DP780_B$ HAZ and resulted in a strain concentration in the softened region when the yield strength was exceeded [58]. The $DP600_B$ did not show any measurable softening in the HAZ; however, there was significant necking observed. The hardness and strength of the $DP600_B$ base metal was still lower than the softened region in the $DP780_B$ HAZ, thus it is expected that the yield strength of the $DP600_B$ was exceeded first; however, due to work hardening, strain was transferred to the $DP780_B$ SC-HAZ and necking was a result of strain concentration. Softening in the HAZ of the $DP780_B$ helped promote a lower transition weld size, or in other words, SC-HAZ softening promotes a pullout failure mode.

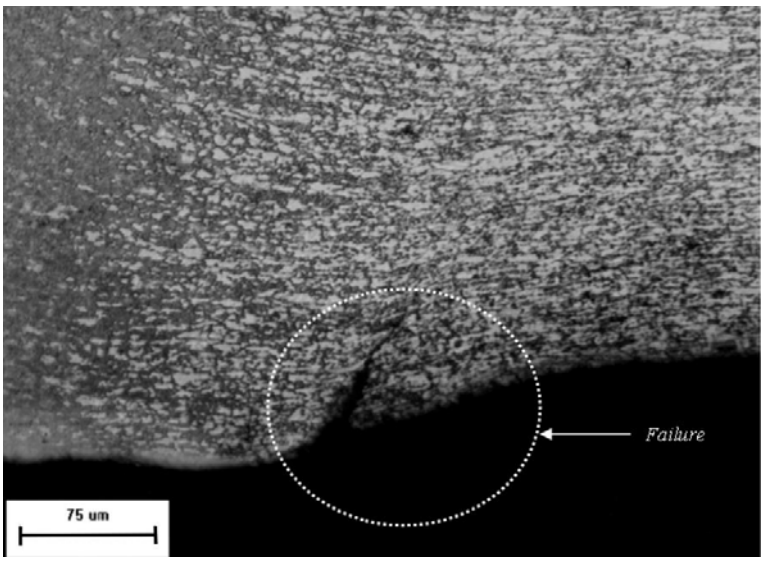

Figure 4.20 Fracture initiation at SC-HAZ in DP600 steel at 2.0 mm of displacement in the partial tensile test.

Detailed observations in the optical micrograph of Figure 4.20 confirmed the fracture in the SC-HAZ of the $DP600_B$ in the dissimilar combination ($DP600_B$-$DP780_B$) at 2.0 mm of displacement. At higher magnifications, the SEM image in Figure 4.21 shows significant micro-voids in the necking region of the DP600. Micro-voids are associated with decohesion of the ferrite-martensite interface or separation of adjacent particles due to local deformation generated at the necking (ductile) region [128].

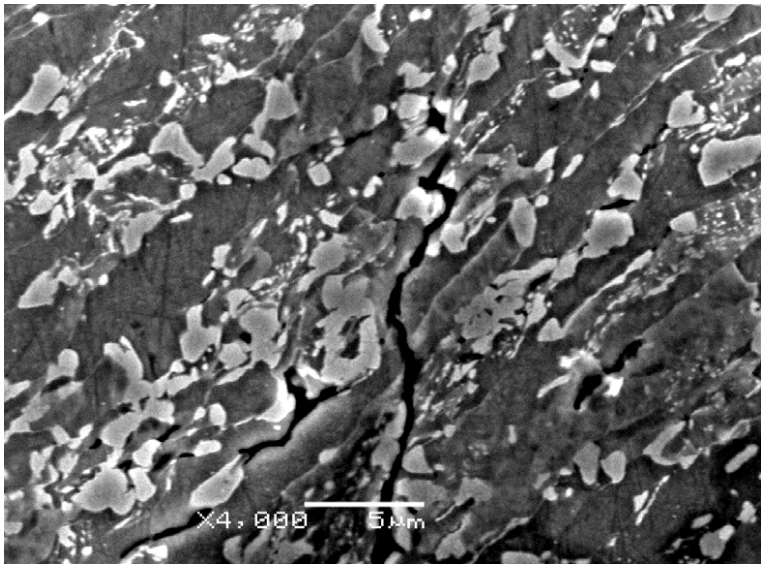

Figure 4.21 Decohesion at martensite-ferrite interface at SC-HAZ in DP600 steel at 2.0 mm of displacement

4.6. Summary

The microstructure and joint performance of resistance spot welds of dual-phase (DP) steels in similar and dissimilar combinations were successfully analyzed by employing microscopy techniques, hardness Vickers indentations and standardized tensile testing.

The measurable softening at the sub-critical HAZ of DP steel was strongly dependent on the volume fraction of the tempered martensite and on the degree or severity of tempering of the martensite sub-structure. Hence, larger HAZ-softening was observed in the higher grades of DP steel, *i.e.*, DP980.

Even though the failure mode was highly dependent on the nugget size, softening occurring in the sub-critical HAZ of $DP980_B$ steel modified the failure mode leading to improved tensile behaviour. The tensile failure mode changed from interfacial to pullout with increased load-carrying capacity and higher energy absorption for higher grades of DP steel. The critical nugget size, at which the failure mode changes from interfacial and/or partial interfacial to full pullout was lower for the $DP980_B$ steel welds. Softening at the sub-critical HAZ due to tempering of martensite was observed to influence the tendency of minimizing interfacial failures in $DP980_B$ welds compared to welds of other grades of DP steel.

A 600 MPa dual phase (DP) steel was welded to 780 MPa DP steel. An in-depth comparison of the interfacial to pullout failure transition in similar $DP600_B$ and $DP780_B$ and dissimilar $DP600_B$-$DP780_B$ welds was performed. The results show that the interfacial to

pullout transition for the $DP600_B$-$DP780_B$ welds is significantly lower than with $DP600_B$ welded to itself. By employing partial tensile testing in the dissimilar combination $DP600_B$-$DP780_B$; it was observed that softening in the HAZ of $DP780_B$ promoted the initiation of failure in this steel and hence pullout failure mode.

HAZ-softening was seen to benefit the tensile joint performance of resistance spot welded DP steels by facilitating pullout failures with increased load-bearing capacity and corresponding higher energy absorption. In addition, HAZ-softening has been associated with the volume fraction of martensite and to the degree of tempering of martensite. However, the contribution of the tempered martensite island (degree of tempering) to softening is not completely clear. This is due to the fact that microhardness indentation covers an area large enough that includes various features within the measurement such as; different phases (*i.e.*, ferrite and tempered martensite), grain boundaries, precipitates, etc. For this reason, there is a need to measure the hardness of individual phases at the SC-HAZ, particularly tempered martensite. The proposed technique instrumented nanoindentaion is utilized in the next chapter to study the influence of individual phases on the softening phenomena.

5. Study of Softening Phenomena in DP steel by Instrumented nano-Indentation Testing

In this chapter, instrumented nano-indentation testing was employed to study the softening phenomena occurring at the sub-critical HAZ of resistance spot welded dual-phase steel grade DP980. With the purpose of obtaining reliable experimental conditions and minimize the factors affecting nanoindentation test data; material surface condition and indentation testing parameters have been optimized for implementing nanoindentation trials. For instance, various surface conditions (sample preparation methods) were evaluated on the base metal of the dual-phase microstructure. In addition, the indentation size effect (load) has been evaluated for ferrite matrix and martensite islands in order to obtain adequate testing loading. Furthermore, nanoindentation track was observed through electron microscopy image and calculations of pile-up were performed in order to avoid overestimation in nanohardness.

Nanoindentation hardness testing was performed along the SC-HAZ for evaluating individual phases of ferrite matrix and tempered martensite islands. A comparison between nanohardness and microhardness testing has been made at different distances from the line of lower critical temperature of transformation (Ac_1). The extension of the SC-HAZ has been acquired through the implementation of higher resolution hardness techniques (nanoindentaion trials). In addition, nanohardness results along the SC-HAZ have correlated to microstructural changes analyzed by electron microscopy. Especial attention has been paid to the tempering of martensite occurring at various distances far from Ac_1 which in fact is related to the tempering of martensite islands in DP steel at low temperatures.

5.1. Microhardness and Microstructure

The BM for the present study was a DP steel with a nominal ultimate tensile strength of 980 MPa ($DP980_A$). The $DP980_A$ steel was used in the form of sheet with a thickness of 1.2 mm overlaid with a galvannealed coating. The chemical composition of the bulk metal of this DP steel is provided in Table 3-1. The volume fraction of martensite phase in BM was estimated to be 48 % from standard metallographic and image analysis techniques (Table 3-2).

Figure 5.1 shows a micro-hardness profile obtained across the welded region from the unaffected base metal (BM) through the fusion zone (FZ), the schematic cross-section of a RSW showing the different regions of the weldment has been provided in Figure 3.11. A reduction in hardness (softening) with respect to BM (avg. 298 HV) was clearly revealed in the sub-critical HAZ. The width of the zone of significant softening was around 0.8 mm and a maximum hardness reduction of 40 HV was identified at location-C. Maximum softening (at C) was located just below the line of critical temperature Ac_1. The location of Ac_1 was determined experimentally through optical microscopy by analysing the cross section macrostructure of the welded region. Detailed procedures for identification of Ac_1 have been explained elsewhere [11].

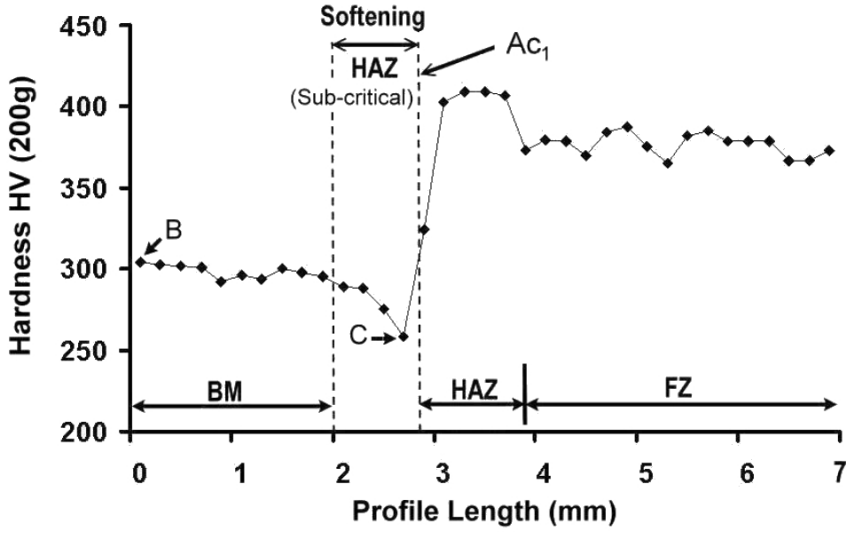

Figure 5.1 Vickers micro-hardness indentation profile across the weld of $DP980_A$ steel.

The SEM image provided in Figure 5.2a depicts the BM microstructure which

corresponds to the point B in Figure 5.1. Solid martensite islands (grey coloured particles) were clearly embedded in the ferrite matrix (black area). Martensitic particles were preferentially situated at the prior austenite grain boundaries [129]. The microstructure in Figure 5.2b which was obtained at the sub-critical HAZ, revealed decomposition of martensite particles (tempered martensite), and corresponds to location C in Figure 5.1. The morphology of the tempered martensite appeared broken with presence of some submicron particles (white), presumably due to precipitation and coarsening of cementite carbides and recovery of martensite.

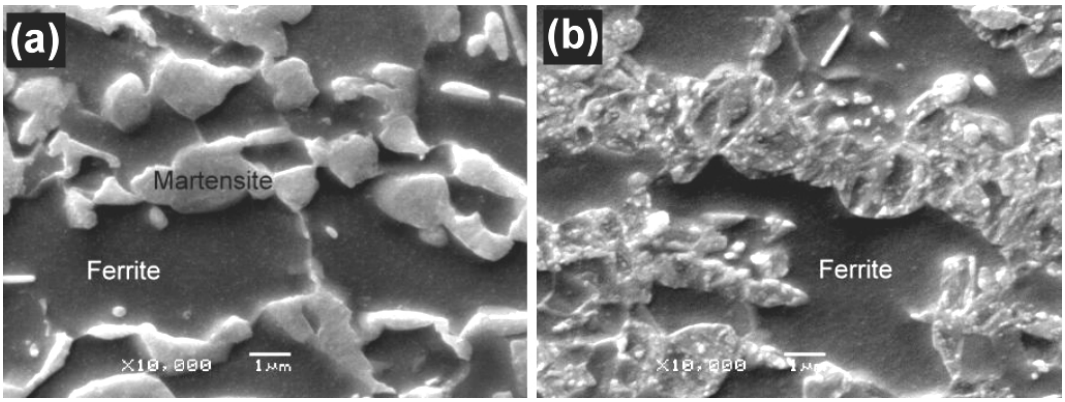

Figure 5.2 SEM micrographs for a) base metal (BM) and b) sub-critical region (HAZ) respectively of $DP980_A$. Images obtained from the location of indentations B and C in Figure 5.1.

During the welding thermal cycle, transient peak temperatures above Ac_1 mean, by definition, that the martensite and part of the ferrite is briefly transformed to austenite and then retransformed to new martensite during cooling. Depending on the location within the HAZ and hence on the peak temperature reached, the local post-weld martensite content could be above the level in the as-manufactured steel [130], leading to higher local hardness in the region called upper-critical HAZ.

5.2. Effects of surface condition

IIT trials were conducted upon three different surface conditions (preparation methods) of the base metal of $DP980_A$ steel in order to obtain the most suitable condition for conducting nanoindentation. Figure 5.3 shows the average nanohardness (H_n) for ferrite and martensite phases on the mechanically fine polished, the chemically etched and the electropolished surfaces under maximum indentation load (P_{max}) of 3000 μN. Variations in nanohardness were

insignificant for martensite between the assessed surface conditions. The dispersion of data for martensite shown by the error bars may be attributed to two main factors: first, due to local variations of supersaturated carbon in the martensitic particles [131,132], and second, due to presence of a diverse number of sub-grains (laths and/or twins) within the martensitic particles [109,133].

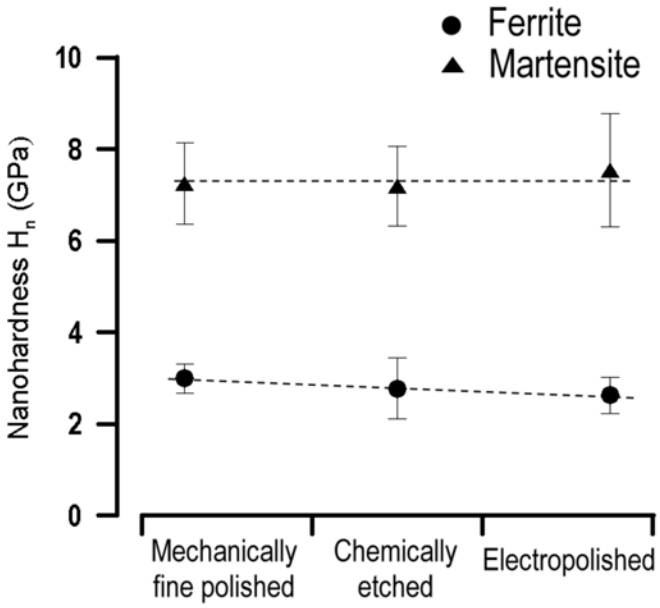

Figure 5.3 Effect of surface condition on nanohardness of microstructural phases in BM of DP980$_A$ steel.

The nanohardness for the ferritic matrix showed slight differences among the three different surface conditions due to possible presence of thin hardened surface layers produced by the mechanical polishing process. Data dispersion for ferrite was lower than for martensite particles; this was probably promoted by a less heterogeneous (free of low and large angle sub-grains) ferritic structure underneath the indenter in contrast to that of martensite (*i.e.,* laths and/or twins) [134,135].

Roughness parameters for three different surface conditions obtained under SPM are outlined in Table 5-1. A relatively lower roughness was found on the mechanically fine polished surface in which Ra laid around one nanometer and Rt around 13 nm. The increased roughness on the etched surface revealed the influence of the chemical attack. A protrusion effect on martensite particles over the ferrite matrix after etching is observed in Figure 5.2a. It may be mentioned here that roughness was measured separately on individual ferrite and martensite phase particles. The local roughness (i.e. individual phase) were lower for the ferrite matrix. The

electropolished surface resulted in the highest roughness values compared to the other surface conditions. Protrusion effect was hardly present on the electropolished surface due to slight etching of the ferrite matrix.

Table 5-1 Roughness parameters for various surface conditions applied to $DP980_A$ steel

Roughness parameter	*Roughness (nm)*				
	Mechanically fine Polished	*Chemically etched*		*Electropolished*	
		Ferrite	*Martensite*	*Ferrite*	*Martensite*
R_a	0.9	6.8	21.2	28.5	51.7
R_t	13.0	42.6	72.0	261.5	351.4

Even though it can be inferred that an electropolished surface is free of any hardened layer; the roughness in this case is relatively higher in comparison to the other surface conditions which might influence the indentation process. Roughness becomes critical when the surface topography is non-negligible compared to the maximum indentation depth [114,136]. Moreover, surface roughness is very important issue owing to the possibility on input errors in the determination of the area of contact between the indenter and the specimen [114]. Accordingly, roughness for the mechanically fine polished followed by etching procedure was reasonable for nanoindentation measurements in which the range of displacements of the indenter was around 50 to 250 nm; additionally, this surface condition further reduced possible hardened layers produced by preliminary fine mechanical polishing procedures. Based on above mentioned observations, mechanically fine polished surface followed by etching was adopted for the remainder of the work carried out in the present study.

5.3. Indentation size effect

The effect of indentation load, in terms of contact depth (h_c), on the nanohardness for martensite and ferrite phases is illustrated in Figure 5.4. A range of P_{max} from 750 µN to 6000 µN was used and the nanohardness was plotted as a function of the contact depth (equation 2-14). The nanohardness appeared almost constant on the ferrite matrix for h_c above 150 nm; however for smaller contact depths (i.e. 100 nm and less) the indentation size effect (ISE) [137,138] was evident and the measured nanohardness for ferrite increased while h_c decreased.

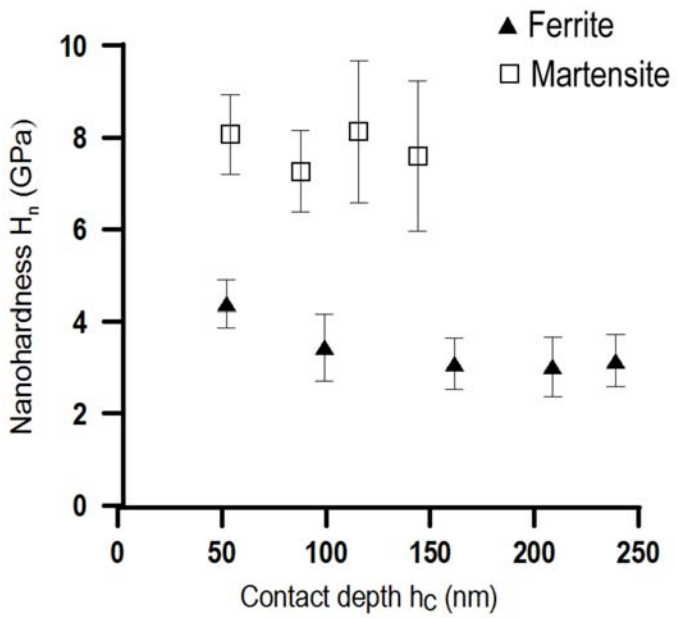

Figure 5.4 Effect of indentation load in terms of contact depth on the nanohardness of DP980$_A$ steel.

A fluctuation in the average nanohardness for martensite was found (i.e. 7.2 GPa to 8.2 GPa) for the assessed range of contact depths. ISE was not observed for the martensite phase. Nanohardness trials are possible to be conducted using an indentation load of 3000 µN (i.e. 161 nm for BM-ferrite and 87 nm for BM-martensite) as it seems appropriate in terms of indentation size (depth-width).

5.4. Load-Displacement Curves

Typical load progression (load-displacement or *P-h)* curves during nanoindentation of the base metal and tempered region are shown in Figure 5.5. Referring to the *P-h* curves for martensite and tempered martensite in Figure 5.5a; the slope of the curves kept on increasing due to increase in contact area during indentation. The maximal indenter displacement (h_{max}) upon a peak load of 3000 µN was larger for tempered martensite (i.e. 140 nm) compared to that of BM-martensite (99 nm). Larger penetration depth was also obtained for ferrite at the tempered region compared to that of the base metal (Figure 5.5b). Maximum penetration depth values for tempered martensite were in between the h_{max} values for BM-ferrite and BM-martensite.

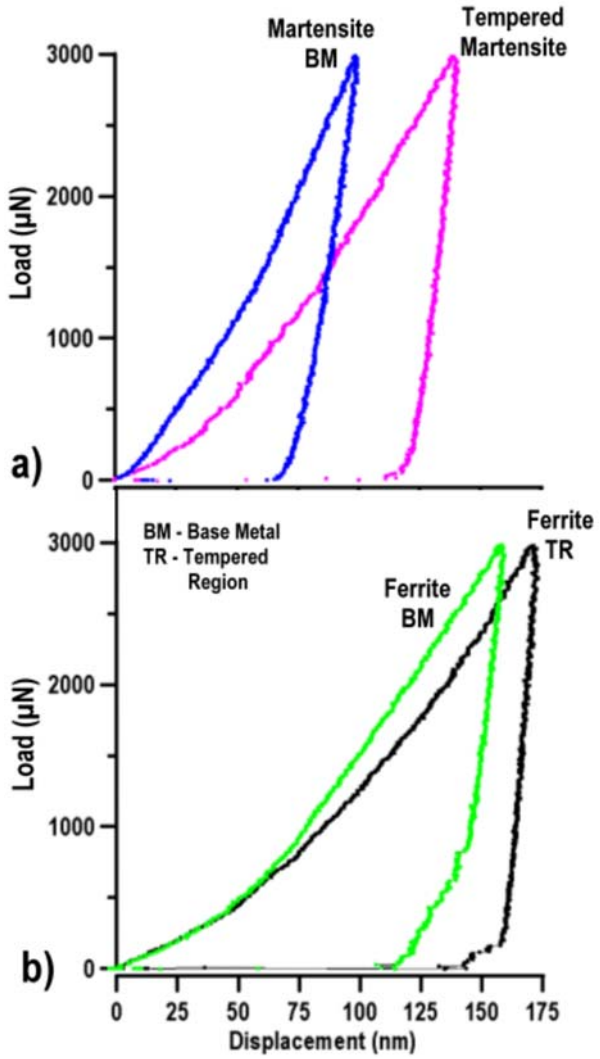

Figure 5.5 BM and tempered region (TR) load-displacement curves (*P-h*) corresponding to: (a) martensite and tempered martensite , and (b) ferrite.

Pop-in behaviour is known as a sudden or abrupt jump in displacement of the indenter associated to large-scale dislocation nucleation at the onset of plastic deformation and it is a function of pre-existing dislocation density [139]. Pop-in has been reported for tempered martensite in Fe-C alloys heat treated below Ac_1 temperature (500 °C and 650 °C) for prolonged periods of time (i.e. 5400 s) in which a considerable reduction of dislocation density by recovery was assumed [140]. It should be noticed that the above mentioned heat treatment is associated to traditional isothermal time-temperature processes well described by the Hollomon-Jaffe tempering parameter [141]. In contrast, in the non-isothermal condition evaluated in this work; continuous deformation without pop-in behaviour was observed for tempered martensite during the loading stage suggesting partial tempering of martensite, this is owing to low fraction of

carbide precipitation and incomplete recovery.

5.5. Pile-up Behaviour

SEM micrographs of representative Berkovich impressions for BM and tempered region (TR) are shown in Figure 5.6 and these impressions correspond to the *P-h* curves plotted in Figure 5.5. Single indentations made on the BM for martensite and ferrite are illustrated in Figure 5.6a, and Figure 5.6b respectively. The size (depth-width) of the nanoindenter impressions appeared appropriate for hardness assessment of individual phases as the measured indentations were located within the area of martensite particles (Figure 5.6a), thus avoiding contributions of grain boundaries between phases to nanohardness.

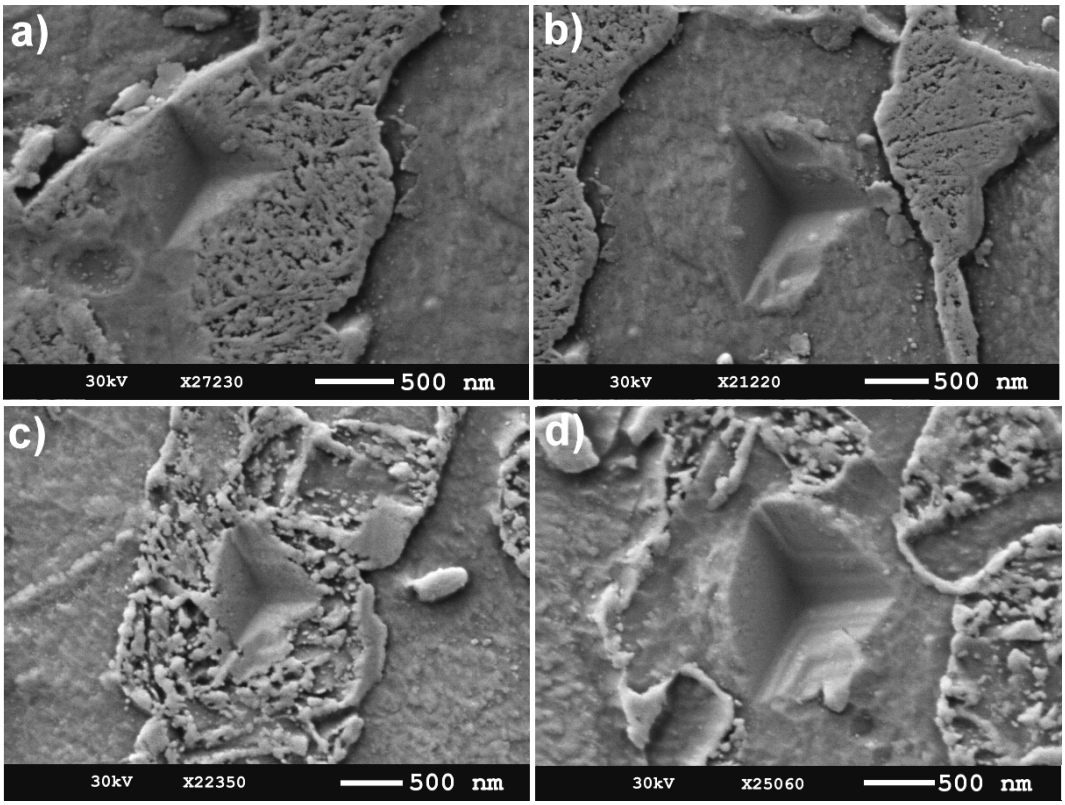

Figure 5.6 Hardness nanoindentation impressions on: (a) martensite, (b) ferrite, and, TR at (c) tempered martensite (d) ferrite.

Pile-up or excursion, defined as plastically flowed material deposited at the perimeter of the indentation [142], was barely observed in martensite as shown in Figure 5.6a. By noting the minimal pile-up effect for martensite it can be inferred that nanohardness for this phase was not

overestimated [113]. Figure 5.6b illustrates the topography of a typical indent on the BM ferrite matrix showing some deformation of the surroundings. Figure 5.6c shows a typical indent located within the boundaries of decomposed (tempered) martensite, showing that the measured nanohardness of the tempered martensite represents all the transformed sub-products such carbides and/or partial recovered zones. The impressions on ferrite at the tempered region in Figure 5.6d resulted in the largest pile-up at the periphery of the indent in comparison to other phases (i.e., martensite). In addition, calculation of h_f/h_{max} yielded a value of 0.85 (where h_f is the final displacement after complete unloading) for ferrite at TR. It has been established that when h_f/h_{max} is higher than 0.7 it suggests pile-up [143].

5.6. Softening behaviour at SC-HAZ

Figure 5.7 depicts a resistance spot welded cross section macrograph of $DP980_A$ steel. Several regions were identified after etching such as: fusion zone (FZ), Ac_1 line dividing the HAZ into upper-critical and sub-critical, and the base metal (BM) at the extreme right of the macrograph. Two grids of a determined number of microhardness indentations were located at the sub-critical HAZ and the BM. The grid of indentations at the sub-critical HAZ was divided into five columns in order for the hardness to be averaged at specific distances from Ac_1. The columns a, b, c, d, and e, were located at 100, 200, 400, 600 and 800 µm respectively from Ac_1 in the direction towards the BM. The grid of microhardness indentations at the BM was located far enough from Ac_1, as seen at the extreme right of the image (Figure 5.7).

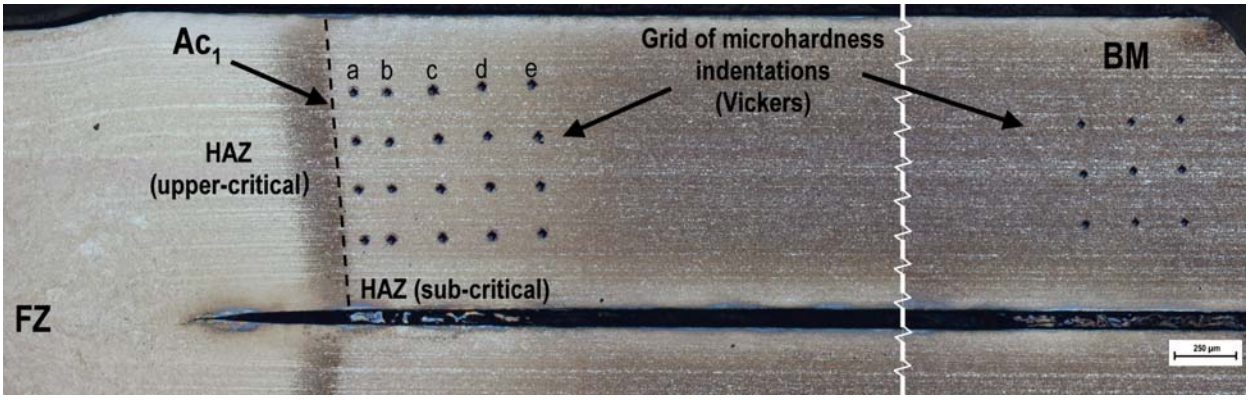

Figure 5.7 Cross-section macrograph of resistance spot welded DP steel showing two grids of microhardness indentations (HV-200 g) on the sub-critical HAZ (left) and BM (right). Distance between Ac_1 and the columns of indentations averaged: a 100 µm, b 200 µm, c 400 µm, d 600 µm, and e 800 µm.

The SEM micrographs shown in Figure 5.8 illustrate the dual-phase microstructures at

the sub-critical HAZ combined with that of the BM. The sub-critical HAZ microstructures were obtained at various distances from Ac_1 on the locations detailed in Figure 5.7 (i.e. 100, 200, 400, 800 μm and BM).

The microstructure at 100 μm away from Ac_1 (Figure 5.8a) shows the ferrite matrix (dark regions) and martensite phase severely decomposed (bright regions), or in other words, tempered martensite. It may be noted that tempered martensite appears broken with presence of sub-micron particles due to nucleation and growth of carbides as indicated by the white arrow marks. Similar microstructural characteristics were observed at 200 μm far from Ac_1 (Figure 5.8b). However, here the grain or phase boundary between ferrite and tempered martensite appeared sparsely wiped in comparison to that of Figure 5.8a, possibly due to a lower volume fraction of carbide precipitation at or near the grain phase boundaries (white arrow).

Figure 5.8c depicts the microstructure at 400 μm far from Ac_1 in which prior martensitic grain boundaries were clearly defined; basically finer sub-micron particles were observed within martensite grains (white arrow) in contrast to those found in Figure 5.8a. An apparent lower volume fraction of fine sub-micron particles were observed in the microstructure obtained at 600 μm far from Ac_1 (Figure 5.8d). Figure 5.8e shows the microstructure at 800 μm far from Ac_1; sub-micron particles were barely visible, however the martensite did have a decomposed appearance, compared to the original BM microstructure (Figure 5.8f) where solid martensitic particle morphology was observed.

A general trend revealed that sub-micron particles for tempered martensite became finer and a reduction of the volume fraction was also evident as the distance from Ac_1 towards the base metal increased. This trend was basically promoted by the welding thermal cycles and the peak temperature profile along the sub-critical region.

Low volume fraction of possible retained austenite was consistently found in all of the above mentioned locations as pointed by the arrow with the label RA in Figure 5.8. Presence of retained austenite in the base metal was due to the relative high Mn content in the alloy that served as austenite-stabilizer [144].

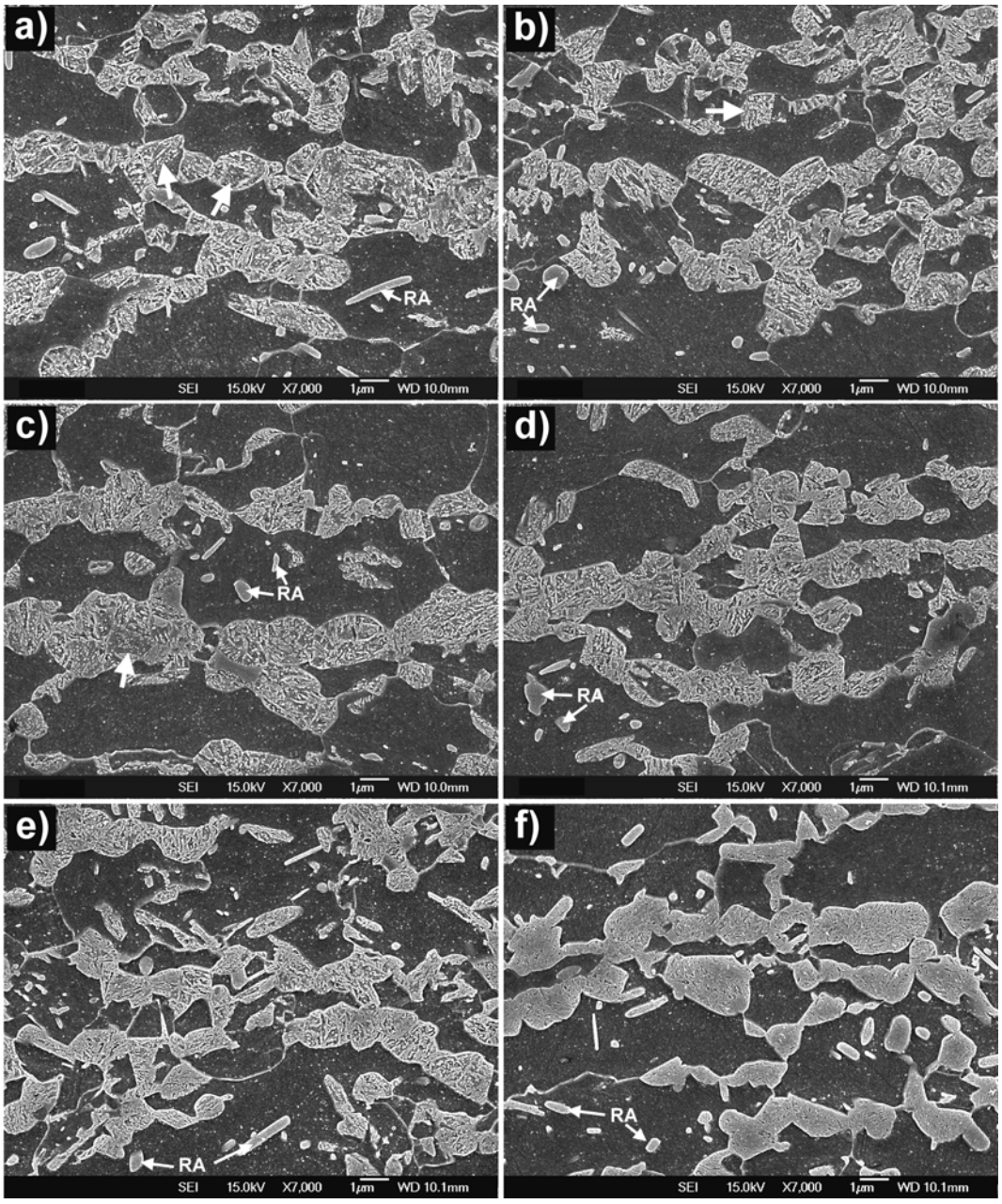

Figure 5.8 Sub-critical HAZ microstructures in DP980$_A$ obtained at a distance of: a) 100 µm; b) 200 µm; c) 400 µm; d) 600 µm; e) 800 µm from Ac_1 line. f) Base metal micrograph showing ferrite matrix (dark regions) and martensite particles (brighter regions).

The average Vickers microhardness (HV) at various distances from Ac_1 towards the base metal in DP980$_A$ steel is shown in Figure 5.9. The average microhardness for base metal was approximately 301±9 HV. An average softening of about 31 HV was obtained at 100 µm with respect to the center of the indentation mark. A gradual increase of microhardness was observed as the distance from Ac_1 increased (.i.e. at 200, 400 and 600 µm). The average microhardness at

800 µm was of 301±6 HV; thus matching with the microhardness of the BM.

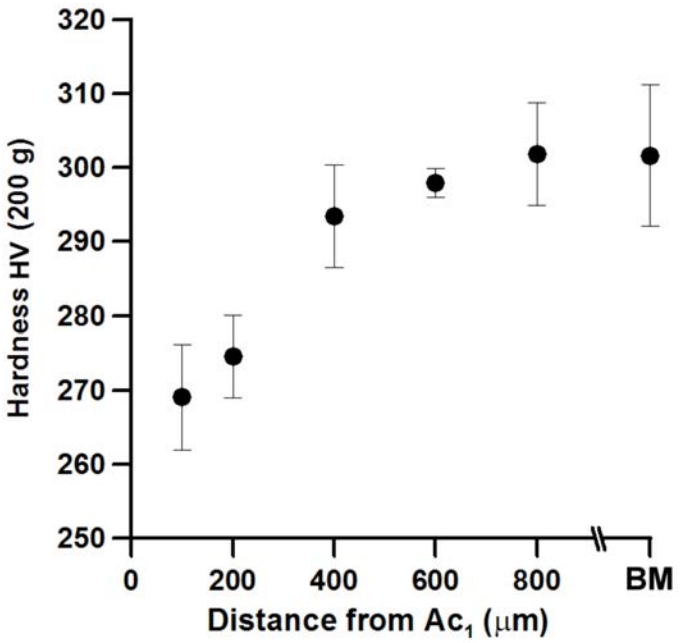

Figure 5.9 Vickers Microhardness at various distances from Ac_1

Figure 5.10 shows the average nanohardness (H_n) of BM-martensite, tempered martensite and that of the ferrite matrix obtained at various distances from Ac_1.

Slight reduction in nanohardness was observed in ferrite near the location of Ac_1. Insignificant variation of H_n was observed in ferrite at 200 µm and farther distances away towards the BM. Martensite in the BM averaged a nanohardness of 7.2±0.8 GPa. In contrast, nanohardness of tempered martensite at 100 µm away from Ac_1 revealed a reduction in hardness (4±1.2 GPa) and approximately similar value was found at 200 µm from Ac_1. A gradual increasing in nanohardness was encountered at 400 µm and above for tempered martensite until it reached the nanohardness value for martensite in the BM.

According to the results plotted in Figure 5.9, the average BM microhardness was measured at a distance of 800 µm respect to Ac_1, while at the same location (i.e. 800 µm) and according to the data from Figure 5.10; the nanohardness value was well below that of martensite in the BM. The reduced nanohardness at this location was presumed to be due to early stages of tempering (i.e. tempering at low temperature). The characteristics of tempering at low temperatures are discussed in more detail further on. The observed microstructure at 800 µm from Ac_1 (Figure 5.8e) contained prior martensite particles still having a tempered

appearance with barely visible submicron particles. The fact that microhardness testing was not able to measure softening at 800 µm from Ac_1; might be attributed to a possible grain boundary effect that was promoted by the size of the indentation (i.e. contribution of high-angle grain boundaries), in contrast, nanoindentation provided an improved resolution in measuring softening due the possibility of avoiding the contribution of the phase boundaries (i.e. tempered martensite at low temperature and ferrite boundary) in DP steel.

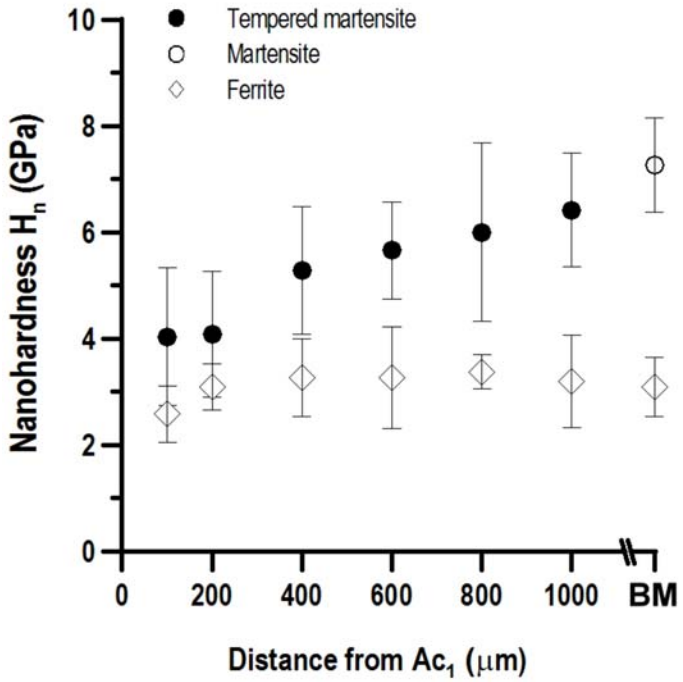

Figure 5.10 Variation of nanohardness (Berkovich) of martensite, tempered martensite and ferrite phase with distance from Ac_1.

Figure 5.11 illustrates the nanoindentation load-displacement (P-h) curves for the BM-martensite and tempered martensite (TM) at 100 µm (TM_{100}), 800 µm (TM_{800}) and 1000 µm (TM_{1000}) from Ac_1. The BM-martensite resulted in the lowest displacement and hence was confirmed to be the hardest phase. The TM_{100} displayed the largest displacement of all the curves confirming that TM at this location had the lowest hardness (Figure 5.10).

Continuous deformation without pop-in was commonly found during the loading stage for all the assessed curves. Instead the P-h curve for TM_{100} showed slight discontinuities which might be attributed to the severity of tempering at this location.

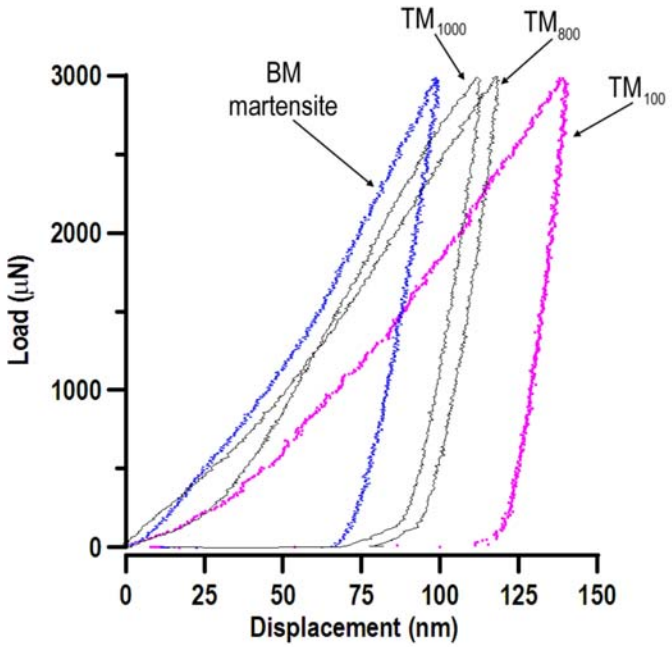

Figure 5.11 *P-h* curves for base metal (BM) and tempered martensite (TM) at 100, 800 and 1000 μm from Ac_1.

5.7. Tempering of martensite along SC-HAZ

Tempering of martensite is dependent on time and temperature of thermal exposure. For transient thermal exposures of similar shape but different peak temperature, the extent of tempering will vary according to the maximum temperature attained by the material [26]. During resistance spot welding, a gradient of peak temperatures will be seen at varying distances from the fusion zone and extended along the HAZ [41]. Logically, it is desired to know the distance from Ac_1 at which particular sub-critical peak temperature is developed; this in fact, would permit on connecting the severity of tempering to the maximum local temperature. There exist limitations in this regard; one important is due to the difficulty on obtaining experimental peak temperature distribution in resistance spot welding owing to the presence of strong magnetic fields generated during the passage of the current. One possible solution to overcome this issue; is to obtain calculated sub-critical peak temperatures [145]. Hence, a numerical simulation was developed in the present work in order to estimate the peak temperature gradient along the sub-critical HAZ. Figure 5.12 provides a reference for the temperature distribution along the sub-critical HAZ in $DP980_A$ in which numerically simulated peak temperatures were plotted versus the distance from Ac_1 (Ac_1 temperature is located at the origin of x-axis).

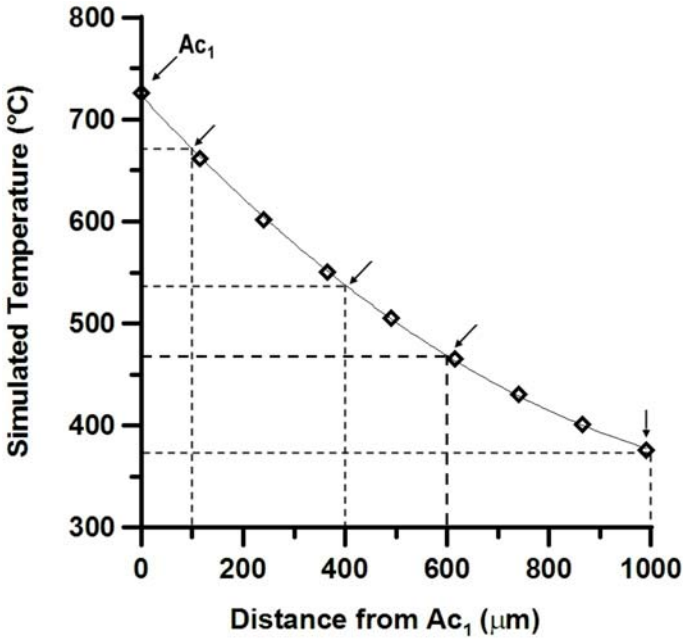

Figure 5.12 Numerical simulation of peak temperature at various distances from Ac_1

Figure 5.13 shows a SEM image recorded at a distance of 1000 μm from Ac_1, which attained a temperature of 376°C as suggested by Figure 5.12, revealed more of the solid prior martensite regions predominantly in the outer periphery, but with presence of slightly broken appearance and submicron particles (carbides).

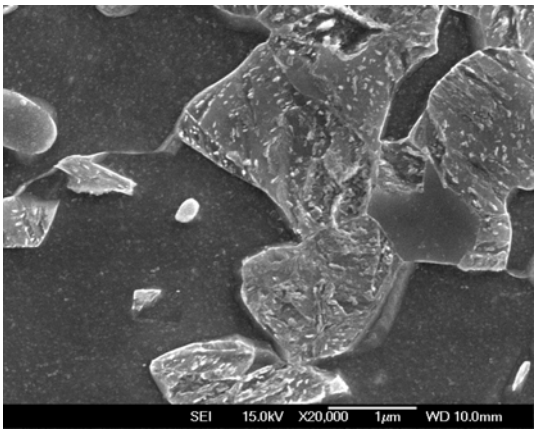

Figure 5.13 SEM micrograph illustrating the tempered martensite morphology at 1000 μm from Ac_1.

Figure 5.14 shows the tempered matrix obtained at a distance of 600 μm far from Ac_1 (attained a peak temperature of 470°C from Figure 5.12) at which considerable larger fraction of precipitated carbides is revealed compared to the specimen observed at 1000 μm from Ac_1 (Figure 5.13).

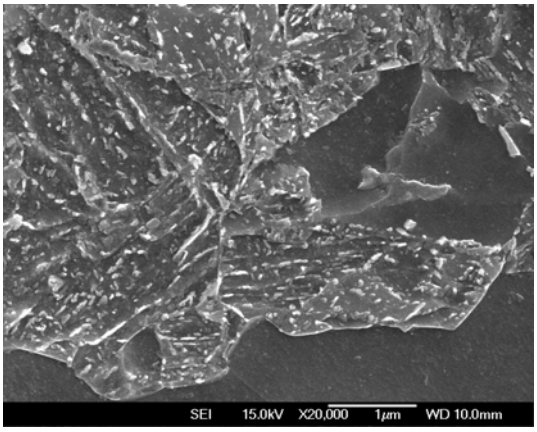

Figure 5.14 SEM micrograph illustrating the tempered martensite morphology at 600 μm from Ac_1.

Figure 5.12 indicated that a peak temperature of 538 °C was achieved at a distance of 400 μm from Ac_1, SEM observation at this location indicates comparable TM morphology to that at 600 μm; however, the sub-micron particles seemed larger in the former (Figure 5.15).

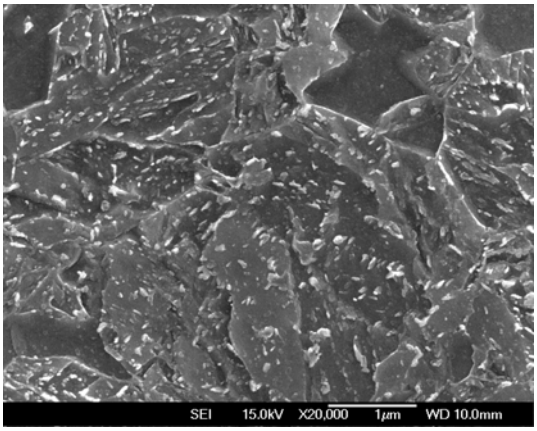

Figure 5.15 SEM micrograph illustrating the tempered martensite morphology at 400 μm from Ac_1.

From Figure 5.12, it is seen that a peak temperature of 671 °C was reached at 100 μm far from Ac_1. At a distance relatively close to Ac_1 (high tempering temperatures) several other reactions might occur. For example, at 100 μm far from Ac_1; the TM shown in Figure 5.16 depicts a broken appearance containing a large number of spherical sub-micron particles (presumably carbides) which are abundant near to boundaries. The broken morphology along with localized wiped regions (marked by arrow) within the prior martensitic regions suggests partial recovery of martensite. Thus, it is believed that partial decomposition of martensite has occurred in the sub-critical HAZ assisted by the rapid thermal cycles (fast heating, extremely short time at peak temperature, and quick cooling) developed in the resistance welding process.

However, this assumption needs to be further confirmed by transmission electron microscopy analysis.

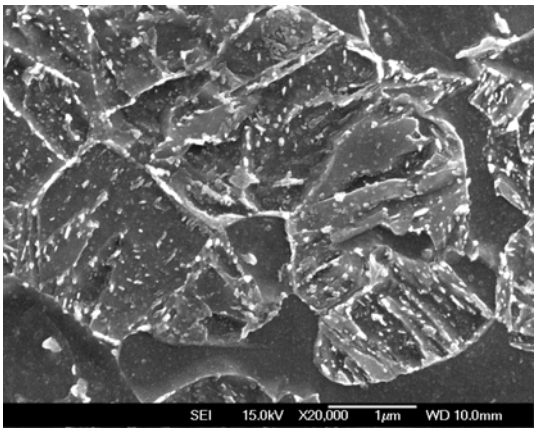

Figure 5.16 SEM micrograph illustrating the tempered martensite morphology at 100 μm from Ac_1.

Figure 5.17 shows transmission electron microscopy bright field (BF) images of tempered martensite in $DP980_A$ steel at various distances from Ac_1 (tempering at low temperature). The tempered martensite structure formed at distance of 3000 μm, 1000 μm and 600 μm from Ac_1 is illustrated in Figure 5.17a, Figure 5.17b and Figure 5.17c, respectively. Figure 5.17a clearly depicts lath substructure from the prior α' phase in the specimen; however, carbide precipitation is barely noticeable. Furthermore, relatively small carbides with plate-like morphology are observed within the tempered matrix at 1000 μm from Ac_1 as shown in Figure 5.17b, additionally, larger plate-like carbides were located along the lath boundaries as pointed by the arrows (Figure 5.17b). Similarly to non-isothermal tempering 1000 μm from Ac_1; plate-like carbides with approximately similar size are observed in the tempered structure 600 μm from Ac_1 in Figure 5.17c, moreover, the lath substructure of the prior α' phase is still clearly revealed in the microstructure.

The above results suggest that the formation of θ-carbides in the tempered matrix of $DP980_A$ steel has been inherited from fast migration of interstitial carbon atoms to lattice defects (*i.e.,* dislocations, lath boundaries) at low temperature. Segregation of carbon to lattice defects has been observed and measured in low-carbon martensites in Fe-C martensitic steels during aging and during the early stages of tempering [21,146]. It has been reported that the segregated carbon is bonded to the lattice defects through a strong binding energy; thus, promoting the formation of carbides in these regions [147].

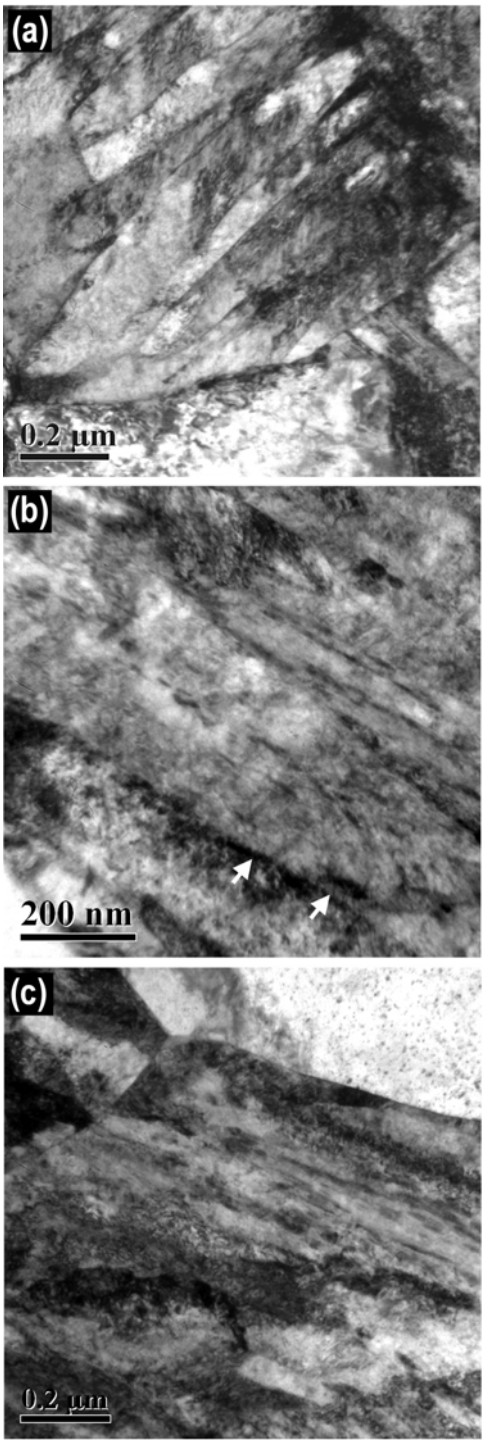

Figure 5.17 TEM-BF images showing the tempered martensite structure of DP980$_A$ steel at a distance of: a) 3000 µm, b) 1000 µm, c) 600 µm, from Ac$_1$ line of critical temperature.

Tempering at low temperatures involves several reactions that often overlap and occur in a very fine scale; for instance, segregation of carbon to lattice defects and/or clustering of carbon [81], formation of transition carbides *viz*. ε-iron, *i.e.,* 100°C ~ 200°C [82] and the further

formation of cementite in the temperature range of 250-500 °C [28]. Evidence on the formation of low-temperature carbides (*i.e.*, epsilon carbide) was not found in $DP980_A$ steel. This is essentially due to the fact that formation of epsilon carbide has been associated to medium- and high-carbon martensites, and to spinodal decomposition and clustering of carbon occurring at aging temperatures [83-87]. In addition, Si has been characterized as an effective stabilizer of the epsilon carbide [37]. Hence, in the case of $DP980_A$ steel with a martensite carbon content of 0.275 pct. (Table 3-2) and the relatively low content of Si (Table 3-1); further reduce the possibility to stabilize epsilon carbides.

The tempering of martensite occurring at a distance of 100 μm from Ac_1 has been subjected of detailed fundamental analysis through transmission electron microscopy and electron diffraction techniques which are further discussed in Chapter 6 of this thesis work.

Maximum softening was measured in tempered martensite TM at 100 μm from Ac_1 under micro- and nano- hardness indentation (Figure 5.9 and Figure 5.10). Both; micro-hardness and nanohardness of the TM increased when moving away from Ac_1 towards the base metal. Interestingly, at the location 1000 μm away from Ac_1; the instrumented nano-indentation hardness technique was capable of revealing softening on TM islands.

TEM bright field images revealed precipitation of carbides at 1000 μm away from Ac_1. The precipitated carbides confirmed martensite tempering at low temperatures. Peak temperature of approximately 360°C is developed at 1000 μm away from Ac_1 at the SC-HAZ according to recent reports [145]. At such temperature, the formation of cementite has been reported in low-carbon martensitic steels [22]. Based on the above analysis and on the observation in this chapter on the carbide morphology; it is believed that the precipitated carbides observed in Figure 5.17b corresponds to cementite carbides.

On the other hand, it is clear that nanoindentation hardness testing can measure with good reliability the hardness changes of the tempered martensite islands in dual phase steels upon at low temperatures.

5.8. Summary

The base metal and the subcritical HAZ (SC-HAZ) of a resistance spot welded dual phase steel have been successfully evaluated by nanoindentation hardness testing. Three different surface conditions have been explored on the base metal from which fine mechanical

polishing was found to provide reliable nanoindentation data.

Nanohardness results revealed “softening” at nano-scale for tempered martensite when compared to martensite in the base metal. At the tempered region, the ferritic matrix presented a slight reduction in hardness while the tempered martensite seemed to have a major contribution to the measured softening at micro-scale.

In addition, softening has been investigated along the SC-HAZ zone by making nanoindentations on individual phases such as ferrite and tempered martensite at various distances from the line of lower critical temperature Ac_1. Additionally, SEM and TEM observations completed the analysis. For example, IIT and SEM observations indicated that large reduction in nanohardness resulted at 100 μm from the Ac_1 line where a broken appearance accompanied with sub-micron particles were consistently observed on tempered martensite, thus suggesting carbide precipitation along with partial recovery of martensite. The morphology of tempered martensite kept on changing while moving away from Ac_1 towards the base metal as the fraction of broken appearance was reduced and the precipitated carbides became finer; accordingly, the nanohardness kept on increasing. At 1000 μm from the Ac_1 line; a slightly broken appearance observed by SEM with presence of finer precipitated carbides confirmed by TEM suggested low temperature tempering at this location and lower nanohardness compared to that of martensite at BM.

SEM and TEM observations, and the simulated peak temperatures, resulted in good agreement with the nanohardness of the tempered martensite phase along the sub-critical heat affected zone at which the “actual” extension of the SC-HAZ was clearly revealed through tempering at low temperatures. In contrast, microhardness results suggested the termination of tempering at a shorter distance with respect to Ac_1 and hence a reduced extension of the softening region.

The improved resolution for assessing softening through nanoindentation was due to the possibility of avoiding the contribution of the phase boundaries because of the smaller size of the indentation; this in fact, permitted evaluation of the tempered martensite matrix with less contribution from high-angle boundaries.

6. Transmission Electron Microscopy Study of the Tempering of Martensite Phase (or islands) in Dual Phase Steel

In this chapter the tempering of martensite at high temperature subjected to non-isothermal (resistance spot welding) and isothermal (heat treatment) conditions has been studied in two different grades of DP steel *i.e.,* DP800 and DP980 by analytical transmission electron microscopy (TEM).

Systematic analysis has been made of the substructure of the base metal martensite (α'-phase) islands based on chemistry and morphology. Details have been provided about the substructure that characterizes α'-phase in the dual-phase microstructure and the influence of carbon content. In order to analyze the effect of thermal cycle; $DP980_A$ steel has been subjected to isothermal tempering (slow heating rate and long holding time at peak temperature), and non-isothermal tempering of martensite (rapid heating and extremely short holding time at peak temperature) by assessing the precipitation of carbides, the decomposition of retained austenite and the recovery of the lath substructure of the tempered islands of martensite. The changes in microstructure of the non-isothermally tempered martensite have been contrasted to those of the isothermally tempered martensite and to α'-phase of the base metal. Analysis of the non-isothermal tempering of the martensite phase has been extended by incorporating various chemistries of dual phase steel in order to obtain the effects of the chemical composition on the tempering. The crystal structure and the chemical composition of the precipitated carbides have been studied through conventional and high resolution analytical techniques.

Finally the above mentioned structural analysis has been correlated to the measurable softening in the higher grades of the DP steel.

6.1. Base metal structure of $DP980_A$

Representative SEM micrographs illustrating the base metal (BM) microstructure for $DP980_A$ steel (Table 3-1) are shown in Figure 6.1a-b. The BM is comprised of dark ferrite matrix (α) along with grey dispersed banded islands of martensite (α') phase aligned parallel to the rolling direction, as marked by an arrow in Figure 6.1a, of the $DP980_A$ steel sheet. Even though a solid smooth featureless appearance of the α' phase is shown in Figure 6.1a; the α' islands are really comprised of a substructure as depicted in the high magnification image in Figure 6.1b. TEM bright field image of $DP980_A$ steel obtained at two different tilt angles clearly delineates the α' phase contained within the α-matrix (Figure 6.1c-d) and the high angle α/α' phase boundary (which corresponds to the prior austenite (γ) grain boundary) can be seen clearly. Random arrays of dislocations were observed in the ferrite matrix as seen in Figure 6.1c-d. High angle boundaries (white dotted line) were seen to separate the blocks within the martensite island in the $DP980_A$ steel as pointed out by the arrow in Figure 6.1c. Furthermore, the martensite blocks within the α' island in $DP980_A$ steel were clearly seen to have parallel martensite laths as pointed by the arrows in Figure 6.1d. It is well known that a martensite block contains a number of parallel laths and blocks are separated by high angle boundaries [109]. The presence of a substructure of lath morphology (Figure 6.1c-d) indicates that $DP980_A$ steel is characterized to contain low-carbon α' phase which is reflected from the carbon content within martensite that was calculated using equation 3-1 to be 0.270 wt.% (Table 3-2). Furthermore, it is worth noting that the martensite islands in the $DP980_A$ steel have comparable characteristics to the microstructure of low-carbon martensitic steels which are characterized by different structural units within the prior austenite grains *viz.* packets (contains many blocks), and blocks which contain parallel martensite laths [62].

High magnification imaging (Figure 6.2a) was carried out in order to clearly analyze the details of lath structure and the high angle α/α' phase boundaries in $DP980_A$ steel. The inherent martensite laths were seen to contain high density of dislocations which is a well-known characteristic feature of martensite laths (Figure 6.2a) in low-carbon martensitic steels [61]. The selected area diffraction (SAD) patterns shown in Figure 6.2b and Figure 6.2c were taken from the locations indicated by circles b and c in Figure 6.2a, respectively. The SAD patterns were indexed to contain spots from $[001]_{\alpha'}$ and $[\bar{1}13]_{\alpha}$ zone axes, thus confirming the presence of α'

phase and α-matrix, respectively, in the regions marked in Figure 6.2a.

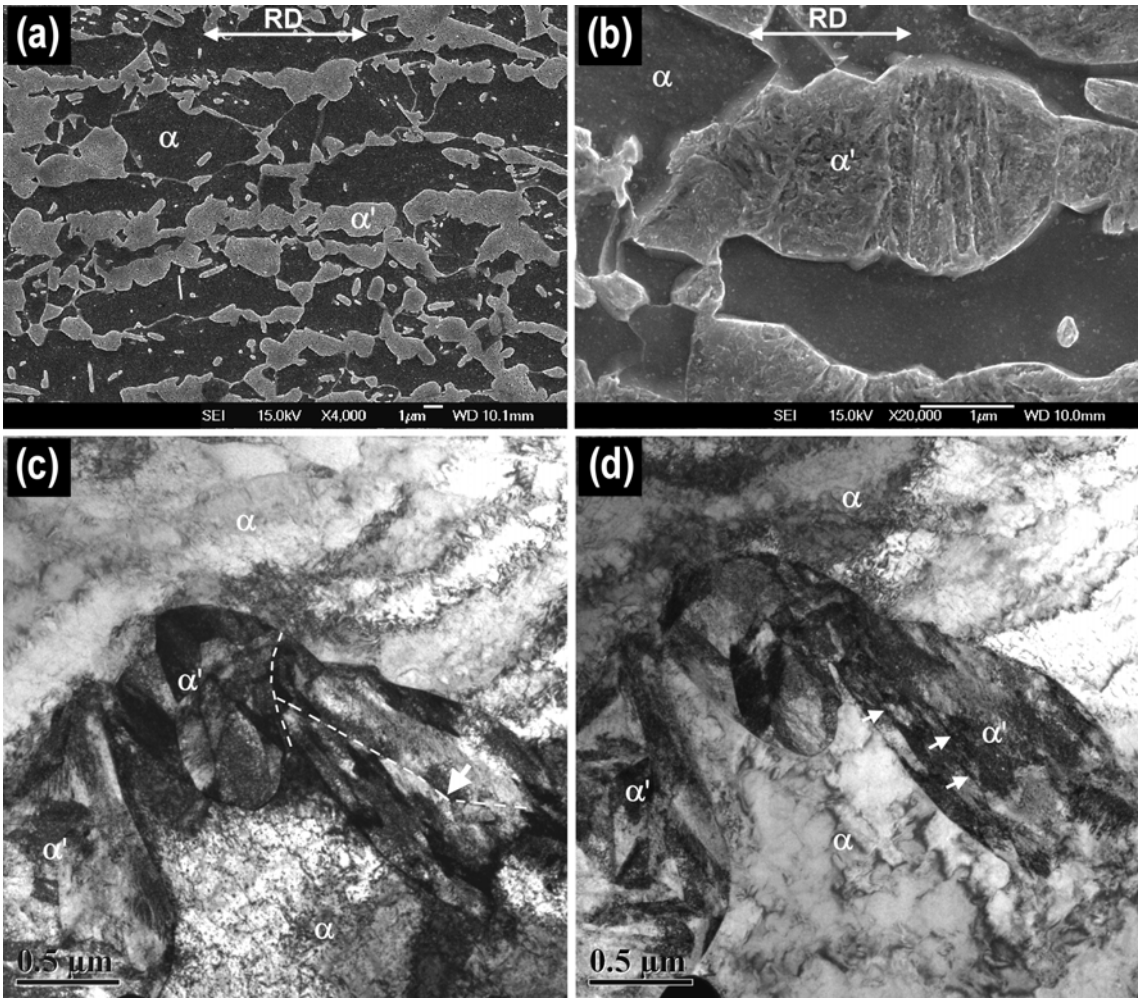

Figure 6.1 Base metal microstructure of DP980$_A$ steel: SEM micrographs showing (a) ferrite α-matrix along with banded islands of martensite (α'), (b) the solid morphology of α'-phase, (c) and (d) TEM bright field images of α'-phase and α-matrix at two tilt angles.

In addition to ferrite and α' phase in the BM microstructure, a relatively small fraction of retained austenite was observed to be located along the lath boundaries (interlath) as depicted by the TEM bright field image (Figure 6.3a), and confirmed by the dark field micrograph taken using the $(\bar{3}\bar{3}1)$ diffraction spot (arrow in Figure 6.3b). Figure 6.3c illustrates the SAD pattern of region shown in Figure 6.3a and its indexing is shown in Figure 6.3d which delineates the diffraction spots from $[\bar{1}13]$ zone axis of α' and $[\bar{2}33]$ zone axis of austenite (γ), thus, indicating an orientation relationship of $[\bar{1}13]_{\alpha'}//[\bar{2}33]_{\gamma}$ in the BM of DP980$_A$ steel.

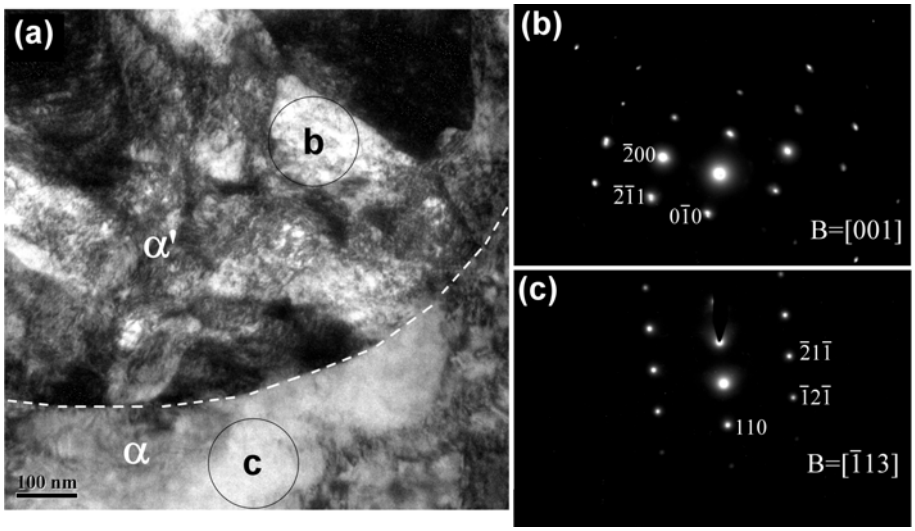

Figure 6.2 (a) TEM bright field image showing: (a) α/α' high-angle boundary, and corresponding SAD patterns for (b) α'-phase and (c) α-matrix, confirming $[001]_{\alpha'}$ and $[\bar{1}13]_{\alpha}$ zone axes, respectively.

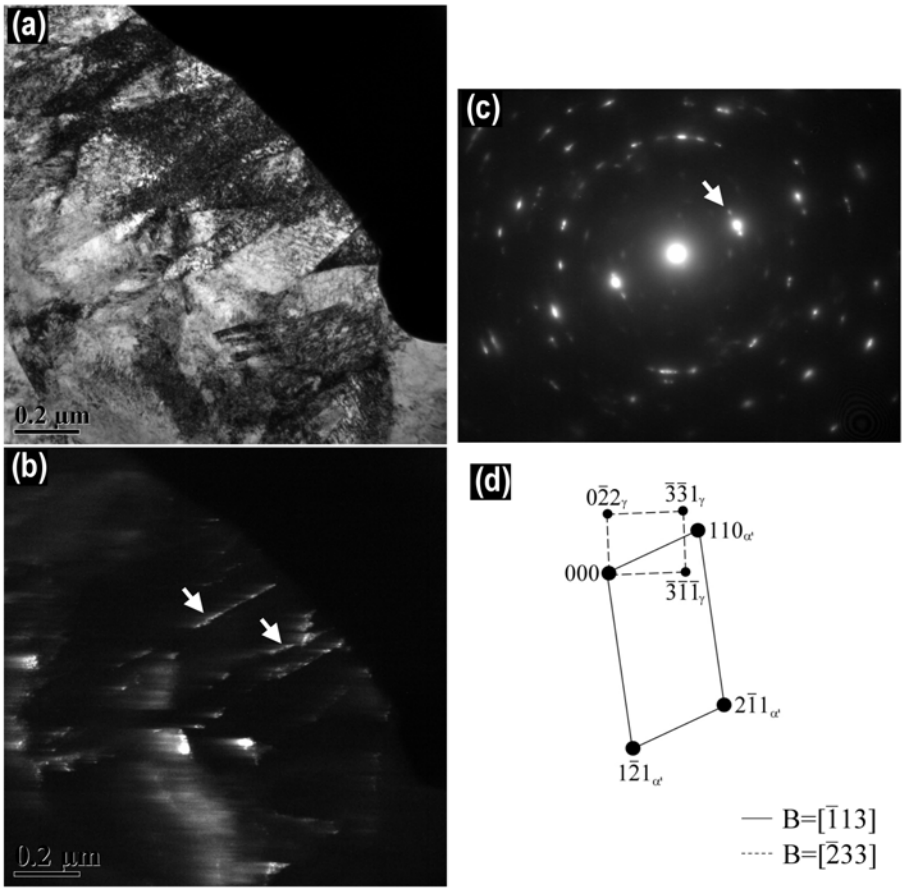

Figure 6.3 Inter-lath retained austenite: (a) BF and (b) DF image taken $(\bar{3}\bar{3}1)_{\gamma}$ reflection, (c) SAD pattern, and (d) schematic illustration of indexing SAD pattern.

Interlath retained austenite in steel is generally formed in medium- and high-carbon martensite in fully martensitic steels [95,97]. However, it has also been observed that additions of Mn promote the formation of interlath retained austenite in steel [2].Thus, it is concluded that despite the low-carbon content within martensite in the $DP980_A$ steel (Table 3-2); there is sufficient Mn which strongly stabilizes inter-lath austenite in α' phase of the $DP980_A$ steel.

6.2. Isothermal tempering at high temperature

Figure 6.4 compares the XRD patterns of $DP980_A$ steel BM and the isothermally tempered specimens at high temperature (650 ºC) for 300s and 5400s.

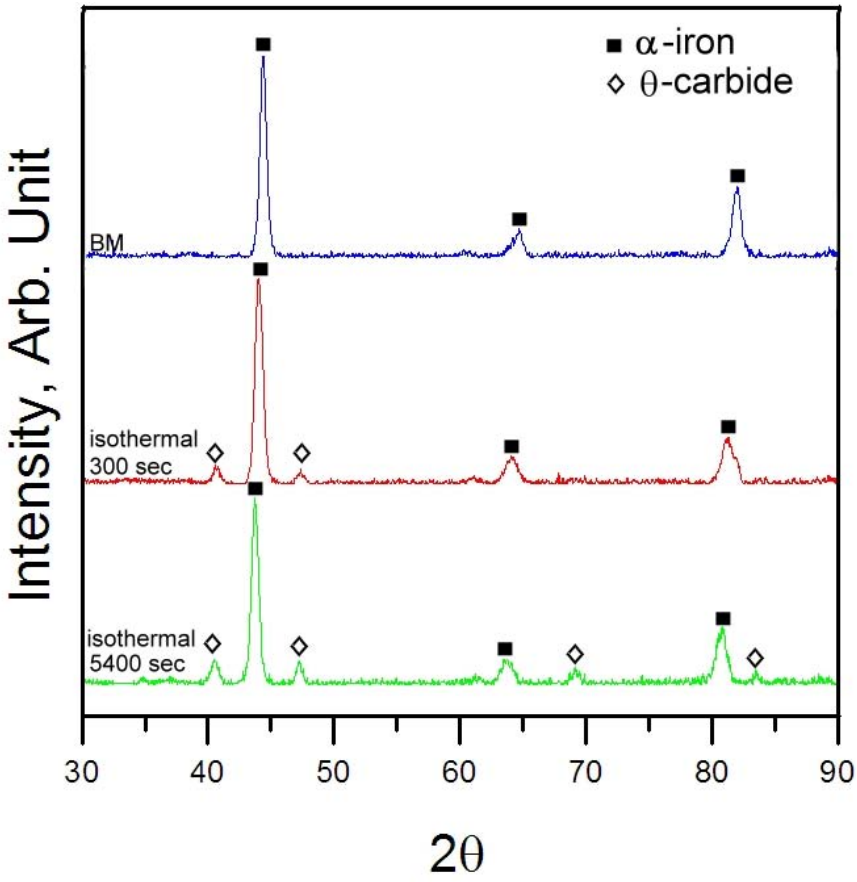

Figure 6.4 XRD patterns of $DP980_A$ steel obtained from the base metal (BM) and the isothermally tempered specimens at 650 °C for 300s and 5400s.

The peaks in the spectrum for BM specimen correspond to the body-centered-cubic (bcc) structure of the α-matrix. It may be noted that the Bragg angle of the peaks of α-matrix and α' phase in the dual-phase steel are very close making it difficult to separate them in the XRD patterns. In the isothermally treated specimen for 300s new peaks associated with the

precipitation of carbides were observed (Figure 6.4). Furthermore, a number of peaks were seen to evolve after prolonged holding time of 5400s, thus suggesting higher volume fraction of precipitated carbides (by approximately 30 pct.). The new peaks in the isothermally treated specimen at high temperature corresponded to those of typical iron carbide with orthorhombic crystal structure similar to that of cementite [148]. For effective comparison with non-isothermal tempering, isothermal tempering at longer holding time (5400s) was selected for further microstructural characterization.

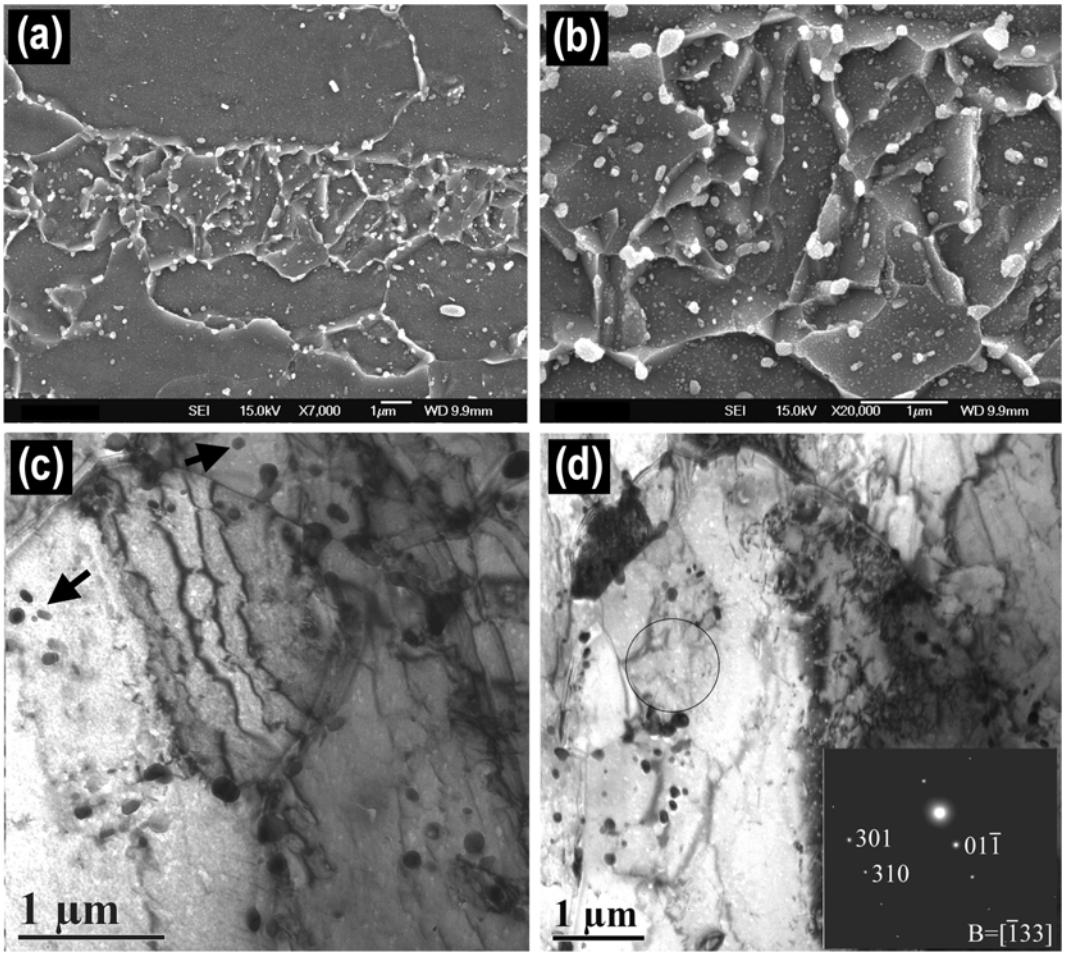

Figure 6.5 DP980$_A$ steel isothermally tempered specimen at 650°C for 5400s: SEM micrographs showing (a) decomposition of the prior α' phase; (b) precipitated carbides predominantly located at the grain boundaries, TEM observations at two tilt angles showing (c) carbide precipitation within the tempered structure, (d) recovery of the lath boundaries. Inset SAD pattern in (d) indicates bcc structure (α) of tempered matrix.

Figure 6.5 depicts SEM and TEM micrographs of the DP980$_A$ specimen isothermally tempered for 5400s. The banded morphology of the parent α' phase (Figure 6.1a) is still remained as depicted in Figure 6.5a. However, a severely decomposed or broken appearance typical of tempered martensite was observed, compared to the BM morphology (Figure 6.1a),

containing high density of precipitated carbides which are uniformly distributed within the tempered martensite regions. Furthermore, from high magnification SEM image (Figure 6.5b) it appears that larger carbides are located predominatly at high angle boundaries in tempered martensite *i.e.* between blocks of the prior α' phase and the prior γ grain boundaries, which was confirmed by TEM BF micrographs (Figure 6.5c-d) obtained at different tilt angles. However, it is interesting to note that density of dislocation density was extensively reduced in comparison to the BM (Figure 6.1c-d) and the prior lath boundaries were completely eliminated confirming complete recovery in $DP980_A$ steel during isothermal tempering at high temperature. The inset in Figure 6.5d illustrates the SAD pattern taken from the circled area (Figure 6.5d) that was indexed to contain spots from $[\bar{1}33]$ zone axis of bcc-Fe affirming the presence of ferrite in the tempered structure of $DP980_A$ steel. Another aspect of isothermal tempering was extensive reduction in the density of dislocation in comparison to the BM coupled with complete disappearance of the prior lath boundaries confirming complete recovery of isothermally tempered $DP980_A$ steel. However, evidence on recrystallization and formation of new grains was not observed as the original prior γ grain boundaries (martensite islands in Figure 6.1a-b) remained with the same banded morphology as depicted in Figure 6.5a-b.

Figure 6.6a delineates the TEM bright field micrograph of precipitated carbides located at the edge of an electropolished specimen of $DP980_A$ steel isothermally tempered at high temperature for 5400s. Such precipitates were utilized for further analysis of the crystal structure. Figure 6.6b depicts a high magnification image of one of such carbides. The SAD pattern taken from this particle (circled region in Figure 6.6b) is illustrated in Figure 6.6c which shows diffraction spots from $[010]$ zone axis of orthorhombic cementite (θ). Thus it is confirmed that the carbides formed during isothermal tempering of $DP980_A$ steel are cementite (θ) matching well with XRD result. The dark field image of the θ -carbide illustrated in Figure 6.6d was taken using (200) reflection in Figure 6.6c, which further confirms that the carbides observed are cementite.

Given that $DP980_A$ steel is characterized by the presence of low-carbon lath martensite phase as described in previous section. Based on this observation, it is interesting to note that the tempered structure of the martensite phase in $DP980_A$ steel (Figure 6.5) is similar to the tempered structure of the low-carbon martensitic steels that were subjected to isothermal

tempering at high temperature [146,149]. For instance, tempering of martensite at high temperature in low-carbon lath martensitic steel is characterized by coarsening and spheroidization of cementite mainly located at grain boundaries as well as extensive recovery of the lath structure and formation of elongated or equi-axed ferrite grains [104,107].

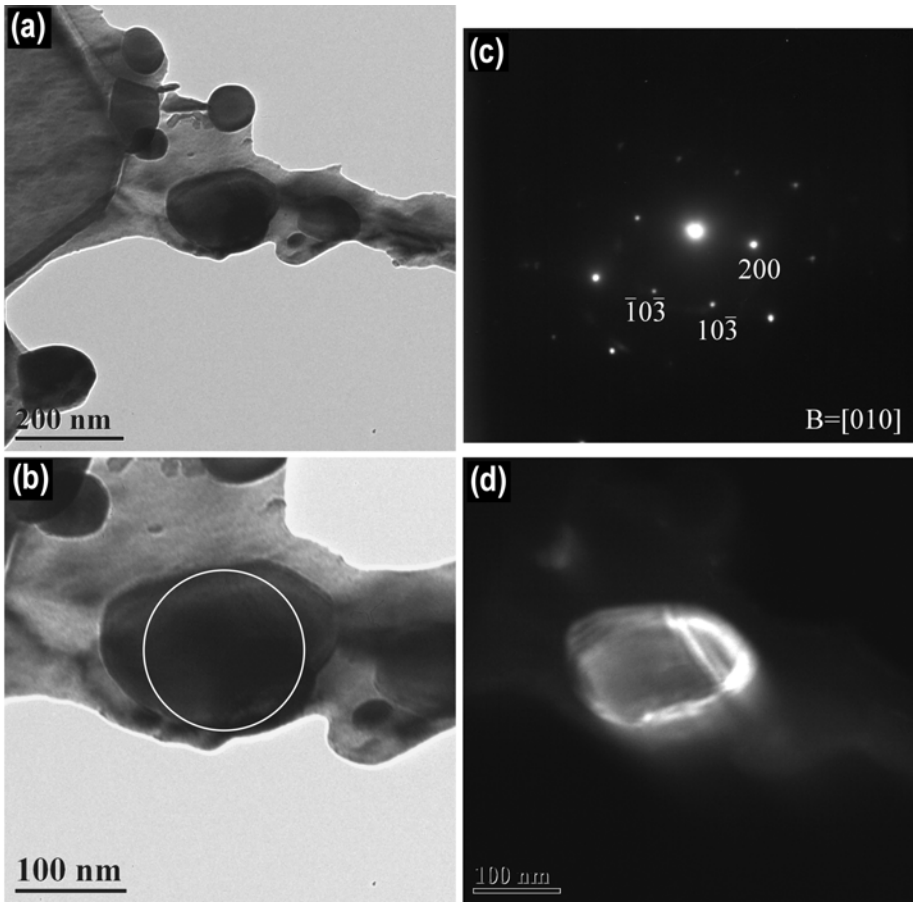

Figure 6.6 $DP980_A$ steel isothermally tempered at 650°C for 5400s illustrating: (a) carbide precipitation, (b) high magnification image of the precipitated carbide, (c) SAD pattern confirming orthorhombic structure of cementite (θ), (d) DF imaging taken using (200) reflection of θ–carbide.

From the above mentioned observation on location of θ-carbide precipitation in tempered martensite region, it can be concluded that precipitation of θ-carbides in $DP980_A$ steel is inherited from diffusion of interstitial carbon atoms to lattice defects (*i.e.* dislocations, lath boundaries: precipitation within martensite matrix) and to high angle boundaries *viz.* block and prior γ boundaries. This assumption has been previously documented based on observations and measurements of segregated carbon to lattice defects in low-carbon martensite in Fe-C martensitic steels during the early stages of tempering [146,149] and further precipitation and coarsening of cementite in these locations at higher temperature [149]. Therefore, the

precipitation of carbides in the tempered martensite of $DP980_A$ steel observed at grain boundaries *i.e.*, blocks and prior γ boundaries (Figure 6.5) further confirms that segregation of carbon to lattice defects plays an important role on the formation and coarsening of the θ-carbides. On the other hand, it has been established that the recovery process is associated either with the migration of dislocation cells and grain boundaries with relatively low density of dislocations (laths) towards grain boundaries with higher density of dislocations (blocks and prior γ grain boundaries) [150,151] or by complete disintegration of the laths during boundary migration [104]. Thus, it is concluded that the complete recovery of the lath boundaries observed in the tempered martensite substructure of $DP980_A$ steel (Figure 6.5c-d) is associated with migration or disintegration of the prior lath boundaries.

6.3. Non-isothermal tempering at high temperature

6.3.1. Characteristics of carbide precipitation

Microstructural changes and precipitation of carbides occurring during non-isothermal tempering at high temperature (Figure 3.8) of the martensite phase in $DP980_A$ steel is illustrated by SEM and TEM micrographs in Figure 6.7. The SEM micrograph in Figure 6.7a clearly depicts the α-matrix (dark regions) along with the decomposed α' phase (tempered martensite). The broken lathy morphology; a clear evidence of the tempered martensite (TM) structure, is well contrasted with the solid smooth featureless morphology of α'-phase in the base metal (Figure 6.7a). By comparing the high magnification SEM images of BM (Figure 6.1b) and the non-isothermally tempered structure (Figure 6.7b); fine decorations of sub-micron particles (white) were delineated along the high angle boundaries (block and prior γ) and the low angle boundaries (interlath) of the TM matrix unlike the finding of sub-micron particles only along high angle boundaries in isothermally TM (Figure 6.5b). In addition, a random distribution of smaller rounded particles (white) also appeared within the martensite block structure. TEM bright field micrographs obtained from non-isothermally tempered $DP980_A$ steel at two different tilt angles (Figure 6.7c-d) confirmed that the lath morphology of the prior α' phase still remained within the TM region and also the prior austenite grain boundaries. However, precipitation of carbides was clearly observed within the TM structure as indicated by the arrows in Figure 6.7c-d.

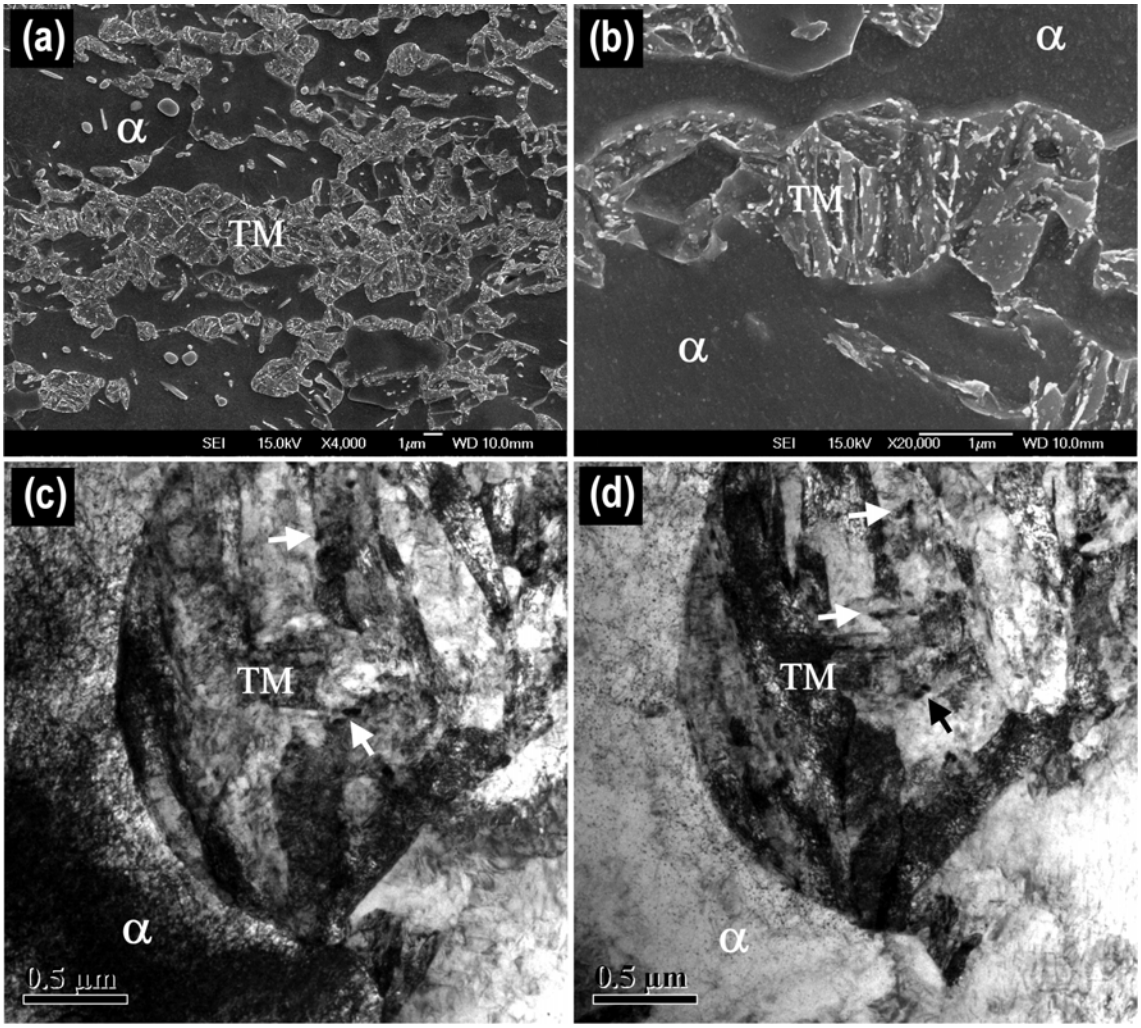

Figure 6.7 SEM and TEM observations of non-isothermally tempered martensite (TM) in DP980$_A$ steel: (a) overall view, (b) details of the tempered martensite (TM), and BF images at two different tilt angles (c) and (d) showing carbide precipitation indicated by arrows.

The distribution of the precipitated carbides within the TM region is depicted in the BF image in Figure 6.8a. Figure 6.8b illustrates the carbides finely distributed along the prior α' lath boundaries and also within the TM region. A close and detailed view at high magnification image (Figure 6.8c), shows that formation of carbides took place also within the lath structure having irregular morphology with an approximate size of 40 to 60 nm (Figure 6.8d). The carbides that precipitated along the lath boundaries have plate-like morphology and are larger in size compared to those that formed within the laths in the TM region.

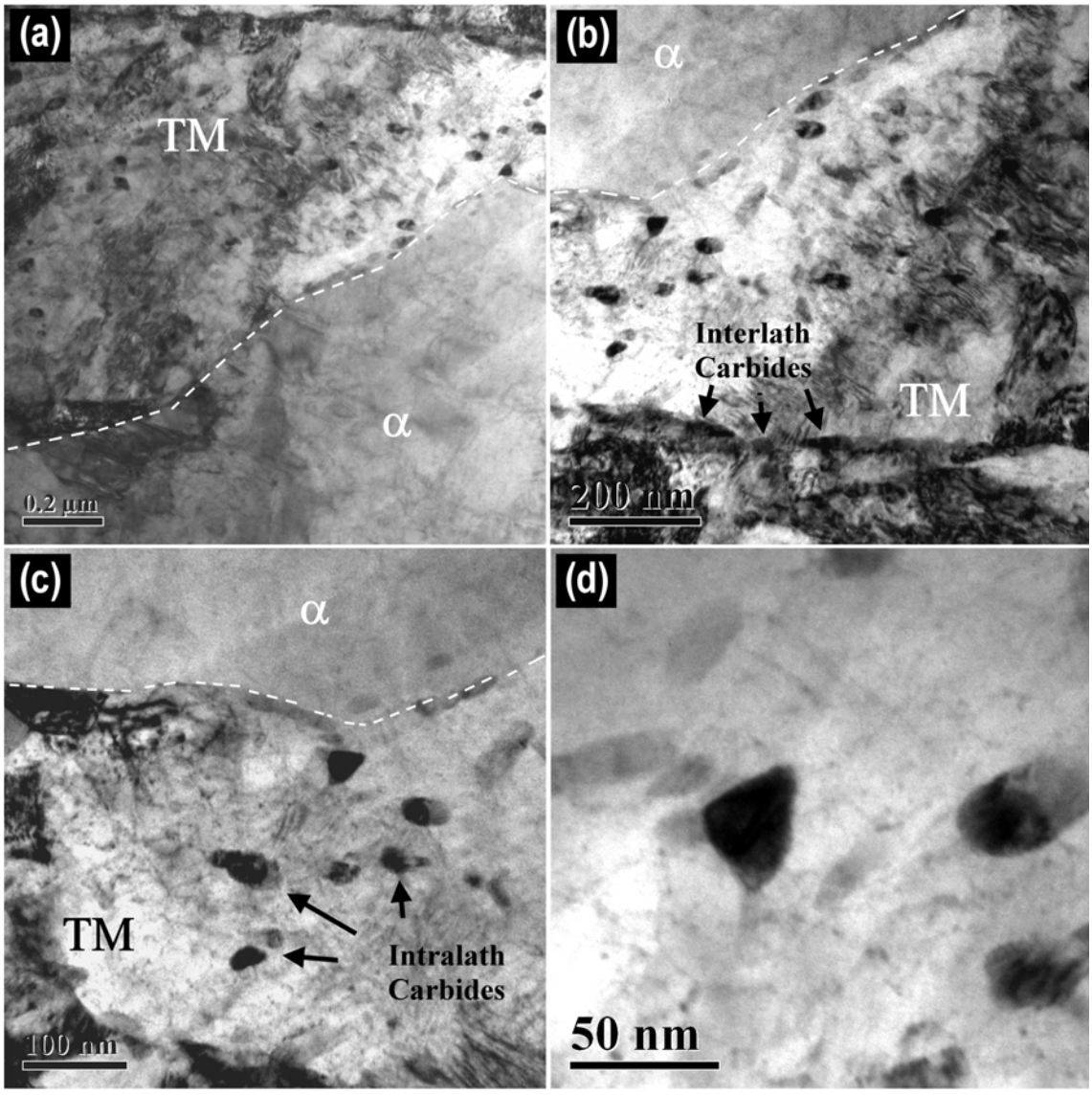

Figure 6.8 BF imaging of the TM substructure (650°C) showing: (a) overview of the α-TM interface, (b) inter-lath carbide precipitation and (c) detailed observation of the precipitated intra-lath carbides, (d) high magnification showing carbide morphology.

The comparison of carbide precipitation behaviour of isothermally and non-isothermally tempered $DP980_A$ steel indicates that a clear difference on the distribution and the morphology of the precipitated carbides exists between the respective TM structures formed at high temperature. Table 6-1 compares the particle size distributions in different regions in the TM structure obtained after isothermal and non-isothermal tempering of $DP980_A$ steel. For instance; coarser spheroidized carbides (~ 200 nm) distributed mainly along high angle boundaries (block and prior austenite grain boundaries) in the isothermally tempered specimen (Figure 6.5) contrast well with the finer carbides at high-angle boundaries (~ 70 nm) in the non-isothermally

tempered specimen. Moreover, the quasi-spherical carbides (~ 44 nm) formed within laths and the plate-like interlath carbides (~ 48 nm) in the non-isothermally tempered matrix (Figure 6.7) contrast the coarser carbides formed within the blocks in the isothermally tempered specimen. It may be noted that the white particles observed in the high magnification SEM image in both tempering conditions (Figure 6.5b and Figure 6.7b) actually correspond to distribution and morphology of the carbides observed in TEM images (Figure 6.6 and Figure 6.8). The precipitation of carbides at interlath boundaries (Figure 6.7b) clearly delineates the lath structure in the non-isothermally tempered martensite. Another aspect of non-isothermally TM structure was the sufficient growth of carbide which made it easy to resolve the individual carbide particles by SEM but at higher magnification (Figure 6.7b). Furthermore, comparing the α' phase lath structure in BM (Figure 6.2) with the non-isothermally tempered martensite structure (Figure 6.8) it can be seen that considerable reduction in dislocation density was accomplished at the location where a larger volume fraction of carbides precipitated (Figure 6.8b).

Table 6-1 Averaged radius of the θ-carbide in tempering of DP980$_A$ steel

Tempering Condition	*DP980$_A$ θ-carbide radius (nm)*			
	Dislocations	*Low-angle boundary*	*High-angle boundary*	
	Within Block		*Block boundary*	*Prior Asutenite Grain Boundary*
Isothermal (5400s)	113 ± 37		214 ± 73	201 ± 73
Non-isothermal	Intra-lath	Inter-lath	73 ± 35	66 ± 25
	44 ± 15	48 ± 20		

A TEM bright field micrograph representing typical low-magnification image of carbon replica of DP980$_A$ steel containing fine carbides and obtained after non-isothermal tempering, is illustrated in Figure 6.9a. The high magnification image of DP980$_A$ replica illustrated in Figure 6.9b confirmed the quasi-spherical morphology of the precipitated carbides observed within the bulk specimen (Figure 6.8d). The indexing of the SAD pattern obtained from the particle shown in Figure 6.9b indicates that the carbide formed during non-isothermal tempering of DP980$_A$ steel corresponds to an orthorhombic crystal structure of cementite (θ) with diffraction spots

from [010] zone axis of cementite (Figure 6.9c) [151]. The dark field image shown in Figure 6.9d was taken using the (101) reflection of cementite in Figure 6.9c, which confirms further the particle to be cementite carbide (θ). The averaged radius of the θ-carbides observed in replicas of $DP980_A$ steel was measured to be approximately 50±11 nm (that matches with the average carbide size observed in intra-lath region of TM structure in Table 6-1), which contrasts well with the coarser θ-carbides observed upon isothermal tempering at 650°C for 5400s; the average sizes of the θ-carbides are listed in Table 6-1. In comparison, refinement of cementite has been also reported when using rapid heating rates by induction tempering in fully martensitic steels [109,110] which has been attributed to the fact that the temperature at which cementite precipitation starts is raised by increasing the heating rate to tempering temperature resulting in a higher nucleation rate and thus finer dispersion of cementite.

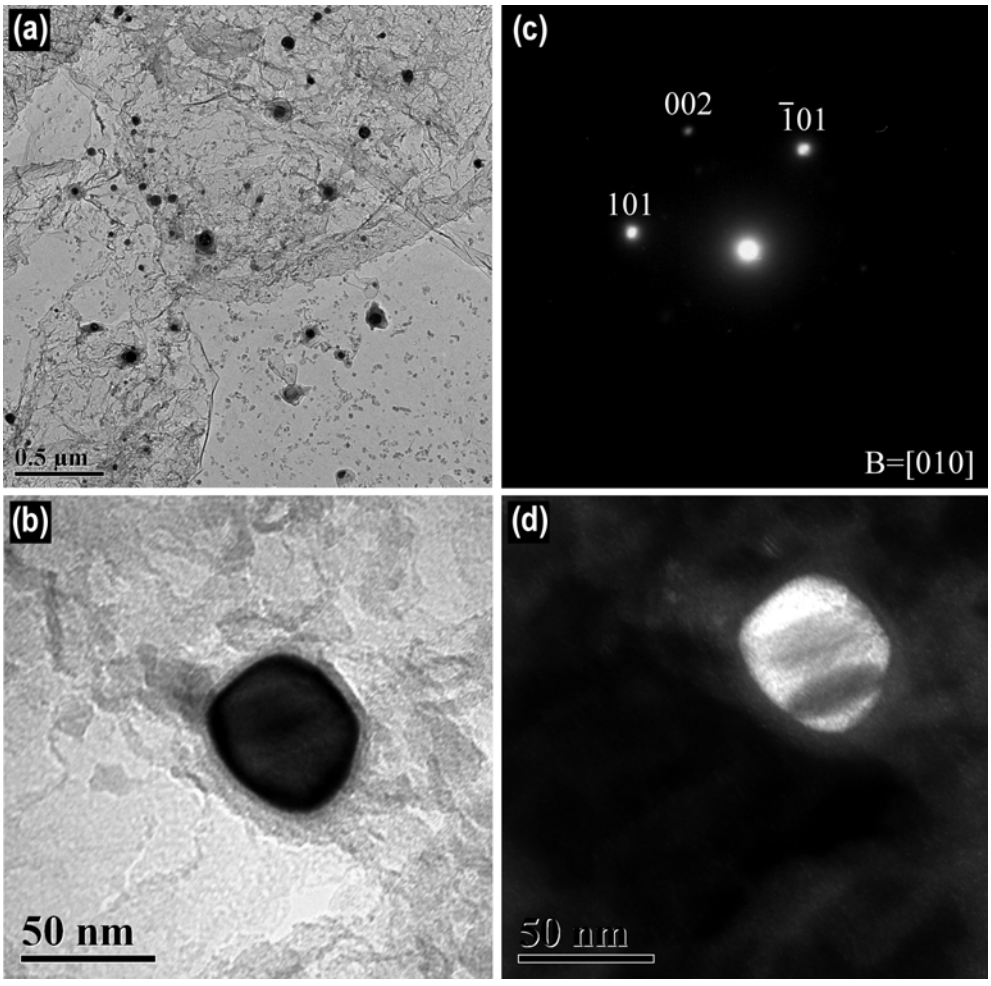

Figure 6.9 TEM images of non-isothermally tempered $DP980_A$ steel showing: (a) extracted replicas containing carbides, (b) quasi-spherical morphology of single carbide, (c) SAD pattern showing orthorhombic structure of carbide, and (d) dark field image taken using (101) reflection of cementite (θ).

The size of the carbides observed during a tempering process solely depends on the diffusion of carbon and other alloying elements [110,111] which in turn depends on the holding time at the high tempering temperature. Hence, to figure out the effect of carbon diffusion on the size difference of the carbides observed during isothermal and non-isothermal tempering of the $DP980_A$ steel, diffusion distance at holding time was calculated for the $DP980_A$ steel using the following equation:

$$x = \sqrt{Dt} \qquad \textbf{equation 6-1}$$

where x is the diffusion distance of carbon after t (holding time in s), and D is the diffusion co-efficient of carbon in bcc-Fe (ferrite) which was calculated at particular temperatures (T in K) given by equation (equation 6-2) below:

$$D = D_0 \exp\left(-\frac{Q}{RT}\right) \qquad \textbf{equation 6-2}$$

where D_0 is the diffusion volume coefficient of carbon in ferrite at infinite time and its value is 6.2 x 10^{-7} m^2/s, Q is activation energy (80000 J/mol) and R is universal constant (8.31 J/mol-K) [152].

The diffusion distances calculated using these equations (equation 6-1) and (equation 6-2) for the different holding times at high temperature are tabulated in Table 6-2. It is to be noted that the holding time in the non-isothermal condition was considered the time required to reach peak temperature during heating (Figure 3.8). It is clearly seen that diffusion distance of carbon in non-isothermal tempering is very low (~ 705 nm) compared to that in isothermal holding (~ 300 μm) which explains clearly the finer size of cementite in the non-isothermally tempered.

Table 6-2 Diffusion distance of carbon at different holding time at high tempering temperature

Tempering condition	***Holding time (s)***	***Diffusion distance of carbon x at holding time (m)***
Non-isothermal	0.5	7.05622E-07
Isothermal	300	6.99985E-05
	5400	0.000298696

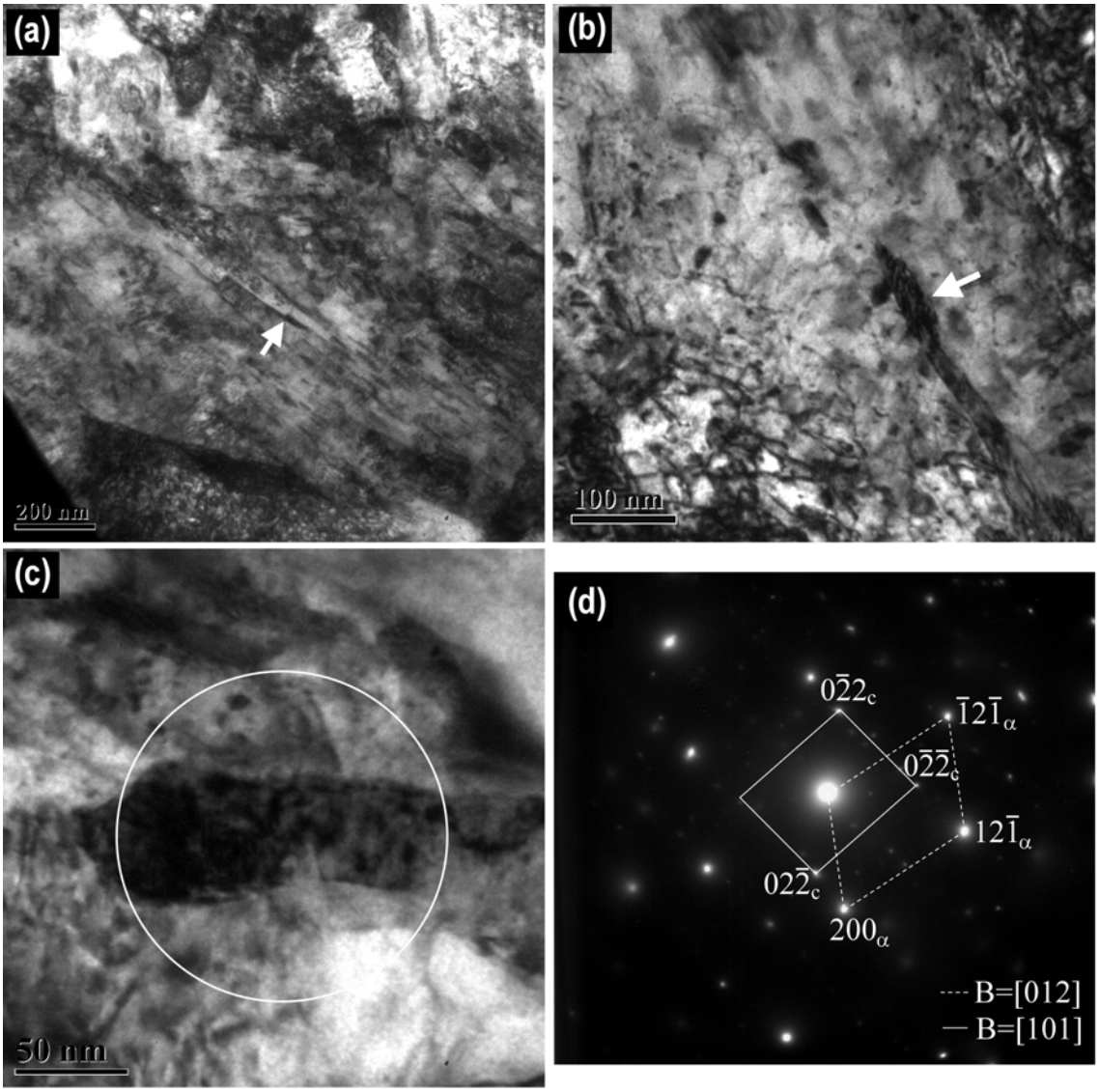

Figure 6.10 BF image showing: (a) cementite along the lath boundaries, (b) detailed morphology of intralath cementite, and (c) high magnification image of (b), and (d) the diffraction pattern of (c) confirming orthorhombic cementite.

Besides the above mentioned formation of fine θ-carbides during non-isothermal tempering; another interesting aspect of non-isothermal tempering at high temperature was observation of a small fraction of elongated carbides at the interlath boundaries as marked by arrows in Figure 6.10a-b. Figure 6.10c illustrates such elongated carbide at higher magnification. The SAD pattern shown in Figure 6.10d was taken from the circled region in Figure 6.10c and shows the composite diffraction pattern with spots from both the carbide (c) and the matrix (α), indicating that the elongated carbides observed are cementite having an orientation relationship $[012]_\alpha//[101]_c$ with the ferrite matrix. Elongated cementite observed in

the non-isothermally tempered (Figure 6.10) structure at high temperature is correlated to the presence of interlath retained austenite within the parent α' phase (Figure 6.3) in the BM microstructure which transforms during non-isothermal tempering to form cementite. In contrast to the above observation in the non-isothermally tempered specimen (Figure 6.10); interlath elongated cementite was not seen in the isothermally tempered $DP980_A$ steel (Figure 6.5) at high temperature.

6.3.2. Partial recovery of martensite laths

Interestingly, apart from cementite precipitation, partial recovery of the martensite lath structure was also seen after the non-isothermal tempering of $DP980_A$ steel at high temperature (Figure 6.11). Figure 6.11a shows a recovered region within the non-isothermally tempered structure (the recovered periphery has been depicted by white dashed lines); this region illustrates a typical recovered morphology characterized by a low density of dislocations which is well contrasted to the surrounded structure [106].

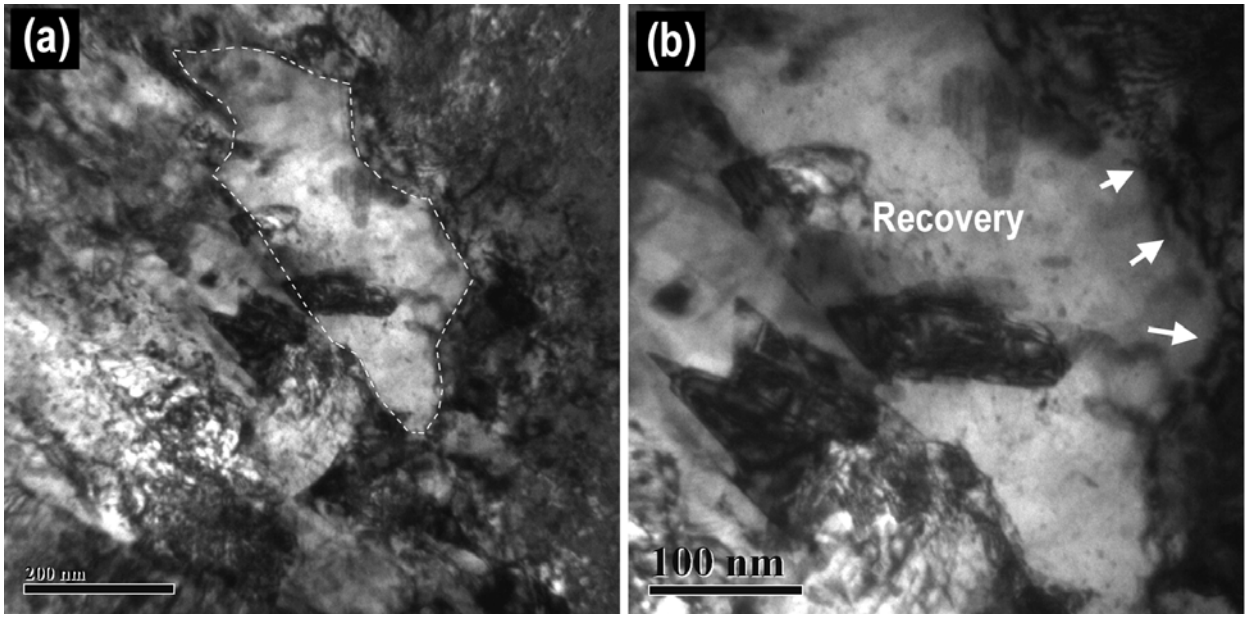

Figure 6.11 Partial recovery of the lath substructure in non-isothermally tempering of $DP980_A$ steel: (a) overview, (b) high magnification image of the recovered region in (a).

Detailed observation in Figure 6.11b shows that some of the lath boundaries from the prior α' phase (pointed by arrows) have possibly started to pull away and migrate towards the high-angle boundaries *i.e.* block boundaries. However, this lath boundary migration seems to have been delayed due to short time available during non-isothermal tempering of $DP980_A$ steel.

Partial recovery of the lath substructure in the non-isothermally tempered martensite is well contrasted to the complete recovery of lath structure in the tempered martensite subjected to isothermal tempering at high temperature longer holding time (5400s). There are two important factors that influence the kinetics of recovery of the lath structure during isothermal tempering of martensitic steel: first; the precipitated carbides inhibit the disintegration or migration of the lath boundaries (pinning effect) [104] and secondly the recovery of the lath structure develops gradually with time [106]. Hence, it is concluded that during non-isothermal tempering of martensite in $DP980_A$ steel, the possibility of lath boundary disintegration or migration to packet boundaries is greatly reduced as shown in Figure 6.11 due to fine carbide precipitation (Figure 6.8 to Figure 6.10) and lack of sufficient time available for the recovery process which was not the case in isothermal tempering at high temperature. Furthermore, the morphology of the precipitated carbides plays an important role in the recovery process; plate-like carbides along lath boundaries delayed the recovery process in non-isothermally tempered $DP980_A$ steel by impeding the movement of dislocations by a pinning effect.

The above observations about the tempered martensite phase in $DP980_A$ steel developed during non-isothermal tempering at high temperature indicate that: (1) precipitation of carbides (intralath and interlath) occurs at a faster rate despite the very short holding time at peak temperature; quasi-spherical carbides are seen within laths whereas coarser interlath carbides adopt a plate-like morphology, (2) decomposition of small amounts of interlath retained austenite into cementite retains an elongated morphology at high temperature, and (3) partial recovery of the martensite lath structure occurs owing to the reduced possibility of lath boundary migration or disintegration. It is interesting to note, that the various tempering reactions which take place during the conventional high temperature (third stage) tempering of martensite are easily delayed in case of non-isothermal tempering at high temperature *i.e.*, coarsening and spheroidization of the precipitated carbides, and the recovery of the lath substructure which is consistent with earlier reports on low-carbon martensitic steel [109-111].

It has been reported earlier [30] that the coarsening kinetics of θ-carbide are a volume-diffusion controlled process; and this coarsening is predominantly controlled by the diffusion of C within the lattice defects *i.e.* along dislocations and grain boundaries. So, it is concluded that the delaying of the coarsening and spheroidization of cementite during non-isothermal tempering of $DP980_A$ steel is related to insufficient time being available for diffusion of

interstitial carbon as indicated by the calculated diffusion distance (Table 6-2). In comparison, the spheroidization process of cementite has also been delayed during rapid heating by induction heating of martensitic steel [111] though that was also attributed to effects of the magnetic field. However, it is believed that such delaying is mainly influenced by the reduced time for diffusion of carbon. On the other hand, it has been claimed that the morphology of the precipitated carbides plays an important role in suppressing the recovery of martensite; this indicates that plate-like carbides that form along the lath boundaries (Figure 6.8b) impede the movement of dislocations by a pinning effect [151] thus delaying the recovery process in non-isothermal tempered structures of $DP980_A$ steel. The precipitation and growth mechanism of carbides during isothermal and non-isothermal tempering of $DP980_A$ steel can be illustrated by the schematic as depicted in Figure 6.12 which also shows the recovery process in both the tempering processes.

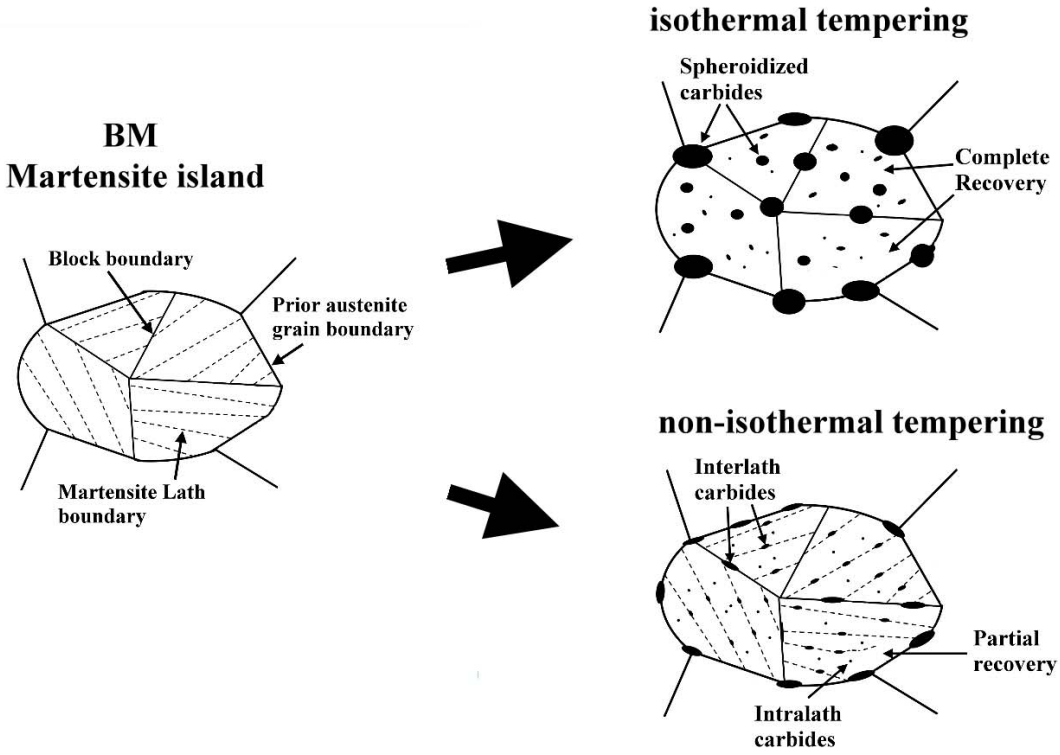

Figure 6.12 Schematic illustration comparing the changes in the substructure of the martensite island in DP steel upon isothermal and non-isothermal tempering.

6.4. Effects of DP steel chemistry on tempering

The BM microstructure of three different DP steels *viz.* $DP980_B$, $DP980_A$ and DP800

(Table 3-1) are illustrated by the SEM and TEM micrographs represented in Figure 6.13. The ferrite matrix (α) and martensite (α') of $DP980_B$, $DP980_A$ and DP800 are clearly illustrated in the SEM micrographs in Figure 6.13a, Figure 6.13b and Figure 6.13c, respectively. Significant differences in the morphology of the α' phase were clearly seen in all three DP steels.

For example, the blocks of the α' phase are finely delineated in $DP980_B$ steel (Figure 6.13a), whereas a solid featureless morphology of the α' phase was observed in $DP980_A$ and DP800 steels (Figure 6.13b-c). In addition, by comparing Figure 6.13a through Figure 6.13c; larger grain size of the α' phase may be seen in the $DP980_B$ whereas smaller grain size was observed in $DP980_A$ steel followed by DP800 steel. TEM bright field micrographs showing the α' phase in $DP980_B$, $DP980_A$ and DP800 steels and their corresponding SAD patterns in the inset images are illustrated in Figure 6.13d, Figure 6.13e and Figure 6.13f, respectively. In Figure 6.13d, coarse lath morphology is clearly shown within the α' phase in $DP980_B$ steel, such martensite block is composed of relatively larger lath grains in comparison to that of the $DP980_A$ steel (Figure 6.13e). The inset images of the SAD patterns correspond to $[011]_{\alpha'}$ and $[\bar{1}11]_{\alpha'}$ zone axes of martensite in $DP980_B$ and $DP980_A$ steels, respectively. Interestingly, a mixed morphology of lath and plates of twinned martensite was observed within the α' phase in DP800 steel (Figure 6.13f). The SAD pattern was indexed to contain spots from $[011]_{\alpha'}$ zone axis of the α' matrix along with strong streaks of $\left(\frac{2}{3}\frac{\bar{5}}{3}\frac{5}{3}\right)$ twin reflections confirming the martensite twin structure in DP800 steel. The martensite carbon content was low for $DP980_B$ (0.27 wt.%) and $DP980_A$ steels (0.275 wt.%), and these steels were comprised of lath martensite which is the typical morphology observed in of low-carbon (< 0.3 wt.%) martensitic steel [22]. On the other hand, a mixture of lath and twinned morphologies was observed in DP800; in this steel the calculated martensite carbon content is 0.367, thus promoting twinned structure. In fact, twinned martensite is associated to medium- and high-carbon martensite [22].

Figure 6.14 illustrates SEM micrographs of tempered martensite and bright field images of carbides obtained by carbon extraction replicas from all the DP steels subjected to non-isothermal tempering at high temperature.

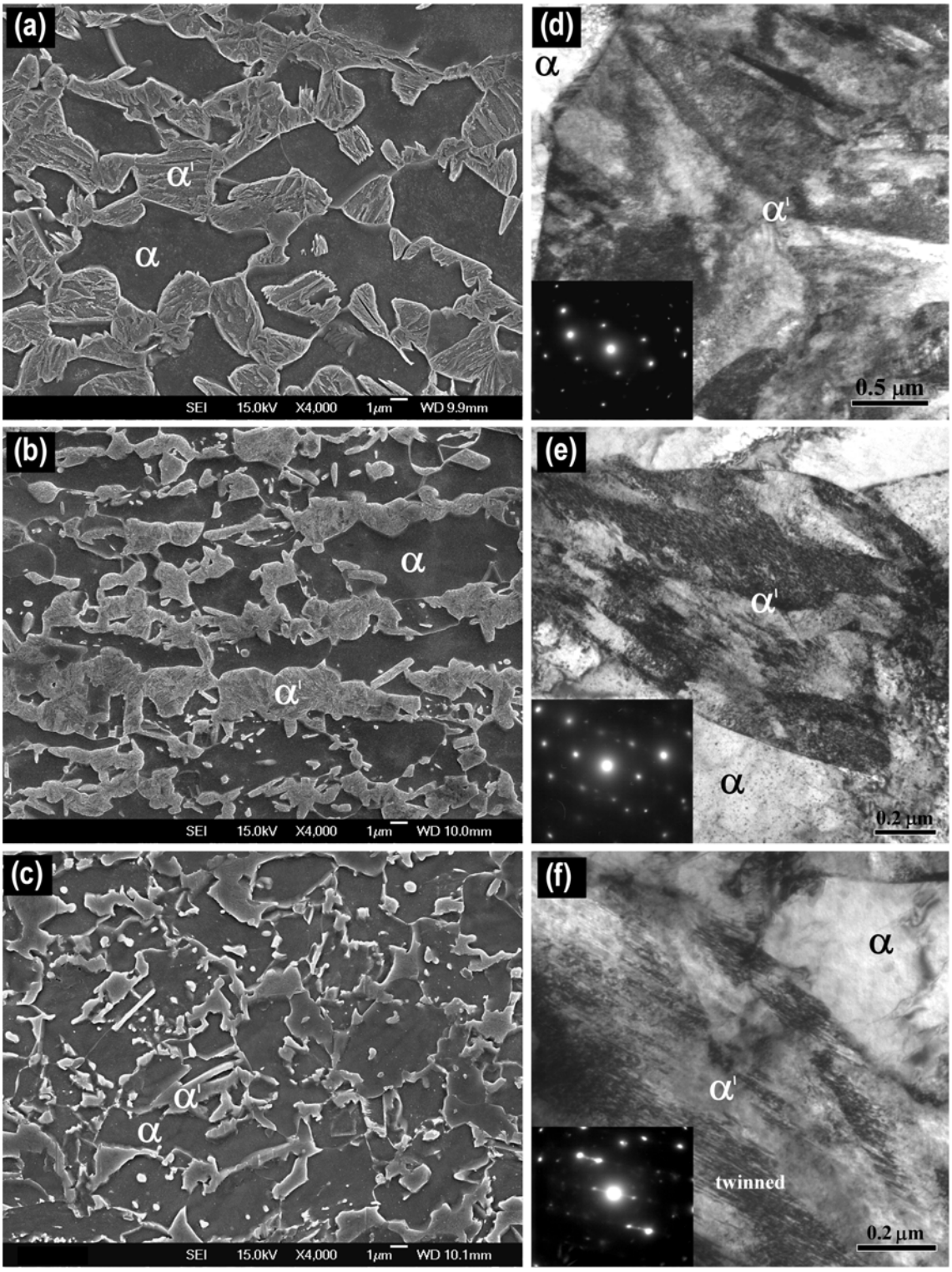

Figure 6.13 SEM micrographs showing non-isothermally tempered martensite in (a) $DP980_B$, (b) $DP980_A$ and (c) DP800. Extracted carbides and corresponding SAD pattern in the inset image confirming $[010]_\theta$ zone axis of cementite from (d) $DP980_B$, (e) $DP980_A$ and (f) DP800 steels, respectively.

SEM micrographs of the tempered matrix in $DP980_B$, $DP980_A$ and DP800 steels are given in Figure 6.14a-c, respectively. By comparing the appearance of the tempered matrix in all the steels; the martensite laths of $DP980_B$ steel is seen severely decomposed (Figure 6.14a), followed by the broken lathy appearance in $DP980_A$ (Figure 6.14b) and DP800 (Figure 6.14c) steels. Even though carbide precipitation is observed thoroughly distributed in all steels; coarser carbides are observed in $DP980_B$ steel, thus contrasting the finer carbides in DP800 steel.

Based on the morphologies of the non-isothermally tempered DP steels discussed above, it may be concluded that the apparent smaller carbides seen in DP800 steel (Figure 6.14c) are associated with the higher carbon content and the twinned substructure of the prior martensite phase (Figure 6.13f). Hence it is seen that martensite phase of the DP steels adopt the similar morphologies as conventional martensitic steel with similar carbon contents. Hence, the tempering behaviour (both isothermal and non-isothermal) of the martensite phase in DP steel is concluded to be similar to that of martensitic steel with similar carbon content, which has also been reported earlier [37].

Representative images of carbides obtained by extraction replicas of $DP980_B$, $DP980_A$ and DP800 steels subjected to non-isothermal tempering at high temperature are illustrated in Figure 6.14d-f, respectively. As shown in the SEM micrographs, the size of the carbides were observed to decrease in the order $DP980_B$(300 nm)→$DP980_A$(50 nm)→DP800(40 nm). The corresponding inset SAD patterns show spots from $[010]_\theta$ zone axes of carbides; confirming the orthorhombic crystal structure of cementite (θ) in all non-isothermally tempered DP steels.

Figure 6.15a shows a dark field image of the θ-carbide obtained from $DP980_A$ steel non-isothermally tempered at high temperature. Typical EELS spectrum plotted in Figure 6.15b indicates peaks of substitutional elements *viz.* Fe, Mn and Cr. Quantification made using Digitalmicrograph ™ software of substitutionals, suggested relatively larger concentration of Fe (*i.e.*, 80 pct.) followed by Mn (*i.e.*, 16 pct) and Cr (*i.e.*, 4 pct) within the θ-carbide obtained in $DP980_A$ steel subjected to non-isothermal tempering at high temperature. Figure 6.15c illustrates the intensity profile of EELS made across the θ-carbide following the path of the electron beam as marked (labelled as spectrum image) in Figure 6.15a. The compositional distribution of substitutionals within the carbide seemed to be quite consistent (~ 25-75 nm) with Fe having high intensity profile confirming the EELS spectrum analysis.

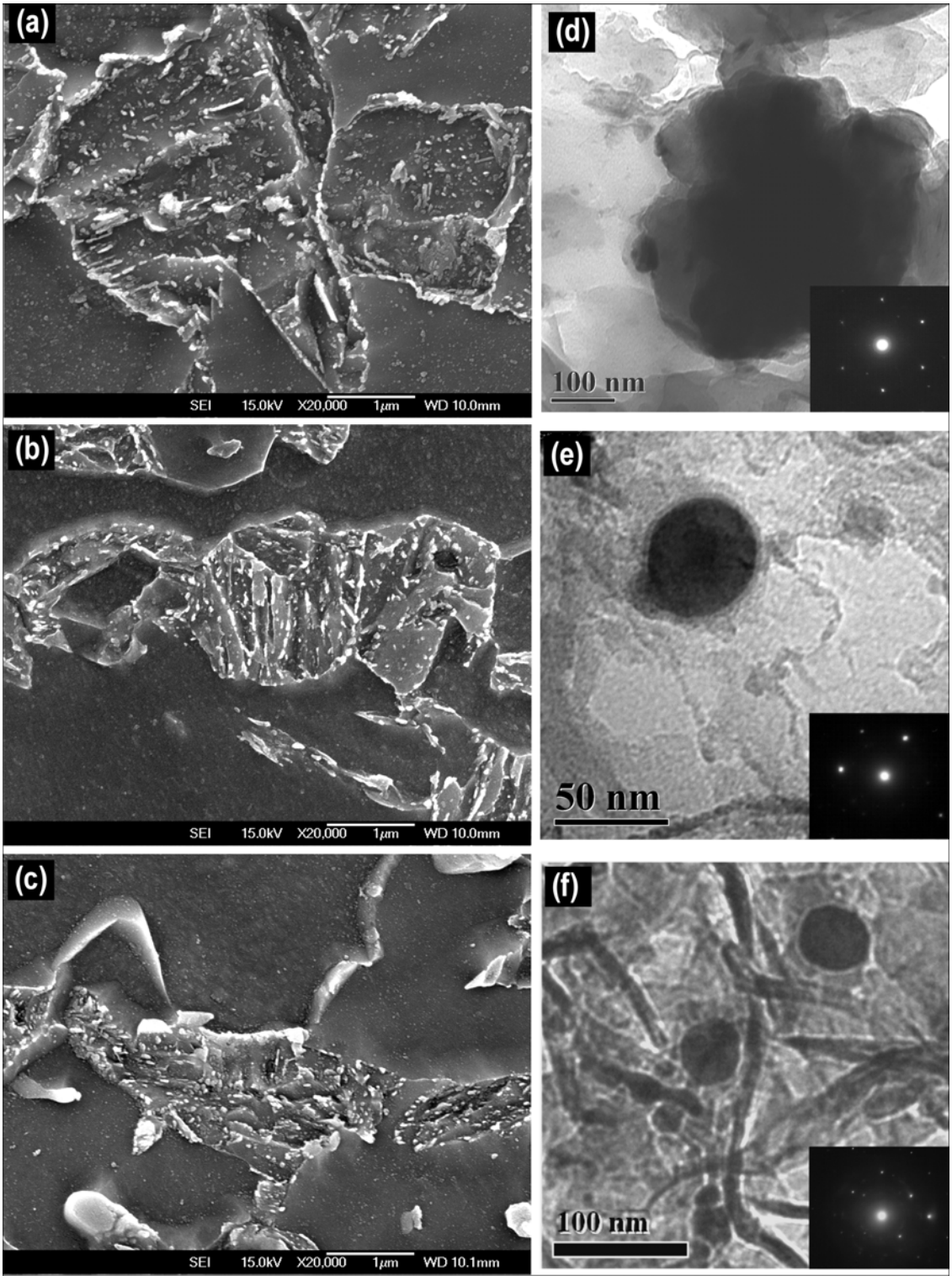

Figure 6.14 SEM micrographs showing non-isothermally tempered martensite in (a) $DP980_B$, (b) $DP980_A$ and (c) DP800. Extracted carbides and corresponding SAD pattern in the inset image confirming $[010]_\theta$ zone axis of cementite from (d) $DP980_B$, (e) $DP980_A$ and (f) DP800 steels, respectively.

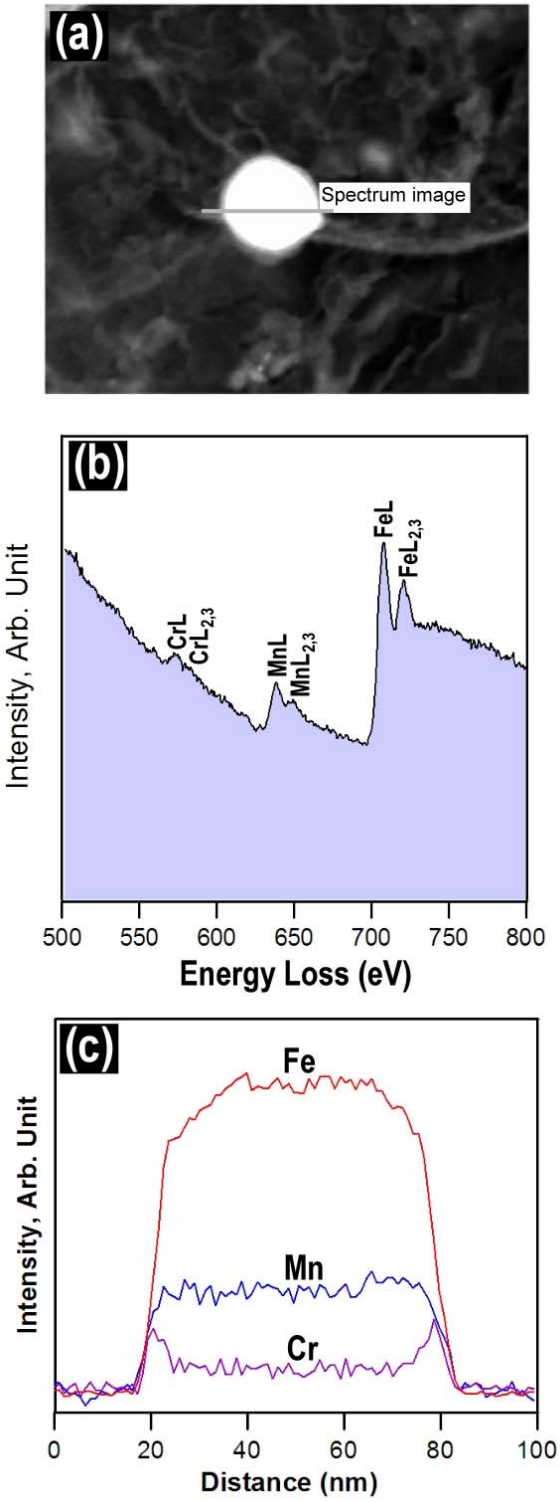

Figure 6.15 Electron energy loss spectroscopy analysis (EELS) of extracted carbides from DP980$_A$ steel: (a) DF image of the analyzed θ-carbide, (b) EELS spectrum indicating peaks of Fe, Mn and Cr, and (c) EELS profile obtained from beam scanning across the θ-carbide as depicted in the DF image in (a).

Energy dispersive X-ray (EDX) spectra of the extracted θ-carbides of non-isothermally

tempered $DP980_B$, $DP980_A$ and DP800 steels, represented in Figure 6.16; show characteristic peaks of Fe in the $DP980_B$ specimen. However, in addition to Fe peaks, substitutional Mn and Cr peaks were also seen in the spectra of the extracted θ-carbides from $DP980_A$ and DP800 steels. In support of the EELS result, the peak of Cr in the θ-carbides was less intense than of Mn in the case of $DP980_A$ specimen. In contrast, stronger peak of the substitutional Cr was observed in the case of the θ-carbides in DP800 specimen.

A summary of the relative percentage of substitutionals within the θ-carbides in $DP980_B$, $DP980_A$ and DP800 steels is listed in Table 6-3. From the above mentioned EELS and EDX analyses; it is clear that the θ-carbides inherited the chemistry from the parent bulk DP steel during non-isothermal tempering at high temperature. For example, high Cr and Mn content was measured in the θ-carbide of the DP800 specimen; thus carbides precipitated with richer chemistry; this in fact, is consistent with the bulk chemical composition of DP800 steel (*i.e.*, CE of 0.525) which has the richest chemistry among all the DP steels studied in this work (Table 3-1). The orthorhombic crystal structure confirmed from SAD patterns (Figure 6.14d-f) and the presence of Mn and Cr in the θ-carbide of the non-isothermally tempered DP steel; suggested that thermodynamically stable cementite adopting the stoichiometric form of M_3C (M=Fe, Mn, Cr) forms in this DP steel which is consistent with the earlier reports of many researchers [30,103,153,154]. For example in the present study, during non-isothermal tempering at high temperature in DP800 steel, cementite carbide adopts a stoichiometric form of $(Fe_{0.7}Mn_{0.12}Cr_{0.18})_3C$ as confirmed from the EELS and EDX analyses.

Table 6-3 Relative pct. of three substitutional elements contained within the non-isothermally precipitated θ-carbide by EDX analysis.

Steel	***Fe (%)***	***Mn (%)***	***Cr (%)***
$DP980_B$	99	1	--
$DP980_A$	74	20	6
DP800	70	12	18

It is reported that some alloying elements are concentrated in cementite (Cr, Mn) or in the interface of cementite and ferrite (Si) and the growth-rate of cementite particles is controlled by their diffusion thus reducing cementite coarsening [110]. There are extensive reports in literature regarding the experimental and theoretical composition of cementite with substitutional elements (*i.e.*, Fe, Mn and Cr) in isothermally tempered martensitic steels

[30,102,103,155]. However, most of the studies have utilized EDX analysis of cementite in extraction replicas; and these reports agreed that the partitioning of substitutionals between cementite and matrix is negligible in the range of temperatures between that of precipitation of cementite (*i.e.*, 350°C) and up to approximately 550°C, thus confirming the para-equilibrium state of the precipitated cementite in which diffusion of carbon dominates [30, 102,103,98].

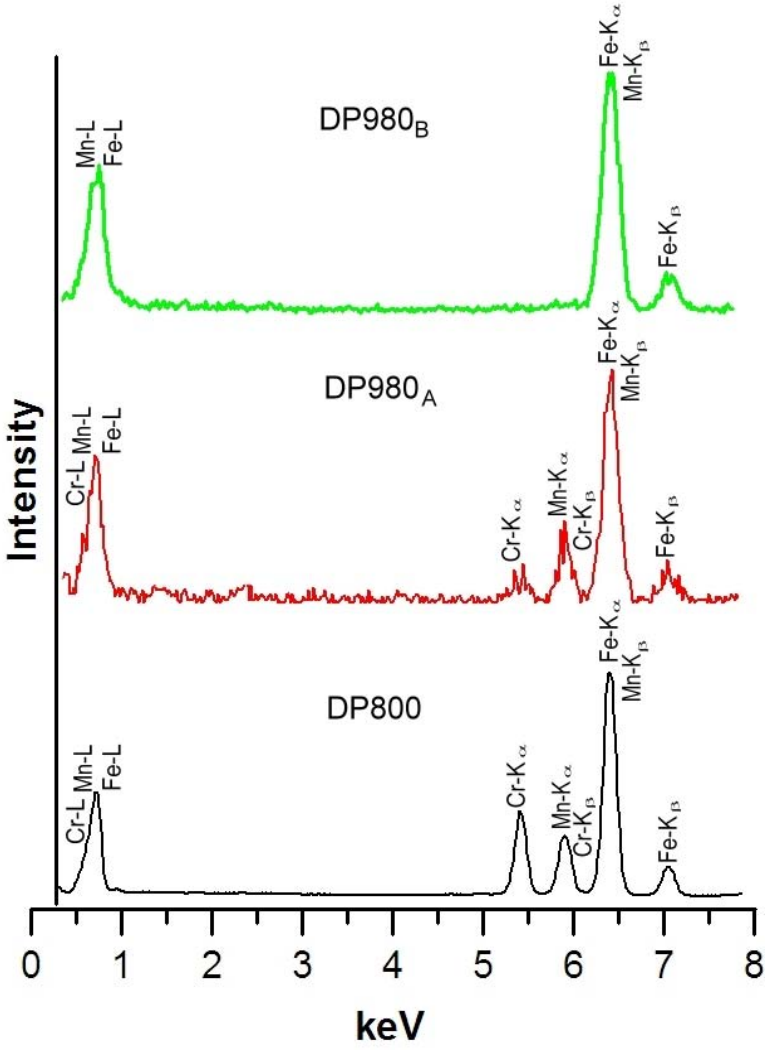

Figure 6.16 EDS X-ray spectra collected from the extracted θ-carbides in non-isothermally tempered $DP980_B$, $DP980_A$ and DP800 specimens.

Thomson and Miller [103] observed that with further increase in isothermal tempering (450°C for 187h) substitutitonals Cr and Mn enrich into cementite. At even higher isothermal tempering temperature (*i.e.*, 650°C), the concentration of Mn in cementite increases gradually during tempering, and this enrichment causes strong retardation in the growth of cementite [30] and similar effect is seen with Cr addition [102]. In fact, Cr partitioning develops more quickly

than Mn [156], and the interface concentrations gradually rise from those dictated by para-equilibrium towards the equilibrium concentrations [103]. In this study, it has been observed that the chemistry of the θ-carbide is consistent with that of the parent metal suggesting that the enrichment of substitutionals in cementite is restricted during non-isothermal tempering even at high temperature (650°C) which is believed to be due to insufficient time available for diffusion of these elements into cementite. Thus corroborating that diffusion of carbon controls the non-isothermal tempering in DP steels.

6.5. Softening behaviour of DP steel

Vickers microhardness measurements were performed in $DP980_A$ steel non-isothermally tempered and isothermally tempered at high temperature for 300s and 5400s (Figure 6.17). To experience the extent of softening, the BM hardness (301 HV) of $DP980_A$ steel is also included (open symbol) in Figure 6.17.

The hardness change in $DP980_A$ steel has been plotted versus the tempering temperature; thus, the non-isothermally tempered specimen at high temperature resulted in hardness reduction (softening) of about 30HV (10%) as shown in Figure 6.17. On the other hand, the hardness dropped 78 HV (26%) and 118 HV (39%) in the isothermally tempered $DP980_A$ specimens at high temperature for 300s and 5400s, respectively. Significant differences are clearly seen in the softening behaviour of non-isothermal and isothermal tempering at high temperature in $DP980_A$ steel (Figure 6.17). Such behaviour is associated with the structural changes occurring in the α' phase during tempering. For example, precipitation of fine carbides, both within the laths and at lath boundaries, and partial recovery of the lath structure was observed in non-isothermal tempering of $DP980_A$ steel at high temperature (Figure 6.8 and Figure 6.11); thus, resulting in less severe softening. Whereas the extensive degree of softening measured in $DP980_A$ steel after isothermal tempering at high temperature is attributed to spheroidization and coarsening of carbides, and to complete recovery of the martensite phase (Figure 6.5). As discussed in an earlier section, Figure 6.12 depicts a schematic illustration of the changes in the substructure of the martensite islands in DP steel after non-isothermal and isothermal tempering at high temperature that strongly influences the softening.

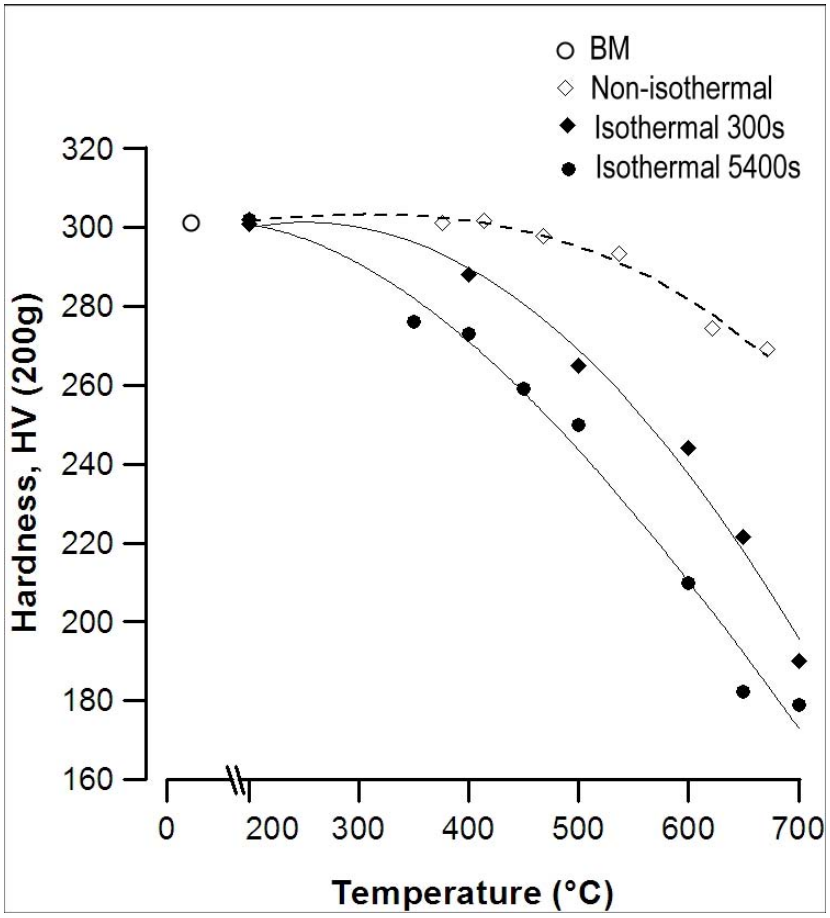

Figure 6.17 Vickers microhardness of DP980$_A$ steel *vs.* tempering temperature subjected to non-isothermal and isothermal tempering for 300s and 5400s.

Furthermore, Vickers microhardness of the BM and the non-isothermally tempered DP980$_B$, DP980$_A$ and DP800 specimens at high temperature is provided in Figure 6.18a, indicating larger hardness reduction after non-isothermal tempering in DP980$_B$ steel, followed by DP980$_A$ and DP800 steels, respectively. The plot indicates that extent of softening follow a trend similar to that of the cementite size (Figure 6.14d-f): DP980$_B$ (high) → DP980$_A$ → DP800 (low). In order to minimize the influence of the different fraction of martensite in the hardness of the assessed DP steels; softening was normalized with respect to the volume fraction of martensite in BM (Figure 6.18b). The results in Figure 6.18b suggest that the richer chemistry steel (DP800) has more resistance to softening upon non-isothermal tempering. Comparable results were observed in recent studies on the softening kinetics of dual-phase steels subjected to rapid thermal cycles (*i.e.*, laser welding) in which higher resistance to softening was seen in richer chemistry DP steels [157]. The higher resistance to softening in DP800 steel in

comparison to $DP980_A$ and $DP980_B$ steels can be well associated with the following observations in this work: fine θ-carbides found in the tempered martensite (Figure 6.14c and Figure 6.14f), less broken appearance in the tempered martensite (Figure 6.14c).

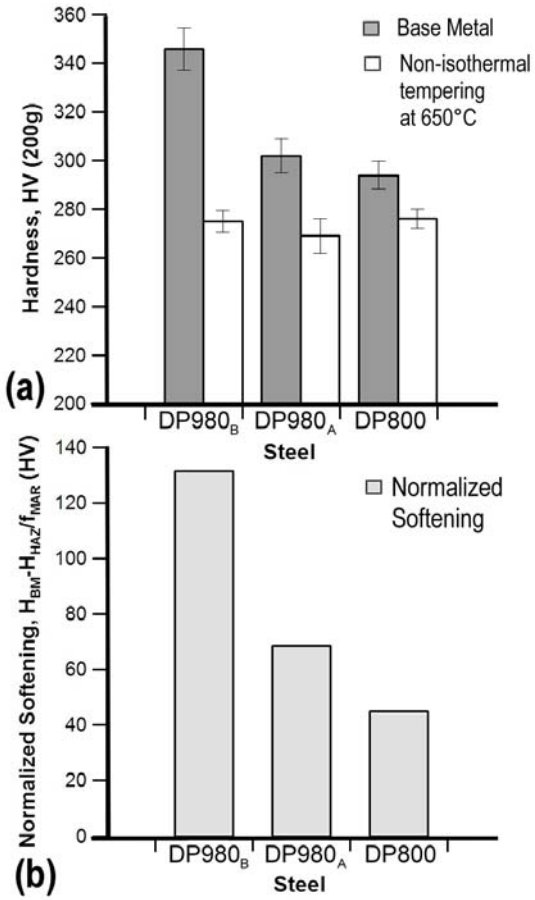

Figure 6.18 (a) Vickers microhardness (HV) obtained at the BM and sub-critical HAZ of $DP980_B$, $DP980_A$ and DP800 steels. (b) Normalized softening with the volume fraction of the BM martensite of $DP980_B$, $DP980_A$ and DP800 steels.

The DP800 steel BM was seen to be composed of mixed structures of lath and twinned martensite (Figure 6.13e) having high carbon content (Table 3-2); in this regard, it is believed that the possible recovery of the martensite substructure is further inhibited in DP800 steel during non-isothermal tempering. In addition, the tremendous drop in hardness observed in $DP980_B$ steel (Figure 6.18) can be associated with the coarser θ-carbides (Figure 6.14a and Figure 6.14d) and the severely decomposed appearance of the tempered martensite (Figure 6.14a). As described previously, $DP980_B$ steel has lower carbon content within α' phase (Table 3-2) and is composed of coarser lath substructure (Figure 6.13d). Hence, it is believed that

possible larger partial recovery of the lath substructure occurred in $DP980_B$ steel in comparison to that in $DP980_A$ steel. These results, however, clearly indicate that softening is more severe in low-carbon containing coarser lath martensite in DP steels subjected to non-isothermal tempering of RSW. Furthermore, the softening is affected strongly by the recovery process of martensite; which is controlled through growth of lath boundary carbides

6.6. Summary

Tempering of the martensite phase in dual-phase (DP) steels has been studied mainly through analytical transmission electron microscopy (TEM) under both isothermal (slow heating and extended time at peak temperature) and non-isothermal conditions (rapid heating, negligible hold time at peak temperature and rapid cooling) and has been correlated to the softening behaviour. TEM analysis of the base metal in the DP steel indicated that the morphology of the martensite phase is dependent on its carbon content, and its tempering characteristics are similar to equal carbon containing martensitic steel. The isothermally tempered structure is characterized by coarsening and spheroidization of cementite (θ) and complete recovery of the martensite laths; whereas precipitation of fine quasi-spherical intralath θ-carbides, plate-like interlath θ-carbides, decomposition of retained austenite into elongated θ-carbides, and partial recovery of the lath structure were observed after non-isothermal tempering of DP steel at high temperature. This difference in tempering behaviour is attributed to synergistic effect of delay in cementite precipitation due to higher heating rate, and insufficient time for diffusion of carbon that delays the later stage of tempering processes (cementite coarsening and recrystalization) during non-isothermal tempering. The finer size and the plate-like morphology of the precipitated carbides along with the partial recovery of the lath structure observed after non-isothermal tempering strongly influenced the softening behaviour of DP steel. The chemical analysis of θ-carbides through extraction replicas for three different chemistries of DP steels revealed that the chemistry of the carbides is inherited from the parent DP steel during non-isothermal tempering at high temperature, confirming that non-isothermal tempering DP steel is predominantly controlled by carbon diffusion.

7. Conclusions and Recommendations

This research work aims at improving the current knowledge on metallurgical interactions occurring in resistance spot welding of dual phase steels by identifying the microstructural characteristics that determine the weldment properties; hence, it has been designed to execute the objectives established in Chapter 1. The results section has been conveniently divided into three chapters. The analysis and discussion of the results have been addressed towards the solution of the exposed problem (Chapter 1). The conclusions of this thesis work presented in the following sections are listed by chapter.

7.1. Influence of HAZ-softening on the joint performance of RSW-DP steel

The objective of this chapter was to analyze the influence of HAZ-softening and the effects of martensite tempering on the tensile performance of resistance spot welded dual-phase steel in similar and dissimilar steel grade combinations. The conclusions are as follows:

The characteristics of the tempered martensite microstructure for DP600, DP780 and DP980 steels have been detailed; the tempered martensite island is comprised of precipitation of carbides dispersed thoroughly along with decomposed substructure (broken appearance) in all DP steel grades. The precipitated carbides were larger in size in the higher grades of DP steel (*i.e.*, DP980) attributed to an extended degree of tempering. Measurable softening in the higher grades of DP steel is attributed to both larger volume fraction of the tempered martensite phase and the severity or degree of tempering occurring within the substructure.

The failure mode changed from interfacial to full pullout failure mode upon lower weld nugget size for DP980. The lowered critical nugget size (d_{Cr}) in DP980 steel is associated to the measurable softening and hence to the degree of tempering of martensite. Measurable softening in DP980 steel promotes strain localization at the sub-critical HAZ and earlier induced failures;

hence, softening phenomena benefits the joint performance (lap-shear tensile) in the dual-phase steel by facilitating pullout failures with increased load-bearing capacity and higher energy absorption.

In comparison of interfacial to pullout failure transition for DP600, DP780 and DP600-DP780, it was found that the transition weld size was driven lower for the dissimilar combination. Pullout failure modes in DP600-DP780 were promoted by HAZ softening in DP780 steel. HAZ softening reduced the strength of the HAZ and resulted in strain localization and primary failure in the DP780 sheet in lap-shear tensile testing of the DP600-DP780 dissimilar welds.

The microstructure and hardness of the fusion zone in dissimilar welds with DP600 paired to DP780 was dependent upon the alloy level of the fusion zone resultant from dilution with the paired material.

7.2. Study of softening phenomena in DP steel by instrumented nano-indentation testing

The objective of this chapter was to evaluate the tempering of martensite in dual phase steel through instrumented nano-indentation testing (nanohardness) measurements on a range of sub-critical heat affected zone microstructures (tempered region).

Several surface preparation procedures were assessed for evaluating the hardness at nano-level. Combination of fine mechanical polishing followed by etching was revealed to produce an acceptable surface condition for assessing BM and SC-HAZ of resistance spot welded dual phase steel through instrumented hardness nanoindentation.

Tempered martensite resulted in significant reduction in nanohardness (softening at nanoscale) with respect to martensitic particles in the base metal. Though ferrite in the sub-critical HAZ was also observed to have minor reduction in nanohardness; it was clear that the tempered martensite was the major contributor to softening when measured at micro-scale.

HAZ-softening was satisfactorily explored by evaluating the tempered martensite at various distances from the line of lower critical temperature Ac_1 through nanoindentation hardness and electron microscopy. Maximum softening was found at 100 μm from Ac_1 where

the tempered martensite was comprised of precipitation of carbides and a broken appearance of the substructure; thus, suggesting partial recovery of martensite. At 1000 μm from Ac_1; finer carbides along with less broken appearance of the substructure suggested low temperature tempering.

SEM and TEM observations resulted in good agreement with the nanohardness of the tempered martensite phase along the sub-critical heat affected zone at which the "actual" extension of the SC-HAZ was clearly revealed. In contrast, microhardness results suggested the termination of tempering at a shorter distance with respect to Ac_1 and hence a reduced extension of the softening region.

The improved resolution for assessing softening through nanoindentation was due to the possibility of avoiding the contribution of the phase boundaries because of the smaller size of the indentation; this in fact, permitted on evaluation of the tempered martensite matrix with less contribution from high-angle boundaries.

7.3. Transmission electron microscopy study of the tempering of martensite phase (or islands) in dual-phase steel

The objective of this chapter was to study the fundamental mechanism and characteristics of martensite tempering at high temperature occurring in the heat affected zone of resistance spot welded dual-phase steel by considering the influence of thermal cycle (isothermal and non-isothermal), prior martensite structure, and chemical composition.

The martensite substructure in DP steels was dependent on its carbon content; for instance, the higher grade (*i.e.*, 1000 MPa) $DP980_B$ and $DP980_A$ steels (< 0.275 wt.% of C) consist of martensite laths and small fraction of retained austenite, whereas the DP800 steel (~ 0.367 wt.% of C) contains a mixture of lath and twin structure.

The isothermal tempering of the martensite islands in $DP980_A$ steel was characterized by coarsening and spheroidization of cementite and complete recovery of the lath substructure suggesting that the tempering characteristics of the martensite phase of DP steel is similar to the tempered structure of low-carbon martensitic steels. The precipitation of θ-carbides is inherited from diffusion of carbon to lattice defects.

Fine quasi-spherical intralath θ-carbides, plate-like interlath θ-carbides, decomposition of

retained austenite into elongated θ-carbides, and partial recovery of the lath structure formed in the non-isothermally tempered martensite in $DP980_A$ steel; attributed to synergistic effect of delay in cementite precipitation due to higher heating rate and insufficient time for diffusion of carbon that delays the third stage of tempering process (cementite coarsening and recovery).The partial recovery of the martensite lath structure was promoted by a pinning effect of the precipitated carbides and to the reduced possibility of lath grain boundary migration or disintegration during non-isothermal tempering.

Analysis of replicas of all DP steels studied indicated that precipitated θ-carbide inherits the bulk chemical composition and adopts a stoichimetric form of M_3C (M=Fe, Mn, Cr) type cementite during non-isothermal tempering.

Softening of $DP980_A$ steel was strongly influenced by the size and the morphology of the precipitated carbides and recovery of the lath structure. Finer carbides and partial recovery of the lath substructure in non-isothermal tempering leads to low softening compared to severe softening in isothermal tempering due to large spheroidized carbides and complete recovery of the lath structure.

The bulk chemistry seemed to strongly influence the softening behavior of the non-isothermally tempered DP steel: lean-chemistry lath martensite ($DP980_B$ steel) resulted in more softening in contrast with the rich-chemistry (mixed lath and twinned martensite) of DP800 steel, which resulted in enhanced resistance to softening. The inherited chemistry in the different DP steels confirmed that tempering (softening) is predominantly controlled by carbon diffusion; however, it seems that substitutionals (i.e., Cr, Mn, etc.) further inhibited the movement of carbon (diffusion) thus delaying the coarsening of carbides and reducing the possibility of recovery (DP800 steel).

7.4. Research contribution

Although extensive knowledge on the tempering of ferrous martensite is available in literature; the process of tempering of martensite subjected to non-isothermal conditions has been barely studied. Particularly, there is no research in this regard on dual phase steels. Fundamental understanding of the mechanism of tempering of martensite phase or islands in dual phase steels has been enhanced in this study and has been connected to measurable softening at two scale levels, *i.e.,* nano- and micro-level. This thesis work provides important

findings that help at understanding the nature of softening phenomena occurring in dual phase steels. Moreover, there exists the possibility of controlling the process parameters in resistance spot welding that might modify but not eliminate softening phenomena within certain limits.

In addition, results in this work permitted on framing the limitations and highlighting the advantages for practical applications (*i.e.*, resistance spot welded dual-phase steel). For instance; tempering of martensite occurs in spite of the non-measurable softening in some grades of DP (*i.e.*, DP600) steel, however, these DP steels are more susceptible to develop undesirable failures. On the other hand, HAZ-softening benefits the joint performance of some DP (*i.e.*, DP980) steels owing to promotion of desirable pullout failures along with increased load bearing capacity and energy absorption.

Results in this work will help on proper design of autobody parts and will enable an increased number of applications of DP steels in the automobile industry. In addition, the attained knowledge of this thesis work can be extended to similar manufacturing processes (*i.e.*, other welding processes, induction heating, resistance heating, etc.) in which non-isotherml tempering of martensite and softening phenomena become important issues.

The following list of journal papers have been accepted for publication in peer review journals:

V.H. Baltazar Hernandez, M.L. Kuntz, M.I. Khan, Y. Zhou, "Influence of microstructure and weld size on the mechanical behaviour of dissimilar AHSS resistance spot welds", Science and Technology of Welding and Joining, Vol. 13, No. 8, pp. 769, (2008), DOI:10.1179/136217108X325470.

V.H. Baltazar Hernandez, S.K. Panda, M.L. Kuntz, Y. Zhou, "*Nanoindentation and microstructure analysis of resistance spot welded dual phase steel*", *Materials Letters*, Vol. 64, pp. 207-210, (2010), DOI:10.1016/j.matlet.2009.10.040.

V.H. Baltazar Hernandez, S.K. Panda, Y. Okita, Y. Zhou, "A study on heat affected zone softening in resistance spot welded dual-phase by nanoindentation", Journal of Materials Science, Vol. 45, pp. 1638-1647, (2010), DOI: 10.1007/s10853-009-4141-0.

S.K. Panda, V.H. Baltazar Hernandez, M.L. Kuntz, Y. Zhou, "Formability analysis of diode-laser welded tailored welded blanks of advanced high strength steel sheets", Metallurgical and Materials Transactions A, Vol. 40A, pp. 1955-1967, (2009), DOI:10.1007/s11661-009-9875-4.

S.K. Panda, J. Li, V.H. Baltazar Hernandez, Y. Zhou, F. Goodwin, “Effect of weld location, orientation and strain path on forming behavior of AHSS tailor welded blanks”, Journal of Engineering Materials and Technology, (2010), Vol. 132, pp. 041003 1-11 (2010), DOI: 10.1115/1.4001965.

7.5. Recommendations for further research

An outlook of future work that could complement the present research field is presented in this section.

Increased hardness (hardening) at the SC-HAZ is an interesting phenomenon that has been observed in some DP600 steels. Such hardening phenomena might influence the mechanical behaviour of spot welds. It is recommended to systematically study the tempering behaviour of this steel through analytical electron microscopy and nanoindentation in order to better understand whether or not tempered martensite islands influence such hardening phenomena and to what degree.

The lower grades of DP steel were characterized by containing some fraction of bainite and/or pearlite; however, it is not understand if bainite tempers (spheroidization) under non-isothermal conditions and if these constituents have some effect on softening at the SC-HAZ of the lower grades of DP steel *i.e.,* DP600 and DP780.

It has been observed that the lower grades of DP steel *viz.* DP600 and DP780 are comprised of comparatively low fraction of martensite. According to calculations in this report; such martensite islands are characterized for containing high carbon content which in fact changed the morphology of the substructure. Such high carbon martensite might promote formation of low-temperature carbides *i.e.,* ε-carbide, however, it is not known whether these carbides are formed, and/or suppressed by the rapid thermal cycles in welding (RSW), particularly, in these steel grades.

Constitutive properties of non-isothermally tempered DP steels become an important issue that needs to be explored. In this regard, it is strongly recommended to simulate weld thermal cycles such as those developed in different welding process (*i.e.,* RSW, LBW, and GMAW). Gleeble simulation machines can be employed to perform simulated thermal cycles and to obtain microstructures and mechanical properties of non-isothermally tempered dual-phase steels. This will enable to combine experimental and analytical results in order to obtain

possible models that could predict structure-property relationships.

Ongoing studies of the effects of weld thermal cycles can be addressed to analyze the influence of cooling rate on HAZ-softening in dual phase steels. It is strongly encouraged designing adequate experimental set up by fixing the heating rate and dwell time, and to vary the cooling rates. This will enable at understanding the degree of affection of cooling rates on softening, especially in welding processes such as RSW in which the cooling rate can be modified through process parameters, *i.e.*, hold time.

Chunky particles of retained austenite (RA) embedded within the ferrite matrix of approximately half micron in size were observed within the SC-HAZ after exposure at subcritical temperatures; there is a lack of information about the properties of RA. The chunky particles of retained austenite should be further investigated in regards to its properties.

References

1. Committee on Automotive Applications: *"Advanced High Strength Steel (AHSS) Application Guidelines"*, International Iron and Steel Institute (eds.), Version 4.1, June, pp. 1-4 (2009).

2. G.R. Speich, *"Physical metallurgy of dual-phase steels"*, in Fundamentals of Dual-Phase Steels, R.A. Kot and B.L. Bramfitt, eds., AIME, New York, NY, p. 3-46 (1981).

3. Advanced high strength steel guidelines: http://www.a-sp.org/publications.htm, accessed March 25 2010.

4. RWMA: *"Resistance Welding Manual"*, Fourth Edition, George H. Buchanan, Bridgeport, NJ. U.S., March (2003).

5. R. D. Stout, *"Weldability of steels"*, Four Edition, Welding Research Council, p. 3 (1987).

6. C. Jian, J. Chiang, J. Zhao, N. Zhou, *"A new perspective on failure modes and weldability lobe of resistance spot welds of advanced high strength steels"*, Sheet Metal Welding Conference XI, AWS Detroit Section, Sterling Heighs Michigan, May 11-14, Paper 6-1 (2004).

7. M. Kuo, J. Chiang, *"Weldability study of resistance spot welds and minimum weld button size methodology development for DP steel"*, SAE World Congress, Technical Paper 2004-01-0169, SAE International, Warrendale PA. USA, March 3-6 (2004).

8. M. Zhou, H. Zhang, S.J. Hu, *"Relationships between quality and attributes of spot welds"*, Welding Journal, April, p. 72-S. (2003).

9. M.I. Khan, M.L. Kuntz, Y. Zhou, *"Effects of weld microstructure on static and impact performance of resistance spot welded joints in advanced high strength steels"*, Sci. Technol. Weld. Joining, vol. 13, no. 1, pp. 49-59 (2008).

10. E. Biro, A. Lee, *"Welded properties of various DP600 chemistries"*, Sheet Metal Welding Conference XI, AWS Detroit Section, Sterling Heighs Michigan, May 11-14, Paper 6-2 (2004).

11. M. Xia, E. Biro, Z. Tian, Y. Zhou, *"Effects of heat input and martensite on HAZ softening in laser welding of dual-phase steels"*, ISIJ Intern., vol. 48, no. 6, pp. 809-814 (2998).

12. P.K. Gosh, *"Thermal cycle and microstructure of heat affected zone (HAZ) of flash butt welded Mn-Cr-Mo dual phase steel"*, ISIJ Intern., vol. 30, no. 4, pp. 317-324 (1990).

13. P.K. Gosh, P.C. Gupta, Ramavtar, B.K. Jha, *"Weldability of intercritical annealed dual-phase steel with the resistance spot welding process"*, Welding Journal, January, p. 7-14 (1991).

14. S.K. Panda, N. Sreenivasan, M.L. Kuntz, Y. Zhou, *"Numerical simulations and experimental results of tensile test behaviour of laser butt welded DP980 steels"*, J. Eng. Mater. Technol., vol. 130, pp. 041003 1-9 (2008).

15. S.K. Panda, M.L. Kuntz, Y. Zhou, *"Finite element analysis of effects of soft zones on formability of laser welded advanced high strength steels"*, Sci. Technol. Weld. Joining, vol. 14, No. 1, pp. 52-61 (2009).

16. N. Sreenivasan, M. Xia, S. Lawson, Y. Zhou, *"Effect of laser welding on formability of DP980 steel"*, J. Eng. Mater. Technol., vol. 130, pp. 041004 1-9 (2008).

17. P.K. Ghosh, P.C. Gupta, R. Avtar, B.K. Jhan, *"Resistance spot weldability of comparatively thick C-Mn-Cr-Mo dual phase steel sheet"*, ISIJ Intern., vol. 30, pp. 233-240 (1990).

18. I. Khan, M.L. Kuntz, E. Biro, Y. Zhou, *"Microstructure and mechanical properties of resistance spot welded advanced high strength steels"*, Materials Transactions, Vol. 49, No. 7, p. 1629-1637 (2008).

19. V.H. Baltazar H., M.L. Kuntz, I.M. Khan, Y. Zhou, *"Influence of microstructure and weld size on the mechanical behaviour of dissimilar AHSS resistance spot welds"*, Sci. Technol. Weld. Joining, vol. 13, no. 8, pp. 769-776 (2008).

20. M. Marya, K. Wang, L. G. Hector, X. Gayden, *"Tensile shear forces and fracture mode in single and multiple weld specimens in dual-phase steel"*, J. Manuf. Sci. Eng. vol. 128, pp. 287-298 (2006).

21. G.R. Speich, W.C. Leslie, *"Tempering of steel"*, Metall. Trans., vol. 3, p. 1043-1053 (1972).

22. G.B. Olson, W.S. Owen: *"Martensite"*, ASM International, USA (1992).

23. R.W.K. Honeycombe, H.K.D.H. Badeshia, *"Steels: microstructure and properties"*, 2nd edition, Edward Arnold ed., London Great Britain (1995).

24. G. Krauss, "Steels Heat Treatment and Processing Principles", ASM International, USA (1990).

25. E.Teking, P.M. Kelly, *"A study of the tempering of steel using transmission electron microscopy"*, in Precipitation from Iron-Base Alloys, G.R. Speich, J.B. Clark, eds., AIM Metallurgical Society Conferences, pp. 173-229 (1965).

26. D. Venugopalan, J.S. Kirkaldy, *"Hardenability concepts with applications to steel"*, Proceedings of a symposium held at Chicago, pp. 249-272 (1977).

27. A.M. Sherman, G.T. Eldis, M. Cohen, *"The aging and tempering of iron-nickel-carbon martensites"*, Metall. Trans. A, Vol. 14A, p. 995-1005 (1983).

28. P.V. Morra, A.J. Böttger, E.J. Mittemeijer: "Decomposition of iron-based martensite – a kinetic analysis by menas of differential scanning calorimetry and dilatometry", J. Therm. Anal. Calorim., vol. 64, pp. 905-914 (2001).

29. R.A. Grange, C.R. Hribal, L.F. Porter: *"Hardness of tempered martensite in carbon and low-alloy steels"*, Metall. Trans., vol. 8A, pp. 1775-1785 (1977).

30. G. Miyamoto, J.C. Oh, K. Hono, T. Furuhara, T. Maki: *"Effect of partition of Mn and Si on the growth kinetics of cementite in tempered Fe-0.6 mass % C martensite"*, Acta Materialia, vol. 55, 5027-5038 (2007).

31. J. Pacyna, A. Jedrzejewska-Strach, M. Strach: "The effect of manganese and silicon on the kinetics of phase transformations during tempering – continuous heating transformation (CHT) curves", J. Mater. Process. Technol., vol. 64, pp. 311-318 (1997).

32. G.R. Speich, A.J. Schwoeble, G.P. Huffman, *"Tempering of Mn and Mn-Si-V dual-phase steels"*, Metall. Trans. A, vol. 14A, pp. 1079-1087 (1983).

33. M.S. Rashid, B.V.N. Rao, *"Tempering characteristics of a vanadium containing dual-phase steel"*, Metall. Trans. A, vol. 13A, pp. 1679-1686 (1982).

34. R.G. Davies, *"Tempering of dual-phase steels"* in Fundamentals of Dual-Phase Steels, R.A. Kot and B.L. Bramfitt, eds., AIME Conference Proceedings, pp. 265-277 (1981).

35. F.H. Samuel, "Effect of dual-phase treatment and tempering on the microstructure and mechanical properties of high strength, low alloy steel", Mater, Sci. Eng. A, vol. 75, pp. 51-66 (1985).

36. P-H. Chang, "Temper-aging of continuously annealed low carbon dual-phase steel", Metall. Trans. A, vol. 15A, pp. 73-86 (1984).

37. A. Joarder, J.N. Jha, S.N. Ojha, D.S. Sarma, *"The tempering behaviour of a plain carbon dual-phase steel"*, Mater. Charact., vol. 25, pp.199-209 (1990).

38. H.S. Lee, B. Hwang, S. Lee, C.G. Lee, S-J Kim, *"Effects of martensite morphology and*

tempering on dynamic deformation behaviour of dual-phase steels", Metall. Mater. Trans. A, vol. 35A, pp. 2371-2382 (2004).

39. S. Subramaniam, R. Koganti, A. Joaquin, A. Elliott, T. Coon and A. Wexler: *"Considerations for spot welding of advanced high strength steels"*, SAE World Congress, Technical Paper 2006-01-0089, SAE International, Warrendale PA. USA, April 3-6 (2006).

40. J.E. Gould, S.P. Khurana, T. Li: "Calculations of cooling rates for a range of automotive welding processes, and their relationship to the hardenability of advanced high strength steels", AWS Sheet Metal Welding Conference XI, Livonia MI, paper 7.1. (2004).

41. Hongyan Zhang, Jacek Senkara, *"Resistance welding: fundamentals and applications"*, 1st Edition, Taylor & Francis Group, Boca Raton Fl., p. 105 (2006).

42. S.S. Babu, M.L. Santella, Z. Feng, B.W. Riemer, J.W. Cohron, *Empirical model of effects of pressure and temperature on electrical contact resistance of metals"*, Science and Technology of Welding and Joining, Vol. 6, No. 3, p.126-132 (2001).

43. W. Li, D. Cerjanec, G.A. Grzadzinski, *"A comparative study of single-phase AC and multiphase DC resistance spot welding"*, Journal of Manufacturing Science and Engineering, Vol. 127, August, p. 583-589 (2005).

44. J.E. Gould, "Modeling primary dendrite arm spacings in resistance spot welds part 1-modeling studies", Welding Journal, Vol. 67, April, p.67-74s (1994).

45. 45 L.E. Svensson, *"Prediction of hardness of spot welds in steels"*, Welding in the World, Vol. 48, no. 11-12, p. 31-35 (2004).

46. J.E. Gould, "An examination of nugget development during spot welding, using both experimental and analytical techniques", Welding J., January, p. 1s-10s (1987).

47. W.L Chuko, J.E. Gould, "Development of appropriate resistance spot welding practice for transformation-hardened steels", Welding Journal, January, p. 1-7 (2002).

48. I. Khan, M.L. Kuntz, Y. Zhou, K. Chan, N. Scotchmer, *"Monitoring the effects of RSW pulsing on AHSS using FEA (SORPAS) Software"*, SAE World Congress, Technical Paper 2007-01-1370, SAE International, Warrendale PA. USA, April 16-19 (2007).

49. V.H. Baltazar Hernandez, M.L. Kuntz, Y. Zhou, K.R. Chan, N. Scotchmer, "*Fusion zone microstructures in resistance spot welding of TRIP to HSLA"*, Sheet Metal Welding Conference XIII, AWS Detroit Section, Livonia Michigan, May 14-16, Paper 1-3 (2008).

50. Keneath Stearling, *"Introduction to the physical metallurgy of welding"*, 1st Edition, Butterworths & Co (Publishers) Ltd., p. 1, 110-112 (1983).

51. R. D. Stout, *"Weldability of steels"*, Fourth Edition, Welding Research Council, p. 3 (1987).

52. J.F. Lancaster, *"Metallurgy of welding"*, Chapman & Hall, Fifth Edition, p. 147-148 (1993).

53. Sindo Kou, *"Welding metallurgy"*, Second Edition, John Willey & Sons Inc., Hoboken New Jersey, p. 143, 393,405 (2003).

54. Y.J. Chao, *"Failure mode of spot welds: interfacial versus pullout"*, Science and Technology of Welding and Joining, Vol. 8, No. 2, pp. 133 (2003).

55. Y. J. Chao, "Ultimate strength and failure mechanism of resistance spot weld subjected to tensile, shear, or combined tensile/shear loads", Journal of Engineering Materials Technology, Vol. 125, April, p. 125-132 (2003).

56. American Welding Society D8 Committee on Automotive Welding AWS D8.1M, *"Specification for automotive weld quality – resistance spot welding of steel"*, American Welding Society, 1st edition, (2007).

57. ANSI/AWS/SAE/D8.9–97, "Recommended practices for test methods for evaluating the resistance spot welding behaviour of automotive steels", p.18 (1997).

58. S. Zuniga, S. Sheppard, *"Resistance spot weld failure loads and modes in overload conditions"*, Fatigue and Fracture Mechanics, Vol. 27, p. 469-489 (1997).

59. M. Pouranvari, H.R. Asgari, S.M. Mosavizadch, P.H. Marashi, M. Goodarzi, *Effect of weld nugget size on overload failure mode of resistance spot welds"*, Science and Technology of Welding and Joining, Vol. 12, No. 3, p. 217-225 (2007).

60. H.K.D.H. Bhadeshia, *"Martensite in steels"*, http://www.msm.cam.ac.uk/phase-trans/2002/martensite.html, accessed on April 10 2010.

61. Gareth Thomas, *"Electron microscopy investigations of ferrous martensites"*, Metall. Trans., vol. 2, pp. 2373-2385 (1971).

62. T. Maki, K. Tsuzaki, I. Tamura: *"The morphology of microstructure composed of lath martensites in steels"*, Trans. ISIJ, vol. 20, pp. 207-214 (1980).

63. R.W.K. Honeycombe, H.K.D.H Bhadeshia, *"Steels – microstructure and properties"*, Metallurgy and Materials Science, Arnold, First Edition, Great Britain (1981).

64. I.B. Timokhina, P.D. Hodgson, E.V. Pereloma, "Transmission electron microscopy characterization of the bake-hardening behaviour of transformation induced plasticity and dual phase steel", Metallurgical and Materials Transactions A, Vol. 38A, October, p.2442-

2454 (2007).

65. S Chatterjee, A.K. Verma, V. Sharma, *"Direct-cast dual-phase steel"*, Scripta Materiala, ELSEVIER, Vol. 58, p. 191-194 (2008).

66. H. Terao, "Structure and mechanical properties of high-manganese dual-phase steels", Journal of Materials Science, Vol. 21, p. 1715-1720 (1986).

67. P. Messien, J-C. Herman, T. Gréday, *"Phase transformation and microstructures of intercritically annealed dual-phase steels"*, in Fundamentals of Dual-Phase Steels, R.A. Kot and B.L. Bramfitt, eds., AIME, New York, NY, p. 161-180 (1981).

68. G.R. Speich, V.A. Demarest, R.L. Miller, *"Formation of austenite during intercritical annealing of dual-phase steels"*, Metallurgical and Materials Transactions A, Vol. 12A, p. 1419-1428 (1981).

69. I.A. EI-Sesy, Z.M. EI-Baradie: *"Influence of carbon and/or iron carbide on the structure and properties of dual-phase steels"*, Mater. Lett., vol. 57, pp. 580-585 (2002).

70. J. Huang, W.J. Poole, M. Militzer, "Austenite formation during intercritical annealing", Metallurgical and Materials Transactions A, Vol. 35A, p. 3363-3375 (2004).

71. A. Joaquin, A.N.A. Elliot, C. Jian, V. Rajan, D. Hartam, C. Karas, *"Gas metal arc welding of advanced high strength steel-developments for optimized welding control and weld quality"*, SAE World Congress, Technical Paper 2006-01-0300, SAE International, Warrendale PA. USA, April 3-6 (2006).

72. M. Milititsky, E. Pakalnins, C. Jian and A. Thompson, *"On characteristics of DP600 resistance spot welds"*, SAE World Congress, Technical Paper 2003-01-0520, SAE International, Warrendale PA. USA, March 3-6 (2003).

73. M. Marya, X.Q. Gayden, *"Development of requirements for resistance spot welding dual phase (DP600) part 1, the causes of interfacial fracture*", Welding Journal, December, pp. 172s-182s (2005).

74. M. Marya, X.Q. Gayden, *"Development of requirements for resistance spot welding dual phase (DP600) part 2,* statistical analysis and process maps", Welding Journal, December, pp. 197s-204s (2005).

75. C. Ma, D.L. Chen, S.D. Bhole, G. Boundreau, A. Lee, E. Biro, *"Microstructure and fracture characteristics of spot-welded DP600 steel"*, Mat. Sci. Eng. A, vol. 485, pp. 334-346 (2008).

76. J. Chiang, C. Jiang, *"Effect of cooling time on fracture toughness at the simulated HAZ of DP600 steels"*, SAE World Congress, Technical Paper 2004-01-0165, SAE International,

Warrendale PA. USA, March 8-11 (2004).

77. M. Kuo, J. Chiang, *"Weldability study of resistance spot welds and minimum weld button size methodology development for DP steel"*, SAE World Congress, Technical Paper 2004-01-0169, SAE International, Warrendale PA. USA, March 8-11 (2004).

78. S. Subramaniam, R. Koganti, A. Joaquin, A. Elliott, T. Coon, A. Wexler, *"Considerations for spot welding of advanced high strength steels"*, SAE World Congress, Technical Paper 2006-01-0089, SAE International, Warrendale PA. USA, April 3-6 (2006).

79. T. Taka, K. Kunishige, N. Yamauchi, N. Nagao, *Hot-rolled steel sheet with excellent flash weldability for automotive wheel rim use"*, ISIJ Intern., vol. 29, no. 6, pp. 503-510 (1989).

80. P.K. Ghosh, P.C. Gupta, O.M. Pal, R. Avtar, B.K. Jha, V. Sagar Dwivedi, *"Influence of weld thermal cycle on properties of flash butt welded Mn-Cr-Mo dual phase steel"*, ISIJ Intern., vol. 33, no. 7, pp. 807-815 (1993).

81. G.B. Olson, M. Cohen, *"Early stages of aging and tempering of ferrous martensites"*, Metall. Trans. A, vol. 14A, pp.1057-1065 (1983).

82. Y. Imai, *"Phases in quenched and tempered steels"*, Trans. JIM, vol. 16, pp. 721-734 (1975).

83. Y. Hirotsu, S. Nagakura, *"Crystal structure and morphology of the carbide precipitated from martensitic high carbon steel during the first stage of tempering"*, Acta Metallurgica, vol. 20, pp. 645-655 (1972).

84. Y. Hirotsu, S. Nagakura, *"Electron microscopy and diffraction study of the carbide precipitated at the first stage of tempering of martensitic steel"*, Trans. JIM, vol. 15, pp. 129-134 (1974).

85. Y. Hirotsu, Y. Itakura, K-C. Su, S. Nagakura, *"Electron microscopy and diffraction study of the carbide precipitated from martensitic low and high nickel steels at the first stage of tempering"*, Trans. JIM, vol. 17, pp. 503-513 (1976).

86. S. Nagakura, M. Toyoshima, *"Crystal structure and morphology of the ordered phase in iron-carbon martensite"*, Trans. JIM, vol. 20, pp. 101-110 (1979).

87. Y. Tanaka, K. Shimizu, *"Carbide formation upon tempering at low temperatures in Fe-Mn-C alloys"*, Trans. JIM, vol. 22, No. 11, pp. 779-788 (1981).

88. M.G.H. Wells, *"An electron transmission study of the tempering of martensite in an Fe-Ni-C alloy"*, Acta Metallurgica, vol. 12, pp. 389-399 (1964).

89. C.J. Barton, *"The tempering of low-carbon internally twinned martensite"*, Acta

Metallurgica, vol. 17, pp. 1085-1093 (1969).

90. R. Padmanabhan, W.E. Wood, *"Precipitation of ε-carbide in martensite"*, Mater. Sci. Eng., vol. 65, pp. 289-297 (1984).

91. K.A. Taylor, G.B. Olson, M. Cohen, J.B. Vander Sande, *"Carbide precipitation during stage I tempering of Fe-Ni-C martensites"*, Metall. Mater. Trans. A, vol. 20A, pp. 2749-2765 (1989).

92. K.A. Taylor, L. Chang, G.B. Olson, G.D.W. Smith, M. Cohen, J.B. Vander Sande, *"Spinodal decomposition during aging of Fe-Ni-C martensites"*, Metall. Trans. A, vol. 20A, pp. 2717-2737 (1989).

93. Y. Ohmori, *"χ-carbide formation and its transformation into cementite during tempering of martensite"*, Trans. JIM, vol. 13, pp. 119-127.

94. E.R. Petty, *"Martensite, fundamentals and technology"*, Longman Group Limited, London GB, (1970).

95. D.L. Williamson, R.G. Schupmann, J.P. Materkowski, G. Krauss, *"Determination of small amounts of austenite and carbide in hardened medium carbon steels by Mössbauer Spectroscopy"*, Metall. Trans., vol. 10A, pp. 379-382 (1979).

96. G. Thomas, *"Retained austenite and tempered martensite embrittlement"*, Metall. Trans. A, vol. 9A, pp. 438-450 (1978).

97. M. Sarikaya, A.K. Jhingan, G. Thomas, *"Retained austenite and tempered martensite embrittlement in medium carbon steels"***,** Metall. Trans. A, vol. 14A, pp. 1121-1133 (1983).

98. G. Ghosh, G.B. Olson, *"Precipitation of paraequilibrium cementite: experiments, and thermodynamic and kinetic modeling"*, Acta Materialia, vol. 50, pp. 2009-2019 (2002).

99. S.S. Babu, K. Hono, T. Sakurai, *"Atom probe field ion microscopy study of the partitioning of substitutional elements during tempering of low-alloy steel martensite"*, Metall. Mater. Trans. A, vol. 25A, pp. 499-508 (1994).

100. G. Miyamoto, J.C. Oh, K. Hono, T. Furuhara, T. Maki, *"Effect of partitioning of Mn and Si on the growth kinetics of cementite in tempered Fe-0.6 mass% martensite"*, Acta Materiallia, vol. 55, pp. 5027-5038 (2007).

101. S.S. Babu, K. Hono, T. Sakurai, *"APFIM studies on martensite tempering of Fe-C-Si-Mn low alloyed steel"*, Appl. Surf. Sci., vol. 67, pp. 321-327 (1993).

102. J. Chance, N. Ridley: *"Chromium partitioning during isothermal transformation of a*

eutectoid steel", Metall. Trans., 1981, vol. 12A, pp. 1205-1213.

103. R.C. Thomson, M.K. Miller, *"Carbide precipitation in martensite during the early stages of tempering Cr and Mo-containing low alloy steels"*, Acta Materiallia, vol. 46, no. 6, pp. 2203-2213 (1998).

104. R. N. Caron, G. Krauss, *"The tempering of Fe-C lath martensite"*, Metall. Trans., vol. 3, pp. 2381-2389 (1972).

105. L.M. Clarebrough, M.E. Hargreaves, M.H. Loretto, *"Changes in internal energy associated with recovery and recrystallization"*, in Recovery and Recrystallization of Metals, L. Himmel, ed., American Institute of Mining, Metallurgical, and Petroleum Engineers, Gordon and Breach, New York (1963).

106. S. Takaki, S. Iizuka, K. Tomimura, Y. Tokunaga, *"Role of carbide in the recovery process of 0.2% carbon lath martensitic structure"*, Mater. Trans. JIM, vol. 32, No. 3, pp. 207-213 (1991)

107. T. Maki, S. Morito, T. Furuhara: *"The change in matrix structure during tempering of lath martensite in Fe-C alloys"*, 19th ASM heat treating society conference proceedings including steel heat treating in the new millennium, Cincinnati OH., 1-4 November, pp. 631-637 (1999).

108. M. Tokizane, N. Matsumura, K. TT. Maki, I. Tamura, *"Recrystallization and formation of austenite in deformed lath martensitic structure of low carbon steels"*, Mater. Trans. A, vol. 13A, pp. 1379-1388 (1982).

109. T. Furuhara, K. Kobayashi, T. Maki, *"Control of cementite precipitation in lath martensite by rapid heating and tempering"*, ISIJ Int., vol. 44(11), pp. 1937-1944 (2004).

110. A. Nagao, K. Hayashi, K. Oi, S. Mitao, N. Shikanai, *"Refinement of cementite in high strength plates by rapid heating and tempering"*, Mat. Sc. Forum, vols. 539-543, pp. 4720-4725 (2007).

111. S. Tae Ahn, D.S. Kim, W.J. Nam, *"Microstructural evolution and mechanical properties of low alloy steel tempered by induction heating"*, J. Mater. Process. Technol., vol. 160, pp. 54-58 (2005).

112. Y. Zhang, N. Gey, C. He, X. Zhao, L. Zuo, C. Esling, *" High temperature tempering behaviors in structural steel under high magnetic field"*, Acta Materialia, vol. 52, pp. 3467-3474 (2004).

113. W.C. Oliver, G.M. Pharr, *"Measurement of hardness and elastic modulus by instrumented indentation: advances in understanding and refinements to methodology"*, J. Mat. Res., vol. 19, no.1, pp. 3-20 (2004).

114. A.C. Fisher-Cripps, *"Nanoindentation"*, Second Ed., Springer, New York (2004).

115. W.C. Oliver, G.M. Pharr, *"An improved technique for determining hardness and elastic modulus using load and displacement sensing indentation experiments*, J. Mat. Res., vol. 7, no.6, pp. 1564-1583 (2004).

116. S. Shim, H. Bei, E.P. George, G.M. Pharr, *"A different type of indentation size effect"*, Scripta Materialia, vol. 59, pp. 1095-1098 (2008).

117. A.A. Zbib, D.F. Bahr, *"Dislocation nucleation and source activation during nanoindentation yield points"*, Metall. Mater. Trans. A, vol. 38A, pp. 2249-2255 (2007).

118. T. Ohmura, T. Hara, K. Tsuzaki, *"Evaluation of temper softening behavior of Fe-C binary martensitic steels by nanoindentation"*, Scrip. Mat., vol. 49, pp. 1157-1162 (2003).

119. M. Delincé, P.J. Jacques, T. Pardoen, *"Separation of size-dependent strengthening contributions in fine-grained dual phase steels by nanoindentation"*, Acta Materialia, vol. 54, pp. 3395-3404 (2006).

120. N. Yurioka, H. Suzuki, S. Ohshita, S. Saito, *"Determination of necessary preheating temperature in steel welding"*, Welding Journal., June, p.147-153 (1983).

121. I.A. EI-Sesy, Z.M. EI-Baradie, *"Influence of carbon and/or iron carbide on the structure and properties of dual-phase steels"*, Mater. Lett., vol. 57, p. 580-585 (2002).

122. Smith William F., Hashemi Javad, *"Foundations of materials science and engineering"*, fourth edition, McGraw-Hill, p. 363 (2006).

123. V.H. Baltazar H., M.I. Khan, M.L. Kuntz, Norman Zhou, *"Mechanical performance of resistance spot welds in dissimilar AHSS combinations"*, Materials Science & Technology Conference and Exhibition**,** Cobo Center, Detroit Michigan, September 16-20 2007, P 217-225 (2007).

124. http://www.rccm.co.jp/seihin/quickspot/index.html. Accessed 21 Jul 2009

125. SORPAS® 8.0 (2007) Swantec Software and Engineering APS.

126. Y. Okita, (2008) JFE Steel, Internal Communications.

127. S.H. Lin, J. Pan, S.R. Wu, T. Tyan, P. Wung, *"Failure loads of spot welds under combined opening and shear static loading conditions"*, International Journal of Solids and Structures, Vol. 39, p. 19-39 (2002).

128. M. Erdogan, S. Tekeli, *"The effect of martensite particle size on the tensile fracture of surface-carburized ASI 8620 steel with dual phase core microstructure"*, Materials &

Design, Vol. 23, p. 597-604 (2002).

129. S.G. Chowdhury, E.V. Pereloma, D.B. Santos, *"Evolution of texture at the initial stages of continuous annealing of cold rolled dual-phase steel: Effect of heting rate"*, Mat. Sci. Eng. A, vol. 480, pp. 540-546 (2008).

130. Easterling K., *"Introduction to the physical metallurgy of welding"*, Butterworths, (1983).

131. A. Garcia-Junceda, F.G. Caballero, C. Capdevila, C. Garcia deAndrés, *"Determination of local carbon content in austenite during intercritical annealing of dual-phase steels by PEELS analysis"*, Scr. Mater., vol. 57, pp. 89-92 (2007).

132. T. Ohmura, K. Tsuzaki, S. Matsuoka, *"Evaluation of temper softening behaviour of Fe-C binary martensitic steels by nanoindentation"*, Scr. Mater., vol. 45, pp. 889-894 (2001).

133. R.W.K. Honeycombe, H.K.D.H. Bhadeshia, *"Steels microstructure and properties"*, Second. ed., Arnold, Great Britain (1995).

134. T.C. Lei, G.Y. Lin, Y.X. Cui, *"Dislocation substructures in ferrite of plain carbon dual-phase steels after fatigue fracture"*, Fatigue Fract. Eng. Mater. Struct., vol. 17, No. 4, pp. 451-458 (1994).

135. A.S. Podder, D. Bhattacharjee, R.K. Ray, *"Effect of martensite on the mechanical behaviour of ferrite-bainite dual phase steel"*, ISIJ Int., vol. 47, no. 7, pp. 1058-1064 (2007).

136. J.Y. Kim, J.J. Lee, Y.H. Lee, J. Jang, D. Kwon, *"Surface roughness effect in instrumented indentation: a simple contact depth model and its verification"*, J. Mater. Res., vol. 21, no. 12, pp. 2975-2978 (2006).

137. W. D. Nix, H. Gao, *"Indentation size effects in crystalline materials: a strain gradient plasticity"*, J. Mech. Phys. Solids, vol. 46, no. 3, pp. 411-425 (1998).

138. D. Ma, C. Wo Ong, S.F. Wong, *"Evaluation of macro-hardness from nanoindentation test"*, J. Mater. Sci., vol. 40, pp. 2685-2687 (2005).

139. A.A. Zbib, D.F. Bahr, *"Dislocation nucleation and source activation during nanoindentation yield points"*, Metall. Mater. Trans. A, vol. 38, pp. 2249-2255 (2007).

140. T. Ohmura, T. Hara, K. Tsuzaki, H. Nakatsu, Y. Tamura, *"Mechanical characterization of secondary-hardening martensitic steel using nanoindentation"*, J. Mater. Res., vol. 19, no. 1, pp. 79-84 (2004).

141. J. H. Hollomon and L. D. Jaffe, *"Time-temperature relations in tempering steel"*, Trans. AIME, vol. 162**,** pp. 223-249 (1945).

142. K.O. Kese, Z.C.Li, B. Bergman, *"Method to account for true contact area in soda-lime glass during nanoindentation with the Berkovich tip"*, Mat. Sci. Eng. A, vol. 404, pp. 1-8 (2005).

143. A. Bolshakov, G.M. Pharr, *"Influences of pileup on the measurement of mechanical properties by load and depth sensing indentation techniques"*, J. Mat. Res., vol. 13, no.4, pp. 1049-1058 (1998).

144. P. Sathiya, S. Aravindan, R. Soundararajan, A. Noorul Haq, *"Effect of shielding gases on mechanical and metallurgical properties of duplex stainless steel welds"*, J. Mater. Sci., vol. 44, pp. 114-121 (2009).

145. V.H. Baltazar Hernández, S.K. Panda, Y. Okita, Y. Zhou, *"A study on heat affected zone softening in resistance spot welded dual-phase by nanoindentation"*, J. Mater. Sci., vol. 45, pp. 1638-1647 (2010).

146. M.K. Miller, P.A. Beaven, D.W. Smith: *"A study of the early stages of tempering of iron-carbon martensites by atom probe field ion microscopy"*, Metall. Mater. Trans. A, vol. 12A, pp. 1197-1204 (1981).

147. D. Kalish, M. Cohen, *"Structural changes and strengthening in the strain tempering of martensite"*, Mater. Sci. Eng., vol. 6, pp. 156-166 (1970).

148. E.J. Fasika, G.A. Jeffrey, Acta Crystallogr., vol. 19, pp. 463 (1965).

149. G.R. Speich: *"Tempering of low-carbon martensite"*, Trans. AIME, vol. 245, pp. 2553 (1969).

150. K.T. Aust, J.W. Rutter: *"Grain boundary migration"*, Recovery and recrystallization of metals, American Institute of Mining, Metallurgical and Petroleum Engineers, pp. 133-169 (1963).

151. F.G. Wei, K. Tsuzaki: *"Crystallography of [001]/54.7° lath boundary and cementite in tempered 0.2C steel"*, Acta Materialia, vol. 53, pp. 2419-2424 (2005).

152. W.D. Callister: *"Materials Science and Engineering"*, 7th Edn, p. 501.

153. X. Huang, N. H. Pryds: *"Crystallography and morphology of cementite precipitates formed during rapid solidification of a ferritic stainless steel"***,** Acta Materialia, vol. 48, pp. 4073-4082 (2000).

154. P. Schaaf, S. Wiesen, U. Gonser: *"Mössbauer study of iron carbides: cementite $(Fe, M)_3C$ (M=Cr, Mn) with various manganese and chromium contents"*, Acta Mater., vol. 40, pp. 373-379 (1992).

155. R.C. Thomson, H.K.D.H. Bhadeshia, *"Changes in chemical composition of carbides in 2.25Cr-1Mo power plant steel: part 2 mixed microstructure"*, Mater. Sci. Technol., vol. 10, pp. 205-208 (1994).

156. R.C. Thomson, M.K. Miller, *"The partitioning of substitutional solute elements during the tempering of martensite in Cr and Mo containing steels"***:** Appl. Surf. Sci., vol. 87/88, pp. 185-193 (1995).

157. E. Biro, J.R. McDermid, J.D. Embury, Y. Zhou: *"Softening kinetics in the sub-critical heat affected zone of dual phase steel welds"*, Metall. Mater. Trans. A, 2010, Vol. 41, pp. 2348-2356.